Solvent Electrostatic Response:

From Simple Solutes to Proteins

by

Mohammadhasan Dinpajooh

A Dissertation Presented in Partial Fulfillment
of the Requirements for the Degree
Doctor of Philosophy

Approved May 2016 by the
Graduate Supervisory Committee:

Dmitry V. Matyushov, Chair
Ranko Richert
Oliver Beckstein

ARIZONA STATE UNIVERSITY

August 2016

ABSTRACT

How water behaves at interfaces is relevant to many scientific and technological applications; however, many subtle phenomena are unknown in aqueous solutions. In this work, interfacial structural transition in hydration shells of a polarizable solute at critical polarizabilities is discovered. The transition is manifested in maximum water response, the reorientation of the water dipoles at the interface, and an increase in the density of dangling OH bonds. This work also addresses the role of polarizability of the active site of proteins in biological catalytic reactions. For proteins, the hydration shell becomes very heterogeneous and involves a relatively large number of water molecules. The molecular dynamics simulations show that the polarizability, along with the atomic charge distribution, needs to be a part of the picture describing how enzymes work. Non-Gaussian dynamics in time-resolved linear and nonlinear (correlation) 2D spectra are also analyzed.

Additionally, a theoretical formalism is presented to show that when preferential orientations of water dipoles exist at the interface, electrophoretic charges can be produced without free charge carriers, i.e., neutral solutes can move in a constant electric field due to the divergence of polarization at the interface. Furthermore, the concept of interface susceptibility is introduced. It involves the fluctuations of the surface charge density caused by thermal motion and its correlation over the characteristic correlation length with the fluctuations of the solvent charge density. Solvation free energy and interface dielectric constant are formulated accordingly. Unlike previous approaches, the solvation free energy scales quite well in a broad range of ion sizes, namely in the range of 2-14 Å. Interface dielectric constant is defined such that the boundary conditions in the Laplace equation describing a micro- or mesoscopic interface are satisfied. The effective dielectric constant of interfacial water is found to be significantly lower than its bulk value. Molecular dynamics simulation results show that the interface dielectric constant for a TIP3P water model changes from

nine to four when the effective solute radius is increased from 5 Å to 18 Å. The small value of the interface dielectric constant of water has potentially dramatic consequences for hydration.

DEDICATION

To Paula, Maryam, and Jamshid

ACKNOWLEDGMENTS

It is reported that Einstein once said: "I prefer an attitude of humility corresponding to the weakness of our intellectual understanding of nature and of our own being." It is with the same sense of humility that I acknowledge those who helped me improve in areas of intellectual understanding as I progressed and achieved this degree at ASU.

First, I would like to thank my advisor Prof. Dmitry V. Matyushov for guiding me through the world of theoretical chemistry. I appreciate his ability to make complex problems simple to understand. The Matyushov research group also offered valuable feedback on my projects. In particular, I appreciate Dr. Daniel Martin for his help with the setup and analysis of cytochrome *c* simulations and sharing the ralated codes.

Second, I am grateful to the faculty members who served on my committees: Professors Ranko Richert, Oliver Beckstein, Andrew Chizmeshya, and Michael Thorpe. Their insights were very valuable as I progressed through the program. I am also indebted to Prof. Austen Angell for his feedback and insights during my presentations at ASU. He helped me to improve backgrounds which are required to advertise my work in academic conferences. Finally and most importantly, I would like to thank my family for their continued support and assistance in ways that are too many to name.

This work was supported by the National Science Foundation (CHE-1464810) and through XSEDE (TG-MCB080116N).

TABLE OF CONTENTS

LIST OF TABLES

LIST OF FIGURES

Chapter 1

INTRODUCTION AND THEORETICAL FRAMEWORK

1.1 Introduction

The solvent electrostatic response has been the focus of well-known theories such as Born theory of ion solvation[1] and Marcus theory of electron transfer[2, 3, 4, 5, 6]. In this work, new theories based on the electrostatic response of solvent under various conditions are developed to address a variety of problems in condensed/soft matter and biology. Molecular simulation methods are often developed and performed to assess the theories. Common themes are the electrostatics of interface and electron transfer, where collective phenomena, such as solvent polarization fluctuations, appear to play an important role due to the correlations that can extend to large length scales and time scales.

The response of the solvent is related to the interaction of solute/reactant with the solvent[7, 8], as well as the excluded volume of the solute[9] and is manifested in the interfacial solvent microscopic structures, the interfacial polarization, and the fluctuations caused by thermal nuclear motions of interface solvent molecules[10, 11, 12, 13]. These properties play important roles in biological and chemical phenomena such as efficient electron transfer in biological systems, where the fluctuations are caused by a heterogeneous water and protein interface (as a part of solvent)[14]. The fluctuations are among the reasons for the low energy loss of electron transport in biological systems such as the mitochondrial membrane interface [13, 15, 16, 17], where 8-9 electrons travel over a relatively large distance (tens of nanometer) to produce one Adenosine Triphosphate (ATP). The problem is, in fact, complicated. Four complexes, i.e., complexes I-IV, as well as

electron carriers such as Quinone and cytochrome *c* are usually involved in this process, where cytochrome *c* transports electron from complex III to complex IV at the membrane interface[18, 19]. In this work, computational and theoretical approaches are used to address several related phenomena at interfaces.

In principle, the electrostatics of interfaces is different from electrostatics of bulk materials due to the electrostatic inhomogeneity, which affects solvation and interaction of charged and polar molecules and produces a broad interfacial region with special structure[20]. In chapter 2, the concept of interface susceptibility[12] is introduced. It considers the fluctuations of the surface charge density caused by thermal motion and its correlation over the characteristic correlation length with the fluctuations of the solvent charge density. Solvation free energy is obtained as a radial integral over the interface susceptibility function for which an exact relation is derived. Making use of this function, an exact formalism is used to report the dielectric constant entering the boundary value problem of electrostatics at micro- to mesoscopic interfaces. This formalism is applied to a number of aqueous interfaces and is shown to provide robust results based on three-particle correlation functions, which can be sampled by numerical simulations. The dielectric constant of interfacial water turns out to be an order of magnitude below its bulk value.

In chapter 3, the recent discovery of a spike in the solvent polarization fluctuations in the non-harmonic regime [21] is presented. In the non-harmonic regime, the reversible work of creating a fluctuation of the solvent field is cancelled by the negative free energy invested in polarizing the solute. Since both of these free energies are quadratic functions of the solvent field, the quadratic terms in electrostatic free energy of solution vanish in this regime. This discovery suggests that some configuration of the solution can produce a greater sensitivity and, as a result, a greater control of the chemical reactivity in (bio)chemistry. This discovery is significant because the change of the solvent effect of

dense liquid solvents at normal conditions is often hard to achieve. It is discussed how the solvent response and microscopic structures change when the electrostatic solvation free energy functional becomes non-harmonic. Motivated by the structural transition that occurs in the non-harmonic regime, as indicated by the change in the number of OH dangling bonds, the possibility of using this phenomenon in the (bio)organic synthesis or heterogeneous on-water catalysis is promising. For example, the change in the microscopic solvent structure is important in the homogeneous and heterogeneous on-water catalyses[22, 23] or the preferential formation of peptide bonds at the liquid-vapor interface[24]. Additionally, solvent polarization fluctuations in the non-harmonic limit can play an important role in reactions such as electron transfer, where the probability to reach the transition states can be enhanced and they can aid the reactants to pass the activation barriers[8].

In chapter 4, a formalism is presented to explain the electrophoretic mobility of air bubbles or oil drops in water, which is based on interfacial polarization and different susceptibilities at the solute interface and shear surface. The discrepancy between the recent surface-sensitive sum frequency generation experiments[25] and macroscopic measurements based on zeta potential[26] can be explained by this formalism. For nearly a century absorbed hydroxide ions were considered to be responsible for the migration of oil drops and air bubbles to the positive electrode and the apparent negative charge extracted from the mobility[27, 28, 29, 30]. The possibility that mobility can be related to the ordering of water in the interface has been suggested[31, 32, 33, 34, 35, 36, 37]. In the attempts to prove it, simulations have suffered from the use of inadequate ensembles[38, 39, 40] and, more importantly, from the lack of an established theoretical framework allowing to analyze the data from both numerical and laboratory experiments in a unified formalism. A simple theoretical framework is proposed to analyze the problem and it has been confirmed that ordering and polarization of water in the interface can produce an elec-

trophoretic charge without free charge carriers. A number of simulations of model solutes in several force field models of water are presented to show that the surface charge density coming from the interfacial order is comparable with experimental estimates. It is suggested that new experiments involving manipulation of nanoparticles with light to prove the theory predictions.

Based on the power-law dependence of optical spectroscopy measurements on the external electric field, linear and nonlinear spectroscopies are classified[41], and can provide important information about solvent response and its dynamics[42, 43, 44, 45]. In chapter 5, lineshapes of linear and two-dimensional (2D) correlation spectroscopies are derived for a model considering a linear plus quadratic dependence of the spectroscopic transition frequency on a Gaussian nuclear coordinate of the thermal bath (linear-quadratic coupling)[46]. These results are significant because they provide a straightforward approach for modeling the lineshape function and projecting that result onto a set of parameters providing insight into the underlying molecular behavior and analysis of the experimental data. Importantly, it is demonstrated that both the statistics and the dynamics of the transition frequency fluctuations are non-Gaussian and that the nonlinear dependence of the transition frequency on the system-bath interaction can cause the two-point frequency correlation function to differ from the bath correlation function. These results have significant implications for the interpretation of 2D correlation spectra. The analytical results are tested against explicit molecular dynamics simulations.

In chapter 6, the solvent response in biological systems is investigated to find potential mechanisms to lower the activation barrier in electron transfer. This is done by performing mixed quantum mechanical/molecular dynamics simulations[47] of half reaction of reduction of cytochrome *c*. The main distinction of this study from previous studies is the inclusion of a large number, i.e. 100, of excited quantum states, which allow the active site

to both be polarizable and change its polarizability when altering the redox state. A significant lowering of the activation barrier for electron transfer is shown when polarizability is allowed. Mechanistically, two reorganization energies, instead of one in the Marcus theory, are required to describe the barrier for electron transfer self-exchange[13, 15]. Polarizability of active sites, along with the atomic charge distribution, needs to be a part of the picture describing how enzymes work.

1.2 Solvent Response

In this section, related experimental and theoretical approaches that are used to measure/obtain the solvent response are presented. First, time-resolved and steady-state emission spectroscopies are discussed, which involve the local inhomogeneous fields (also known as cavity fields). Second, related nonlinear spectroscopies are introduced[41, 48]. Then, a brief discussion of dielectric relaxation experiments is presented[49], which involves homogeneous Maxwell fields. This section is followed by a discussion of theoretical and simulation approaches used to investigate solvent response. At the end of this section, it is discussed how the solvent response in proteins and large solutes is different from small solutes whose global multipole moments and the excluded volume effects determine their solvent responses.

1.2.1 Experimental Approaches

1.2.1.1 Time-resolved and Steady State Emission Spectroscopies

A common way to measure the solvent response is based on monitoring the relaxation of the excited state of the chromophore. When the excited state is prepared by fluorescence spectroscopy, the lifetime is typically between 1 ps to 1 ns and many liquids near room temperature display relaxation processes in this time regime[50]. Water at standard conditions is a low viscous solvent, and fluorescence spectroscopy may be used to investigate water response. When the chromophore has phosphorescence properties, the excited state lifetime is long, typically between 1 ms to 1 s. In this case the nuclear solvent response can be measured only if the solvent is very viscous and shows orientational relaxation processes within the time window of the excited state lifetime. However, most solvents crystallize at such high viscosities and supercooled or glass-forming solvents, such as 2-methyltetrahydrofunran (MTHF) at low temperatures, are used. In addition, the number of appropriate chromophores that has phosphorescence properties and exhibits a high change in the dipole moment upon electronic excitations is not as numerous. Quinozaline, quinoline, and naphthalene are famous chromophores[51].

Here, the time-dependent frequency shift of the fluorescence spectrum of a probe solute after ultrafast excitation is discussed[52]. This measurement is based on the instantaneous change in the charge distribution of a dissolved solute by pulsed excitation when the solute is exposed to a pulse of light, where the pulse width is typically shorter than the decay time. Before excitation, the solvent surrounding the solute is in equilibrium with its ground-state electronic charge distribution. When the excitation occurs, it is instantaneous on the time scale of solvent reorientation; therefore, the solute excited state is initially prepared in this

ground-state solvent configuration. Therefore, this initially prepared state is a nonequilibrium one with respect to the solvent. As the solvent reorganizes so as to achieve equilibrium with the new charge distribution, the emission frequencies shift, and the progress of the solvation energy relaxation is monitored. The time-evolving spectra are used to determine an experimental response function,

$$S_\nu(t) = \frac{\bar{\nu}(t) - \bar{\nu}(\infty)}{\bar{\nu}(0) - \bar{\nu}(\infty)} \tag{1.1}$$

where ν refers to the frequency of peak emission frequency and the average response time may be reported as

$$\langle \tau \rangle = \int_0^\infty S_\nu(t)\, dt \tag{1.2}$$

A schematic Stokes shift dynamics of a rigid dipolar molecule at room temperature water is shown in Figure 1.

When the solute is illuminated with a continuous beam of light instead of a pulse of light, a steady state can be prepared, where Stokes shift is measured as the difference between the center frequencies of the absorption and fluorescence.

One-half Stokes shift can be used experimentally to estimate the solvation reorganization energy[53, 54]. In addition, one can get information about the reaction free energy by making use of the mean energy of absorption and emission maxima. When the excited state lifetime is known for a given probe, one may also use steady state measurements to report the solvent relaxation times by making use of data at various temperatures and noting that the solvent relaxation times should not be significantly different from the excited state lifetime as discussed in Ref. [50].

Similarly, Stokes shift dynamics can be reported for phosphorescence spectroscopy,

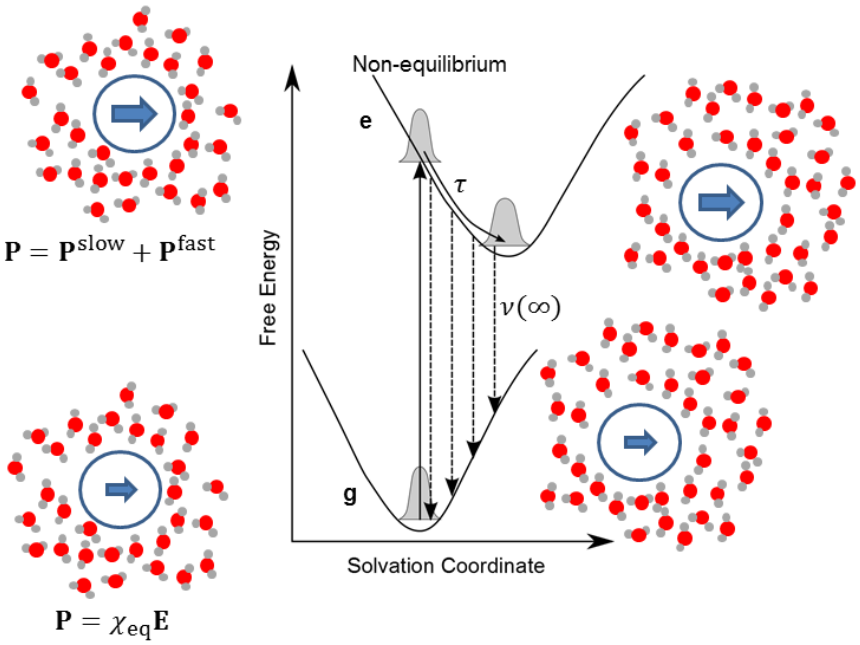

FIGURE 1: Stokes shift dynamics of a rigid dipolar molecule at room temperature water (for simplicity, the dipolar molecule is considered to be rigid during the electronic transitions). The vertical axis corresponds to the free energy surface of a reaction (solvation) coordinate, which corresponds to nuclear degrees of freedom in solvent. Before the excitation, the dipolar solute is in ground state (g) and in equilibrium with water. The vector fields $\mathbf{E}$ and $\mathbf{P}$ are electric field and polarization density field, respectively and can be conceived as coarse grained vector fields (see section 1.2.3 for details). $\mathbf{E}$ consists of the field of the external charges and the electric field of all molecular bound charges. The equilibrium susceptibility χ_{eq} establishes the direct proportionality between the vector fields $\mathbf{P}$ and $\mathbf{E}$. After the excitation, the electronic degrees of freedom of solvent have fast responses, while the nuclear degrees of freedom have slow responses creating a nonequilibrium state. The solvent molecules will reorient and relax with a relaxation time of τ during which the emission frequencies can be monitored to report on the solvation dynamics.

where emission now occurs from the corresponding metastable excited state to the ground state and the measurements are often done in the low temperature, high viscosity range. Minor temperature changes can induce significant changes in the solvation dynamics time scale as shown in Figure 2 for quinoxaline in MTHF solvent.

1.2.1.2 Nonlinear Spectroscopy: Two Dimensional Infrared Spectroscopy

The relevant quantity in nonlinear spectroscopy is the optical polarization $\mathbf{P_o}$[41].

$$\mathbf{P_o} = \mathbf{P_o^{(1)}} + \mathbf{P_o^{(2)}} + \mathbf{P_o^{(3)}} + \cdots \tag{1.3}$$

where, the polarization component to nth order in the field is denoted by $\mathbf{P_o^{(n)}}$.

Consider a molecule in the gas phase, which is described quantum mechanically, and a time-dependent laser electric field, which is treated classically, and its frequency matches the transition from quantum state 0 to quantum state 1 in the molecule. The laser pulse creates a coherent linear superposition of the two quantum states. The time dependence of this wavepacket corresponds to the molecular response $\mathbf{R}$ and the time-dependent optical polarization is given by

$$\mathbf{P_o}(t_1) = \mathrm{Tr}\left[\hat{\mathbf{m}}\rho(t_1)\right] \tag{1.4}$$

where $\hat{\mathbf{m}}$ is the dipole moment operator and $\rho(t_1)$ denotes the time evolution of the density matrix of this single molecule in the gas phase during the coherence time

$$\rho_{01}(t_1) \propto \exp\left(-i\int_0^{t_1}\omega_{01}(t)dt\right) \tag{1.5}$$

Note that when the frequency is constant in time, the above reduces to $e^{-i\omega_{01}t_1}$.

In linear response (weak laser pulse), the optical polarizations scale linearly with the laser electric field strength. Here, the first-order response function that is convoluted with the laser pulse electric field $\mathbf{E}_{\text{las}}$ is given.

$$\mathbf{P}_{\mathbf{o}}^{(\mathbf{1})}(t) = \int_0^\infty dt_1 \mathbf{E}_{\text{las}}(t - t_1)\mathbf{R}^{\mathbf{1}}(t_1) \tag{1.6}$$

where the first-order (linear) molecular response function is given by

$$\mathbf{R}^{\mathbf{1}}(t_1) = im_{01}^2 e^{-i\omega_{01}t_1} e^{-t/T_h} \tag{1.7}$$

Here, m_{01} is the magnitude of transition dipole from state 0 to state 1 and t_1 corresponds to dephasing time period, where the off-diagonal matrix ρ_{01} oscillates at a frequency of ω_{01} and decays with the homogeneous lifetime T_h. In case of vibrational spectroscopy, the homogeneous lifetimes are $1 - 5$ ps and only recently femtosecond infrared pulses made these measurements possible because the emitted electric field can now reflect the molecular response and not only the envelope of the laser pulse.

To incorporate the solvent effects into the above formalism, one may average the density matrix in Eq. (1.5) as follows

$$\rho_{01}(t_1) \propto \left\langle \exp\left(-i \int_0^{t_1} \omega_{01}(t)dt\right) \right\rangle \tag{1.8}$$

where $\langle \cdots \rangle$ denotes the ensemble average and can explain the dephasing mechanism. The solvent fluctuations change the instantaneous frequencies $\omega_{01}(t)$, leading to oscillating terms that will eventually become out of phase. Therefore, the amplitude of the ensemble averaged density matrix decays in time. Replacing $\omega_{01}(t) = \omega_{01} + \delta\omega_{01}(t)$ in Eq. (1.8) gives

$$\rho_{01}(t_1) \propto e^{-i\omega_{01}t_1}\left\langle \exp\left(-i\int_0^{t_1}\delta\omega_{01}(t)dt\right)\right\rangle \tag{1.9}$$

where ω_{01} is the average frequency.

The solvent effects can therefore be incorporated by replacing the molecular response function of the form $e^{\pm i\omega_{01}t}e^{-t/T_h}$ with the response function of Eq. (1.9) or its complex conjugate[48].

$$\mathbf{R^1}(t_1) = im_{01}^2 e^{-i\omega_{01}t_1}\left\langle \exp\left(-i\int_0^{t_1}\delta\omega_{01}(t)dt\right)\right\rangle = im_{01}^2 e^{-i\omega_{01}t_1}e^{-g(t_1)} \tag{1.10}$$

where $g(t_1)$ is the lineshape function and involves the solvent response.

Making use of cumulant expansion and truncating after the second term, the lineshape function can be written as

$$g(t_1) = \int_0^{t_1} dt \int_0^{t} dt' \langle \delta\omega_{01}(t')\delta\omega_{01}(0)\rangle \tag{1.11}$$

In this approximation (known as Gaussian approximation), the lineshape function only involves equilibrium two-point correlation function, and the nonequilibrium solvent dynamics can be formulated only in terms of equilibrium two-point correlation functions[46].

Nonlinear response terms (nonlinear spectroscopy) provide higher order correlation functions, which allows one to investigate the solvent dynamics in a more rigorous way[55, 56]. The third-order nonlinearity is the lowest-order nonzero nonlinear term in isotropic media. Two-dimensional infrared (2DIR) spectroscopy is the most common third-order spectroscopy in infrared spectroscopy. The most general form of 2DIR spectroscopy in a time domain consists of three input laser pulses all having different wavevectors. The first interaction of a laser pulse with the sample generates a coherence state, which is a superposition of two quantum states. The system dephases for time t_1. The second field

interaction creates the population state, which corresponds to diagonal terms in the density matrix. During the waiting time T, the system experiences population relaxation. The last pulse creates a coherence state again, where the system dephases during time t_3. The generated field will then have a wavevector $\mp\overrightarrow{k_1} \pm \overrightarrow{k_2} + \overrightarrow{k_3}$, where the signs correspond to rephasing and non-rephasing wavevectors[48]. To obtain the frequency domain spectra, the Fourier transform is usually performed with respect to the t_1 and t_3 coherence times while time T corresponding to the population relaxation time is not transformed.

For 2DIR, the generated emitted field from the third-order response functions consists of terms combining pure dephasing terms. By considering only one of these such terms, one can set up the calculation of the third-order lineshape function for the rephasing diagram[48]. For the two-state system, the rest of them can be obtained by changing the sign of the coherences in the dephasing diagrams:

$$g(t_1, T, t_3) = \left\langle \exp\left(-i \int_0^{t_1} d\tau \delta\omega(\tau)\right) \exp\left(i \int_{t_1+T}^{t_1+T+t_3} d\tau \delta\omega(\tau)\right) \right\rangle \tag{1.12}$$

where t_1 and t_3 are the durations of the pump and probe pulses, respectively, and T is the waiting time. Spectral diffusion can be identified by monitoring the changes in the peak-shape as the population time varies (see section 5.5 for more details). As the population time increases, the anti-diagonal linewidth broadens indicating the loss of correlations between coherence states.

1.2.1.3 Dielectric Relaxation Spectroscopy

The inhomogeneous response of a solvent in the presence of a solute may be formulated in terms of a homogeneous susceptibility of solvent in the absence of the solute[57]. The latter may be obtained by dielectric relaxation spectroscopy, which measures the collective

orientation of the dipolar molecules. It is used to identify the dynamics of liquid/solvent over a wide range of temperatures due to access to a wide range of frequencies. The total frequency range that can be measured (after combining several techniques) to date spans from $\nu = 5$ nHz (τ = 1 year) to beyond $\nu = 1$ THz (τ = 0.2 ps)[49]. The experiments can be done either in time-domain or frequency domain. Details of these experiments can be found in Ref. [49]. Here, it is only discussed how one can obtain the liquid/solvent response in these measurements with the focus on frequency-domain measurements.

The interaction of mobile charges within the sample with the external electric field, usually applied by virtue of two electrodes, is the origin of observed signal. Therefore, both the magnitude of the interaction and the time scales involved in charge displacements are measured by this method. It is worth mentioning that the magnitude of local fields in emission spectroscopies are orders of magnitude greater than (Maxwell) fields used in dielectric experiments[54]. Liquid/solvent response corresponds to microscopical or macroscopical charge displacements. The microscopical charge movements are manifested in chemical reactions, solvation, and electron transfer. The macroscopical charge movements are manifested in conductivity, capacitance, and energy storage. The charge displacement can stem from rotational motion of dipoles and/or translational mobility of charges and the amount of energy that the external field can store in the sample is the static dielectric constant (permittivity), ϵ_s.

The common feature in frequency-domain measurements is the relation of two equilibrium sinusoidal signals, i.e., the voltage, $V(\omega)$, across the sample and the current, $I(\omega)$, through the sample. The ratio $Z(\omega) = V(\omega)/I(\omega)$ is called the impedance and its inverse is called admittance, Y. The above relations involve amplitude and phase, and are complex valued. The liquid/solvent dielectric constant, $\tilde{\epsilon}(\omega)$, can be obtained based upon measurement of impedance Z or admittance Y of a sample capacitor, where $\tilde{\epsilon}(\omega)$ is com-

plex valued, which includes the amplitude and phase relation between displacement and field at each frequency:

$$\tilde{\epsilon}(\omega) = \tilde{\epsilon}^{'}(\omega) - i\tilde{\epsilon}^{''}(\omega) \tag{1.13}$$

where $\tilde{\epsilon}^{'}(\omega)$ is referred to as storage factor and $\tilde{\epsilon}^{''}(\omega)$ is referred to as loss factor. The storage factor describes the component of the polarization density in phase with the Maxwell field while the loss factor determines the component of the polarization with a phase difference with respect to the Maxwell field, which gives rise to the dissipation of energy of the electric field in the medium.

The relaxation behavior of liquid/solvent in time-domain measurements may be treated by time-dependent dipole reorientation in liquid/solvent via rotational diffusion on a sphere as proposed by Debye[58]

$$\epsilon(t) = \epsilon_{\infty} + (\epsilon_s - \epsilon_{\infty})(1 - \exp(-t/\tau)) \tag{1.14}$$

where ϵ_{∞} is the high frequency dielectric constant, ϵ_s is the static dielectric constant and τ is the dielectric relaxation time. Liquid/solvent dipoles respond to the field and can be characterized by an exponential response function, which captures reorienting permanent liquid/solvent dipoles.

Performing a Fourier-Laplace transform, the exponential response function can be represented in the frequency-domain to obtain the so-called Debye form of dielectric constant.

$$\tilde{\epsilon}(\omega) = \epsilon_{\infty} + \frac{(\epsilon_s - \epsilon_{\infty})}{(1 + i\omega\tau)} \tag{1.15}$$

It is worth mentioning that a simple and exact relation exists to calculate the loss factor on the basis of the storage component for this type of single-exponential behavior. However, there exists asymmetry in many viscous liquids when $\epsilon^{''}(\omega)$ is plotted versus $\log\omega$.

Havriliak-Negami (HN) function[59] has been suggested to capture the aforementioned asymmetry:

$$\tilde{\epsilon}(\omega) = \epsilon_\infty + \frac{(\epsilon_s - \epsilon_\infty)}{(1 + (i\omega\tau)^\alpha)^\beta} \tag{1.16}$$

The exponents α and β control the symmetric and asymmetric broadening, respectively, with their limitations being $0 < \alpha$, and $\alpha\beta < 1$. From this parameterization, the characteristic time constant, $\tau_m = 1/\omega_m$, can be obtained, where ω_m is the angular frequency at which the maximum of $\tilde{\epsilon}''(\omega)$ is observed. The resulting peak dielectric relaxation time, is plotted in Figure 2 as a function of temperature for MTHF.

1.2.2 Theoretical and Simulation Approaches

A preliminary step towards the theoretical and simulation approaches is to describe the solvent. In this work, we only consider classical solvents which can be treated theoretically by the methods of classical statistical mechanics[60]. A simple test of this assumption for atomic solvents is to compare the de Broglie thermal wavelength and the mean nearest-neighbor separation. Below three common approaches to investigate the solvent polarization (response) are presented briefly. First, dielectric continuum methods are presented. Second, integral equation methods are discussed. This is followed by explicit solvent models. At the end of the discussion of these approaches, a concise connection to related quantum mechanical methods is given. Added to the above approaches, perturbation theories[60, 61] and physical approaches based on lattice models are worth mentioning. In the cell theory, each solvent particle moves in a certain potential in a free volume from which a single-particle partition function may be derived. The total partition function is then obtained as the product of all the single-particle partition functions. In a dipole-lattice

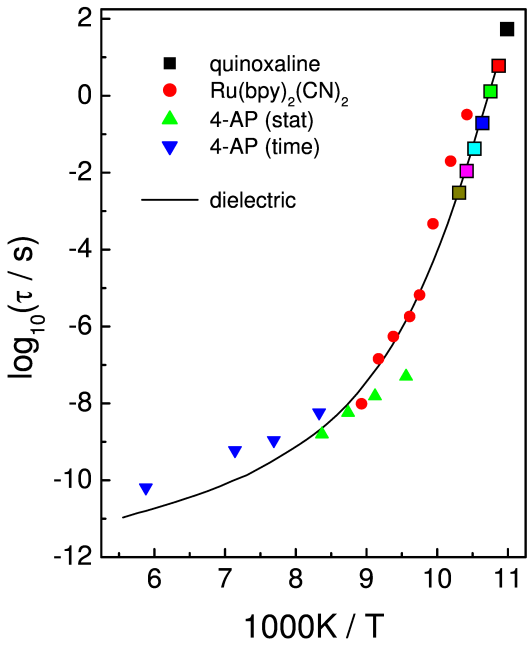

FIGURE 2: Average solvent (2-methyltetrahydrofunran) relaxation times as defined by Eq. (1.2) within 13 decades in time in three different probes: quinoxaline and $Ru(bpy)_2(CN)_2$ as phosphorescence probes, and 4-aminophthalimide (4AP) as a fluorescence probe for which time resolved and steady state data has been reported. The solid line shows the results of dielectric relaxation experiments for the solvent. Reprinted, with permission, from Ref. 52

approach[62, 63], the solvent response of a solute is represented by a lattice of dipoles with the proper polarity to explicitly retain the dipolar nature of solvent polarization.

At the end of this section, a separate part is devoted to discussing the linear response of the solvent because it has broad applications in the aforementioned theoretical and simulation approaches.

1.2.2.1 Dielectric Continuum Methods

A dielectric continuum method replaces the explicit charge distribution of the solvent with a continuous electric field, which ignores the microscopic variations due to the molecular structure of the solvent[64]. The continuous electric field, in fact, represents a statistical average over all solvent degrees of freedom at thermal equilibrium. The Born model of ion solvation[1] presented in 1920 is the first model which uses an isotropic dielectric continuum to represent the solvent, where the ion is represented by a point charge and its electric field penetrates into the solvent. The polarization of the solvent at a given point may be written as

$$\mathbf{P}(\mathbf{r}) = \chi \mathbf{E_0}(\mathbf{r}) = \frac{1}{4\pi}(1 - \frac{1}{\epsilon})\mathbf{E_0}(\mathbf{r}) \tag{1.17}$$

where χ is the solvent susceptibility, which is a scalar due to the isotropy of the dielectric continuum. $\mathbf{E_0}$ is the bare electric field of the ion and ϵ is the pure solvent dielectric constant. Therefore, the value of $\mathbf{P}$ at any position within the solvent is solely determined by the value of $\mathbf{E_0}$ at that position and a local linear relationship holds between $\mathbf{E_0}$ and $\mathbf{P}$ in the Born model.

One may note that the spherical symmetry of the field of an ion and also the spherical symmetry of the cavity (solute) in the solvent leads to a radial solvent polarization. In addition, the electric field of an ion is longitudinal because $\mathbf{E_0} = -\nabla\Phi$, where Φ is the electrostatic potential. For a spherical ion of radius a, the Fourier transform of $\mathbf{E_0}(\mathbf{r})$, $\tilde{\mathbf{E}}_\mathbf{0}(\mathbf{k})$, can be obtained analytically as

$$\tilde{\mathbf{E}}_\mathbf{0}(\mathbf{k}) = -\frac{4\pi i q \mathbf{k}}{k^2} j_0(k\mathrm{a}) \tag{1.18}$$

where j_0 is the spherical Bessel function of zeroth order. This can be combined with the spherical symmetry of the cavity to result in the longitudinal projection of the Fourier

transform $\tilde{E}_0(k)$, $\tilde{E}_0^L(k) = \hat{\mathbf{k}} \cdot \tilde{\mathbf{E}}_\mathbf{0}(\mathbf{k})$, where $\hat{\mathbf{k}} = \mathbf{k}/k$. Therefore, in the Born model, where $k \to 0$, the solvent polarization response to a spherical ion is longitudinal. It is important to note that for non-spherical solutes, where the symmetry of the cavity does not coincide with the symmetry of the electric field, both longitudinal and transverse projections are involved (see below).

Sixteen years after the Born model, Onsager considered the solvation of a spherical solute with a central point dipole, in a dielectric continuum[65]. The electric field of the dipole in such a cavity polarizes the solvent, and the resulting inhomogeneous polarization of the solvent gives rise to a continuous field at the dipole. This field is called the Onsager reaction field and its direction is the same as the direction of the dipole moment vector. The reaction field coefficient, $(2/\mathrm{a}^3)(\epsilon-1)/(2\epsilon+1)$, involves the solvent dielectric constant and the radius of the solute and corresponds to solvation susceptibility (see chapter 3). One may note that the electric field of the dipole is no longer spherically symmetric and the solvent polarization response involves both longitudinal and transverse projections. To provide an analytical explanation, one can obtain the Fourier transform of a point dipole at the center of a spherical cavity as

$$\tilde{\mathbf{E}}_\mathbf{0}(\mathbf{k}) = -4\pi \left[3\hat{\mathbf{k}} \left(\hat{\mathbf{k}} \cdot \mathbf{m}_0 \right) - \mathbf{m}_0 \right] \frac{j_1(k\mathrm{a})}{k\mathrm{a}} \tag{1.19}$$

where a is the radius of the cavity, j_1 is the spherical Bessel function of first order and $\mathbf{m}_0$ is the dipole moment vector.

In many quantum mechanical continuum solvent models, an Onsager polarization energy operator is defined, which invokes the dipole moment operator to form an effective Hamiltonian of a molecular solute embedded in the solvent reaction field[66] , i.e., the reaction field is a first-order perturbation of the Hamiltonian. The Schrödinger equation in solution becomes

$$\left\{\hat{H}_g - \left[\frac{2(\epsilon-1)}{(2\epsilon+1)}\right]\frac{\langle\Psi|\hat{m}|\Psi\rangle}{\mathrm{a}^3}\hat{m}\right\}\Psi = E\Psi \tag{1.20}$$

where $\hat{H}_g$ is the Hamiltonian operator in the gas phase and $\hat{m}$ is the dipole moment operator. This non-linear Schrödinger equation is then solved by making use of a self-consistent reaction field calculation.

In apparent surface charge models, also known as polarizable continuum models (PCM)[67], the solvent polarization is represented as a set of apparent surface charges, which are placed on the surface of the cavity containing the solute. The cavity is usually determined by multiple overlapping spheres for each of the atoms within the molecule inside of the solvent and the electrostatic problem is then solved on the cavity boundary to obtain the apparent surface charges.

1.2.2.2 Integral Equation Methods

In the liquid state, the solvent molecules are in thermal and diffusive motion, and changing their positions and orientations continuously. Therefore, the density of solvent molecules is different from space to space and time to time. The integral equation methods describe the solvent structure through these density fluctuations and the corresponding intermolecular pair correlation functions[68, 69, 70, 71]. They fall into two general classes. When the solvent is described by rigid molecules, the full, angular dependent, intermolecular correlations analogous to the corresponding theory for atomic liquids are used. When the solvent molecules are described by interaction site models, the relative intermolecular distribution of pairs of sites is considered. This second type of equation is usually referred to as the RISM (reference interaction site method or model) equation.

The Ornstein-Zernike (OZ) equation is most popularly used to describe the density fluc-

tuations in liquids. The equation defines a correlation function called the direct correlation function $c(\mathbf{r}, \mathbf{r}')$ in terms of the total correlation function $h(\mathbf{r}, \mathbf{r}')$. The total correlation between two particles involves the direct correlation between them and also the indirect correlation of the two particles via the influence of the first particle on particle i'' and the influence of particle i'' on the second particle summed over all such particles with their corresponding densities (ρ):

$$h(\mathbf{r}, \mathbf{r}') = c(\mathbf{r}, \mathbf{r}') + \int_V c(\mathbf{r}, \mathbf{r}'')\rho(\mathbf{r}'')h(\mathbf{r}', \mathbf{r}'')\mathrm{d}\mathbf{r}'' \tag{1.21}$$

In order to solve the OZ equation, a closure is required, which relates $h(\mathbf{r}, \mathbf{r}')$ and $c(\mathbf{r}, \mathbf{r}')$. The general closure reads

$$c(\mathbf{r}, \mathbf{r}') = \exp\left[-\beta u(\mathbf{r}, \mathbf{r}') + t(\mathbf{r}, \mathbf{r}') + b(\mathbf{r}, \mathbf{r}')\right] - 1 - t(\mathbf{r}, \mathbf{r}') \tag{1.22}$$

where $t(\mathbf{r}, \mathbf{r}') = h(\mathbf{r}, \mathbf{r}') - c(\mathbf{r}, \mathbf{r}')$ and $b(\mathbf{r}, \mathbf{r}')$ is a functional of $h(\mathbf{r}, \mathbf{r}')$ and is known as the bridge function and include multiple difficult integrals. Approximate methods are therefore developed to solve the OZ equation. Here the hypernetted-chain (HNC), Percus-Yevick (PY), and mean-spherical approximations (MSA) (see also chapter 2) are discussed briefly.

In the HNC closure[72, 73], the bridge function is ignored:

$$c(\mathbf{r}, \mathbf{r}') = \exp\left[-\beta u(\mathbf{r}, \mathbf{r}') + t(\mathbf{r}, \mathbf{r}')\right] - 1 - t(\mathbf{r}, \mathbf{r}') \tag{1.23}$$

The HNC approximation works reasonably for many systems such as hard spheres and those which involve Coulombic forces.

In the PY closure[74], $\exp\left(t(\mathbf{r}, \mathbf{r}')\right)$ is also linearized:

$$c(\mathbf{r}, \mathbf{r}') = \exp\left[-\beta u(\mathbf{r}, \mathbf{r}')\right]\left[1 + t(\mathbf{r}, \mathbf{r}')\right] - 1 - t(\mathbf{r}, \mathbf{r}') \tag{1.24}$$

Although the PY approximation works reasonably for the systems consisting of hard spheres, it leads to unphysical behavior for Coulombic systems.

When the systems of interest consist of spheres which interact with each other via potential functions $u(r) = \infty$ for $r \leq \sigma$ and $u(r) = w(r)$ for $r > \sigma$, the mean-spherical closure[75] is used:

$$\begin{aligned} h(r) &= -1 \quad \text{for} \quad r \leq \sigma \\ c(r) &= -\beta w(r) \quad \text{for} \quad r > \sigma \end{aligned} \tag{1.25}$$

where $w(r)$ is the attractive or repulsive part of the potential, and σ is the diameter of the spheres. The MSA approximation is used for polar fluids and ionic solutions[76] and is known to give a reasonable account of critical phenomena[77]. However, the radial distribution functions are ill-behaved for Coulombic systems similar to the predictions of the PY closure.

In the RISM methods, the solvent is described by interaction sites, similar to the expressions that are use in force fields in classical molecular simulations. An important approximation that is used in the RISM methods is to represent the molecular direct correlation functions by a sum of the site-site direct correlation functions. When the RISM theory is applied to single site spherical particles, it reduces to the PY theory for hard sphere fluids. Extensions of the RISM theory have been applied to study polar and associated liquids[78].

The RISM theory can be combined with *ab initio* methods to incorporate the electronic quantum mechanical aspects of the solvent. For instance, the reaction field in quantum mechanical continuum models can be replaced by a microscopic expression in terms of the site-site radial distribution functions between solute and solvent as calculated by the RISM theory. The electronic structure of the solute determines the statistical solvent distribution and it, in turn, influences the electronic structure of the solute. Therefore, a self-consistent approach is required to solve the RISM equation (RISM-SCF)[79].

1.2.2.3 Explicit Solvent Methods

Explicit solvent models treat the solvent molecules explicitly and are usually used in computer molecular simulations such as molecular dynamics (MD) or Monte Carlo (MC) simulations. When classical force fields are used, the solvent molecules are represented by interaction sites. These empirical molecular models are obtained by fitting parameters to a set of experimental data, which, to some extent, capture quantum and many body effects in an effective way for the corresponding experimental properties[80, 81, 82]. Relatively long trajectories can be obtained: in 2016, atomistic MD simulations of hundreds of thousands of atoms up to microseconds is achievable[13, 15].

To offer the possibility of a parameter-free way of incorporating electronic quantum effects in condensed phase simulations, first principle molecular simulations are used. *Ab initio* MD or MC methods solve the Schrödinger equation and are computationally expensive. A popular method is the Car–Parrinello MD (CPMD)[83], where the core electrons of molecules are usually described by a pseudopotential (see below) and a plane wave basis set is used to represent the wavefunction of the valence electrons. The ground state electronic density is calculated at each step from which the forces on the nuclei are calculated. To prevent expensive self-consistent iterative minimizations at each time step, the electronic degrees of freedom are treated by fictitious dynamical variables such as small fictitious masses of the electrons, which avoid a significant energy transfer from nuclei to electrons. Depending on the problem of interest, special pseudopotentials may be developed as for the hydrated electron, e^-_{aq}, a metastable localized species in liquid water. They replace the complicated many-body interaction between an excess electron and solvent molecules by an effective potential, assuming that the core electrons are static during the chemical pro-

cess and noting that the valence electron wave function is orthogonal to the core electron wave functions[84].

Often long trajectories, together with realistic potential energies, are required to unravel the physics of a problem or the corresponding mechanism. If the whole system of interest can be divided into inner (quantum) and outer (classical) regions, then hybrid quantum mechanics/molecular mechanics (QM/MM) approaches are used[85, 86, 87, 88, 89, 90, 91]. This approach gained considerable attention after the seminal work of Warshel and Levitt in 1976. The calculation of the hybrid QM/MM potential energy of the entire system is expressed as

$$U_{\mathrm{tot}} = U_{\mathrm{QM}} + U_{\mathrm{MM}} + U_{\mathrm{QM/MM}} \tag{1.26}$$

where the first two terms are the quantum mechanical and classical potential energies, respectively. The third term is the coupling term and includes the inductive effect of the classical point charges on the quantum mechanical charges[85]. Mixed QM/MM approaches may also be developed by merging the unperturbed electronic properties of the quantum region with the solvent field (as a perturbation), which can be obtained from classical MD simulations[47]. The assumption is that the forces acting on the atoms of the classical thermal bath can be well characterized by classical force fields. In chapter 6, an example of this approach is used to investigate the role of polarizability in the electron transfer of cytochrome *c*.

1.2.2.4 Linear Response of Solvent

Consider a solvent in thermal equilibrium with a solute and the solvent is exposed to a weak perturbation from the solute. How does the solvent respond? This is the type

of question that is addressed in linear response theory, which is essentially an application of the fluctuation dissipation theorem[92, 93]. Based on this theory, the electrostatic response of the solvent to the perturbation can be obtained from knowledge of the equilibrium fluctuations of the unperturbed solvent. A large amount of theoretical works has been formulated in terms of the linear response of the solvent, which involves the continuum, explicit solvent, and integral equation approaches. Important relevant examples are the Born[1], Onsager[65], Li-Kardar-Chandler[9], Matyushov microscopic theories of solvation[57], and the Marcus theory of electron transfer, which is based on a linear response dielectric continuum theory and the solvent fluctuations to obtain the parabolic electron transfer free energies of reactants and products[2, 3, 4, 5, 6]. Here, the static linear response is mostly discussed. Dynamic linear response, which is usually used to investigate solvent dynamics, is discussed in chapter 5 (see Eq. 5.14) and appendix C.

In the Born theory of ion solvation, the free energy of ion hydration scales quadratically with the ion charge[1]. In the Onsager theory of dipole solvation, the free energy of dipole solvation scales quadratically with the dipole moment of solute. The proportionality coefficient, the solvation susceptibility, may be investigated in molecular details as discussed in chapters 2 and 3. The quadratic scaling with the solute multipole leads to relations between the cumulants of the solute-solvent interaction energies ($u_{0\mathrm{s}}$), where 0 and s correspond to solute and solvent, respectively. The linear response approximation results in the Gaussian statistics of solute-solvent energy, and predicts the equality of the first and second (multiplied with β) cumulants of the solute-solvent energy, i.e., $\langle u_{0\mathrm{s}} \rangle = -\beta \langle (\delta u_{0\mathrm{s}})^2 \rangle$, where $\langle \dots \rangle$, stands for the statistical average over the solvent configurations in equilibrium with the solute with a given multipole moment[11]. Note that $\langle u_{0\mathrm{s}} \rangle$ includes the potential due to spontaneous polarization of interface that can occur for neutral non-polar non-polarizable solutes and also the potential produced by the solvent in response to the solute multipole

moment. It is the latter potential which generates the quadratic scaling of the free energy of solvation with the solute multipole. When the linear response does not hold, the free energy of solvation is determined by an infinite expansion in the cumulants of $u_{0\mathrm{s}}$, which may be truncated up to high order terms. In addition, the linear response approximation predicts the equality of $\langle(\delta u_{0\mathrm{s}})^2\rangle_0 = \langle(\delta u_{0\mathrm{s}})^2\rangle$, where $\langle\dots\rangle_0$ now stands for the statistical average over the configurations of the solvent in equilibrium with a neutral non-polar non-polarizable solute, which has the repulsive part of the potential of the real solute. In chapter 2, we found that this equality holds well for neutral, anion, and cation Kihara solutes, where the solute charges are placed at the center of solute.

Therefore, the electrostatic free energy of solvation in linear response[94] can be obtained as

$$F_{0\mathrm{s}} = -\frac{\beta}{2}\langle(\delta u_{0\mathrm{s}})^2\rangle_0 \tag{1.27}$$

This implies that the excluded volume effect (repulsive core of the solute) by itself plays an important role in the theory of solvation. In other words, the excluded volume effects are more important than effects originated from the solute external field.

In dipolar solvents, $u_{0\mathrm{s}}$ corresponds to the interaction of the solute's electric field $\mathbf{E}_0(\mathbf{r})$ with the dipolar solvent dipolar polarization $\mathbf{P}(\mathbf{r})$

$$u_{0\mathrm{s}} = -\int \mathbf{E}_0(\mathbf{r})\cdot\mathbf{P}(\mathbf{r})d\mathbf{r} \tag{1.28}$$

In real space Eq. (1.27) can be written as

$$F_{0\mathrm{s}} = -\frac{\beta}{2}\int E_{0\gamma}(\mathbf{r}')E_{0\kappa}(\mathbf{r}'')\langle\delta P_\gamma(\mathbf{r}')\delta P_\kappa(\mathbf{r}'')\rangle_0 d\mathbf{r}'d\mathbf{r}'' \tag{1.29}$$

where γ,κ subscripts denote Cartesian projections and the summation over the common indexes is assumed. In chapter 2, the solvent response function and free energy of ion hydration is addressed based on the above equation (see Eqs. (2.7) and (2.8)). Here, the

nonlocal response of the solvent is discussed in the reciprocal space. Eq. (1.27) can be written directly in the form of the Fourier integral

$$F_{0\mathrm{s}} = -\frac{\beta}{2}\int \frac{d\mathbf{k_1}\, d\mathbf{k_2}}{(2\pi)^6}\tilde{\mathbf{E}}_0(\mathbf{k_1})\cdot\langle\delta\tilde{P}_\gamma(\mathbf{k_1})\delta\tilde{P}_\kappa(\mathbf{k_2})^*\rangle_0\cdot\tilde{\mathbf{E}}_0(\mathbf{k_2})^* \tag{1.30}$$

where $\tilde{E}_0(\mathbf{k})$ is the Fourier transform of the solute field over the solvent volume Ω_{out} outside the solute

$$\tilde{\mathbf{E}}_0(\mathbf{k}) = \int_{\Omega_{\mathrm{out}}} \mathbf{E}_0(\mathbf{r})\mathrm{e}^{i\mathbf{k}\cdot\mathbf{r}}d\mathbf{r} \tag{1.31}$$

and $\tilde{\mathbf{E}}_0(\mathbf{k})^*$ and $\tilde{P}_\kappa(\mathbf{k})^*$ are the complex conjugates, and the nonlocal solvent response function may be defined as a second rank tensor as

$$\chi_{\gamma,\kappa}(\mathbf{k_1},\mathbf{k_2}) = \beta\langle\delta\tilde{P}_\gamma(\mathbf{k_1})\delta\tilde{P}_\kappa(\mathbf{k_2})^*\rangle_0 \tag{1.32}$$

However, the calculation of this function is still a major challenge and various approaches have been suggested. A preliminary step is to approximate $\chi_{\gamma,\kappa}$ with the response function of a pure solvent in the absence of the solute, i.e., $\chi\left(\mathbf{k_1},\mathbf{k_2}\right) = \delta_{\mathbf{k_1},\mathbf{k_2}}\chi_{\mathbf{s}}(\mathbf{k_1}) = (2\pi)^3\,\delta\left(\mathbf{k_1}-\mathbf{k_2}\right)\chi_{\mathbf{s}}(\mathbf{k_1})$, where the pure solvent response function may be written in terms of longitudinal and transverse structure factors

$$\chi_{\mathbf{s}}(\mathbf{k}) = \frac{3y}{4\pi}\left[\left(S^L(k)\hat{\mathbf{k}}\hat{\mathbf{k}}\right) + \left(S^T(k)(\mathbf{1}-\hat{\mathbf{k}}\hat{\mathbf{k}})\right)\right] \tag{1.33}$$

where $y = (4\pi/9)\beta m^2\rho$ is the density of permanent dipoles, m is the magnitude of the solvent dipole moment, and ρ is the solvent number density, and the longitudinal and transverse structure factors are given in terms of unit-vector orientations $\hat{\mathbf{e}}_i = \mathbf{m}_i/m$ and posi-

tions $\mathbf{r}_i$ of molecular dipoles in the bulk

$$\begin{aligned} S^L(k) &= \frac{3}{N}\sum_{i,j}\left\langle(\hat{\mathbf{e}}_i\cdot\hat{\mathbf{k}})(\hat{\mathbf{k}}\cdot\hat{\mathbf{e}}_j)e^{i\mathbf{k}\cdot\mathbf{r}_{ij}}\right\rangle \\ S^T(k) &= \frac{3}{2N}\sum_{i,j}\left\langle\left[(\hat{\mathbf{e}}_i\cdot\hat{\mathbf{e}}_j)-(\hat{\mathbf{e}}_i\cdot\hat{\mathbf{k}})(\hat{\mathbf{k}}\cdot\hat{\mathbf{e}}_j)e^{i\mathbf{k}\cdot\mathbf{r}_{ij}}\right]\right\rangle \end{aligned} \tag{1.34}$$

Here, $\mathbf{r}_{ij}=\mathbf{r}_i-\mathbf{r}_j$ and the statistical average is over the configurations of N molecules of the bulk liquid occupying the volume V.

The approximation above is known as homogeneous approximation; however, the excluded volume can have significant effects on the dipole-dipole correlations outside the excluded volume as reported previously by the Song-Chandler-Marcus study and verified by our work (see chapter 2)[12, 95]. Note that the transverse structure factors do not vanish when there is spherical asymmetry in the electric field or the cavity (solute) shape. In the continuum limit, this can lead to a transverse catastrophe, meaning that very high, unreasonable values of $F_{0\mathrm{s}}$ can be obtained.

The excluded volume effects are considered in the Gaussian field model of Li-Kardar-Chandler[96, 9]. In this model, the solvent is described in terms of a linear responding field (a Gaussian fluctuating field) that is expelled from the volume occupied by the solute, where the excluded volume affects the normal modes of the system. Matyushov showed that a correct renormalization of the inhomogeneous solvent polarization response function is obtained in this model, which eliminates the transverse catastrophe[97]. The corresponding free energy, $W(\mathbf{J})$, can be considered as the generating functional of correlation function $\langle\delta\tilde{P}(\mathbf{k_1})\delta\tilde{P}(\mathbf{k_2})^*\rangle_0$.

$$W(\mathbf{J})=\ln\left[\int\exp\left(\int\mathbf{J}\cdot\mathbf{P}d\mathbf{r}-\beta H_{\mathrm{B}}\right)\prod_{\mathbf{r}\in\Omega_{\mathrm{in}}}\delta\left[\mathbf{P}(\mathbf{r})\right]\mathcal{D}\mathbf{P}\right] \tag{1.35}$$

where $\mathbf{J}$ is the auxiliary field, $\mathbf{P}$ is the polarization field, Ω_{in} is the volume enveloped by the

solute, $\mathcal{D}$ indicates functional integration, and H_{B} is the Hamiltonian of the pure solvent in the absence of the solute, which may be given in the reciprocal space by

$$H_{\mathrm{B}} = \frac{1}{2}\int \frac{d\mathbf{k}}{(2\pi)^3}\delta\tilde{\mathbf{P}}(\mathbf{k})\cdot\chi_{\mathbf{s}}(\mathbf{k})^{-1}\cdot\delta\tilde{\mathbf{P}}(\mathbf{k})^{*} \tag{1.36}$$

The solvent response function can be obtained as the second functional derivative of the generating functional

$$\chi_{\mathrm{exc}}(\mathbf{k_1},\mathbf{k_2}) = \beta\frac{\delta^2 W(\mathbf{J})}{\delta\tilde{\mathbf{J}}(\mathbf{k_1})\delta\tilde{\mathbf{J}}(\mathbf{k_2})}\Big|_{\mathbf{J=0}} \tag{1.37}$$

This results in an exact solution for the reciprocal space response function:

$$\chi_{\mathrm{exc}}(\mathbf{k_1},\mathbf{k_2}) = \chi_{\mathbf{s}}(\mathbf{k_1})\delta_{\mathbf{k_1},\mathbf{k_2}} - \chi^{''}(\mathbf{k_1})\theta_0(\mathbf{k_1}-\mathbf{k_2})\chi_{\mathbf{s}}(\mathbf{k_2}) \tag{1.38}$$

where $\chi^{''}(\mathbf{k_1})$ includes $\chi_{\mathbf{s}}$ and the information about the solute shape and the kernel $\theta_0(\mathbf{k_1}-\mathbf{k_2})$ is the Fourier transform of the step function equal to unity inside the solute and zero elsewhere. The free energy of solvation may then be obtained by replacing Eq. (1.38) into Eq. (1.30). However, it results in a six dimensional integral convolution in $\mathbf{k}-$space, which is numerically not tractable. The SolvMol software program is developed to perform these calculations. Details can be found in Ref. [98].

1.2.3 Inhomogeneous Interfacial Polarization

As mentioned in the previous section, the homogeneous approximation used in the solvation theories is not a good one. In this section, the solvent response is discussed based on the inhomogeneous Maxwell fields corresponding to interfacial polarization. The Maxwell field has played a prominent role in the theories of dielectrics. In the case of a homogeneous field produced by a planar capacitor, one gets the direct experimental access to the Maxwell

field E through the voltage on the plates V and the distance between them d: $E = V/d$. The dielectric/solvent response to the external field is therefore most conveniently represented in terms of the susceptibility to the Maxwell field. This can be viewed as both an advantage and disadvantage since $\mathbf{E}$ itself is never accessible experimentally and only the line integral $\int \mathbf{E} \cdot d\boldsymbol{\ell} = V$, producing the voltage V, can be measured[99]. In the case of an inhomogeneous field there is no way to extract the field from the integral and experiment generally does not have direct access to inhomogeneous fields. The problem was realized already at the time of birth of the electromagnetic theory. Since inhomogeneous fields cannot be accessed directly, Thompson suggested using small cavities to measure internal fields inside dielectrics[100] to map inhomogeneous fields. This approach has in fact been realized by modern-day spectroscopy, which allows one to evaluate the local field acting on a dye molecule through the field-induced shift of its spectral line[101, 102]. However, the connection between such a local field and the macroscopic Maxwell field has been elusive beyond the standard prescriptions of the dielectric theory[103]. In addition, the ability to spatially resolve the distribution of the electric field and inhomogeneous polarization within molecular systems of nanometer scale has been limited[104].

From the theoretical perspective, the Maxwell field is well defined by the Coulomb law. The starting point is the overall microscopic electric field $\mathbf{E}_m$, combining the field $\mathbf{E}_0$ of the external charges with the electric field of all molecular bound charges distributed with the charge density ρ_b ("b" stands for the bound charge). The result is obviously

$$\mathbf{E}_m = \mathbf{E}_0 + \mathbf{E}_b \tag{1.39}$$

where

$$\mathbf{E}_b = -\nabla \int |\mathbf{r} - \mathbf{r}'|^{-1} \rho_b' d\mathbf{r}' \tag{1.40}$$

The primes here and below denote vector and scalar fields taken at the point $\mathbf{r}'$, e.g., $\rho_b' = \rho_b(\mathbf{r}')$. The Maxwell field is produced from this equation as the result of two steps: (i)

statistical average $\langle \mathbf{E} \rangle$ of the instantaneous $\mathbf{E}_m$ over the configurations of a statistical ensemble and (ii) coarse graining of $\langle \mathbf{E} \rangle$ over a "physically small" volume averaging out the microscopic correlations between the molecules of the material[105]. This volume is not precisely defined and, in fact, is never explicitly involved. The theory, as it is formulated for bulk dielectrics and interfaces, instead introduces coarse graining through constitutive relations as discussed in section 2.3.

By taking the divergence of $\mathbf{E}_m$ and substituting $\nabla \cdot \mathbf{E}_0 = 4\pi\rho_0$ for the density of the external charge ρ_0, one arrives at $\nabla \cdot \mathbf{E}_m = 4\pi(\rho_0 + \rho_b)$. Further, due to the conservation of charge, the instantaneous density of bound charge can be replaced with the divergence of the polarization vector field $\mathbf{P}_m$, such as $\rho_b = -\nabla \cdot \mathbf{P}_m$[105]. One arrives at the equation for instantaneous fields

$$\nabla \cdot (\mathbf{E}_m + 4\pi \mathbf{P}_m) = 4\pi\rho_0 \tag{1.41}$$

which looks very much like the standard Maxwell equation, except that the fields in this equation refer to an arbitrary statistical configuration of the system. Of course, this equation is just a different form of the Coulomb law, which applies to microscopic dimensions and arbitrary configurations of charges. The two-step averaging and coarse graining procedure mentioned above will produce the average smoothed-out fields $\mathbf{E}$ and $\mathbf{P}$ and the corresponding electric displacement vector $\mathbf{D} = \mathbf{E} + 4\pi\mathbf{P}$. The Maxwell equation for this coarse grained displacement vector follows from Eq. (1.41) as $\nabla \cdot \mathbf{D} = 4\pi\rho_0$.

Equation (1.41) and its coarse grained version still cannot be solved without applying a closure relation between $\mathbf{P}_m$ and $\mathbf{E}_m$ or between $\mathbf{P}$ and $\mathbf{E}$. The connection between microscopic fields $\mathbf{P}_m$ and $\mathbf{E}_m$ is a complex problem of statistical mechanics of liquids[60]. It is therefore assumed that coarse graining helps in eliminating this complexity and leads to local constitutive relations between coarse grained fields

$$\mathbf{P} = \chi \mathbf{E} \tag{1.42}$$

This constitutive relation thus establishes the direct proportionality between the vector fields $\mathbf{P}$ and $\mathbf{E}$ through the susceptibility χ, which is a scalar for isotropic materials. Empirical evidence suggests that this approximation, when used for macroscopic dielectrics, yields the bulk dielectric susceptibility χ_s, which is a material property, i.e., a parameter characterizing bulk dielectric and independent of the sample shape (the surface effects die off in the macroscopic limit). Correspondingly, the dielectric constant of bulk dielectric $\epsilon_s = 1 + 4\pi\chi_s$ is a material property as well.

This result is quite non-trivial since even for coarse grained vector fields the susceptibility χ_0 to the field of external charges $\mathbf{E}_0$ does not share insensitivity to the surface effects (boundary conditions). χ_0 is not a material property and it depends on the shape of the sample through the dielectric boundary value problem. Given that the inhomogeneous Maxwell field $\mathbf{E}$ is not accessible experimentally, most problems of interest for applications involving inhomogeneous fields (solvation of molecules, solvent-induced shifts of spectral lines, interfacial problems, etc.) are formulated in terms of the response to an inhomogeneous external electric field $\mathbf{E}_0$. Nevertheless, the Maxwell field has to be introduced in order to solve the problem since only this field is believed to provide local constitutive relations between $\mathbf{E}$ and $\mathbf{P}$ required to arrive at the Laplace equation. The locality of the Maxwell field for inhomogeneous external fields does not have firm experimental support and is likely to be an approximation. This difficulty is responsible for many problems arising in the general problem of electric polarization of interfaces[106].

The problem of interfacial polarization is solved in dielectric theories by replacing the microscopic fields $\mathbf{E}_m$ and $\mathbf{P}_m$ in each point of the interface with the corresponding coarse grained fields and then applying the local constitutive relation (1.42) to each point of the interface. When substituted to Eq. (1.41), it leads to the Laplace equation for $\mathbf{E}$ fully specified in terms of external charges. However, there is no factual coarse graining when this

procedure is applied to microscopic problems, and it is nearly impossible even to define an algorithm of volume coarse graining when fields are changing on the scale of molecular dimensions. The Laplace equation is obtained in such cases by direct substitution $\mathbf{E}_m \to \mathbf{E}$ and $\mathbf{P}_m \to \mathbf{P}$ and the subsequent use of the constitutive equation. As mentioned, coarse graining of microscopic fields is not achieved directly by averaging over a judiciously chosen volume, but is produced by applying a specific local form of the constitutive relation. The smooth function $\mathbf{E}$ obtained from the solution of the Laplace equation then leads to a smooth $\mathbf{P}$, instead of a highly oscillatory function characteristic of interfaces[107, 108]. It is the constitutive relation that replaces coarse graining over a small volume in converting the microscopic into macroscopic fields.

Since coarse graining is in fact not performed, one can adopt a somewhat different form of the constitutive relation involving only the statistical averaged fields in the interface

$$\langle \mathbf{P} \rangle = \chi \langle \mathbf{E} \rangle \tag{1.43}$$

Of course, Eq. (1.43) is an approximation. In chapter 2, it is discussed how to build a consistent theory of interfacial polarization when this approximation is applied. The advantage of Eq. (1.43) over Eq. (1.42) is that statistical averages are well-defined even on the microscopic scale and one can proceed with ensemble-based algorithms of defining susceptibilities. In other words, in contrast to smoothly varied functions P and E in Eq. (1.42) the corresponding fields in Eq. (1.43) will be highly oscillatory, as usually produced by liquid-state theories and numerical simulations. Eq. (1.43) may be only applied to the dividing surface separating the solute from the solvent. In this way the microscopic calculations is connected to the electrostatic boundary value problem.

If the constitutive relation is the only step separating the microscopic Coulomb law in Eq. (1.41) from the dielectric boundary value problem, one wonders if this procedure can be supplemented with susceptibilities reflecting the microscopic structure of the polarized

interface, i.e., the susceptibility χ in Eq. (1.43). The standard Maxwell dielectric boundary value problem in fact implements one additional approximation of replacing χ in Eq. (1.43) with the susceptibility χ_s of bulk dielectric[109]. This approximation is not required and any scalar susceptibility can be used in solving the boundary value problem. Not surprising, the idea of an effective susceptibility or interfacial dielectric constant has been actively discussed in the literature[110, 111, 107, 112, 113]. In chapter 2, it is discussed how the interface dielectric constant can be obtained from the microscopic interfacial polarization.

1.2.4 Proteins and Large Solutes

The global multipole moment of solutes accounts for solvent and interfacial polarizations and the free energy of solvation of simple small solutes as presented in previous sections. However, in the case of hydrated proteins, interface polarization can be quite different. A typical-sized protein is a heteropolymer consisting of a chain of $\sim$50-500 amino acids. Water-soluble proteins usually have non-polar, hydrophobic groups in their core and polar or charged residues at their surface[114]. The charged residues polarize the water molecules surrounding the protein and make the protein-water interface very heterogeneous. This can result in high electrostatic noise of the protein-water interface[13].

A simple way to investigate the surface polarization is to place point dipoles close to the solute-water interface. Recent studies by Friesen *et al.* found that in contrast to the linear response expectations, the electrostatic free energy of the solution is non-harmonic at intermediate dipole moment magnitudes[115]. Surface excited states as well as the structural transition of water at the interface were observed by increasing the strength of the surface dipole. It was concluded that the statistics of the solvent electric field fluctuations can be different from linear response predictions once surface water molecules have close prob-

abilities to occupy surface excited states. The non-Gaussian statistics indicate nonlinear solvent response.

Surface polarization at a protein-water interface almost determines the properties of the protein hydration shells and significantly disturbs the corresponding network of hydrogen bonds. The protein hydration shells consist of a large number of water molecules, i.e., ~ 500 water molecules in the first hydration shells of a typical globular protein, and involve a large number of microscopic configurations of the shell. Therefore, in contrast to simple small solutes, the solvent polarization now involves a large number of water molecules from the hydration shells, which can have different significant properties as compared to bulk water. A recent study by Martin *et al.* investigated the dipolar response of hydration shells of lysozyme at a wide range of temperatures by MD simulations and suggested the existence of dipolar nanodomains in the protein hydration shells[116].

1.3 Electron Transfer

Electrons that are exchanged during a redox reaction in a solution are the source of perturbing charges in the solvated solute/protein (reactant or product). This creates the external perturbing field $\xi \mathbf{E}_0$ in the solvent, where ξ is the charging parameter or the strength of perturbation. Note that the energy gap X is the energy difference between the reactant and product electronic states for a given instantaneous configuration of the system. In linear response theory, the solvent response is related to the equilibrium fluctuations of the unperturbed solvent ($\langle \dots \rangle_0$)

$$\langle \mathbf{P} \rangle_\xi = \xi \beta \langle \delta \mathbf{P}(\mathbf{r}') \delta \mathbf{P}(\mathbf{r}'') \rangle_0 * \mathbf{E}_0 \tag{1.44}$$

where $*$ means a dot product and a spatial integration. Making use of the thermodynamic integration method, one can obtain

$$\frac{\partial F}{\partial \xi} = \langle \frac{\partial(-\xi \mathbf{E}_0 * \mathbf{P})}{\partial \xi} \rangle_\xi \approx -\xi \mathbf{E}_0 * \beta \langle \delta\mathbf{P}(\mathbf{r}')\delta\mathbf{P}(\mathbf{r}'') \rangle_0 * \mathbf{E}_0 \tag{1.45}$$

Integrating over the perturbation parameter $d\xi$ results in parabolic free energies. Therefore, two simple routes can be used to assess the validity of linear response in electron transfer. One can investigate $\frac{\partial F}{\partial \xi}$ as a function ξ such as electron transfer between an infinitely separate cytochrome *c* and small heme complexes[117, 118]. When the corresponding electron transfer free energies are available (see section 1.3.1), one can also check their parabolicities. As long as there is no polarizable species involved in the reaction, in linear response the free energies are parabolic with the same curvature.

Solvent reorganization energies can also be used to test the linear response. They correspond to the energy that is required to push the equilibrium nuclear configuration of solvents in reactants to equilibrium nuclear configuration of solvents in products when electron transfer does not occur. They are often reported by the first and second cumulants of energy gaps in reactants and/or products[119, 120].

$$\lambda^{\mathrm{St}} = |\langle X_{\mathrm{r}} \rangle - \langle X_{\mathrm{p}} \rangle|/2 \tag{1.46}$$

where r and p stand for reactant and product, respectively and St stands for Stokes shift.

$$\lambda^{\mathrm{var(r/p)}} = \frac{\beta}{2} \langle (\delta X_{\mathrm{r/p}})^2 \rangle \tag{1.47}$$

In linear response, when the system of interest (in electron transfer reaction) is ergodic, $\lambda^{\mathrm{St}} = \lambda^{\mathrm{var(r/p)}}$. This equality is therefore one of the predictions of the Marcus theory.

1.3.1 Electron Transfer Free Energy Surfaces

Consider a chromophore that is dissolved in a solvent. One can trace out the fast electronic degrees of freedom of the chromophore and the solvent to obtain the (partial) free energy of the chromophore in its electronic state i

$$\exp\left[-\beta E_i\right] = \mathrm{Tr}_{\mathrm{el}}\left(\exp\left[-\beta H_i^{\mathrm{tot}}\right]\right) \tag{1.48}$$

where H_i^{tot} is the Hamiltonian of the system in the ground ($i = 1$) and excited states, $\beta = 1/k_{\mathrm{B}}T$, and $\mathrm{Tr}_{\mathrm{el}}$ means the trace over the quantum states of the fast electronic degrees of freedom. Therefore, the instantaneous free energies E_i depend on the nuclear coordinates and correspond to the Born-Oppenheimer energies. One can therefore define the Hamiltonian of the chromophore-solvent system, where chromophore is coupled to the collective nuclear solvent modes q, as

$$H_i = I_i - C_i q + (\kappa_i/2)q^2 \tag{1.49}$$

where I_i is the intrinsic gas phase energy of a diabatic state i ($i = \mathrm{g}, \mathrm{e}$), C_i is the parameter which defines the strength of chromophore-solvent coupling in the linear solvation approximation, and κ_i is the collective force constant, which involves the free energy of polarizing the chromophore and nonlinear chromophore-solvent coupling. The above model, known as the "Q-model", was pioneered by Matyushov *et al.* to address the electron transfer in condensed phase[119].

The fluctuations of the nuclear coordinates can result in the resonance $E_1 = E_2$ during the electronic transition. Therefore, the electron transfer free energy surface in the classical limit can be defined based on the probability distribution of the instantaneous energy gaps $X = E_2 - E_1$.

$$-\beta F_i(X) = \ln P_i(X) = \frac{\int d\Gamma \delta(\Delta E - X) e^{-\beta E_i}}{\int d\Gamma e^{-\beta E_i}} \tag{1.50}$$

where Γ shows the phase space. Sections 5.6.2 and 6.4.1 discuss practical calculations of these free energies for electron transfer in "Q-model" and cytochrome *c*, respectively.

Chapter 2

INTERFACE SUSCEPTIBILITY: FREE ENERGY OF HYDRATION AND INTERFACE DIELECTRIC CONSTANT

2.1 Summary

In this chapter, the concept of interface susceptibility is introduced. It involves the fluctuations of surface charge density, $\delta\sigma_p(r)$, caused by thermal motions and its correlations over the characteristics correlation length with the fluctuations of the solvent charge density, $\delta\rho'_s$ (see Fig. 3). The result of these mutually correlated fluctuations, integrated with the weight of inverse distance (a reminiscent of the usual inverse distance dependence of the Coulomb law), is what makes the interface susceptibility function, $\chi_0(r)$:

$$\chi_0(r) \propto \int (d\mathbf{r}'/r')\langle\delta\sigma_p(r)\delta\rho'_s\rangle_0. \tag{2.1}$$

The electrostatic free energy of ion hydration and the interface dielectric constant are formulated based on the interface susceptibility function and studied for a spherical ion solvated in TIP3P water by numerical simulations. The scaling of the free energy of ion hydration with the solute size obtained from simulations significantly deviates from the Born equation and its empirical off-set corrections. However, representing the solvation free energy as a radial integral over the interface susceptibility function describes well the scaling of the solvation free energy with the ion size produced in a broad range of ion sizes by the simulations. In addition, it is found that the corresponding interface dielectric constant changes from 9 to 4 when the effective solute radius is increased from 5 Å to 18 Å.

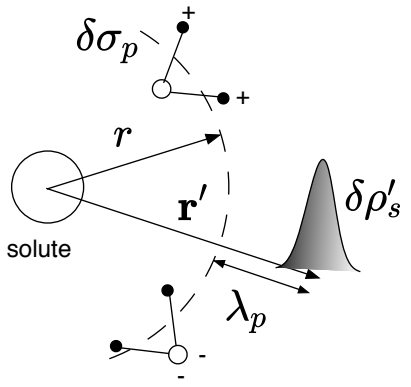

FIGURE 3: Surface charge density σ_p produced by the water molecules crossing the mathematical surface of the radius r ("+" indicates the partial atomic charge of the hydrogen atoms of the water molecules). Fluctuations of the surface charge density $\delta\sigma_p$ caused by thermal motion correlate over the characteristic correlation length λ_p with the fluctuations of the solvent charge density $\delta\rho'_s = \delta\rho_s(\mathbf{r}')$. These mutual correlations are responsible for the interface susceptibility in Eqs. (2.21) and (2.1).

2.2 Free Energy of Hydration

The free energy F_0 of solvating an ion in a polar molecular liquid is usually described by the linear-response equation connecting it to the ion charge q through the solvation susceptibility χ

$$F_0 = -\tfrac{1}{2}\chi q^2. \tag{2.2}$$

Many computer simulation studies have shown that the quadratic scaling with the charge is fulfilled remarkably well and solvation can be described as linear[121, 122, 123, 124]. Given this success, the main focus, in particular in applications[125, 126, 127], is to link the solvation susceptibility χ to the properties of the ion and the solvent. This study is mostly concerned with the problem of the scaling of χ with the size of a spherical solute. We show that χ can be represented as a one-dimensional radial integral of the local susceptibility function $\chi_0(r)$. An exact formula for $\chi_0(r)$ is derived [Eq. (2.21)] and evaluated by numerical simulations.

The Born model of ion solvation represents the solvent by a continuum polarizable medium and the ion by a spherical cavity with the radius a carved in the continuum.[1] The resulting solvation susceptibility is given by the relation

$$\chi_{\mathrm{B}} = \frac{1}{a}\left(1 - \frac{1}{\epsilon}\right). \tag{2.3}$$

The model thus factors χ into the geometric cavity parameter a^{-1} and the longitudinal susceptibility[128, 129] of the bulk polar solvent $\propto (1 - \epsilon^{-1})$ defined by its dielectric constant ϵ. It is typically assumed that the cavity radius a can be connected to the solute radius R_0 by a distance off-set δ[130, 131],

$$a = R_0 + \delta. \tag{2.4}$$

We show here that this phenomenological relation does not stand the test against numerical simulations in a sufficiently broad range of solute sizes. We propose instead a new equation for the cavity radius in terms of the solute-solvent radial distribution function.

The dependence on the solvent polarity is more complex than prescribed by the Born equation when the assumption of the continuum polarizable solvent is lifted and finite size of the solvent molecules is explicitly included. For instance, solvation of ions by a fluid of dipolar hard spheres with diameter σ can be calculated in the mean-spherical approximation (MSA). One gets for the cavity radius in the Born equation[132] $a(p,T) = R_{0s} - \Delta(p,T)$. Here, $R_{0s} = R_0 + \sigma/2$ is the distance of the closest approach of the solvent to the solute repulsive core, which is also the position of the first maximum r_{max} of the solute-solvent pair distribution function. The MSA solution thus predicts $\delta = \sigma/2 - \Delta(p,T)$ in Eq. (2.4), where $\Delta(p,T)$, by which R_{0s} is reduced, is the length of longitudinal dipolar correlations in the bulk solvent[128, 129]. Based on this theoretical prediction and fitting the experimental data[130], it is commonly assumed that the phenomenological cavity radius a should fall between R_0 and R_{0s}[133]. For "soft" solutes, the position of

the first maximum $r_{\max}$ of the solute-solvent radial distribution function replaces R_{0s}[134, 135].

The parameter $\Delta(p,T)$ carries the dependence on the thermodynamic state of the solvent, which is indicated by its dependence on pressure p and temperature T. This particular solution exemplifies the general result that the cavity radius cannot be defined as a constant even for a given solvent/solute combination and needs instead to be a function of the solvent thermodynamic state[136, 135]. Assuming $a = Const$ gives unreliable values for the solvation entropy and, most likely, for other thermodynamic derivatives of the solvation free energy[135, 137, 64, 98]. What we show here is that the dependence of the cavity size on both the thermodynamic state of the solvent and on the solute-solvent potential can be accommodated in terms of the solute-solvent radial distribution function.

The specific problem of ion hydration presents additional complications. The solvation susceptibility χ in Eq. (2.2) gains an additional dependence on the sign of q, even though the linear scaling $F_0 \propto q^2$ is preserved for the positive and negative charges separately[135, 122, 137]. In addition, spontaneous polarization of hydration shells around solutes carrying no charge creates a non-zero electrostatic potential within a zero-charge solute[138]. A solute of zero charge does not polarize the solvent in the standard dielectric theories. This is because of the assumption that the interface susceptibility is identical to the susceptibility of the isotropic bulk liquid (homogeneous approximation discussed below). In fact, inserting even a charge neutral solute into an isotropic solvent breaks the isotropic symmetry. Zero polarization at zero charge is not required by symmetry any longer and can be violated depending on the solvent, as indeed happens for aqueous solutions.

In the case of water, a nonpolar[137, 139] or a hard-sphere (HS)[138] solute carrying no charge produces a spontaneous polarization of the interface with a resulting nonzero potential $\langle\phi\rangle_0$ at $q = 0$ (subscript "0"). The magnitude of $\langle\phi\rangle_0$ is hard to establish experimentally

even at a planar interface[140, 127], and the results of simulations show a significant dependence of $\langle\phi\rangle_0$ on the adopted force field[141, 142, 124, 108, 143]. The sign of $\langle\phi\rangle_0$ also depends on the definition of the cavity potential and whether cavity repulsion is applied to water's hydrogen atoms[144]. Given these uncertainties, we do not discuss $\langle\phi\rangle_0$ in this paper, focusing instead on the charge susceptibility χ in Eq. (2.2).

The positive sign of $\langle\phi\rangle_0$ inside HS and Lennard-Jones (LJ) cavities in point-charge force field water was calculated from a number of previous simulations[138, 124] and also, for an extended range of radii, in our simulations as shown by Fig. 37 in chapter 7. It adds negative solvation free energy to an anion. However, although accounting for some solvation asymmetry, this shift of the potential is not sufficient and lower values of the cavity radii for anions compared to cations are required in the Born solvation susceptibility $\chi_{\rm B}$ in Eqs. (2.2) and (2.3)[124]. Along the same lines, we find here that the second cumulant $\langle(\delta\phi)^2\rangle_0$, which is the main contributor to the solvation free energy[124], is asymmetric between cations and anions, as first discussed by Hummer *et al*[122]. We attribute this asymmetry to different local densities of water around ions of opposite charge. Once the density profile of the interface is accommodated into the definition of the cavity radius (Eq. (2.18) below), the Born linear susceptibility successfully accounts for the scaling with the solute size produced by the simulations.

2.2.1 General Formalism

The linear-response free energy of ion solvation can be written as the multipolar expansion of the solute-solvent Coulomb potential in solvent multipoles[109, 145]

$$F_0 = -\tfrac{1}{2}\int \left[\mathbf{E}_0\cdot\langle\mathbf{P}\rangle_E + \tfrac{1}{3}\nabla\mathbf{E}_0 : \langle\mathbf{Q}\rangle_E + \dots\right] d\mathbf{r}. \tag{2.5}$$

Here, $\mathbf{E}_0$ is the electric field of the ion charges and $\mathbf{P}$ and $\mathbf{Q}$ are the dipolar and quadrupolar (defined according to Ref. 145) polarization densities of the solvent, respectively. The brackets $\langle \dots \rangle_E$ denote the two polarization fields in equilibrium with the solute.

The quadrupolar term is potentially important for hydration because of a large non-axial quadrupole moment of the water molecules reflecting its charge asymmetry. We will, however, drop it from our discussion here and focus solely on the dipolar polarization of the interface. This assumption is justified for relatively large solutes since quadrupolar solvation decays faster with the solute size than dipolar solvation[146]. Our starting point is, therefore, the linear solvation free energy[105] written as the integral of the electric field of an ion with the dipolar equilibrium polarization density

$$F_0 = -\tfrac{1}{2} \int \mathbf{E}_0 \cdot \langle \mathbf{P} \rangle_E d\mathbf{r}. \tag{2.6}$$

Returning to the symmetry arguments presented above, the charge inversion $q \to -q$ results in $\mathbf{E}_0 \to -\mathbf{E}_0$, which reverses the sign in Eq. (2.6). The same reversal can be achieved by flipping all the dipoles in the solvent $\mathbf{m}_j \to -\mathbf{m}_j$ thus producing $\mathbf{P} \to -\mathbf{P}$. The Hamiltonian of the liquid in the external field, $H = H_0 - \int \mathbf{E}_0 \cdot \mathbf{P} d\mathbf{r}$, will remain invariant to the simultaneous $q \to -q$ and $\mathbf{P} \to -\mathbf{P}$ transformation when the unperturbed Hamiltonian H_0 is invariant to $\mathbf{P} \to -\mathbf{P}$. This is the case with the homogeneous approximation, which assumes that the solute does not strongly perturb the solvent and its response can be given in terms of response functions of the homogeneous solvent (Born formula, Eq. (2.3)). This implies that H_0 is effectively the Hamiltonian of the bulk solvent. The transformation $\mathbf{P} \to -\mathbf{P}$ does not change any properties of an isotropic liquid. Therefore, the solvation susceptibility in this homogeneous approximation should be invariant to the $q \to -q$ transformation.

Alternatively, when the isotropic symmetry of the homogeneous solvent is broken by the repulsive core of the solute, the dipole flip $\mathbf{m}_j \to -\mathbf{m}_j$ in the interface will produce a

physically distinct configuration even at $q = 0$. In other words, the Hamiltonian H_0, which includes the repulsive core of the solute, is not invariant to $\mathbf{P} \to -\mathbf{P}$. One therefore expects that the observables measured even in the linear response will not demonstrate the $q \to -q$ invariance, in contrast to the models based on the homogenous approximation. This feature is captured by the local approximation introduced below to contrast with the homogeneous approximation of the standard dielectric theories. We stress that the $q \to -q$ asymmetry does not violate the quadratic scaling of the solvation free energy with the ion charge. It only implies that the solvation susceptibility χ in Eq. (2.2) should be given different values for positive and negative ions.

We also note that the quadrupolar polarization in Eq. (2.5) eliminates the symmetry to the simultaneous transformation $q \to -q$ and $\mathbf{m}_j \to -\mathbf{m}_j$. Therefore, this term, when included, will also contribute to the asymmetry of the observables to the charge inversion $q \to -q$. This is what is often referred to as charge asymmetry of water contributing to solvation asymmetry[137, 147, 148]. However, a potentially more important cause of solvation asymmetry is the difference in the density profiles of water around cations and anions, which is ultimately related to the asymmetric molecular shape and asymmetric distribution of molecular charge in water, but cannot be pinned down to one specific molecular property, such as molecular quadrupole. We present below arguments suggesting that this is essentially a "zero-order" effect, which accounts for most of the solvation asymmetry in terms of a density-weighted effective cavity radius of ion solvation.

2.2.2 Approximate Interface Susceptibilities

The integral in Eq. (2.6) can be re-written, in the linear response, in terms of two fields and a two-point correlation function of the polarization field

$$\chi_{0s}^{\alpha\beta}(\mathbf{r}', \mathbf{r}'') = 4\pi\beta\langle\delta P_\alpha(\mathbf{r}')\delta P_\beta(\mathbf{r}'')\rangle_0, \tag{2.7}$$

where the average $\langle \dots \rangle_0$ is now taken over the configurations of water around the repulsive core of the solute carrying no charge and δX for a spatially varying field X, such as δP_α, is used here to describe deviations from statistically average values. Equation (2.6) turns into the following relation

$$F_0 = -\frac{1}{8\pi}\int E_{0\alpha}(\mathbf{r}')E_{0\beta}(\mathbf{r}'')\chi_{0s}^{\alpha\beta}(\mathbf{r}', \mathbf{r}'')\, d\mathbf{r}' d\mathbf{r}''. \tag{2.8}$$

Here and in Eq. (2.7) α, β subscripts denote Cartesian projections and the summation over the common indexes is assumed.

The fundamental complexity of the solvation problem arises from the fact that the second-rank tensor susceptibility $\boldsymbol{\chi}_{0s}$ defined by Eq. (2.7) is a three-particle correlation function involving correlations of translations and orientations of two water molecules with the position and orientation of the solute. This difficulty has mostly been resolved over many years of studies by attempting to reformulate the problem in terms of two-particle correlation functions[106]. Two possible general directions for formulating such approximations can be identified. They can be labelled as either (i) a "homogeneous" approximation or (ii) a "local" approximation (to which all models with the distance-dependent dielectric constant can be assigned[149]).

In the homogeneous approximation, one assumes that the water-water correlations are not significantly broken by the solute and one can replace $\boldsymbol{\chi}_{0s}(\mathbf{r}', \mathbf{r}'')$, depending on positions of two water molecules $\mathbf{r}'$ and $\mathbf{r}''$ separately, with a homogeneous susceptibility

$\boldsymbol{\chi}_s(\mathbf{r}' - \mathbf{r}'')$ depending only on $\mathbf{r}' - \mathbf{r}''$ (isotropic liquids)[150]

$$\boldsymbol{\chi}_{0s}(\mathbf{r}', \mathbf{r}'') = \theta_V(\mathbf{r}')\theta_V(\mathbf{r}'')\boldsymbol{\chi}_s(\mathbf{r}' - \mathbf{r}''), \tag{2.9}$$

where $\theta_V(\mathbf{r})$ is a step function equal to zero inside the solute and equal to unity otherwise. It specifies the volume V of the solvent from which the homogeneous solvent response is calculated.

The alternative, local approximation would take the opposite view that inserting a solute produces a major alteration of the water structure. Therefore, in this view, the structure of the interface, and not the correlations present in bulk water, is of main significance for the hydration thermodynamics. One then can go to the limit of neglecting the correlations between different water molecules in the interface altogether and replace $\boldsymbol{\chi}_{0s}(\mathbf{r}', \mathbf{r}'')$ with a local function [107]

$$\boldsymbol{\chi}_{0s}(\mathbf{r}', \mathbf{r}'') = \delta\left(\mathbf{r}' - \mathbf{r}''\right)\boldsymbol{\chi}_0(\mathbf{r}'). \tag{2.10}$$

While each of these assumptions, Eqs. (2.9) and (2.10), involve approximations, both have been widely used since they significantly simplify the problem. In terms of going beyond the static dielectric constant of a bulk liquid, the homogeneous and local approximations correspond to k-dependent, $\epsilon(k)$[151], and distance-dependent, $\epsilon(r)$, dielectric constants, respectively. The wavevector-dependent dielectric constant $\epsilon(k)$ of a bulk material has a solid foundation in the Kubo linear response theory[60]. On the contrary, $\epsilon(r)$ was originally introduced as a phenomenological prescription to account for inhomogeneity of the interface[125, 152, 153] and has only recently received microscopic-based definitions for spherical[107, 154, 155], planar[111, 107, 156, 113, 157], or cylindrical[155] interfacial geometries.

What we want to accomplish here is to give a clear mathematical foundation of using the distance-dependent polarization susceptibility $\chi_0(r)$ of the interface. This study is limited to spherical solutes and, therefore, only the radial, angular-symmetric susceptibility

is considered. We in fact find that this susceptibility provides a good reference point for describing ion solvation upon which more advanced theoretical algorithms can be developed. We first apply each of two closures, homogeneous and local, to the linear-response solvation free energy in Eq. (2.8) with the goal of arriving at the Born equation. We then provide in Section 2.2.4 an exact analytical solution for $\chi_0(r)$ in terms of binary correlations accessible from numerical simulations.

The free energy in the homogeneous approximation is the convolution of two electric fields at points $\mathbf{r}'$ and $\mathbf{r}''$ with the susceptibility function depending on $\mathbf{r}' - \mathbf{r}''$. These types of integrals are best taken in the inverted $\mathbf{k}$-space, which both eliminates the convolution and allows one to reduce the problem to scalar susceptibility projections. In the case of a spherical ion, this latter reduction is the consequence of the radial symmetry of the electric field which couples to the longitudinal projection of the susceptibility[41, 158]

$$F_0 = -\frac{1}{2}\int \frac{d\mathbf{k}}{(2\pi)^3}\left|\tilde{E}_0^L(k)\right|^2 \chi_s^L(k). \tag{2.11}$$

Here, $\tilde{E}_0^L = \hat{\mathbf{k}}\cdot\tilde{\mathbf{E}}_0$, $\hat{\mathbf{k}} = \mathbf{k}/k$ is the longitudinal projection of the Fourier transform $\tilde{\mathbf{E}}_0$ of the electric field of the ion taken outside its repulsive core, $\theta_V\mathbf{E}_0$. Its longitudinal character, stressed by the subscript "L", is the combined result of the longitudinal field $\mathbf{E}_0$ and the spherical symmetry of the ion's repulsive core assumed here. Non-spherical repulsive cores require both longitudinal and transverse response projections to determine the free energy[158, 106].

The longitudinal susceptibility[159, 129, 160] in Eq. (2.11) is given in terms of the longitudinal structure factor of the polar liquid[161]

$$\chi_s^L(k) = (3y/4\pi)S^L(k), \tag{2.12}$$

where $y = (4\pi/9)\beta m^2\rho$ is the usual parameter of the dipolar density of molecular

dielectrics[162] carrying molecular dipoles m and having the number density $\rho = N/V$. The longitudinal structure factor $S^L(k)$ is given by Eq. 1.34.

We can now apply the **k**-space field of the spherical ion, $\tilde{E}_0^L(k) = (4\pi iq/k)j_0(ka)$ ($j_n(x)$ is the spherical Bessel function of order n[163]), and note that $\chi^L(k)$ depends on the product of k and the solvent molecular diameter σ. The solvation susceptibility χ in Eq. (2.2) takes the form

$$\chi = \frac{2\chi_B}{\pi}\int_0^\infty dx j_0(x)^2 \chi^L\left(x\frac{\sigma}{a}\right)/\chi^L(0), \tag{2.13}$$

where χ_B is the Born susceptibility in Eq. (2.3). The dependence of the longitudinal susceptibility on the wavevector k can be neglected when $\sigma \ll a$. The function $\chi^L(x\sigma/a)$ can be then replaced with $\chi^L(0) = (4\pi)^{-1}(1-\epsilon^{-1})$, with the result $\chi = \chi_B$. More generally, $\chi^L(x\sigma/a)$ can be expanded in σ/a at $\sigma \ll a$ and one gets the solvation susceptibility in the form $\chi = \chi_B \sum_n c_n(\sigma/a)^n$ consistent with the MSA solution[132].

The solution for the solvation free energy simplifies even further in the local approximation given by Eq. (2.10). The solvation susceptibility in Eq. (2.2) becomes

$$\chi = \int_0^\infty \frac{dr}{r^2}\chi_0(r). \tag{2.14}$$

From this equation, one arrives at the Born result if one assumes $\chi_0(r) = \theta(r-a)(1-\epsilon^{-1})$, where $\theta(x)$ is the Heaviside function. More generally, from Eqs. (2.7) and (2.10) and with the account for the radial symmetry of the ion field, $\chi_0(r)$ is a scalar function given by the relation

$$\chi_0(r) = 4\pi\beta\langle\delta P_r(r)\delta M_r\rangle_0. \tag{2.15}$$

Here, $P_r = \hat{\mathbf{r}}\cdot\mathbf{P}$, $\hat{\mathbf{r}} = \mathbf{r}/r$ and $M_r = \sum_j \mathbf{m}_j\cdot\hat{\mathbf{r}}_j$ is the sum of all radial projections of the liquid dipoles assuming that the spherical ion is positioned at the origin of the laboratory coordinate frame[145].

Equation (2.15) is the direct consequence of the local response approximation in Eq. (2.10) and is similar in structure to analogous relations recently proposed in the literature[154, 113]. The local approximation is a useful device for deriving analytical approximations, but is not required for producing the interface susceptibility from simulation trajectories. In section 2.2.4, we derive an alternative, and exact, equation based on the correlation of fluctuations of the radial polarization field and the solvent "reaction"[65] potential at the position of the ion. The connection between χ and $\chi_0(r)$ in Eq. (2.14) is also exact in that formulation and does not require the local assumption of Eq. (2.10).

2.2.3 Cavity Radius

The average over the solvent configurations around the solute excluding the solvent from its volume, $\langle \dots \rangle_0$, in Eq. (2.15) can be expressed in terms of the three-particle distribution function $g(\mathbf{r}_1\omega_1, \mathbf{r}_2\omega_2)$ representing the probability to find two water molecules at the positions $\mathbf{r}_1$ and $\mathbf{r}_2$ and orientations of their dipole ω_1 and ω_2 with the solute considered as the center of the laboratory coordinate frame[145]. The average can be taken by employing the Kirkwood superposition approximation, $g(\mathbf{r}_1\omega_1, \mathbf{r}_2\omega_2) \simeq g_{0s}(\mathbf{r}_1\omega_1) g_{ss}(\mathbf{r}_{12}\omega_1\omega_2) g_{0s}(\mathbf{r}_2\omega_2)$, where g_{0s} and g_{ss} stand for the solute-solvent and solvent-solvent distribution functions, respectively. This derivation is given in appendix A. The closed-form expression for the local susceptibility $\chi_0(r)$ can be achieved by taking the long-range, continuum limit for the longitudinal structure factor $S^L(k) \to S^L(0)$ appearing in the integral representation of $\chi_0(r)$. The $k = 0$ value of the structure factor produces the standard longitudinal dielectric susceptibility, $S^L(0) \propto (1 - \epsilon^{-1})$, with the final result

$$\chi_0(r) = \left(1 - \epsilon^{-1}\right) \left[g_{0s}(r)\right]^2 . \tag{2.16}$$

Here, $g_{0s}(r)$ is the solute-solvent radial pair distribution function.

The radial susceptibility $\chi_0(r)$ represents the longitudinal response function of radial hydration shells and therefore can be connected to a radial, distant-dependent dielectric constant of the interface

$$\epsilon_r(r)^{-1} = 1 - \chi_0(r). \tag{2.17}$$

It is easy to see that this function crosses zero and becomes negative in the vicinity of the peaks of $g_{0s}(r)$ in Eq. (2.16)[113]. The radial dielectric constant itself hardly has any significant physical meaning and only the radial longitudinal susceptibility $\chi_0(r)$ represents the longitudinal polarization response of the interface. This notion also implies that attempts of producing radial dielectric constants $\epsilon_r(r)$, and perhaps more generally position-dependent dielectric constants, in terms of phenomenological smooth functions have no support of microscopic theories[107].

When Eq. (2.16) for $\chi_0(r)$ is substituted into Eq. (2.14), one arrives at the standard Born equation with the cavity radius defined as

$$\frac{1}{a} = \int_0^\infty \frac{dr}{r^2} \left[g_{0s}(r)\right]^\alpha , \tag{2.18}$$

where $\alpha = 2$ is required by Eq. (2.16). Our calculations of the response from simulations below show that this choice of α, following from the local approximation, overestimates the oscillatory behavior of $\chi_0(r)$ and instead $\alpha < 1$ is required to reproduce the simulations.

Berne and co-workers[164] suggested $\alpha = 1$ in Eq. (2.18) whereas Linder and Hoernschemeyer[136] used $3g_{0s}(r)/r^4$ as the integrand in Eq. (2.18) to define $1/a^3$. All these original propositions were given without proof, although representing the electrostatic energy by a sum over a dipolar lattice can be used to justify[63] $\alpha = 1$ in Eq. (2.18). A dipolar lattice of course does not display an interfacial density alteration and is not a good model for testing the cavity concepts. On the other hand, our empirical α-scaling follows from the exact formula for $\chi_0(r)$ taken from Eq. (2.21) derived in the next section and used in Eq. (2.14), combined with its direct calculation from simulation trajectories.

One can use Eq. (2.18) for a crude estimate of the scaling of the solvation free energy with the cavity radius. This follows from the $r \to \infty$ asymptote[145] of $g_{0s}(r) = 1+h_{0s}(r)$: $h_{0s}(r) \propto r^{-1}$. If $h_{0s}(r)$ dominates in $g_{0s}(r)$ near the contact, one can replace $[g_{0s}(r)]^{\alpha}$ with $\theta(r-a)[h_{0s}(r)]^{\alpha}$ in Eq. (2.18) to obtain $F_0 \propto 1/a^{\alpha+1}$. The power law decay in fact gives a reasonable account of our simulation data (Fig. 5 below). However, the complete integral representation for the cavity radius in terms of Eq. (2.18) is more consistent with simulations. Note also that Eq. (2.18) yields the standard definition of the cavity size for a structureless continuum interfacing the solute when the solute-solvent pair distribution function reduces to the Heaviside function, $g_{0s}(r) = \theta(r-a)$.

2.2.4 Exact Interface Susceptibility

In the previous section, we have discussed two approaches to handle the inhomogeneous character of the interfacial response of a polar solvent in terms of the distribution functions formalisms of liquid-state theories. Here, we provide an exact representation of the interface susceptibility $\chi_0(r)$ in terms of correlation functions accessible from configurations produced by numerical simulations.

The starting point of our analysis is the recognition of the fact that the electric field of the ion $\mathbf{E}_0$ has longitudinal symmetry, implying that its curl is identically zero[109], $\nabla \times \mathbf{E}_0 = 0$. The symmetry of the field of charges imposes a corresponding symmetry on the dipolar polarization density $\mathbf{P}$, which should be longitudinal as well[165]. The longitudinal component of the polarization density $\mathbf{P}_L$ is directly related to the electrostatic potential Φ_p produced by the charges of the solvent[166, 20]

$$4\pi\mathbf{P}_L = \nabla\Phi_p. \tag{2.19}$$

This connection can be productively used to derive the exact relation for the interface sus-

ceptibility in Eq. (2.14), which can be re-written as follows

$$\chi_0(r) = (r^2/q) \int \chi_{0s}^{r\beta}(\mathbf{r}, \mathbf{r}') E_{0\beta}(\mathbf{r}') d\mathbf{r}', \tag{2.20}$$

where $\chi_{0s}^{r\beta}$ is given by Eq. (2.7) and the "r" superscript denotes the radial projection: $\chi_{0s}^{r\beta} = \hat{r}^{\alpha}\chi_{0s}^{\alpha\beta}$. Note that this form of $\chi_0(r)$ in Eq. (2.14) is exact and does not require the local approximation of Eq. (2.10).

By substituting Eq. (2.19) in place of the δP_β projection in Eq. (2.7) and integrating by parts, one can eliminate the volume integral in Eq. (2.20) by noting that $\nabla \cdot \mathbf{E}_0(\mathbf{r}) = 4\pi q \delta(\mathbf{r})$. The final result for the interfacial susceptibility is

$$\chi_0(r) = -4\pi\beta r^2 \langle \delta P_r(r) \delta\phi \rangle_0. \tag{2.21}$$

Here, $\phi = \Phi_p(0)$ is the electrostatic potential produced by the solvent at the position of the ion at the center of the solute and $\delta\phi = \Phi_p(0) - \langle \Phi_p(0) \rangle$. Further, ϕ can be directly related to the molecular charge density of the solvent $\rho_s' = \rho_s(\mathbf{r}')$ as follows

$$\phi = \int \frac{\rho_s'}{r'} d\mathbf{r}' = \sum_j \frac{q_j}{r_j}, \tag{2.22}$$

where the sum in the second part of the equation runs over all (partial) atomic charges q_j in the solvent with radial distances from the ion r_j.

As in Eq. (2.15) above, the average in Eq. (2.21) is taken over the configurations of the solvent in equilibrium with the repulsive core of the solute (subscript "0"). This prescription allows one to calculate the interfacial susceptibility from computer simulations with $q = 0$, as is done in this study. Further, the radial projection of the polarization density $P_r(r)$ is calculated in the radial shell between r and $r + dr$ as follows

$$P_r(r) = \frac{1}{4\pi r^2 dr} \sum_{r \le r_j \le r+dr} \mathbf{m}_j \cdot \hat{\mathbf{r}}_j. \tag{2.23}$$

Finally, $\delta P_r(r)$ in Eq. (2.21) are the deviations of $P_r(r)$ from average values in each shell.

Given the obvious non-locality of the dipolar interactions in a polar liquid, Eq. (2.21) might look misleadingly local, suggesting a possibility to define a local polarization response in the interface. Clarifying the physical meaning of the correlation function in the right-hand side of Eq. (2.21) seems therefore useful.

The radial projection of the polarization density is also the normal projection of the vector field $\mathbf{P}$ on the sphere of radius r. Consequently, $P_r(r) = \sigma_p(r)$ defines the density of surface charge[109] $\sigma_p(r)$ arising from the mathematical surface cutting through the water molecules crossing the surface and by that creating surface monopoles (Fig. 3). Fluctuations of P_r correspond, therefore, to fluctuations of the surface charge density, $\delta P_r = \delta\sigma_p$. These surface fluctuations correlate with the fluctuations of the molecular charge density $\delta\rho'$ over some correlation length λ_p. The result of these mutually correlated fluctuations, integrated with the weight $1/r'$, is what makes the interface susceptibility function defined in the introduction section. The non-locality of the interfacial response is in fact preserved in the correlation function and is ultimately determined by the extent of interfacial charge-charge correlations.

2.2.5 Numerical Simulations

Several routes to access the free energy F_0 are available within the linear response. The most widely used and fastest to converge by numerical simulations[121] is through the average potential $\langle\phi\rangle$ [Eq. (2.22)] of the water solvent in equilibrium with the charge q: $F_0 = (q/2)\left(\langle\phi\rangle_0 + \langle\phi\rangle\right)$. Here, the equilibrium potential $\langle\phi\rangle$ includes the potential $\langle\phi\rangle_0$ of the spontaneously polarized interface and an additional potential $\langle\phi_q\rangle$ produced by the solvent in response to placing charge q at the center of the solute. It is this second potential that produces the quadratic scaling of the free energy with the ion charge [Eq. (2.2)] and is

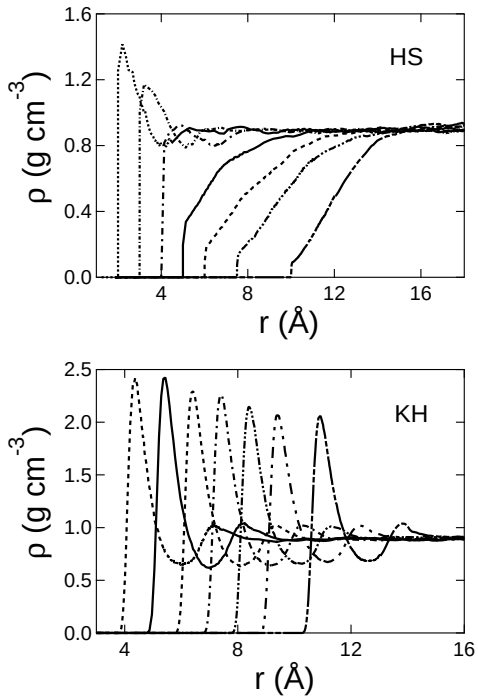

FIGURE 4: Water density profiles, $\rho(r) = \rho g_{0s}(r)$, around the hard-sphere (HS) and Kihara (KH) solutes as a function of growing size of the solute hard-sphere core ($R_{\rm HS}$ for KH and R_{0s} for HS solute). The density profiles are calculated from MC simulations with a single solute in the simulation cell containing TIP3P water at 298 K (see chapter 7 for detail).

our focus here. The use of the average potential to calculate F_0 has its disadvantages when combined with Ewald sums used to treat electrostatic interactions in simulations. Ewald sums require compensating the ion charge q with the uniform background of the opposite charge to neutralize the simulation cell[167, 168] and a corresponding correction for the potential of the uniform background is required to calculate $\langle\phi_q\rangle$.

To avoid this somewhat artificial situation of running simulations in a continuum background charge[169], one can simulate the solute carrying zero charge. The potential $\langle\phi_q\rangle$ can then be calculated from the perturbation theory, leading to the solvation susceptibility in Eq. (2.2) in the form[123, 124, 147]

$$\chi = \beta\langle\delta\phi^2\rangle_0. \tag{2.24}$$

The simulation cell is neutral in this case and the problem of artificial background charge is avoided. Furthermore, the variance of the potential does not depend on the presence of the charge in the linear response, $\langle \delta\phi^2 \rangle_0 = \langle \delta\phi^2 \rangle$, and this route can be applied to the calculations involving both neutral and charged solutes because the constant potential of the charged background is subtracted in the variance. We find from our simulations that the equality of two variances is not satisfied for HS solutes carrying positive and negative charges[122]: $\langle \delta\phi^2 \rangle_{q<0} > \langle \delta\phi^2 \rangle_{q>0}$. The structure of the interface around hard-core objects is strongly modified by introducing even weak attractions[170], in this case Coulomb solute-solvent interactions, but can be accommodated into the solvation susceptibility through the effective cavity radius depending on the solute-solvent density profile (see below). As the size of the HS core increases, the density profiles of the cations and anions converge and the gap between the corresponding variances narrows.

2.2.6 Simulation Details

The second cumulant route to the solvation free energy [Eq. (2.24)] was adopted in our Monte Carlo (MC) and molecular dynamics (MD) simulations of solutes of varying size and solute-solvent potential hydrated by TIP3P[80] water at 298 K. The main goal here is to see how the structure of the solute-water interface affects the dependence of χ in Eq. (2.2) on the solute size. Here, we have significantly extended the range of solute sizes typically studied in the field of ion solvation[133, 124, 131] to the range of ~ 1 nm when a substantial restructuring of the interface is expected to occur[171, 172, 173]. Our goal is also to compare the performance of the homogeneous and local approximations against simulations and to explore the possibility of establishing a measure of the local polarity of

the interface that can potentially replace the dielectric constant in the Born equation. We indeed find that this local polarity can be defined in terms of the radial susceptibility $\chi_0(r)$.

A detailed description of the MC/MD simulation protocols is given in chapter 7. Here, we only briefly describe the system setup. Two types of solutes interacting with TIP3P water[80] at 298 K were used in the simulations. The first solute is a HS characterized by the distance of the closest approach R_{0s} of the water solvent to the solute. The size of the HS solute was varied by changing this parameter in the range $R_{0\mathrm{s}} = 2 - 10$ Å. We observed a strong dewetting[171, 173] of TIP3P water at $R_{0s} \geq 5$ Å (Fig. 4). Since the dewetting phenomenon is strongly affected by the solute-solvent attraction and might not occur for more realistic solutes of this size[170], two types of the solute-solvent attractions were introduced. A number of single-charged ($|q| = 1$) anions and cations were simulated. These introduce electrostatic attractions with the interfacial water multipoles oriented along the ion field. These attractions, however, become weaker with increasing the solute size and dewetting still occurs (Fig. 39 in chapter 7).

Real multi-atomic ions always involve solute-solvent dispersion attractions, which typically prevent dewetting of the interface[170]. In order to represent this situation in our modeling, simulations with the Kihara solute-solvent potential[174] were carried out as well. The Kihara potential adds a layer of LJ 6-12 potential to a HS core characterized by the radius R_{HS} (see chapter 7). The extent of solute-solvent attraction can be controlled by the solute-solvent LJ energy ϵ_{LJ}. The size of the solute was varied by changing R_{HS} in the range $1 - 7.5$ Å. The electrostatic potential of water at the center of the solute was calculated from the MC configurations and used to calculate the potential variance in Eq. (2.16). Since Kihara potential does not have the problem of discontinuous forces characteristic of HS repulsion, we used the NAMD 2.9[175] software package to calculate $\chi_0(r)$ from Eq.

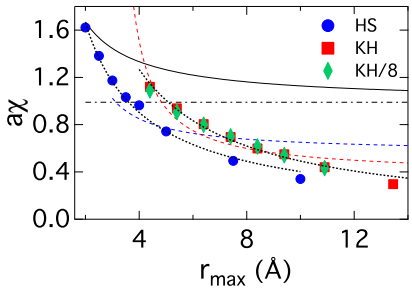

FIGURE 5: Ion dimensionless solvation susceptibility $a\chi$ from Eq. (2.2) obtained in MC simulations and different models using the parameters of TIP3P water: $\epsilon = 97$, $\sigma = 2.87$ Å (effective HS diameter), and $m = 2.35$ D. The horizontal dashed line shows the Born result, Eq. (2.3). The points are results of MC simulations for HS and Kihara solutes with the solute-solvent LJ energy $\epsilon_{\rm LJ} = 3.7$ kJ/mol ("KH") and 8 kJ/mol ("KH/8"). The solvation free energies extracted from MC simulations are multiplied with the distance $r_{\rm max}$ from the solute center to the first maximum of the solute-solvent pair distribution function ($a = r_{\rm max}$). The points in the plot therefore show $-2r_{\rm max}F_0/q^2$, where the solvation free energy F_0 is determined according to Eq. (2.24). The blue and red dashed lines are fits of the simulation data to the dependence $r_{\rm max}/(r_{\rm max} - \Delta)$ (see text for explanation). The solid line is the calculation with the homogeneous approximation, Eq. (2.13). The black dotted lines are fits to the power decay $\propto r_{\rm max}^{-\gamma}$ with $\gamma = 0.9$ (HS) and 1.0 (KH).

(2.21) for two Kihara solutes. The susceptibility $\chi_0(r)$ is fundamentally a three-particle correlation function, requiring long trajectories (~ 200 ns) to converge.

2.2.7 Solvation Free Energy

Figure 5 shows the ion solvation susceptibility $a\chi$ in Eq. (2.2) as a function of the cavity radius for HS and Kihara solutes (the results for anions and cations are given in Fig. 40 in chapter 7). The Born equation, Eq. (2.3), predicts a constant value, fully determined by the dielectric constant, which is shown by the horizontal dash-dotted line. The homogeneous approximation is shown by the solid line, and it approaches the continuum limit from above with increasing the solute size a, as expected from the general arguments. The calculations

were done by applying Eq. (2.13), in which the longitudinal structure factor from numerical simulations[176, 98] of TIP3P water was used.

The points shown in the plot refer to the dimensionless parameter $r_{\max}\chi$ with χ calculated according to Eq. (2.24) and $r_{\max}$ referring to the first maximum of the solute-solvent pair distribution function. We note that the solvation susceptibility is affected by the nature of the solute-solvent potential (HS vs Kihara), but is less affected by the strength of LJ attraction. The two nearly coinciding sets of points in Fig. 5 refer to the solute-solvent LJ energy of $\epsilon_{\rm LJ} = 3.7$ kJ/mol (squares) and 8.0 kJ/mol (diamonds) in the Kihara potential. They demonstrate low sensitivity of the solvation susceptibility to the strength of solute-solvent LJ attraction.

Since the cavity radius a is an empirical parameter, which does not have to coincide with $r_{\max}$, the Born equation would predict $r_{\max}\chi \propto r_{\max}/(r_{\max}-\Delta)$ (Eq. (2.4)), where Δ is a distance offset to obtain the cavity radius from $r_{\max}$, $a = r_{\max} - \Delta$. The simulation results do not follow these expectations, as is shown by the dashed lines in Fig. 5 attempting to fit the simulation points. A numerically better fit follows from the power decay $r_{\max}\chi \propto r_{\max}^{-\gamma}$ with $\gamma \simeq 0.9 - 1.0$. We can conclude that the scaling of the solvation susceptibility with the solute size anticipated by the Born equation is not supported by the simulations.

The alternative to the Born equation is the integral form in Eq. (2.14), which involves the local radial susceptibility $\chi_0(r)$. Equation (2.21) provides an exact solution for this function, while the local approximation involves simplifications of two levels: the neglect of the spatial extent of dipolar correlations in the hydration shell that leads to Eq. (2.15), followed by the use of the continuum approximation in evaluating the correlator between radial polarization and the radial dipole moment that leads to Eq. (2.16). Two MD simulations of Kihara solutes of different size were carried out to access $\chi_0(r)$ and test both approximations.

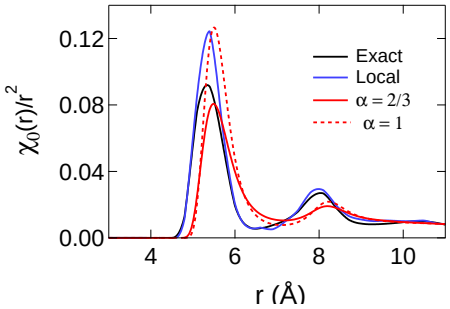

FIGURE 6: Integrand function $\chi_0(r)/r^2$ in Eq. (2.14) for Kihara solutes with $R_{\rm HS} = 2$ ÅṪhe exact susceptibility function [Eq. (2.21)] calculated from MD simulations (black lines) is compared to the empirical relation [Eq. (2.25)] with $\alpha = 2/3$ (solid red lines) and $\alpha = 1$ (dashed red lines). The blue lines indicate χ_0 calculated in the local approximation given by Eq. (2.15).

We first find that $\chi_0(r)$ as calculated from the exact relation in Eq. (2.21) is an oscillatory function, with oscillations compatible with the density profile around the solute (Fig. 6). This result is consistent with Eq. (2.16), but the amplitude of oscillations is significantly overestimated by that relation (not shown in the plot). At the same time, the local approximation itself, without the use of the continuum limit in Eq. (2.16), is a much better representation of $\chi_0(r)$, with only a slight overestimate of the oscillations amplitude (cf. blue and black lines in Fig. 6). This comparison is a strong evidence in support of the local approximation compared to the homogeneous one, suggesting that the focus on the local structure of the hydration shell, in contrast to the bulk-like dipolar correlations, is a better starting point for constructing predictive theories of ion hydration.

The focus on the solute-solvent density profile to determine the solvation susceptibility as suggested by Eq. (2.16) is still a useful perspective, which needs to be corrected to provide quantitatively reliable results. A better agreement with simulations can be obtained by taking a fractional power, instead of a square, of the pair distribution function in Eq. (2.16). This results in the radial susceptibility function in the form

$$\chi_0(r) = \left(1 - \epsilon^{-1}\right) \left[g_{0s}(r)\right]^{\alpha} . \tag{2.25}$$

Figure 6 shows $\chi_0(r)/r^2$ (the integrand in Eq. (2.14)) with $\alpha = 2/3$ compared to the MD results. This empirical prescription is used to calculate the effective cavity radius in Eq. (2.18).

It is important to understand the physical origin of a sublinear scaling of the interface susceptibility function with the density profile of the interface. Allowing long-range, bulk-like dipolar correlations in the interface leads to $\alpha = 2$ in Eqs. (2.16) and (2.25). This result physically implies that the dipolar correlations act cooperatively and enhance the susceptibility in denser parts of the shell characterized by peaks of the radial distribution function. When the correlations between the dipoles are neglected and only a one-particle dipolar response is considered in the perturbation theory, one arrives[164, 63] at $\alpha = 1$ in Eq. (2.25). The sublinear scaling obtained from fitting the simulation data implies that denser parts of the shell significantly hinder one-particle dipolar reorientations and a response weaker than the one-particle one is produced. The linear scaling of the distant-dependent dielectric constant with the density profile ($\alpha = 1$) was noticed previously[107, 177], but this scaling seems to apply better to the approximate, local form of the susceptibility function [Eq. (2.15)] used in those simulations (cf. blue lines with dashed red lines in Fig. 6).

2.2.8 Effective Cavity Radius

Figure 7 compares the effective cavity radius a calculated from Eq. (2.18) to the position of the first peak maximum r_{max} of the solute-solvent radial distribution function. The height of the peak is affected by packing advantages close to a solute of large size, increasing its amplitude, and by the balance between the solute-solvent and solvent-solvent attractions. The existence of the peak implies that the effective cavity radius a is below r_{max}, as is seen for the Kihara solute (red squares in Fig. 7), for which the amplitude of the

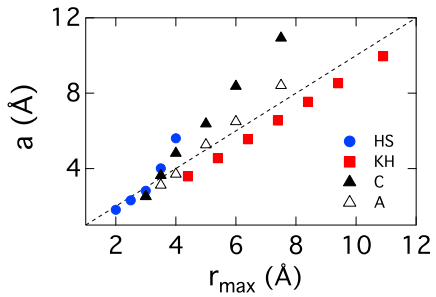

FIGURE 7: Cavity radius a determined from Eq. (2.18) plotted against the position of the first peak of the solute-solvent radial distribution function $r_{\max}$. The dashed line is $a = r_{\max}$ line drawn to guide the eye. The simulations points are for hard-sphere (HS), Kihara (KH), hard-sphere anion (A), and hard-sphere cation (C) solutes. $r_{\max} = R_{0s}$ for HS solutes.

density peak stays nearly constant with the growing HS core (Fig. 4, lower panel). The situation, however, becomes more complex when the interfacial structure significantly changes with increasing solute size.

This is the case with the HS solutes, where without the surface LJ attraction of the Kihara potential, dewetting of the interfacial water occurs as the solute size increases (Fig. 4, upper panel). Lowering density of the interface results in an upward shift of the cavity radius a, which becomes greater than $r_{\max}$ (blue circles in Fig. 7). HS anions and cations show a weaker dewetting of the interface due to the solute-water attraction (Fig. 39 in chapter 7), but the increase of the cavity radius is still observed as the attraction of the water molecules to the solute becomes weaker with the growing solute size. In addition, the cavity size of the cations (filled triangles in Fig. 7) is consistently greater than the cavity size of the anions (open triangles in Fig. 7). This implies higher in magnitude solvation energies of the anions compared to the cations of the same size, a phenomenon well documented for ion hydration.

The simple and significant outcome of this calculation is that assuming a constant distance offset of $r_{\max}$ to define the cavity radius, such as $a = r_{\max} - \Delta$ (as follows from the

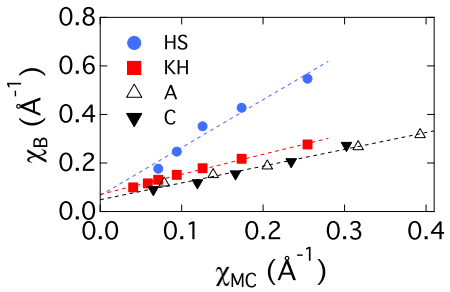

FIGURE 8: Solvation susceptibility χ (Eq. (2.2)) calculated from MC simulations as $\chi_{\rm MC} = -2F_0/q^2 = \beta\langle(\delta\phi)^2\rangle_0$ and from the Born equation $\chi_{\rm B} = a^{-1}\,(1-\epsilon^{-1})$ with the cavity radius a calculated from Eq. (2.18). The results are reported for the hard-sphere (HS), Kihara (KH), and ionic (cations "C" and anions "A") solutes. The dashed lines are linear fits through the points with the slopes 2.0 (HS), 0.8 (KH), and 0.7 (C+A).

MSA and often empirically assumed), has little chance to perform well for a broad range of solute radii and solute-solvent potentials. Figure 7 in fact shows that the offset Δ can be either positive or negative depending on the interaction potential. The Kihara potential might be a fortuitous case when this prescription works relatively well because the interfacial density profile remains almost unchanged with growing HS core due to the specific form of this potential.

The cavity radius from Eq. (2.18) gives a good account of the free energy change with the solute size. Figure 8 compares the solvation susceptibility $\chi_{\rm MC}$ from MC simulations [Eq. (2.24)] to $\chi_{\rm B}$ [Eq. (2.3)] with the cavity radius a given by Eq. (2.18). The slope of the straight line between $\chi_{\rm B}$ and $\chi_{\rm MC}$ deviates from unity because of the $k \to 0$ approximation for the correlations between the dipoles in the hydration shell used to derive Eq. (2.18). Nevertheless, the distinction in solvation energies of cations and anions of equal size (Fig. 7) is successfully accommodated in terms of their corresponding cavity radii.

2.3 Interface Dielectric Constant

Some of phenomenological recipes proposed to deal with microscopic interfaces, such as the popular distance-dependent dielectric constant for solvation problems[125], do not withstand the scrutiny of microscopic formulations[12]. The problem with such formulations is that spatial correlation functions describing microscopic interfacial polarization are typically highly oscillatory[107, 108] and do not allow defining simple distance-dependent susceptibilities. If any meaningful microscopic susceptibility has a chance to enter the standard boundary value problem, it should be consistently derived from the microscopic Coulomb law in Eq. (1.41) and not introduced as *ad hoc* phenomenological recipe justified by fitting to experimental data or results of numerical simulations. Providing such a consistent approach is the goal of this article. In other words, the main question addressed here is what is the dielectric constant, absorbing into itself the microscopic properties of the interface, that should enter the standard dielectric boundary value problem? We provide a general formulation of the problem, followed by specific calculations of the dielectric response of water interfacing a spherical solute.

2.3.1 Boundary Value Problem

When one takes the statistical average in Eq. (1.41), one arrives at $\nabla \cdot \langle \mathbf{D} \rangle = 0$ inside the dielectric where there are no external charges. This relation translates, through Gauss' theorem, into the condition of discontinuity of the projection of $\langle \mathbf{D} \rangle$ on the unit vector $\hat{\mathbf{n}}$ normal to the interface. This condition can be written as[105]

$$\hat{\mathbf{n}} \cdot (\nabla \langle \phi_1 \rangle - \nabla \langle \phi_2 \rangle) = 4\pi\sigma, \tag{2.26}$$

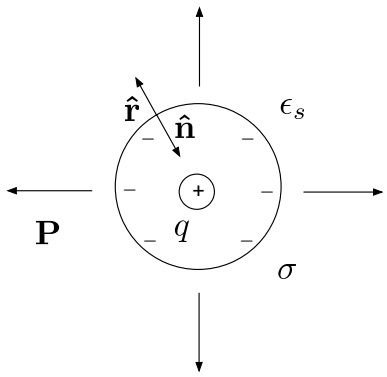

FIGURE 9: Surface charge density at the interface between a spherical cavity and a dielectric with the dielectric constant ϵ_s. The polarization density field $\mathbf{P}$ is aligned with the radial field of a positive charge q placed at the center of the cavity. The surface charge density σ is opposite in charge to q to screen its interactions with charges placed outside of the cavity. $\hat{\mathbf{n}}$ denotes normal to the interface and $\hat{\mathbf{r}} = -\hat{\mathbf{n}}$ is the unit radial vector.

where σ is the surface charge density determined by the normal projections of the polarization density $P_{ni} = \hat{\mathbf{n}} \cdot \mathbf{P}_i$ ($i = 1, 2$) in two media in contact in the interface

$$\sigma = P_{n1} - P_{n2}. \tag{2.27}$$

In the standard dielectric theories, the surface charge density σ screens the external charge. It means that if a probe charge is placed at a large distance from the interface, the effective force between the external charge q and the probe charge is reduced by the opposite charge of the interface polarization and an effective charge q_{eff}, instead of q, is measured by the force. This is illustrated in Fig. 9 for the simple case of a spherical cavity of radius a with a charge q placed at its center, as discussed in the numerical simulations of aqueous solutions below. The positive charge q will, in dielectric theories, create the opposite in sign surface charge density $\sigma = -(1 - \epsilon_s^{-1})(q/S)$, where $S = \pi a^2$ is the area of the cavity. The effective charge producing the measurable force on an external probe charge, $q_{\text{eff}} = q + \sigma S = q/\epsilon_s$, is then reduced by the dielectric constant of the dielectric ϵ_s.

When the constitutive relation (1.43) is applied to statistically averaged fields $\langle \mathbf{E} \rangle$ and

$\langle \mathbf{P} \rangle$ in Eq. (1.41), $\langle \mathbf{E} \rangle = -\nabla \langle \phi \rangle$ satisfies the Laplace equation $\Delta \langle \phi \rangle = 0$ inside the dielectric where there are no external charges. The properties of the interface enter the problem through the boundary condition in Eq. (2.27). Therefore, the goal of reformulating the standard Maxwell boundary value problem needs to focus on introducing microscopic properties of the interface into the boundary conditions of the Laplace equation. This is the goal we are pursuing here.

Equation (2.27) suggests that the only property of the interface one needs to supply to the solution of the Laplace equation is the surface charge density or the normal projection of the polarization density. The linear response approximation[60] provides the desired property in terms of a non-local susceptibility function $\boldsymbol{\chi}_0(\mathbf{r}, \mathbf{r}')$ (generally a tensor) depending on two coordinates in the interface

$$\langle P_n(\mathbf{r}) \rangle = \int \hat{\mathbf{n}} \cdot \boldsymbol{\chi}_0(\mathbf{r}, \mathbf{r}') \cdot \mathbf{E}_0(\mathbf{r}') d\mathbf{r}', \tag{2.28}$$

where the 2-rank tensor of susceptibility is

$$\boldsymbol{\chi}_0(\mathbf{r}, \mathbf{r}') = \beta \langle \delta\mathbf{P}(\mathbf{r}) \delta\mathbf{P}(\mathbf{r}') \rangle. \tag{2.29}$$

Here, $\beta = 1/(k_{\mathrm{B}}T)$ and $\delta\mathbf{P} = \mathbf{P} - \langle \mathbf{P} \rangle$.

The susceptibility $\boldsymbol{\chi}_0$ in Eq. (2.29) is a second rank tensor defined by the corresponding Cartesian components[165]. For some geometries of the interface, it is convenient to consider specific projections of $\boldsymbol{\chi}_0$. For instance, for the planar interface, one defines parallel ($\hat{\mathbf{n}}_{\parallel}$) and perpendicular ($\hat{\mathbf{n}}_{\perp}$) projections[111, 107] as the scalar functions $\chi_{\parallel} = \hat{\mathbf{n}}_{\parallel} \cdot \boldsymbol{\chi}_0 \cdot \hat{\mathbf{n}}_{\parallel}$ and $\chi_{\perp} = \hat{\mathbf{n}}_{\perp} \cdot \boldsymbol{\chi}_0 \cdot \hat{\mathbf{n}}_{\perp}$. Similarly, for spherical solutes which we consider below, one can define the scalar projection on the radial direction[107], $\chi_0^{rr} = \hat{\mathbf{r}} \cdot \boldsymbol{\chi}_0 \cdot \hat{\mathbf{r}}$. Such definitions become less useful for interfaces of arbitrary shape. Using longitudinal and transverse symmetries of the polarization field provides a more general formulation[97, 158, 106]. Our goal here does not involve calculating distance-dependent projections of the susceptibility.

We focus instead on the normal projection of the polarization density field in Eq. (2.27), taken at the dividing surface, which can be defined for an arbitrary interface.

The two-point tensor $\boldsymbol{\chi}_0(\mathbf{r}, \mathbf{r}')$ depends on two positions, $\mathbf{r}$ and $\mathbf{r}'$, separately to reflect its interface character and the involvement of three-body solvent-solvent-solute correlations. This needs to be contrasted with the non-local susceptibility of bulk dielectrics depending only on $\mathbf{r} - \mathbf{r}'$.

One can further assume that the length of polarization correlations in the interface is much shorter than the characteristic dimension of the interfacial region and apply the local approximation neglecting such correlations altogether[112]

$$\boldsymbol{\chi}_0(\mathbf{r}, \mathbf{r}') = \delta(\mathbf{r} - \mathbf{r}')\boldsymbol{\chi}_0(\mathbf{r}'). \tag{2.30}$$

This approximation obviously eliminates the integral in Eq. (2.28) shifting the focus to the inhomogeneous susceptibility $\boldsymbol{\chi}_0(\mathbf{r})$. It can be obtained by integrating Eq. (2.29) over $\mathbf{r}'$

$$\boldsymbol{\chi}_0(\mathbf{r}) = \beta\langle\delta\mathbf{P}(\mathbf{r})\delta\mathbf{M}\rangle, \tag{2.31}$$

where $\mathbf{M}$ is the total dipole moment of the dielectric. Analogues of this equation for different symmetries of the interface have been proposed by by Stern and Feller[111] and by Ballenegger and Hansen[107, 112] and extensively used in a number of recent simulations of interfacial polarization[156, 155, 113, 178]. We note that the local approximation becomes exact in the limit of a uniform external field considered by Stern and Feller[111].

Before we proceed to the exact formula for the susceptibility tensor, not involving the local approximation of Eq. (2.30), it is useful to provide the connection between Eq. (2.31) and the dielectric experiment performed by applying a uniform electric field to the bulk dielectric. One obtains for an isotropic dielectric

$$(\beta/\Omega)\langle(\delta\mathbf{M})^2\rangle = \Omega^{-1}\int_{\Omega}\mathrm{Tr}[\chi_0(\mathbf{r})]d\mathbf{r}, \tag{2.32}$$

where the integration is performed over the volume Ω of the dielectric and $\mathrm{Tr}[\boldsymbol{\chi}_0] = \sum_\alpha \chi_0^{\alpha\alpha}$. The fluctuation expression on the left-hand side of this equations enters the Kirkwood-Onsager equation for the dielectric constant[179] and thus provides the connection between the volume integrated susceptibility to the bulk dielectric constant ϵ_s. Such a connection is, however, not straightforward when one considers the distance dependence of a specific projection of $\boldsymbol{\chi}_0(\mathbf{r})$. In other words, polarization fluctuations $\delta\mathbf{P}(\mathbf{r})$ still carry microscopic information, no matter how far from the interface. These fluctuations are coarse-grained, with the microscopic information lost, by volume integration.

Even though the local approximation provides a fast resolution of the problem, it is not required[20]. One can take into account the longitudinal character of the field of external charges $\mathbf{E}_0$ and the fact that $\int \mathbf{P}'_T \cdot \mathbf{E}'_0 d\mathbf{r}' = 0$ for the transverse projection of the polarization field $\mathbf{P}_T$ (Helmholtz theorem[99]). Therefore, only the longitudinal projection of the polarization $\mathbf{P}' = \mathbf{P}'_L$ enters $\boldsymbol{\chi}_0$ in Eqs. (2.28) and (2.29). The longitudinal projection of the polarization is in turn connected to the potential of the bound charge as[20] $4\pi\mathbf{P}_L = -\mathbf{E}_b$, where $\mathbf{E}_b$ is given by Eq. (1.40). Given that $\mathbf{E}_b = -\nabla\phi_b$, one can apply the Gauss theorem to eliminate the integral in Eq. (2.28). The result is the exact relation for P_n not requiring the use of the local approximation

$$\langle P_n \rangle = -\beta \langle \delta P_n \delta U^C \rangle. \tag{2.33}$$

Here,

$$\delta U^C = \sum_i q_i \delta\phi_{bi} \tag{2.34}$$

is the fluctuation of the Coulomb interaction energy of the dielectric with the external charges q_i; ϕ_{bi} is the potential of the bound charges of the dielectric at the location of the charge q_i, $\delta\phi_{bi} = \phi_{bi} - \langle\phi_{bi}\rangle$.

Equation (2.33) is the exact solution for the problem of the surface charge density in the interface assuming linear response to the field of external charges. Deriving it does

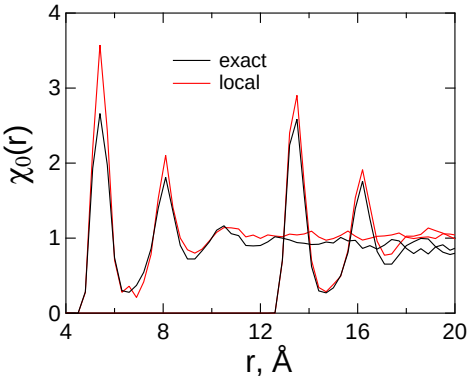

FIGURE 10: Comparison of the local [Eq. (2.37)] and exact [Eq. (2.38)] formulas for the interface susceptibility of TIP3P water interfacing Kihara solutes of different size. The Kihara solutes are characterized by the hard-sphere core of the radii $R_{\rm HS} = 2$ and 10 Å and the Lennard-Jones (LJ) diameter of $\sigma_{\rm LJ} = 3$ Å for the LJ interaction between the solute and water's oxygen. The position of the first peak of the radial distribution function is approximately located at $R_{\rm HS} + \sigma_{\rm LJ}$.

not require constitutive relations. If the constitutive relation (1.43) is adopted, one can find the statistically averaged electrostatic potential of the interface $\langle\phi\rangle$ from the solution of the Laplace equation and, in addition, ask the question of what susceptibility, or dielectric constant, can be assigned to the interface. Such scalar interface susceptibility can be defined by the equation

$$\langle P_n\rangle = \chi_{0n} E_{0n}. \tag{2.35}$$

It is important to emphasize that no specific assumptions regarding either the origin of the polarization density P_n or the electrostatic energy U^C have been introduced in deriving Eq. (2.33). Both parameters can be microscopic quantities sampled by numerical computer simulations. For instance, a polar liquid with molecular dipoles $\mathbf{m}_j$ with coordinates $\mathbf{r}_j$ will have the polarization density $P_n(\mathbf{r}) = \hat{\mathbf{n}} \cdot \sum_j \mathbf{m}_j \delta(\mathbf{r} - \mathbf{r}_j)$. Correspondingly, U^C can be viewed as the energy of Coulomb interactions of all atomic partial charges of the dielectric with the external charges. This property is routinely provided by numerical simulations.

Equation (2.35) can be substituted back to Eqs. (2.26) and (2.27) to produce the boundary conditions for the Poisson equation

$$\hat{\mathbf{n}} \cdot (\nabla\langle\phi_1\rangle - \nabla\langle\phi_2\rangle) = 4\pi \left(\chi_{0n,2} - \chi_{0n,1}\right) \hat{\mathbf{n}} \cdot \nabla\phi_0, \tag{2.36}$$

where ϕ_0 is the electrostatic potential of external charges remaining continuous at the dividing surface. This is the only place where the susceptibility of the interface enters the boundary value problem. The local constitutive relations, Eqs. (1.42) and (1.43), applied globally to the entire dielectric sample in dielectric theories, are replaced with the constitutive relation in Eq. (2.35) applied to the dividing surface only.

The constitutive equation (2.35) might be a reasonable approximation for a few molecular layers in the interface, but is not expected to hold globally. Likewise, the susceptibility χ_{0n}, and the interface dielectric constant ϵ_{int} defined for spherical solutes below, are parameters characterizing the interface. We, therefore, do not expect them to approach the dielectric susceptibility or the dielectric constant of the bulk material in any specific limit. Even for a macroscopic interface, χ_{0n} is still an interfacial parameter (like the surface tension), which should not be expected to be simply related to the bulk susceptibility χ_s.

2.3.2 Interface of a Spherical Solute

Here we apply the arguments presented above to the problem of water polarization at the interface of a spherical solute. The normal to the interface is defined outward from the dielectric[105], $\hat{\mathbf{n}} = -\hat{\mathbf{r}}$, $\hat{\mathbf{r}} = \mathbf{r}/r$ (Fig. 9). A further simplification of the geometry is achieved by locating the external charges at the center of the solute. All susceptibility tensors become scalars with the only non-zero diagonal radial component $\chi_0^{rr} = \hat{\mathbf{r}} \cdot \boldsymbol{\chi}_0 \cdot \hat{\mathbf{r}}$. We will drop the indexes for brevity with the notation $\chi_0(r) = \chi_0^{rr}(r)$. For this specific

type of interface, the local approximation leads to

$$\chi_0(r) = \beta\langle\delta P_r(r)\delta M_r\rangle, \tag{2.37}$$

where $P_r = -P_n$ and $M_r = -M_n$ denote the radial projections of the corresponding vectors (Fig. 9).

Since the electric field of the central charge q is $E_{0n} = -q/r^2$, one can define the distance-dependent linear interfacial susceptibility $\chi_{0n}(r)$ analogous to the one in Eq. (2.35)

$$\chi_{0n}(r) = -\beta r^2\langle\delta P_r(r)\delta\phi_b\rangle, \tag{2.38}$$

where ϕ_b is the electrostatic potential produced by the dielectric at the center of the spherical solute where the external charge is placed. The interfacial susceptibility χ_{0n} follows from this function by adopting $r = a$, i.e., the radius of the spherical surface separating the solute from the surrounding dielectric. We note that our Eq. (2.38) is equivalent to its integral form earlier derived by Ballenegger and Hansen[107]

$$\chi_{0n}(r) = 4\pi r^2\beta\int_a^\infty\langle\delta P_r(r)\delta P_r(r')\rangle dr', \tag{2.39}$$

where the integral over r' produces $\delta\phi_b$ in our Eq. (2.38).

The definition of the position of the dividing dielectric surface presents a major difficulty for all dielectric theories, and it is not going to go away in our formulation recasting the problem of a microscopic polarized interface as the dielectric boundary problem. The question we are addressing here is what is the susceptibility or the surface charge density that needs to enter the boundary conditions once such a dividing surface is defined. However, the question relevant to this goal is how sensitive such a definition would be to possible variations of the position of the dividing surface. One ideally wants a robust definition, little sensitive to changes in the cavity radius a.

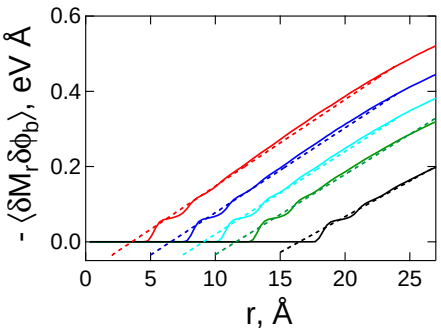

FIGURE 11: Definition of the interface susceptibility χ_{0n} in terms of the slope of $-\langle \delta M_r(r) \delta \phi_b \rangle$ according to Eq. (2.40). The dashed lines show linear fits to $-\langle \delta M_r(r) \delta \phi_b \rangle$ calculated from MD simulations of Kihara solutes interfacing TIP3P water. The hard-sphere core of the Kihara solutes was varied in simulations: $R_{\rm HS} = 2$ (red), 5 (blue), 7.5 (cyan), 10 (green), and 15 (black) Å.

Figure 10 shows $\chi_0(r)$ in the local approximation [Eq. (2.37)] and the exact $\chi_{0n}(r)$ [Eq. (2.38)] calculated from molecular dynamics (MD) simulations performed in this study. The simulations are done for TIP3P water[80] interfacing spherical solutes of varying diameter and interacting with the oxygen of water by the Kihara potential (a hard-sphere repulsion core with the radius $R_{\rm HS}$ combined with a surface layer of soft Lennard-Jones potential)[180, 154]. One has to keep in mind that correlation functions in Eqs. (2.33) and (2.38) are fundamentally three-particle correlations involving two solvent molecules and the solute. Relatively long MD simulations, ~ 200 ns, were therefore required to converge them for each solute studied here. More detail on the simulation protocol is given in chapter 7 and here we discuss the results.

It is clear from the calculations that the local [Eq. (2.37)] and exact [Eq. (2.38)] formulations for the radial interface susceptibility generally agree with each other. The exact formulation is obviously preferable since it is free of the locality assumption. Both results show an oscillatory behavior of the interface susceptibility, leading to potential uncertainties when the cavity radius is altered. Some type of averaging over the oscillations is needed to arrive at a robust definition of interfacial susceptibility and the corresponding

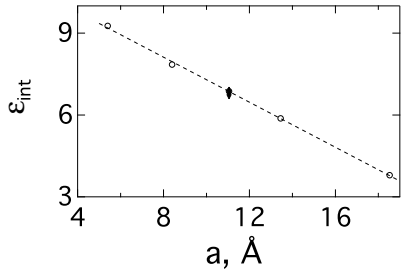

FIGURE 12: Interface dielectric constant ϵ_{int} plotted against the cavity radius $a = r_{\text{max}}$ defined as the distance r_{max} to the first peak of the solute-oxygen pair distribution function. Circles refer to neutral Kihara solutes, while diamonds refer to anion and cation Kihara solutes ($R_{\text{HS}} = 10$ Å, $r_{\text{max}} = 11.05$ Å) with charges $q = \pm 1$ placed at the solute's center (not distinguishable on the scale of the plot). The dashed line is a linear regression through the points drawn to guide the eye.

dielectric constant. An approach developed previously[20] and adopted here is to define χ_{0n} as the slope of the integrated correlation function involving the instantaneous dipole moment $M_r(r)$ of water within the sphere of radius r and the electrostatic potential ϕ_b. The resulting expression provides the scalar susceptibility of the interface, averaged over the oscillations caused by molecular granularity,

$$\chi_{0n} = -\frac{\beta}{4\pi}\frac{d}{dr}\langle \delta M_r(r)\delta\phi_b\rangle. \tag{2.40}$$

If differential in the above equation is taken at each point, one recovers $\chi_{0n}(r)$, with its oscillatory behavior shown in Fig. 10. Alternatively, instead of taking the differential at each point, we determine the linear slope in respect to r to average out the oscillations of $\chi_{0n}(r)$ caused by molecular granularity. This linear slope then provides us with the scalar coarse grained susceptibility of the interface with oscillations averaged out. Figure 11 shows that indeed the slope can be well defined from the correlation function $\langle \delta M_r(r)\delta\phi_b\rangle$.

The susceptibility χ_{0n} to a radial external field E_{0n} should be associated with the interface dielectric constant ϵ_{int} according to the relation $(\epsilon_{\text{int}} - 1)/(4\pi\epsilon_{\text{int}}) = \chi_{0n}$[107, 20],

which leads to

$$\epsilon_{\text{int}} = \left[1 - 4\pi\chi_{0n}\right]^{-1} . \tag{2.41}$$

These values, obtained from the slopes of the radial correlation functions shown in Fig. 11, are presented in Fig. 12. We find that ϵ_{int} decreases slowly from ~ 9 to 4 as the effective size of the solute increases from ~ 5.5 Å to 18.5 Å. Overall, the value of the interface dielectric constant is much smaller than the bulk value for TIP3P water, $\epsilon_s \simeq 97$[181]. While there is no *a priori* reason to anticipate $\epsilon_{\text{int}} = \epsilon_s$, it is this assumption that is used in the standard dielectric boundary value problem.[109] We also note that the definition of ϵ_{int} by Eq. (2.41) is prone to numerical instabilities when $4\pi\chi_{0n}$ becomes greater than unity due to calculation errors. ϵ_{int} is not required for the solution of the boundary value problem in Eq. (2.36) and χ_{0n} is sufficient. It is presented here solely because of the history of the subject casting the dielectric boundary value problem in terms of the dielectric constant.

The results shown by circles in Fig. 12 are obtained for neutral Kihara solutes. Even though Eq. (2.33) contains the electrostatic interaction energy with the external charge of the ion, which is proportional to the charge magnitude, charge cancels out when the surface susceptibility is defined by dividing the surface polarization by the ion field in Eq. (2.35). We therefore operate in the linear response domain, when one can assume that the presence of the external charge does not alter the structure of the interface used to perform the statistical averages. That this is indeed the case is demonstrated by simulating Kihara solutes with positive and negative charges placed at their centers. These results are shown by diamonds in Fig. 12 and are indistinguishable from the results obtained for neutral solutes (see chapter 7 for more detail). Our simulations are indeed consistent with the linear response approximation.

The small value of the interface dielectric constant of water has potentially dramatic consequences for the problem of hydration. Our formalism anticipates that ϵ_{int} is used in the

dielectric boundary value problem. Therefore, the solvation free energy of a spherical ion carrying charge q and assigned the cavity radius a is given by the standard Born equation[1, 122] $F = -(1/2)\chi_B q^2$, where the Born solvation susceptibility is

$$\chi_B = \frac{1}{a}\left(1 - \frac{1}{\epsilon_{\text{int}}(a)}\right). \tag{2.42}$$

Here, $\epsilon_{\text{int}}(a)$ indicates that the dependence of the Born solvation susceptibility on the cavity radius can be more complex than the traditionally anticipated a^{-1} scaling.

The reasons for the relative success of the Born equation in predicting the free energy of solvation and its dramatic failure in describing entropy of solvation have long been known[135, 182, 137, 124]. Both are related to the low sensitivity of the Born formula to the solvent properties when the bulk dielectric constant $\epsilon_s \gg 1$ is used instead of ϵ_{int} in Eq. (2.42). The traditional form of the Born equation significantly underestimates the entropy of solvation[135] since the term $\epsilon_s^{-2}\partial\epsilon_s/\partial T$, appearing in the entropy, is too small. This deficiency can be potentially remedied if, according to our calculations, $\epsilon_{\text{int}} \ll \epsilon_s$. The final verdict requires knowledge of $\epsilon_{\text{int}}(T)$. Our estimate for TIP3P water gives $(\partial\epsilon_{\text{int}}/\partial T)_V \simeq -0.8\times10^{-4}$ K^{-1}, which is significantly lower than $(\partial\epsilon_s/\partial T)_P = -0.36$ K^{-1} of bulk water. Whether this low value is shared by more realistic force fields of water is not clear at the moment.

2.4 Conclusions

We have presented here a consistent derivation of the radial dipolar susceptibility of water hydrating a spherical ion. This function is viewed as a microscopic foundation of the distant-dependent dielectric constant of phenomenological models. An exact solution for this function is given in terms of the correlation between fluctuations of the radial polarization density of water with fluctuations of the electrostatic potential created by water

at the position of the ion [Eq. (2.21)]. The susceptibility calculated from numerical simulations shows an oscillatory behavior consistent with the density profile of the interface. This function is empirically approximated by a power law of the solute-water pair distribution function. Oscillations of the interface susceptibility make approximations based on smooth distance-dependent dielectric constants of the interface inconsistent with the exact solution.

The connection between the interface radial susceptibility and the pair distribution function has allowed us to determine the effective cavity radius in the Born expression for the solvation free energy. This connection would not have been possible in the absence of the susceptibility function since developing cavity models by fitting the overall solvation energy is unreliable. The proposed algorithm incorporates the density profile of the interface into the definition of the electrostatic cavity [Eq. (2.18)]. This expression provides correct scaling of the hydration free energy with the solute size and successfully accounts for different solvation energies of anions and cations of the same size in terms of different density of water in their hydration shells.

In addition, a formalism is presented connecting the Maxwell boundary value problem with the microscopic structure of the interface. In other words, the dielectric constant that should enter the boundary conditions in the Laplace equation describing a polarized dielectric interface is investigated. The problem is formulated in terms of the interface susceptibility or, alternatively, the interface dielectric constant. This property is calculated from an exact equation statistically averaging correlated fluctuations of the interface polarization density and the electrostatic energy of external charges interacting with the polarized dielectric. Evaluated by MD simulations of water interfacing spherical solutes, the interface dielectric constant is found to be significantly lower than the corresponding bulk value.

Chapter 3

SOLVATION SUSCEPTIBILITY IN THE NON-HARMONIC REGIME: POLARIZABLE SOLUTES

3.1 Summary

Interfacial structural transition in hydration shells of a polarizable solute at critical polarizabilities is discovered. The transition is manifested in maximum water response, the reorientation of the water dipoles at the interface, and an increase in the density of dangling OH bonds. This discovery suggests that some configuration of the solution can produce a greater sensitivity and, as a result, a greater control of the chemical reactivity in (bio)chemistry.

3.2 Introduction

When the electric field $\mathbf{E}_0$ is introduced by a solute into a condensed polar material, the response of the medium (solvent) is largely linear: the electrostatic potential or field of the solvent is a linear function of solute's charge or dipole. The linear response (also known as the Gaussian approximation) assumes a harmonic free energy as a function of the medium collective coordinate coupled to $\mathbf{E}_0$[122]. In polar solvents, the dipolar polarization density of the solvent $\mathbf{P}$ becomes such collective coordinate when higher-order multipolar fields, such as the quadrupolar polarization density, are neglected[109]. The harmonic electrostatic free energy of the solution reads

$$\mathcal{F}[\mathbf{P}] = -\mathbf{E}_0 * \mathbf{P} + (2\chi)^{-1}\mathbf{P} * \mathbf{P}, \tag{3.1}$$

where the asterisk implies both the tensor contraction and the volume integration over the space occupied by the solvent[165]. The solvation susceptibility χ is an analog of the susceptibility of a material to an external field, but it also depends on the geometry of the solute repulsive core. This dependence enters through the Maxwell boundary conditions when $\mathbf{P}$ is approximated by a continuum polarization field.

The minimization of $\mathcal{F}[\mathbf{P}]$ in respect to $\mathbf{P}$ yields the equilibrium solvation free energy $F_0 = -(\chi/2)\mathbf{E}_0 * \mathbf{E}_0$, which becomes the standard Born equation for a spherical ion when the longitudinal susceptibility $\chi^L \propto (1 - \epsilon^{-1})$ is used in Eq. (3.1). Since the solvent dielectric constant ϵ is large for many polar solvents, F_0 is close to its saturation limit at $\epsilon \to \infty$. Only minor changes in the solvation free energy can be achieved by changing either the solvent or the thermodynamic state of the solution.

The situation can potentially change near the critical point of the phase diagram where the second, harmonic term in Eq. (3.1) vanishes[183]. This term describes the reversible work (free energy) required to change the polarization of the liquid from $\mathbf{P} = 0$ to $\mathbf{P}$ when the solute produces no field ($\mathbf{E}_0 = 0$). Correspondingly, a large quadratic penalty for increasing the polarization makes strong variations of F_0 hard to achieve. The general question we address here is whether one can significantly reduce the quadratic penalty and what kind of solvent response might be expected if the quadratic term in the free energy functional approaches zero, which corresponds to $\chi \to \infty$.

Using the analogy with bulk phase transitions[183], we consider here a specific physical mechanism of reaching a state of vanishing harmonic expansion term. The molecular polarizability of the solute is used to tune the harmonic response. In order to simplify the electrostatic part of the problem, the solute is a dipole $\mathbf{m}$ at the center of a spherical core characterized by the isotropic dipolar polarizability α. The electrostatic problem can be recast in terms of the instantaneous field E, which is the projection of the electric field of

the solvent on the solute dipole

$$\mathcal{F}[E] = -mE + (\kappa/2)E^2 - (\alpha/2)E^2 + G[E]. \tag{3.2}$$

Similarly to Eq. (3.1), the second term in this equation is the harmonic free energy penalty for producing an electric field inside the solute carrying no dipole and no polarizability. The ″spring constant″ $\kappa \propto \chi^{-1}$ carries the meaning of the solvation modulus; $\kappa^{-1} = (2/R^3)(\epsilon - 1)/(2\epsilon + 1)$ for a spherical dipole in a dielectric[65]. The third term is the free energy of polarizing the polarizable solute, and $G[E]$ includes the higher-order expansion terms.

3.3 Discussions and Results

It is clear from Eq. (3.2) that the harmonic term vanishes at $\kappa = \alpha$. The harmonic truncation becomes inadequate in the vicinity of this point and higher-order expansion terms, given by $G[E]$, are needed. A general form of $G[E]$ is, however, unknown. Therefore, numerical Monte Carlo (MC) simulations are used here to study the vicinity of the critical point $\kappa = \alpha$ and the transition to non-harmonic solvation when the harmonic truncation in Eqs. (3.1) and (3.2) becomes inapplicable. The questions addressed here are whether one can achieve a stronger solvent response near $\kappa = \alpha$ compared to the standard harmonic (Gaussian) models and whether microscopic changes in the structure of the interface are realized near the critical point.

The answers to both these questions are affirmative. Figures 13 and 14 illustrate our main findings. Figure 13 shows the average field at the solute dipole (Onsager's reaction field[65]) and the variance of the solvent electric field, both as functions of the solute polarizability. We observe an inflection of the average field at $\alpha^* \simeq 20 - 22$ Å^3 (Fig. 13a)

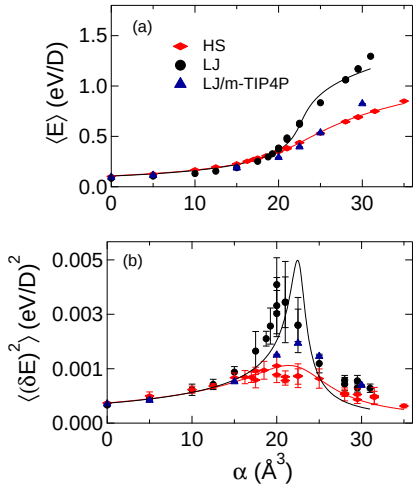

FIGURE 13: (a) Onsager reaction field $\langle E \rangle$ for the hard-sphere (HS) and Lennard-Jones (LJ) solutes with the dipole moment $m_0 = 5$ D and varying polarizability in TIP3P water at $T = 298$ K. The solid lines are fits to the Landau functional in E; simulation errors are smaller than symbol sizes. (b) The variance of E with error bars indicating the simulation uncertainties. The solid lines refer to the Landau theory based on the fitting of $\langle E \rangle$ shown in (a). The blue triangles indicate the results of molecular dynamics simulations for the LJ solute in modified TIP4P water (see chapter 7).

and a corresponding spike in the field variance (Fig. 13b). The field variance is proportional to the dipolar susceptibility and the spike in the variance implies a corresponding spike in the susceptibility. The divergence $\chi \to \infty$ is avoided by the higher-order expansion terms in $G[E]$ as discussed below. We start the discussion with the question of the microscopic origin of the susceptibility spike. We have found that it is driven by a structural transition of the hydration shell.

The MC simulations reported here were done for two solutes: a hard-sphere (HS) solute with the HS radius $R_{\rm HS} = 4.15$ Å and a Lennard-Jones (LJ) solute with the LJ radius $R_{\rm LJ} = 3$ Å. Each solute carried two opposite charges, $+q$ and $-q$, placed symmetrically relative to the solute center at the short distance of $d = 0.05$ Å to model an ideal dipole. The LJ solute additionally had a LJ 12–6 site located at its center with the LJ energy $\epsilon_{\rm LJ} = 280$ K. The dipole moment of the solute was varied by changing the magnitude of q (see

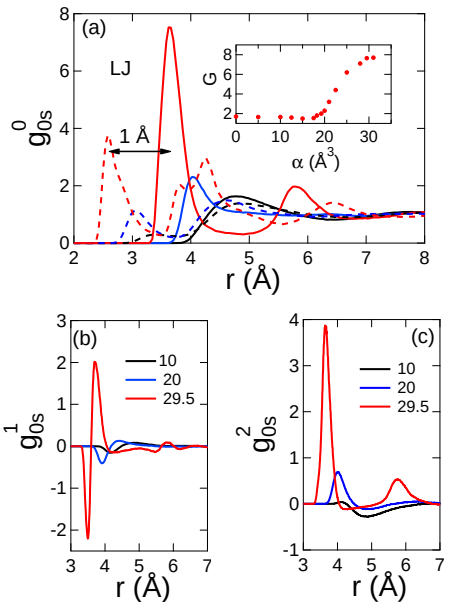

FIGURE 14: Solute-water distribution functions $g^{\ell}_{0s}(r)$ (Eq. (3.3)) for the LJ solutes with the polarizabilities α indicated in the plot. (a) The solute-oxygen (solid lines) and solute-hydrogen (dashed lines) radial distribution functions ($\ell = 0$). The inset shows the height of the first solute-solvent peak G. The horizontal arrow indicates the separation of the first oxygen and hydrogen peaks. The orientational functions with $\ell = 1$ and $\ell = 2$ are shown in panels (b) and (c), respectively.

chapter 7 for the details of the simulation protocol). Most of the results are reported for TIP3P water[80]. Our conclusions are not sensitive to the choice of either the water model or specifics of the solute. This is indicated by the comparison with the results obtained with a slightly modified TIP4P water model[80] (Fig. 13) combined with a larger distance between opposite charges in the solute ($d = 1.5$ Å).

The reason for choosing two solutes was to show that the general phenomenology reported here is not a property of some specific solute-solvent interaction potential, but instead reflects a more general competition between the free energy gain of polarizing the solute and the free energy penalty of orienting the solvent dipoles to create the electric field. Two different solute sizes were adjusted to produce nearly equal polar response of TIP3P water to the solute dipole. The reaction field is a linear function of m at $\alpha = 0$:

$\langle E \rangle = \kappa^{-1} m$. The HS and LJ solutes were chosen to produce close values of κ in two cases ($\kappa_{\mathrm{HS}} = 28.7$ Å^3 and $\kappa_{\mathrm{LJ}} = 29.6$ Å^3, see Fig. 41 in chapter 7).

Figure 14 illustrates the structure of the hydration shell of the polarizable LJ solute as defined by the orientational solute-solvent distribution functions $g^{\ell}_{0s}(r)$ of increasing order ($g^{\ell}_{0s}(r)$ of the HS solute are shown in Fig. 44 in chapter 7). The function $g^{\ell}_{0s}(r)$ is given as the average Legendre polynomial of order ℓ specified by the scalar product of the unit dipole moment $\hat{\mathbf{m}}_j$ and the radial unit vector $\hat{\mathbf{r}}_j$ of the water molecule j positioned at distance r_j from the solute center

$$g^{\ell}_{0\mathrm{s}}(r) = \rho^{-1} \sum_j \langle P_\ell(\hat{\mathbf{m}}_j \cdot \hat{\mathbf{r}}_j) \delta(\mathbf{r}_j - \mathbf{r}) \rangle \,. \tag{3.3}$$

Here, ρ is the number density of bulk water.

The orientational structure of interfacial water next to HS and LJ solutes is consistent with the phenomenology established for planar hydrophobic surfaces[184], molecular nonpolar solutes[171], and hydrated nanoparticles[185] when α is small. The height of the first maximum G of the solute-water radial distribution function ($\ell = 0$) is below the maximum of bulk water (inset in Fig. 14a), indicating a weak dewetting of the interface[186]. In addition, the water dipoles are preferentially oriented tangentially to the dividing surface[184]. The increase of the solute polarizability dramatically changes this phenomenology, producing a structural transition in the hydration shell. Unlike the gradual change to the hydrophilic behavior caused by increasing surface polarity[187], the transition observed here is abrupt and analogous to the global loss of stability at the point of phase transition[183].

Increasing the solute polarizability substantially alters the density profile ($\ell = 0$) and the orientational structure ($\ell > 0$) of the hydration shell. One clearly sees an increase in the density of the first hydration layer (Fig. 14a): the maximum of the radial distribution function grows with increasing polarizability and the first minimum decreases in amplitude

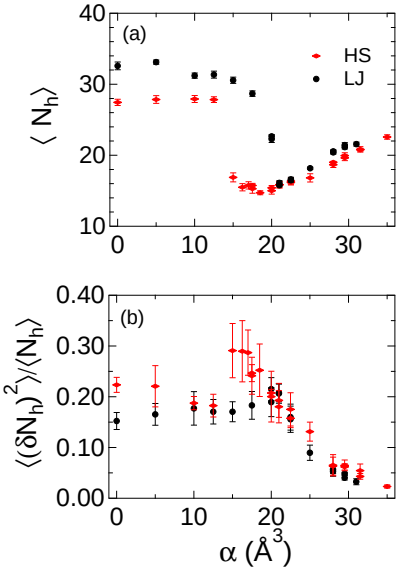

FIGURE 15: (a) The average numbers of water molecules in the first hydration shell of HS and LJ solutes. (b) Hydration shell compressibilities. The error bars indicate the simulation uncertainties.

and becomes increasingly shallow. Near the critical polarizability α^*, producing the spike in the electric field variance (Fig. 13b), a layering transition[188] occurs separating the first and the second hydration layers. This transition is particularly distinct for the HS solute (Fig. 44 in chapter 7).

Collapse of the first hydration layer is also seen as a stepwise drop in the number of hydration waters N_h (Fig. 15a) calculated within the shell geometrically defined to extend up to the first minimum of the radial distribution function. The variance of the number of shell waters drops, however, faster than the average with increasing α, resulting in an overall decrease of the shell compressibility[189] $\langle(\delta N_h)^2\rangle/\langle N_h\rangle$ at $\alpha > \alpha^*$ (Fig. 15b). The structural collapse of the hydration layer is accompanied by an orientational transition to accommodate the high density of the first-shell waters.

The first peak of the solute-hydrogen distribution function shifts, with increasing α, to shorter distances compared to the first solute-oxygen peak (Fig. 13a). This shift indicates

the switch of the preferential outward (into water) orientation of the interfacial hydrogens to the inward (toward the solute) orientation. In the range of $\alpha > \alpha^*$, the distance between the oxygen and hydrogen peaks is $\simeq 1$ Å, essentially equal to the O-H distance in TIP3P water. This implies that the corresponding OH bonds are protruding from water toward the solute, thus forming "dangling" OH bonds[190, 191].

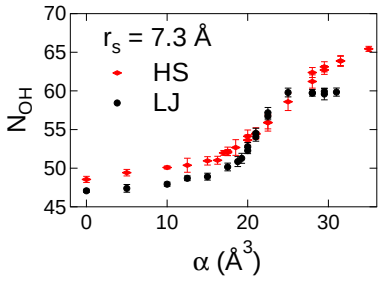

FIGURE 16: The number of unsatisfied hydrogen bonds $N_{\rm OH}$ within the sphere of radius $r_s = 7.3$ Å measured from the center of HS and LJ solutes.

The appearance of dangling bonds seen from the radial distribution functions is consistent with the growth of a positive first peak of the orientational distribution $g^2_{0s}(r)$ in Fig. 14c. It is also clear that the release of dangling OH eliminates the restrictions imposed by the bulk-like tetrahedral arrangement of the water molecules and, therefore, allows the collapse of the hydration layer to a higher density. The result is a distinct structural transition releasing dangling OH bonds and occurring at the critical value of the solute polarizability zeroing out the quadratic term in the free energy functional. The number of dangling OH bonds can be viewed as an order parameter of the structural interfacial transition, which can be experimentally monitored[190, 191].

The dangling bonds are identified experimentally by their separate vibrational line[190]. There is no clear connection between this spectroscopic identification and structural information available from simulations[191]. Since we cannot directly count spectroscopically active dangling bonds, we have calculated unsatisfied hydrogen bonds according to Wernet

et al.[192]. The numbers of unsatisfied bonds are typically higher[191] than spectroscopic dangling OH: about one dangling OH per four water molecules at extended hydrophobic interfaces[190] or even lower numbers around molecular-sized solutes[191]. Nevertheless, the numbers of unsatisfied bonds vs α might mirror the corresponding trend for dangling bonds. Those numbers indeed increase with α when counted in water layers of different thickness. Figure 16 shows the results for the closest hydration layer with the thickness of the water diameter. A similar trend is seen for a wider shell (Fig. 45 in chapter 7).

The simulation data for the reaction field were fitted (solid lines in Fig. 13a) by applying a Landau functional[183] involving the fourth and sixth order expansion terms in $G[E]$ in Eq. (3.2): $G[E] = -(b/4)E^4 + (c/6)E^6$. The exclusion of the odd powers in E is required by the invariance under the inversion $E \to -E$ when $m = 0$. The fit to the reaction field from simulations is then used to calculate the variance of E: $\langle(\delta E)^2\rangle = [(\partial^2\mathcal{F}/\partial E^2)|_{E=0}]^{-1}$. The results of these calculations are shown by the solid lines in Fig. 13b. We also find that the spike in $\langle(\delta E)^2\rangle$ does not produce a non-monotonic dependence of the overall solvation free energy on α: $F_0(\alpha)$ is significantly steeper at $\alpha > \alpha^*$, but the overall dependence is still monotonic (Fig. 46 in chapter 7).

Several systems and observables can display the phenomenology reported by our simulations. The first two moments of the solvent electric field largely determine the shift and inhomogeneous line width of optical dyes. The non-monotonic behavior of the field variance vs α should therefore be mirrored by the spectral width. The overall line-shape can be calculated from the Landau functional $\mathcal{F}(E)$, which extends the harmonic theory of spectroscopy of polarizable chromophores[193] to non-harmonic solvation.

Non-harmonic solvation can be anticipated for several systems. For instance, the polarizability of a semiconductor nanoparticle scales as the fourth power of its radius, $\alpha \propto R^4$. The proportionality coefficient can be very high: $\alpha \simeq 0.08\text{Å}^3(R/\text{Å})^4$ has been reported

for photoexcited CdSe nanoparticles in the range of radii 1–2.5 nm[194]. From a general scaling perspective, $\kappa \propto R^3$ for dipolar solutes in Eq. (3.2)[65] (Fig. 41 in chapter 7). With $\alpha \propto R^4$, there is always a critical size at which the transition to non-harmonic solvation should occur. When the values of κ obtained in our simulations are rescaled to nanoparticle sizes used in Ref. 194 we find them to fall in the regime of non-harmonic solvation, $\kappa < \alpha$. Similar arguments apply to organic ionic solutes (such as tetraalkylammonium cations studied in Ref. 191). The force constant scales as $\kappa \propto R$ for spherical ions, while the polarizability of many organic molecules scales as R^3. The transition to non-harmonic solvation, and the related structural transition of the hydration layer, can be predicted for this configuration as well.

3.4 Conclusions

We have discovered a structural density collapse of the hydration shell promoted by a polarizable solute. The density collapse induces an orientational transition of the hydration shell dipoles. Both transitions are manifested in an increase in the density of dangling OH bonds which have been viewed as potential catalytic centers to promote heterogeneous catalysis[22]. Our picture is distinct from the traditional "iceberg model" anticipating enhanced structuring of water around a non-polar solute[195]. In contrast, high polarizability breaks the bulk-like water structure, creating a high density of surface OH defects. The crossover is abrupt since it is caused by zeroing of the quadratic term in the free energy, analogous to the point of criticality in bulk phase transitions. The phenomenology reported here is not limited to hydration of polarizable solutes, but will extend to similar crossovers caused by polarizable substrates in contact with interfacial water. The abrupt change of the interfacial structure will affect water-mediated forces on the nanometer scale.

Chapter 4

MOBILITY OF NANOMETER-SIZE SOLUTES IN WATER DRIVEN BY ELECTRIC FIELD

4.1 Summary

The relationship of solvent response to electrokinetic phenomena is investigated. In particular, the possibility that electrophoretic mobility, the drag experienced by a dissolved (usually colloidal) particle in a uniform external electric field, can be related to the ordering of water in the interface has been suggested. Attempts to prove it my simulations have suffered from the use of inadequate ensembles and, more importantly, from the lack of an established theoretical framework allowing to analyze the data from both numerical and laboratory experiments in a unified formalism. A simple theoretical framework to analyze the problem and confirm that ordering and polarization of water in the interface can produce electrophoretic charge without free charge carriers. Simulations of various solutes in several force-field models of water are presented to show that the surface charge density coming from the interfacial order is comparable with experimental estimates.

4.2 Introduction

Mobility of oil drops and air bubbles in water has been known for a long time[25] and is traditionally linked to preferential adsorption of ions. Their counterions form the diffuse double layer. The overall charge measured by mobility is determined by an incomplete compensation between the charge of the adsorbed ions and the part of the diffuse layer

within the shear surface. The latter encircles the stagnant layer of the electrolyte moving together with the dissolved particle. While the overall force acting on the ions of the electrolyte is zero, the electrokinetic drag is the result of choosing a limited volume within the electrolyte, surrounding the colloidal particle, with an uncompensated charge. The dragging force is thus the product of the average charge $\langle Q_R \rangle$ within the shear surface with the electric field acting on the charges. We show here that the idea of a limited volume cut from the liquid and producing an excess charge can be extended to the dipolar polarization of the interface. While the dielectric surrounding the nanoparticle is neutral overall, like the electrolyte in the standard models, the divergent polarization of the interface produces an uncompensated bound charge when integrated over a finite volume.

The excess of the adsorbed charge over the diffuse-layer charge, i.e., uncompensated charge $\langle Q \rangle_R \neq 0$, is reflected in the sign of the ζ-potential at the shear surface [26]. A negative ζ-potential, typically recorded for oil drops and air bubbles in water, has been attributed to the excess of the adsorbed negative charge, with the hydroxide anion being a long-time favorite [27, 28, 29, 30].

Recent calculations [196, 197] and measurements by surface-sensitive second-harmonic generation techniques [198, 34, 199, 200] do not support excessive adsorption of hydroxide to the oil-water [34] and air-water [198, 199] interfaces. In addition, the total X-ray reflection fluorescence spectroscopy [201] provides the upper estimate for the free surface charges at the air-water interface at the level of 0.002 (e/nm^2). Depending on the pH and other conditions, this estimate is up to two orders of magnitude below the surface charge density of 0.02–0.4 (e/nm^2) extracted from mobility [27, 29, 34, 200]. It seems plausible that either the formalism of estimating the surface charge density from mobility requires modification or alternative mechanisms of mobility, not involving ion adsorption, might be involved.

The possibility of charge-free electrophoretic mobility in water has been discussed in the literature [31, 32, 33, 34, 35, 36, 37]. The main idea here is that the microscopic structure of the interface, allowing molecular order within the hydration layers, can either produce an effective electrokinetic charge, not related to charges of free carriers, or substantially modify the effect of adsorbed ions on the overall mobility. This proposal has faced two difficulties. From the theoretical side, there is no established framework of how to translate the microscopic structure of the interface, captured by atomistic numerical simulations, into the macroscopic current. Care is required in implementing correct cutoff/boundary conditions [38, 39, 40] and statistical ensembles adequately representing the conditions of mobility measurements (as discussed briefly below). In addition, the field strengths required to produce sufficient sampling in simulations are significantly higher than experimental fields [185] and can potentially modify the structure of the solution. From the experimental side, it is not clear how to connect the results of surface-sensitive spectroscopies, which directly report on the polarization structure of the interface [202, 203], with measured mobilities.

Here we address the calculation of the force acting on a nanometer-size particle dissolved in water and placed in a uniform external field. We do not directly calculate the current produced in response to the external field assuming that, once the force is known, the mobility can be calculated by applying standard equations of hydrodynamics [204, 199] (as shown for the capillary flow in the Appendix). Mobility of the hydrated solute is typically expressed, through Smoluchovski's equation (Eq. (4.2) below), in terms of either the ζ-potential or its effective charge. We derive a relation between the effective mobility (electrokinetic) charge and the interfacial structure of the water dipoles represented by the first-order orientational order parameter of the interface. This parameter is in princi-

ple accessible by surface-sensitive spectroscopies [202, 203, 205, 206] and by equilibrium computer simulations of solutions [187, 103].

This model shows that the effective charge of the solute responding to the uniform external field is not equal to the charge of the free carriers. It is therefore possible that the effective electrokinetic charge reported by mobility measurements significantly overestimates the number of adsorbed ions. The orientational structure of interfacial dipoles is the key in understanding these differences. Since the interfacial structure and dipolar orientations in the interface can be altered by modifying the solute/substrate [187, 207, 34], one gains the means to experimentally test both the effect of the interface on the effective electrokinetic charge and the hypothesis of charge-free mobility. In particular, we suggest that changing the polarizability of a (semiconductor) nanoparticle by exciting electron-hole pairs can invert the sign of the mobility. This effect is driven by the relation between the orientation of dipoles in the hydration layer with the nanoparticle polarizability [21] manipulated by light [208].

4.3 Interfacial Structure and Particle Mobility

4.3.1 General Arguments

We start by considering a single spherical ion with the charge q at its center and with the radius a. It is placed in a polar liquid with the bulk static dielectric constant ϵ_s. We will further consider a spherical liquid sample with the macroscopic radius L and place the ion at its center to simplify the geometry. The instantaneous charge density in the sample is

$$\rho = \rho_i + \rho_b, \tag{4.1}$$

where $\rho_i = q\delta(\mathbf{r})$ and $\rho_b(\mathbf{r}) = \sum_j q_j \delta(\mathbf{r} - \mathbf{r}_j)$ is the density of bound charge at a given instantaneous configuration of the liquid with the atomic partial charges q_j located at the coordinates $\mathbf{r}_j$. Based on charge conservation [105], $\rho_b = -\nabla \cdot \mathbf{P}$ is expressed in terms of the polarization density field $\mathbf{P}$. No specific approximation, such as the dielectric boundary value problem, is assumed here. The instantaneous polarization field is given by the microscopic expression [145, 109]

$$\mathbf{P}(\mathbf{r}) = \sum_j \mathbf{m}_j \delta(\mathbf{r} - \mathbf{r}_j) - \tfrac{1}{3}\nabla \cdot \sum_j \mathbf{Q}_j \delta(\mathbf{r} - \mathbf{r}_j) + \ldots . \tag{4.2}$$

Here, $\mathbf{m}_j$ denotes the molecular dipole, $\mathbf{Q}_j$ is the molecular quadrupole (defined according to Ref. [145]), and the dots refer to the higher-order multipolar terms. When the statistical average over the configurations of the liquid is performed, one arrives at statistically averaged scalar and vector fields, $\langle \rho_b \rangle$ and $\langle \mathbf{P} \rangle$.

From Eq. (4.1), one can calculate the overall charge within a spherical volume Ω_R with the radius R surrounding the ion at its center

$$\langle Q_R \rangle = \int_{\Omega_R} [\rho_i - \nabla \cdot \langle \mathbf{P} \rangle] \, d\mathbf{r}. \tag{4.3}$$

By using the Gauss theorem, integration in Eq. (4.3) yields

$$\langle Q_R \rangle = q + [S_a P_a - S_R P_R] . \tag{4.4}$$

Here, P_a and P_R are the average radial projections of the polarization density, $P_r = \hat{\mathbf{r}} \cdot \langle \mathbf{P} \rangle$, $\hat{\mathbf{r}} = \mathbf{r}/r$ taken at $r = a$ and $r = R$, respectively. Further, $S_a = 4\pi a^2$ and $S_R = 4\pi R^2$ are the surface areas. The polarization is locally proportional to the field in the continuum electrostatics and $P_r = (q/4\pi r^2)(1 - \epsilon^{-1})$. Therefore, in this case, $r^2 P_r$ is independent of r and the two summands in the brackets in Eq. (4.4) cancel out. One gets $\langle Q_R \rangle = q$.

The dielectric sample is overall neutral and one can additionally require

$$\int_\Omega \langle \rho_b \rangle d\mathbf{r} = 0, \tag{4.5}$$

where the integral is taken over the liquid volume Ω between the spheres $r = a$ and $r = L$. This relation imposes the boundary condition

$$a^2 P_a = L^2 P_L, \tag{4.6}$$

which is satisfied for continuum electrostatics.

The normal, outward to the dielectric component of the polarization field $\sigma_q = P_n = -P_a$ plays the role of the surface charge density of a discontinuous dielectric interface [105]. While this charge originates from a divergent polarization of bound molecular charges, it is experimentally observable. To show that, one can consider the electrostatic potential created by free and bound charges inside or outside of the macroscopic sample. It is given as a sum of the electrostatic potentials arising from the free and bound charges [99]

$$\phi = \frac{q}{r} + \oint_{S_a} \frac{\sigma_q}{|\mathbf{r} - \mathbf{r}_S|} dS = \frac{q}{r} - \left(1 - \frac{1}{\epsilon_s}\right) \frac{q}{r}, \tag{4.7}$$

where the surface integral is over the surface of the ion S_a. The overall potential $\phi = q/(r\epsilon_s)$ is said to be dielectrically screened. This physically implies that any probe charge placed outside of the dielectric sample will sense the combined charge $q_{\text{eff}} = q/\epsilon_s$, resulting from adding the ion charge with the opposite bound charges non-uniformly distributed around the ion and producing a non-zero divergence $\nabla \cdot \mathbf{P}$.

We now move to the next step to point out that the polarization field of liquid interfaces often shows a behavior more complex than $P_r \propto r^{-2}$ of continuum electrostatics [107, 108, 113]. The function P_r often displays overscreening, which means that it can be much larger in the magnitude at the contact with the ion than predicted by dielectric models. It also shows oscillations caused by molecular granularity as it decays to the r^{-2} asymptote at $r \to \infty$. While the overall neutrality condition (4.6) still must hold, the charge $\langle Q \rangle_R$

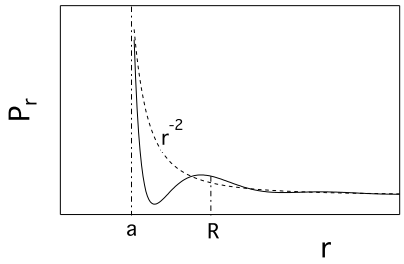

FIGURE 17: The radial projection of the microscopic polarization density P_r (solid line) and its dielectric form $\propto r^{-2}$ (dashed line). The volume integral of $\partial P_r/\partial r$ between surfaces $r = a$ and $r = R$ in Eq. (4.3) can be non-zero, while it always vanishes in the dielectric limit.

obtained by integrating in Eq. (4.3) over a small volume Ω_R can be nonzero for a function $P_r(r) = p(r)/r^2$ with a generally oscillatory $p(r)$ such that $p(\infty) = 1$ (Fig. 17).

This simple observation is the basis of our proposed alteration of the standard model of ionic mobility under the drag of a uniform electric field. We suggest that $\langle Q\rangle_R \neq q$ if the liquid within the shear surface, dragged along with the ion, carries some molecular interfacial structure affecting the radial distribution of the polarization density. The effective charge associated with mobility is affected by the distribution of the bound charge within the shear surface, in addition to the total charge of free carriers.

4.3.2 Ionic Mobility

The hydrodynamic mobility of an ion is determined by the shear surface of the radius R, which is coarse-grained to smooth out the details of molecular granularity by averaging out the molecular motions on the time short compared to the time-scale of hydrodynamic flow (Fig. 18). Electrostatics suggests that the force acting on the ion and its stagnant layer is the product of the average charge $\langle Q_R\rangle$ within the shear surface with the field acting on these charges. This field is the cavity field E_c [109] combining the field from external

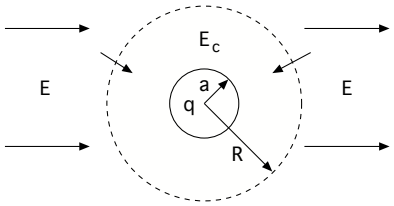

FIGURE 18: Ion with the charge q and the radius a immersed in a polar liquid in the uniform macroscopic (Maxwell) field E. R indicates the radius of the shear sphere incorporating the stagnant layer of the liquid dragged by the field along with the solute. E_c is the cavity field of the uniformly polarized liquid created inside the shear sphere. The arrows on the opposite sides of the spherical cavity indicate water dipoles oriented favorably (left) and unfavorably (right) along the external field. The difference in the chemical potential between right and left is positive. It creates an osmotic pressure pushing the particle in the direction opposite to the field and corresponding to an effective negative charge.

charges with the field of the polarized dielectric outside of the shear surface

$$\langle F\rangle = \langle Q_R\rangle E_c. \tag{4.8}$$

In dielectric theories, the cavity field inside a sphere is related to the macroscopic Maxwell field E by the equation [109]

$$E_c = \frac{3\epsilon_s}{2\epsilon_s + \epsilon_p} E, \tag{4.9}$$

where ϵ_p is the dielectric constant of the particle.

The steady flow of dissolved particles with the speed u is reached when the electrostatic drag is counterbalanced by hydrodynamic friction, $\langle F\rangle = 6\pi\eta u R$, where η is the bulk viscosity. The resulting mobility $\mu = u/E \simeq \langle Q_R\rangle/(4\pi\eta R)$ [$\epsilon_s \gg \epsilon_p$, $\epsilon_s \gg 1$ in Eq. (4.1)] gives direct access to the total charge $\langle Q_R\rangle$. Smoluchovski's equation, typically used in the literature, re-writes this relation in terms of the ζ-potential defined as the electrostatic potential at the shear surface $\zeta = \langle Q_R\rangle/(\epsilon_s R)$ [209]. The result is the equation for the mobility [26]

$$\mu = \frac{\epsilon_s \zeta}{4\pi\eta}. \tag{4.10}$$

This formalism is well established, and the results of mobility measurements are often cast in terms of the effective surface charge density $\sigma_{\text{eff}} = \langle Q_R \rangle / S$, where S is the surface area of the particle. We follow this established practice and focus mostly on $\langle Q_R \rangle$ and the corresponding σ_{eff}. The arguments given here need to be modified with the account for the diffuse potential when electrolyte is present [209]. We do not consider these effects here and focus instead on charged or uncharged particles dissolved in a polar molecular solvent, which establishes a microscopic multipolar structure in the interface. The main outcome of this perspective is the modification of the effective charge $\langle Q_R \rangle$ by the dipolar order of the interface expressed in terms of the average cosine of the interfacial dipoles (order parameter) p_1.

Starting from Eq. (4.4), one can proceed in two steps and first apply a reasonable approximation to the surface charge density at the shear surface. The surface charge density at the actual physical surface of the solute then becomes our main focus. Since the shear surface does not involve any physical disruption of the liquid structure, it is reasonable to assume that P_R can be related to the field of the ion charge by the rules of continuum electrostatics [109] $S_R P_R = q(\epsilon_s - 1)/\epsilon_s$. We stress that this assumption does not affect the main points of our reasoning, as will be clear from the discussion below. With the continuum polarization at the shear surface one gets in Eq. (4.5)

$$\langle Q_R \rangle = q\epsilon_s^{-1} - \sigma_q S_a. \tag{4.11}$$

Since the microscopic susceptibility of the nanometer interface can significantly deviate from the rules of macroscopic continuum electrostatics [107, 154, 113], $\sigma_q = P_n = -P_a$ is left unspecified in Eq. (4.11). The simple message delivered by Eqs. (4.10) and (4.11) is that asymmetry in the water susceptibility between the shear and solute dividing surfaces leads to a modification of the standard result $\langle Q_R \rangle = q$.

Since σ_q is given by the normal projection of the polarization density in the interface,

Eq. (4.11) offers a new result typically absent in standard dielectric models. Those suggest that σ_q is proportional to the ion charge q. However, if the polar liquid is spontaneously polarized in the interface, i.e., if the interfacial dipoles possess preferential non-random orientations caused by the interfacial order [108, 143, 210], $\langle Q_R \rangle \neq 0$ even at $q = 0$. What is required is a nonzero radial projection of the dipolar polarization density at the solute surface.

The dipole ordering in the interface can be described by the first-order orientational order parameter $p_1 = \langle \hat{\mathbf{m}} \cdot \hat{\mathbf{r}} \rangle_a$, which is the average cosine of the water dipole moment projected on the radial direction and calculated in a narrow layer at the solute surface $r = a$ [154, 103]. The surface charge density can be written in terms of the water dipole moment m and the order parameter, $-\sigma_q = (mp_1/S)(dN_s/dr)\big|_{r=a}$. Here, $N_s = N_s(r)$ is the number of water molecules within the shell of the radius $r > a$. By using the definition of the number of water molecules in the shell in terms of the solute-solvent radial distribution function (RDF) $g_{0s}(r)$, one can re-write σ_q as

$$-\sigma_q = \rho m p_1 G, \tag{4.12}$$

where $G = g_{0s}(a)$ is the contact value of the solute-solvent RDF and ρ is the number density of bulk water. Equation (4.12) is written for an arbitrary value of q, which means that $p_1 G$ should be calculated in the presence of the ion charge q; σ_0 corresponds to $q = 0$.

The value of σ_q for large particles can be estimated from the $a \to \infty$ asymptote for the hard-sphere (HS) solute [211] $G_{\mathrm{HS}} \to \beta P/\rho$, which results in $-\sigma_q \to \beta m p_1 P$, where P is the hydrostatic pressure. This gives for water at ambient conditions $-\sigma_q \simeq 10^{-3} p_1 (G/G_{\mathrm{HS}})(P/\mathrm{atm})$ e/nm^2, where $G/G_{\mathrm{HS}} \simeq \exp[-\beta \Delta\mu_w]$ defines the affinity of water toward the solute $\Delta\mu_w$ beyond simple HS packing preferences.

Equation (4.12) establishes the effective charge of a closed spherical interface within a polar liquid. Its sign is fully defined by the orientational order parameter p_1: it is negative

when the water dipoles preferentially orient toward the solute/cavity and is positive when they point toward the bulk. This equation shows that any closed dividing surface, cutting a volume from a polar liquid, will be dragged by an external electric field if a preferential orientation of dipoles in the interface is established. This result is independent of the presence of the electrolyte since bound charges are not screened by the ions.

The proposed formalism equally applies to the problem of a water drop in a nonpolar solvent (oil) [36]. Equation (4.12) still defines the surface charge density with the convention that the orientational order parameter is calculated by projecting the surface water dipoles on the radial direction pointing toward water (inward in the case of a drop). To make our assignment clear, the water-oil interface with water's hydrogen pointing toward the oil phase [212, 34, 213] will, according to Eqs. (4.11) and (4.12), produce a negative charge of the water drop.

It is important to note that the electrostatic force linear in the external field, $\langle F\rangle \propto E_c$, assumes an unperturbed orientational structure of the interface projected on the order parameter p_1. The relaxation of the interfacial order in response to the external field would represent the interfacial polarizability, which contributes to the overall force as a term quadratic in the external field. We do not consider the interface polarizability here assuming that macroscopic fields used in experiment are weak compared to microscopic interfacial fields [108] and do not significantly alter dipolar orientations in the interface.

The electrolyte is overall neutral and the overall force acting on the electrolyte ions is zero $F = \sum_i q_i E = 0$. However, producing current requires work of the external source. The power P, or the rate of doing work, is related to the current density $\mathbf{j}$ [109]

$$P = \int \mathbf{j}\cdot\mathbf{E}\, d\mathbf{r} = P_{\text{el}} + N_0\langle Q_R\rangle u E, \tag{4.13}$$

where $P_{\text{el}} = (J_+ - J_-)E$ is the power required to move the electrolyte ions with the overall current of cations and anions given as $J_\pm$; N_0 is the number of colloidal particles (see

Supplemental Material for detail). Equations (4.5) and (4.13) in principle allow a non-zero current and power production at $q = 0$, i.e., for overall neutral solutes surrounded by a polarized interface. This possibility was viewed in Ref. [214] as contradicting to Saxen relations between the streaming potential and electro-osmotic current, which are specific forms of the Onsager reciprocal relations [204]. We show in the Appendix that the Onsager relations are obeyed in our model by the simple fact of being based on the Coulomb law applied to both free and bound charges.

The drag experienced by a closed surface can be viewed as a specific form of osmosis [215]. The gradient of the chemical potential of interfacial waters at the opposite sides of the surface is created by the external field. It is the consequence of the favorable orientation with the field of the molecules on one side of the surface compared to the unfavorable orientation on the opposite side [216] (surface arrows in Fig. 18). The chemical potential gradient will result in the osmotic pressure difference on the opposite sides of the surface as long as spontaneous order in the interface persists. This physical interpretation of non-zero mobility implies that direct numerical simulations of this effect will require the μVT ensemble [211, 216], keeping the chemical potential of water constant. Since these results are presently not available, we use more conventional NVT and NPT simulations of non-polar and ionic solutes in water to estimate the interfacial charge density σ_q in Eq. (4.12) from the computed $p_1 G$ parameter.

4.4 Computer Simulations

We have considered HS and Kihara (KH) solutes dissolved in force-field water. The Kihara potential is the HS core modified with the Lennard-Jones (LJ) layer at its surface

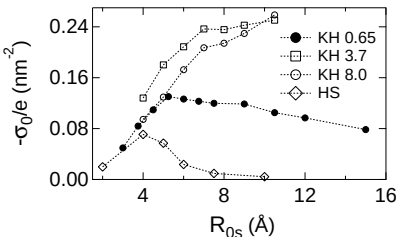

FIGURE 19: Surface charge density of hard-sphere (HS) and Kihara (KH) solutes of varying solute size R_{0s} in SPC/E water (solid points) and TIP3P water (open points). The LJ energy ϵ_{0s} in Eq. (4.10) was varied in the simulations: 0.65, 3.7, and 8.0 kJ/mol. The dotted lines connect the points to guide the eye.

[180]. Specifically, the solute-solvent potential is given as

$$\phi_{0s}(r) = 4\epsilon_{0s}\left[\left(\frac{\sigma_{0s}}{r - R_{\rm HS}}\right)^{12} - \left(\frac{\sigma_{0s}}{r - R_{\rm HS}}\right)^{6}\right], \tag{4.14}$$

where ϵ_{0s} in the LJ energy and σ_{0s} is the distance between the solute HS core with the radius $R_{\rm HS}$ and water's oxygen. $\sigma_{0s} = 3$ Å was kept constant in the simulations, while $R_{\rm HS}$ and ϵ_{0s} were varied.

The molecular dynamics (MD) and Monte Carlo (MC) simulations presented here address the question of whether the product $p_1 G$ characterizing water interfacing these solutes will produce σ_q comparable to experiment. The experimental σ_q reported in the literature are derived from mobility through Smoluchovski's equation [29, 34] [Eq. (4.2)]. The details of the simulation protocols have been discussed elsewhere [154, 21, 12] and are given in chapter 7. Here we focus only on the results.

Figure 19 shows σ_0/e ($q = 0$, e is the elementary charge) from the simulation data changing with the size of the HS and KH solutes in TIP3P and SPC/E water models [80]. The size of the KH solute is measured as $R_{0s} = R_{\rm HS} + \sigma_{0s}$ [Eq. (4.10)]. It approximates well the position of the first peak of the solute-solvent RDF. The size of the HS solute R_{0s} is defined as the distance of the closest approach of the water oxygen to the solute. It gives the exact position of the RDF's first peak.

The sign of the surface charge density is negative for both HS and KH solutes, reflecting the preferential orientation of the surface water dipoles into the bulk. Increasing the solute-solvent LJ attraction makes the hydration shell denser, as reflected by a higher $-\sigma_0$. The fast drop of $-\sigma_0$ for the HS solute is caused by its partial dewetting [189] when $R_{0s} \geq 5$ Å.

The magnitude of σ_0 is somewhat higher than the values typically reported from mobility measurements (~ -0.04 (e/nm^2) for hexadecane in 0.2 mM NaCl at $\mathrm{pH} = 7$ [29]). We estimated the ζ-potential for the $\epsilon_{0s} = 0.65$ kJ/mol Kihara solute [154] (Fig. 19). It turned out that $\sigma_0 R_{0s}^2$ is an approximately linear function of R_{0s} (Fig. B1 in appendix B) such that $\zeta \simeq 0.026(\mathrm{e/nm})(R_{0s}/R)$ for large Kihara solutes. Neglecting the difference between R_{0s} and R in this limit results in $\zeta \simeq 38$ mV. This number is not very different in magnitude from those typically reported experimentally. For instance, $\zeta \simeq -81 \pm 14$ mV was reported for xylene droplets in 10^{-5}M NaCl electrolyte at $\mathrm{pH} = 6$ [27]. For water at room temperature, the Debye-Hückel length is $\kappa^{-1} \simeq 3/c^{1/2}$ Å for a single-charge electrolyte with the molar concentration c [217]. For the cited experiment, one gets $\kappa^{-1} \simeq 10^3$ Å and the amount of counterion charge within the stagnant layer of < 1 nm in thickness [218] can be neglected. The measured ζ-potential thus reflects the effective electrokinetic surface charge. We stress that our solutes are significantly smaller in size than oil drops used in the mobility measurements (~ 100 [200] to $\sim 200 - 300$ [34] nm) and have a smooth surface, in contrast to the corrugated surface of oil emulsions [213].

The experimental ζ-potential [27] has the sign opposite to that calculated for the Kihara solutes. The reason is the positive sign of p_1 in the Kihara-water interface, while negative p_1 values have been recently reported for the oil-water interface [34, 205]. The access to water orientation in the interface is experimentally provided by heterodyne-detected vibrational sum-frequency generation (VSFG) spectroscopy through the imaginary part of the

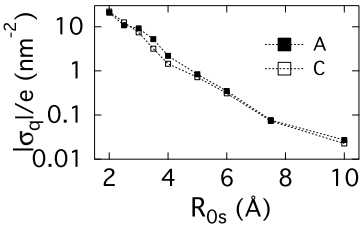

FIGURE 20: Surface charge density of HS cations (C) and anions (A) in TIP3P water. The calculations are done according to Eq. (4.12); the dotted lines connect the points. σ_q is negative for cations and positive for anions.

VSFG signal $\mathrm{Im}\chi^{(2)}$ [205, 206]. The combination of the sign of $\mathrm{Im}\chi^{(2)}$ and its intensity in principle gives access to p_1, although in reality fitting of simulations to experimental spectra is required [219]. Resolving all features of the experimentally reported $\mathrm{Im}\chi^{(2)}$ requires including three-body interactions in the force field model of water [219]. Whether the same is true regarding the values of p_1 is not clear at the moment, although there are indications that three-site models of water somewhat overestimate its spontaneous orientational structure in the interface [143]. In addition to spontaneous orientation in the uncharged interface, the orientation of water dipoles and corresponding p_1 are strongly affected by the presence of ions [206, 220] as we discuss next.

The potential situation with hydrated ions is illustrated in Fig. 20, where σ_q is calculated from Eq. (4.12) for HS cations and anions of varying size in TIP3P water in the absence of counterions [12]. The main observation here is that σ_q significantly exceeds in the absolute magnitude the prediction of the continuum electrostatics. This means $|\langle Q_R \rangle| \gg |q|$ in Eq. (4.10), which should lead to an overestimate of the number of adsorbed ions when the standard equations for the screening of free charge carriers in electrolytes are applied to the analysis of the mobility data [209].

The overpolarization of the water dipoles attached to the surface ions might have significant implications for the interpretation of the mobility data. Figure 20 indicates that

the microscopic orientational order of the water dipoles next to a positive ion will significantly enhance its effective electrokinetic charge determined from the mobility measurement. Correspondingly, a negative adsorbed ion will appear more negative in the particle mobility. Therefore, the actual concentration of adsorbed ions can be significantly lower than estimated from mobility. This observation might help to explain the disagreement between the electrokinetic measurements [29, 34, 200] and surface-sensitive spectroscopies [198, 34, 199, 200] regarding the concentration of the surface adsorbed ions. The actual extent of overpolarization requires more extensive simulations in realistic electrolytes. One also should not underestimate the potential effect of corrugation of any real water-oil interface [213], which will affect the average contact RDF G in Eq. (4.12).

Figure 20 indicates that surface charge densities of large positive and negative ions with $|q| = 1$ charge at the center are close in magnitude. However, this outcome might not hold for small ions adsorbed at the surface of a large particle. The product $p_1 G$ is generally asymmetric between cations and anions because of the asymmetry in the charge distribution of the water molecule [137]. In that case, the orientational order and the corresponding surface charge density will not compensate between the oppositely charged adsorbed ions, and a non-vanishing σ_q will follow even at the total zero charge. The observable consequence of this asymmetry would be a shift between the iso-electric point of electrokinetic mobility and the point of zero charge, as reported for some systems [221]. Overall, the main result of the general formalism summarized by Eq. (4.11) and simulations performed here is that the charge of free carriers and the effective electrokinetic charge incorporating the interfacial dipolar order can be significantly different.

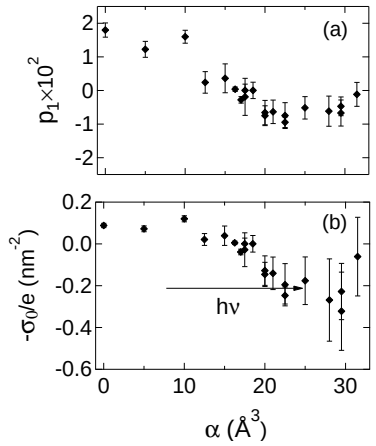

FIGURE 21: The order parameter p_1 (a) and the surface charge density σ_0 (b) vs the polarizability of a polarizable HS solute, carrying the isotropic polarizability α and dipole moment $m_0 = 5$ D, in TIP3P water (error bars show the uncertainties of calculations). The horizontal arrow indicates the photoinduced alteration of the polarizability that inverts the mobility of the nanoparticle.

4.5 Experimental Testing and Conclusions

In conclusion, we have derived a simple equation [Eqs. (4.11) and (4.12)] relating the effective charge of a hydrated nanoparticle to the orientational order in the interface and the water density in contact with the solute. Both parameters carry asymmetry between positive and negative charges. Therefore, the surface charge density σ_q induced by the positive and negative free carriers will not compensate and produce an overall nonzero value even when the total charge is zero. The electrokinetic charge can be substantially enhanced by the dipolar order in the interface and the theory predicts a non-zero effective charge when the interface is spontaneously polarized in the absence of free charge carriers (charge-free mobility). The values of the surface charge density derived from simulations of uncharged nanometer-size solutes are consistent or exceed those typically reported from mobility measurements.

Our development traces in spirit the well-established mechanism of electrophoretic mobility due to ions of electrolyte. Both ions and the dipoles of the solution surrounding the

colloidal particle are neutral overall. However, there is an excess of ions within the shear surface of the particle, which results in the electrokinetic charge. Similarly, due to specifics of the divergent interfacial polarization, there is an inbalance in the bound charge between the polarized liquid inside and outside of the shear surface. The excess bound charge needs to be added to the excess free charge to establish the effective electrokinetic charge.

The derivation is performed here for a spherical solute, where the geometry of the interface produces a divergent radial polarization field. The model is not directly extendable to flat interfaces studied by simulations in the past [32, 39]. While the polarization field is clearly inhomogeneous next to a planar surface, it often demonstrates positive and negative spikes [32, 108], which can potentially compensate each other when the field is applied parallel to the interface to produce electrophoretic flow. The force $\langle F_x \rangle$ along the plane of the surface (x-axis) writes

$$\langle F_x \rangle = E_x S \int \rho_b(z) dz, \tag{4.15}$$

where S is the surface area. If the density of the bound charge $\rho_b(z)$ integrates to zero, there is no net force. In this regard, the roughness of the interface, as suggested by Knecht *et al.* [32], can provide the required conditions for a divergent polarization field which cannot be reduced to a one-dimensional integral shown above.

The direct connection between the mobility of nanoparticles in water and the orientational order of the water dipoles in the interface offers opportunities for testing this prediction by experiment. One possible direction is the modification of the surface with chemical groups (surface dipoles) altering the interfacial order [187]. We, however, recently discovered another property dramatically affecting the interfacial dipoles: the polarizability of the solute. Increasing the solute polarizability drives the solute-water system to the point of instability of harmonic fluctuations expressed in terms of the solvent electric field inside the solute as the order parameter. Reaching the point of global instability toward fluctua-

tions drives a structural transition of the hydration layer, which reorients the water dipoles and creates a high density of dangling OH bonds [21]. The emergent new structure of the interface also suggests, according to Eq. (4.11), the alteration of the sign of σ_0 ($q = 0$).

The results of MC simulations of HS solutes with changing isotropic dipolar polarizability α at the solute's center are presented in Fig. 21. The size of the solute is maintained constant and only the polarizability is varied. One observes a switch from a positive to a negative surface charge with increasing polarizability. In other words, the isoelectric point of electrophoretic mobility can be reached, and crossed, by manipulating the polarizability of the dissolved particle. This observation opens the door to experimental testing of the model. Polarizability of semiconductor nanoparticles can be dramatically increased by photoexcitation [208], which is predicted to invert the nanoparticles' mobility (horizontal arrow in Fig. 21b).

Chapter 5

NON-GAUSSIAN LINESHAPES AND DYNAMICS OF TIME-RESOLVED LINEAR AND NONLINEAR (CORRELATION) SPECTRA

5.1 Summary

A model is proposed for treating non-Gaussian frequency fluctuations that arise from nonlinear system-bath coupling. It provides an analytical, closed-form expression for the lineshape function. This result is significant because it provides a straightforward approach for modeling the lineshape function and projecting that result onto a set of parameters that provide insight into the underlying molecular behavior. The analytical results are compared to explicit MD simulations to verify the validity of the approach showing that the analytical method exhibits good agreement with the MD simulation.

5.2 Introduction

Statistics and dynamics of the frequency of light absorption/emission in either visible/UV or infrared parts of the spectrum are widely used to study the nuclear dynamics of condensed media. Lineshapes of stationary optical absorption and emission report on the statistics of microscopic (molecular-scale) fluctuations, while time-resolved changes of the lineshape (predominantly the line peak and width) report on their dynamics[42, 43, 44, 45]. In these types of experiments, linear time-resolved spectroscopies provide the time evolution of the spectral moments (one-point averages)[45], while nonlinear spectroscopies give access to two-point time correlation functions of the transition frequency[41, 222, 48, 223].

Time evolution of the transition frequency directly reports on the dynamics of the thermal bath when it is a linear function of some subset of the bath nuclear coordinates (linear chromophore-bath coupling). Standard electrostatic models of solvation indeed suggest a linear coupling between permanent charges of the solute and the solvent. For instance, if the distribution of the chromophore's molecular charge is given by a dipole $\mathbf{m}_0$, it couples linearly to the electric field of the medium $\mathbf{E}$ and the electrostatic solute-solvent interaction energy is simply $-\mathbf{m}_0 \cdot \mathbf{E}$[224, 101]. If the electric field is a Gaussian stochastic variable, i.e., only the first two cumulants of $\mathbf{E}$ contribute to the cumulant generating functional (line broadening function)[225, 41, 226], the statistics of the transition frequency is Gaussian as well.

While the interaction of the solute dipole with the solvent electric field is linear, the free energy of polarizing the chromophore, $-(\alpha_0/2)E^2$, scales quadratically with E and linearly with the electronic polarizability of the chromophore α_0[101]. When the dipolar and polarization terms are combined together, the solute-medium coupling is linear plus quadratic in the solvent field, which we call the "quadratic coupling" for brevity. As a consequence, the statistics of the energy gap[227, 119] and the time evolution of the spectral lineshape[193, 228] show non-Gaussian character even for a Gaussian thermal bath driving the transition. In other words, the statistics of the electric field $\mathbf{E}$ is Gaussian by virtue of long range electrostatic interactions involving many molecules (central limit theorem), but this Gaussian many-particle statistics is projected on non-Gaussian statistics of an internal variable (transition frequency) of a single/dilute solute when the coupling to the Gaussian thermal bath is nonlinear.

The same quadratic dependence of the transition energy on nuclear coordinates appears when frequencies of a subset of nuclear modes change between two electronic states involved in the transition (Duschinsky's rotation[229]). Given that several phys-

ical mechanisms result in the same phenomenology[119], it is not surprising that non-Gaussian statistics and/or nonlinear dynamics of spectral lineshapes, implying deviations from expectations of linear coupling models, have been recently reported for a number of systems[230, 231, 232, 233, 234, 235].

One faces, however, the dilemma of whether to assign the observations to either intrinsically non-Gaussian fluctuations of the medium[233, 56, 234] or to a nonlinear chromophore-medium coupling[227, 119, 236]. However, the two perspectives can be merged into one question of what can be expected as observable consequences of non-Gaussian statistics and/or dynamics of the transition frequency, produced in either scenario, when recorded by linear and nonlinear spectroscopies[237].

Addressing this question is the goal of this study. We report here on the development of a model based on the quadratic dependence of the transition frequency on a subset of Gaussian nuclear modes of the thermal bath. The model exactly sums up infinite series of cumulants and thus does not rely on truncated cumulant approximations[41]. It can, therefore, attribute non-Gaussian lineshapes and their complex dynamics to either the non-Gaussian statistics of the transition frequency (originating from either the quadratic solute-solvent coupling or from changes of intrinsic solvent frequencies) or to non-Gaussian dynamics (existence of higher-order time correlation functions not reducible to the second-order one). Our agenda here is to provide a closed-form analytical framework for analyzing stationary and time-resolved, linear and nonlinear, spectroscopic lineshapes. The model's ability to incorporate both the non-Gaussian statistics and non-Gaussian dynamics significantly expands its reach compared to models based on the linear coupling to the thermal bath.

The quadratic solute-solvent coupling (known as the Q-model, "Q" for the quadratic term in the coupling) was previously applied to study the effects of non-Gaussian statistics of the donor-acceptor energy gap on electron-transfer reactions[119, 120]. The main

property of interest in that problem is the equilibrium distribution $P(\Omega)$ of the transition frequency Ω. The rate of an electron-transfer reaction is proportional to the probability $P(0)$ of radiationless transition at $\Omega = 0$. Two main distinctions from the traditional linear coupling models[5] are seen as the asymmetry of the distribution and a linear exponential decay of the probability at the distribution's shallower wing, in contrast to the Gaussian quadratic exponential decay (Figure 22). Both non-Gaussian features arise from the summation of an infinite series of cumulants of Ω, instead of applying a two-cumulant approximation[5]. The question this model naturally poses is how this non-Gaussian statistics extends to the realm of dynamics probed by linear time-resolved and non-linear correlation spectroscopies[41, 48]. This is the question addressed in this article.

Recent studies of vibrational lineshapes by 2D correlation spectroscopy[48] have indicated that higher-order time correlation functions influence the time evolution of the observed lineshapes[233, 56, 238]. There is also growing evidence that these non-Gaussian dynamics might be linked to quadratic solute-solvent coupling. The statistics of the vibrational frequency has been successfully mapped on the statistics of the medium electric field $E_{\|}$ projected on the direction of vibrational stretch[231]. This Stark-effect parameterization is usually achieved by fitting $\Omega(E_{\|})$ to a quadratic function of $E_{\|}$[239, 240]. The electrostatic field is often found to be a nearly Gaussian stochastic variable, while the frequency becomes a non-Gaussian variable, both statistically and dynamically, because of the quadratic term in $\Omega(E_{\|})$[238]. The physical reason for the quadratic term in the Stark-effect parameterization is the polarizability of the vibrational mode[241]. This is the same physics as was originally suggested in the Q-model of optical transitions[227, 193] and, given the Gaussian statistics of the fluctuating electric field, the mathematical formalism is identical in both applications.

Since the mathematical framework behind nonlinear/non-Gaussain spectral features re-

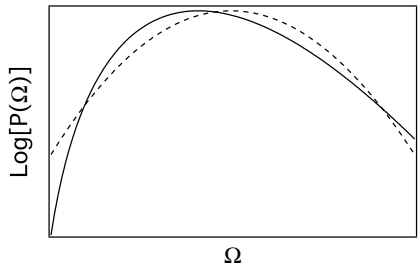

FIGURE 22: The distribution of transition frequencies in the Gaussian approximation (dashed line) and in the non-Gaussian Q-model (solid line). The Gaussian dashed line corresponds to the Q-model parameter $\alpha = \kappa/\Delta\kappa \to \infty$ (Eqs. (5.3) and (5.4)); the solid line was calculated with $\alpha = 1.8$.

ported by optical and vibrational spectroscopies might be common, we use here a physical system that is easier to implement in force field Molecular Dynamics (MD) simulations. Following our early studies of electron-transfer reactions[120], we consider a single solute carrying the dipole moment and polarizability. Both change with the electronic transition. By altering the relative magnitudes of changes in the dipole moment (linear coupling) and polarizability (quadratic coupling) one can adjust the statistics and dynamics of the transition energy from Gaussian (zero polarizability) to increasingly non-Gaussian. We stress, however, that the reach of the model is broader than this specific physical situation since it can be mapped on a number of phenomena involving the quadratic dependence of a collective coordinate on Gaussian nuclear modes of the thermal bath.

The standard formalism for setting up the dynamical equations of motion follows two steps. One first calculates the potential energy as a function of a dynamic coordinate. In the case of a collective coordinate (transition frequency $\Omega(t)$ in our case), this potential energy becomes the potential of mean force, a free energy. This part of the calculation is accomplished exactly within the Q-model[119]. The potential of mean force $F(\Omega) = -\beta^{-1}\ln[P(\Omega)] + \mathrm{Const}$ is obtained from the statistical distribution function $P(\Omega)$, such as

the one shown in Figure 22. The next step is to use $F(\Omega)$ to produce the mechanical force acting on the collective coordinate in an equation of motion describing its evolution[242]. For the problem of fluctuating transition frequency, one can set up a Langevin equation for $\Omega(t)$ evolving in the potential $F(\Omega)$. The solution of the Langevin equation, or of the corresponding Fokker-Planck equation[225], would produce the propagator $P(\Omega, t|\Omega_0, 0)$ sufficient to calculate two-point time correlation functions of any order.

The second step in this program currently cannot be carried out exactly because of the lack of established solutions for stochastic dynamics in anharmonic potentials in general and in the one produced by the Q-model in particular (Figure 22). Therefore, for the sake of calculating the two-point correlation functions, we make an approximation following two steps. We first assume that the medium coordinate (electric field $\mathbf{E}$ or the coordinate q below) is a Gaussian overdamped stochastic variable obeying the well-characterized Ornstein-Uhlenbeck stochastic process[243, 225]. We then project the known propagator $P(q, t|q_0, 0)$ on the coordinate $\Omega(q)$. While this approach allows an analytical solution for 2D correlation spectra[48], it is clearly an approximation when applied to time correlation functions, which needs testing against direct MD simulations. We will, therefore, start below with outlining the analytical formalism, followed by the simulation results.

5.3 Time-resolved Lineshapes

We will consider a chromophore coupled to the nuclear mode q of the medium and residing in either the ground (g) or excited (e) state. The Hamiltonian of the chromophore-medium system is H_g in the ground state and H_e in the excited state. The absorption of the radiation photon at $t = 0$ results in the $\mathrm{g} \rightarrow \mathrm{e}$ transition with the time-dependent

Hamiltonian

$$H(t) = H_g + \hbar\Omega(q)\theta(t) \tag{5.1}$$

Here, the vertical (Franck-Condon) transition frequency is

$$\hbar\Omega(q) = H_e(q) - H_g(q) \tag{5.2}$$

and $\theta(t)$ is the Heaviside step function.

We will further assume that each of the states is characterized by a Hamiltonian quadratic in the coordinate q, with both coefficients C_i and κ_i ($i = \mathrm{g}, \mathrm{e}$) changing with the excitation[119]

$$H_i = I_i - C_i q + (\kappa_i/2)q^2 \tag{5.3}$$

The transition frequency is then a quadratic function of q

$$\hbar\Omega(q) = \hbar\Omega_0 - \Delta C q + (\Delta\kappa/2)q^2 \tag{5.4}$$

where $\hbar\Omega_0 = I_e - I_g$, $\Delta C = C_e - C_g$, and $\Delta\kappa = \kappa_e - \kappa_g$. The standard linear coupling models of spectroscopy assume $\Delta\kappa = 0$. We will label this limit as the L-model ("L" for linear), while the case of $\Delta\kappa \neq 0$ will be labeled as the Q-model ("Q" for quadratic)[119].

Time-resolved linear spectroscopy monitors the time change of the spectral lineshape[244]

$$I(\Omega, t) = \langle\delta[\Omega - \Omega(q(t))]\rangle_t \tag{5.5}$$

where the average is taken over the evolving distribution function of the coordinate q at time t.

Non-equilibrium distribution of nuclear coordinates is created by moving the ground state equilibrium distribution function

$$P_g(\Omega) = \int \delta(\Omega - \Omega(q))P_g(q)dq \tag{5.6}$$

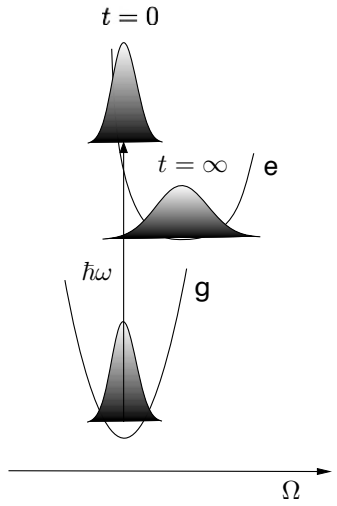

FIGURE 23: Time evolution of the lineshape after the ground state equilibrium distribution at $t = 0$ is promoted, by photoexcitation, to a non-parabolic free energy excited surface. The time change of the spectral line-width is caused by a nonzero value of $\Delta\kappa$ in Eq. (5.4). The consequence of this term in the transition frequency is a non-Gaussian time-dependent lineshape described by Eq. (5.24). An example calculation of the time-dependent line-width is shown in Figure 24.

to the excited state potential curve at time $t = 0$ (Figure 23); $P_g(q)$ is the equilibrium ground state distribution of q. The evolution of the nuclear coordinates of the system with the chromophore in its excited state is described by the conditional probability[225] (propagator) $P_e(q, t|q_0, 0)$. It gives the probability to find the nuclear coordinate with the value q at $t = t$ given that it was q_0 at $t = 0$. The average in Eq. (5.5) then becomes

$$\langle \dots \rangle_t = \int \dots P_e(q, t|q_0, 0) P_g(q_0) dq dq_0 \tag{5.7}$$

Equation (5.7) projects the dynamics of the coordinate $q(t)$ on the dynamics of $\Omega(q(t))$[193]. There is no approximation involved in this procedure for calculating one-time averages, but it becomes approximate for two-time correlation functions as we discuss below.

There are a number of established results for L-models of spectroscopy based on the assumption of the Gaussian statistics of the stationary medium fluctuations and, for time-

resolved measurements, of their Gaussian dynamics[234]. The former assumes that only the first two cumulants of q are significant for time-independent (stationary) lineshapes measured in the limit $t \to \infty$. The corresponding absorption and emission lineshapes are given by Gaussian functions[245], with their maxima separated by the Stokes shift $\Delta\Omega = \bar{\Omega}_g - \bar{\Omega}_e$,

$$I_i(\Omega) \propto \exp\left[-\frac{(\Omega - \bar{\Omega}_i)^2}{2\sigma^2}\right] \tag{5.8}$$

Here, $\bar{\Omega}_i$ is the first spectral moment, equal to the position of the line maximum for Gaussian lineshapes. Further, the Gaussian width

$$\sigma^2 = \langle(\delta\Omega)^2\rangle = 2\lambda/(\beta\hbar^2) \tag{5.9}$$

is related to the Stokes shift by the condition $2\lambda = \hbar\Delta\Omega$[120]; λ is the (nuclear) reorganization energy[246].

Time-dependent lineshapes are often empirically approximated by Gaussian functions with a time-dependent maximum $\bar{\Omega}_i(t)$ and a time-dependent spectral width $\sigma(t)$[247, 228]

$$I_i(\Omega, t) \propto \exp\left[-\frac{(\Omega - \bar{\Omega}_i(t))^2}{2\sigma(t)^2}\right] \tag{5.10}$$

The evolution of the maximum position gives the normalized dynamic Stokes-shift function

$$S_{\Omega,i}(t) = \frac{\bar{\Omega}_i(t) - \bar{\Omega}_i(\infty)}{\bar{\Omega}_i(0) - \bar{\Omega}_i(\infty)} \tag{5.11}$$

A similar function can be defined for the spectral width

$$S_\sigma(t) = \frac{\sigma(t)^2 - \sigma(\infty)^2}{\sigma(0)^2 - \sigma(\infty)^2} \tag{5.12}$$

where the stationary spectral width $\sigma(\infty) = \sigma$ (Eq. (5.9)) is reached in the limit $t \to \infty$.

The empirical Gaussian approximation of the time-dependent lineshape, as in Eq. (5.10), does not imply Gaussian dynamics of the transition frequency. The common meaning assigned to this term is the neglect of all time correlation functions $\langle\delta\Omega(t_1)\ldots\delta\Omega(t_n)\rangle$

with $n > 2$ in the cumulant generating functional. Alternatively, this approximation implies expressing all even-order time correlation functions as powers of the two-time correlation function, known as Wick's theorem (odd correlation function vanish)[248]. What it practically means is known as the second-cumulant approximation, which replaces the generating functional of the transition frequency with the corresponding second cumulant[41, 226]

$$\begin{aligned} e^{-g_i(t)} &= \left\langle \exp\left(-i\int_0^t d\tau \delta\Omega(\tau)\right)\right\rangle_i \\ &\simeq \exp\left[-\int_0^t d\tau \int_0^\tau d\tau' C_{2,i}(\tau,\tau')\right] \end{aligned} \tag{5.13}$$

where $C_{2,i}(\tau,\tau') = \langle \delta\Omega(\tau)\delta\Omega(\tau')\rangle_i$. This approximation results in Kubo-type functions $g_i(t)$ evolving the spectral lineshape from a Lorentzian to a Gaussian on the relaxation time of the thermal bath[41, 48]. These models thus predict that $\sigma(t)$ reaches a constant value, $\sigma(t) = \mathrm{Const}$ in Eq. (5.10), once the lineshape becomes Gaussian. There are, however, other approximations than just the second-cumulant approximation that are typically assumed in analyzing spectral dynamics.

It is commonly assumed that the correlation function $C_{2,i}(t)$ in Eq. (5.13) does not depend on the electronic state[249, 250], $C_{2,g}(t,0) = C_{2,e}(t,0) = C_2(t,0)$, which is true for the L-models. Further, the linear response approximation[60] in $\Omega(q)$ relates non-equilibrium dynamics of the spectral maximum to the equilibrium two-point correlation function[251, 250, 252], as is also derived in appendix C.

$$S_{\Omega,i}(t) = S_2(t) \tag{5.14}$$

where $S_2(t) = C_2(t,0)/C_2(0,0)$. Equation (5.14) holds for either of the two states[249, 250, 252] and, therefore, the index indicating the state has been dropped on its right-hand side. Since the second-cumulant approximation in Eq. (5.13) and the linear relation in Eq. (5.14) are not necessarily equivalent, we will reserve the term "Gaussian dynamics" for the former[253] and "linear dynamics" for the latter[251, 249, 250, 252].

The linear response approximation also allows one to calculate $S_\sigma(t)$ in Eq. (5.12), which yields (see appendix C)

$$S_\sigma(t) = \frac{(\beta\hbar\sigma)^{-1}S_3(t) + 2S_2(t) - S_2(t)^2}{1 + (\beta\hbar\sigma)^{-1}S_3(0)} \tag{5.15}$$

Here,

$$S_3(t) = \sigma^{-3}\langle\delta\Omega(t)^2\delta\Omega(0)\rangle \tag{5.16}$$

is the skewness correlation function[234], with the stationary spectral width σ given by Eq. (5.9). Note that linear response does not stipulate Gaussian dynamics, and only the smallness of the perturbation introduced in the solvent by the electronic transition is required.

The linear function $\Omega(q)$ of the L-models directly relates the Stokes-shift correlation function in Eq. (5.11), calculated in the linear response approximation, to the medium dynamics

$$S_\Omega(t) = S_2(t) = \chi(t) \tag{5.17}$$

Here,

$$\chi(t) = \sigma_q^{-2}\langle\delta q(t)\delta q(0)\rangle \tag{5.18}$$

represents the dynamics of the bath and $\sigma_q^2 = \langle(\delta q)^2\rangle = (\beta\kappa)^{-1}$ is the variance of q. Equation (5.17) is, therefore, the basis for using spectroscopy to study the intrinsic dynamics of condensed media.

The results of applying the linear response approximation to the Stokes-shift dynamics are identical to the exact solution for the diffusive, overdamped dynamics over parabolic free energy surfaces obtained as a linear projection of $q(t)$ on the reaction coordinate $\Omega(t)$ (L-models)[254, 244]. The dynamics of $q(t)$ is given by the stochastic Ornstein-Uhlenbeck process with the propagator[243, 225]

$$P_e(q,t|q_0,0) \propto \exp\left[-\frac{\beta\kappa_e}{2}\,\frac{(\delta q - \delta q_0\chi(t))^2}{1-\chi(t)^2}\right] \tag{5.19}$$

where $\delta q = q - q_e$ and $\delta q_0 = q_0 - q_e$ are the deviations of the, respectively, final and initial coordinates from the equilibrium value q_e in the excited state. When this propagator is used in Eqs. (5.5) and (5.7) with $\kappa_g = \kappa_e$, one arrives at the linear response result for the Stokes-shift correlation function in Eq. (5.17) and, in addition, at a time-independent spectral width in Eq. (5.10)

$$\sigma(t) = \mathrm{Const} \tag{5.20}$$

The physical meaning of Eq. (5.20) is straightforward: the relaxation of the ground state population, promoted to the exited surface with the same parabolic curvature as of the ground surface, produces no change in the distribution width (Figure 23). Only a time-dependent shift of the spectral maximum should be observed. Ornstein-Uhlenbeck dynamics of $\Omega(t)$ (L-models) also yield vanishing odd time correlation functions and a direct relation between higher order correlation functions and $S_2(t)$, for instance

$$S_4(t) = \langle(\delta\Omega)^4\rangle^{-1}\langle\delta\Omega(t)^2\delta\Omega(0)^2\rangle = \tfrac{1}{3} + \tfrac{2}{3}S_2(t)^2 \tag{5.21}$$

This relation will be used below to test the Gaussian character of the dynamics of $\Omega(t)$ produced by MD simulations.

Equations (5.19) and (5.20) suggest that a nonlinear dependence $\Omega(q(t))$ on the Ornstein-Uhlenbeck stochastic variable $q(t)$ is required to produce a time-dependent width in the time-resolved lineshape in Eq. (5.10). This is indeed a feature of the dynamic version of the Q-model[193]. Another consequence of this extension is the loss of a direct link between spectroscopic and bath dynamics, as we discuss below.

The quadratic solute-solvent coupling also makes the dynamics of the transition frequency non-Gaussian. This can be demonstrated by calculating the skewness time correlation function (Eq. (5.16))

$$S_{3,i}(t) = (\alpha_i\sqrt{2\beta\lambda_i})^{-1}\chi(t)(2 + \chi(t)) \tag{5.22}$$

Here, $\alpha_i = \kappa_i/\Delta\kappa$ and

$$\lambda_i = \beta\hbar^2 C_{2,i}(0,0)/2 \tag{5.23}$$

is the state-dependent reorganization energy. In deriving Eq. (5.22), the terms of the order $(\beta\lambda_i)^{-1}$ compared to the main contribution were dropped. When the same procedure is applied to $S_4(t)$, one arrives at the Gaussian formula for the correlation function in Eq. (5.21).

5.4 Linear Time-resolved Spectroscopy

The time average in Eq. (5.5) can be directly carried out with the Ornstein-Uhlenbeck propagator in Eq. (5.19). The calculations are outlined in appendix C and here we only present the final result for the time-dependent lineshape function[193]

$$\begin{aligned} I(\Omega,t) \propto & \left|\Omega-\omega_0\right|^{-1/2} e^{-\beta\hbar|\alpha(t)(\Omega-\omega_0)|} \\ & \times I_1\left(2\beta\sqrt{|\alpha(t)^3\lambda(t)\hbar(\Omega-\omega_0)|}\right) \end{aligned} \tag{5.24}$$

Here, $I_1(x)$ is a modified Bessel function and the proportionality coefficient normalizes the lineshape. The $t \to \infty$ limit gives the stationary probability of the transition frequency in the excited state $P_e(\Omega)$ shown by the solid line in Figure 22.

The lineshape function in Eq. (5.24) is clearly non-Gaussian, with two time-dependent functions, $\lambda(t)$ and $\alpha(t)$. The former determine the width dynamics, $\sigma(t)^2 \propto \lambda(t)$, the latter, $\alpha(t) = \kappa(t)/\Delta\kappa$, controls the extent of non-Gaussian character of the evolving lineshape. Here, $\kappa(t)$ is the dynamically evolving force constant of the medium coordinate q, which changes from κ_g at $t = 0$ to κ_e at $t \to \infty$ (see appendix C). The parameter $\alpha(t)$ is inversely proportional to the change in the force constant $\Delta\kappa$ in Eq. (5.4). Therefore, Eq. (5.24) becomes a Gaussian function of Eq. (5.10) in the limit $\Delta\kappa \to 0$. In addition,

the limiting frequency $\omega_0 = \Omega_0 - \Delta C^2/(2\hbar\Delta\kappa)$ in Eq. (5.24), beyond which the Q-model intensity is identically zero[119], shifts to infinity at $\Delta\kappa \to 0$.

The reorganization function $\lambda(t)$ in Eq. (5.24) evolves in time between the initial, λ_g, and final, $\lambda_e \neq \lambda_g$, values given by Eq. (5.23). This time-dependent function (Figure 24) is given by the equation

$$\lambda(t) = \frac{\kappa_g^2}{2\kappa_e}\left(\frac{C_e}{\kappa_e} - \frac{C_g}{\kappa_g}\right)^2 \zeta(t)\left[1 + \frac{\Delta\kappa}{\kappa_g}\chi(t)^2\right] \tag{5.25}$$

where

$$\zeta(t) = \left[1 + (\Delta\kappa/\kappa_g)\chi(t)\right]^2 \tag{5.26}$$

It is clear that $\lambda(t) = \mathrm{Const}$ and $\sigma(t) = \mathrm{Const}$, in agreement with the result of L-models in Eq. (5.20), when $\kappa_g = \kappa_e$ and $\Delta\kappa = 0$.

The non-Gaussian lineshape in Eq. (5.24) can often be represented by a time-dependent Gaussian function given by Eq. (5.10). The reorganization function $\lambda(t)$ then gives the time dependent linewidth $(\hbar\sigma(t))^2 = 2\lambda(t)/\beta$, while the line maximum $\bar{\Omega}(t)$ is given by the relation

$$\bar{\Omega}(t) = \omega_0 + \zeta(t)\Delta C^2/(2\hbar\Delta\kappa) \tag{5.27}$$

From this equation, the Stokes-shift correlation function becomes

$$S_\Omega(t) = \rho\chi(t) + (1-\rho)\chi(t)^2 \tag{5.28}$$

where $\rho = (2\kappa_g)/(\kappa_g + \kappa_e)$. This function is a quadratic function in $\chi(t)$ and, obviously, is not the same as $\chi(t)$. Therefore, Eq. (5.17) does not hold and the Stokes-shift dynamics do not directly report on the medium dynamics. From Eq. (5.25), $S_\sigma(t)$ is a linear combination of powers of $\chi(t)$ up to the fourth order and one gets $S_\sigma(t) \neq S_\Omega(t)$. At the same time, $S_\sigma(t)$ becomes an algebraic function of $S_\Omega(t)$ and that relation can be used for testing the consistency of the observed dynamics with the predictions of the dynamic

Q-model. Another important consequence of Eq. (5.28) is that the Stokes-shift dynamics are bi-exponential even if the medium dynamics are single-exponential.

Returning to equilibrium correlation functions, the Ornstein-Uhlenbeck propagator in Eq. (5.19) can be used to calculate $S_2(t)$ in the Q-model. The result, neglecting a small correction of the order $1/(\beta\lambda_i)$, is $S_2(t) = \chi(t)$. We, therefore, obtain

$$S_\sigma(t) \neq S_\Omega(t) \neq S_2(t) = \chi(t) \tag{5.29}$$

We find the last equality to hold very accurately in our MD simulations of polarizable solutes in water presented below, even for a non-exponential $\chi(t)$.

We show in appendix C that the skewness correlation function does not contribute significantly to the linear response correlation function $S_\sigma(t)$ in Eq. (5.15), which then becomes a quadratic function of $\chi(t)$. On the other hand, $\sigma(t)^2 \propto \lambda(t)$ in Eq. (5.25) is a fourth-order function in $\chi(t)$. Therefore, $S_\sigma(t)$ is of fourth order in $\chi(t)$ as well. We conclude that the linear response approximation cannot be applied to the width dynamics in the Q-model scenario.

It is useful to illustrate the analytical results with specific calculations. We show in Figure C1 in appendix C functions $S_\Omega(t)$ and $S_\sigma(t)$ plotted directly vs. $\chi(t)$ for different values of $\Delta\kappa/\kappa_g$. The deviations of two spectral functions from the bath dynamics increase with growing $|\Delta\kappa|$, but the effect of this quadratic coupling term on the width dynamics is more significant than on the Stokes-shift dynamics. This is also illustrated in Figure 24 in application to a more specific model related to our MD simulations.

Our simulations described below are done for a model solute in water, changing both its dipole moment and polarizability with photoexcitation. In anticipation of the specific results presented below, we use this model here to illustrate the nonlinear time evolution of the lineshape, which is not directly accessible by equilibrium MD simulations.

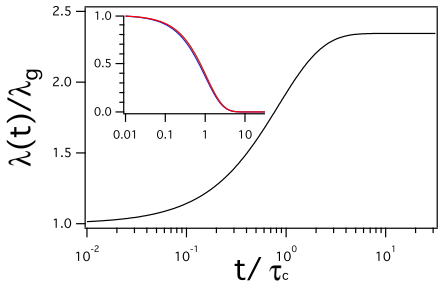

FIGURE 24: $\lambda(t)$ from Eq. (5.25). The inset shows $\chi(t)$ given by single exponential decay (Eq. (5.30), blue) and $S_\Omega(t)$ (Eq. (5.28), red) vs. t/τ_c. The calculations are done for a transition with $\Delta m/m_g = 1$ and $\Delta\kappa/\kappa_g = -0.5$; $\lambda(0) = \lambda_g$ and $\lambda(\infty) = \lambda_e$.

Figure 24 shows $\lambda(t)$, representing the evolution of the line width, and the Stokes-shift correlation function $S_\Omega(t)$ (inset in Figure 24). The parameters are chosen to allow the reorganization energy to increase by approximately a factor of two while evolving on the excited state surface (Figure 23). Despite this large increase in the spectral width, in contrast to expectations of the L-models (Eq. (5.20)), the Stokes-shift correlation function is nearly identical to $\chi(t)$ chosen in the form of a single-exponential decay

$$\chi(t) = e^{-t/\tau_c} \tag{5.30}$$

where τ_c is the relaxation time of the bath[42]. Even though $S_\Omega(t)$ does not directly reproduce the medium dynamics (Eq. (5.29)), $S_\Omega(t)$ and $\chi(t)$ are very close, consistent with the MD results presented below.

To summarize, the Stokes-shift dynamics is a good reporter of the medium dynamics even for a quadratic solute-solvent coupling. Therefore, the time dependence of the spectral width should be used as an indicator of nonlinear dynamics[228]. The next question is whether nonlinear correlation spectroscopy can provide a more sensitive tool. This question was partially addressed in the past, and it was shown[233, 56] that 2D spectra are not very sensitive to intrinsic non-Gaussian fluctuations of the thermal bath in L-models of spectroscopy. Below we explore a different scenario of Gaussian medium fluctuations

combined with the Q-model of spectroscopy. Distinct and observable effects of nonlinear dynamics on 2D spectra are reported.

5.5 2D Correlation Spectroscopy

5.5.1 Line Broadening Function

The lineshape of linear spectroscopy involves the average of the off-diagonal element of the density matrix $\rho_{ge}(t)$ over the individual molecules. This average defines the line broadening function $g(t)$ in Eq. (5.13)[41, 48]. Third order response functions of nonlinear correlation spectroscopy involve terms, typically represented by double sided Feynman diagrams, combining pure dephasing with population relaxation. We will consider only one such term here, since, for the two-state system, the rest of them can be obtained by changing the sign of the coherences in the dephasing diagrams[48]. We, therefore, set up the calculation of the third-order lineshape function for the rephasing diagram (altering signs in the complex exponent)

$$\Psi(t_1,T,t_2) = \left\langle \exp\left(-i\int_0^{t_1} d\tau\delta\Omega(\tau)\right) \exp\left(i\int_{t_1+T}^{t_1+T+t_2} d\tau\delta\Omega(\tau)\right)\right\rangle \tag{5.31}$$

where t_1 and t_2 are the durations of the pump and probe pulses, respectively, and T is the population evolution, or waiting, time.

The frequency fluctuations are driven by the quadratic coupling to the stochastic variable q performing overdamped fluctuations in a harmonic potential and thus described by the Ornstein-Uhlenbeck process (Eq. (5.19))[225]. Since the statistics and dynamics are non-Gaussian, the truncated cumulant approximation does not apply here and the problem needs to be directly integrated. This goal is achieved by path integration[255] in the space

of stochastic trajectories $q(\tau)$ as shown in appendix C. The path integral can be evaluated exactly for a quadratic $\Omega(q)$, leading to a novel analytical form for the line broadening function. We start the discussion with the standard L-model to set up the analytical framework for the next step incorporating the quadratic coupling with the bath.

For the L-model ($\Delta\kappa = 0$ in Eq. (5.4)), Eq. (5.31) gives the Gaussian lineshape function[42, 41]

$$\Psi(t_1, T, t_2) = \exp\left[\phi(t_1, T, t_2)\right] \tag{5.32}$$

Here,

$$\phi(t_1, T, t_2) = -g(t_1) - g(t_2)^* + \chi(T)p(t_1)p(t_2)^* \tag{5.33}$$

where asterisks denote complex conjugation. Further,

$$g(t) = (\Delta\tau_c)^2\left[t/\tau_c - 1 + \chi(t)\right] \tag{5.34}$$

with $(\hbar\Delta)^2 = (\Delta C)^2\sigma_q^2$ is the standard Kubo's lineshape function[42, 41, 48] and

$$p(t) = (\Delta\tau_c)\left[1 - \chi(t)\right] \tag{5.35}$$

Equation (5.33), even though not presented in this form previously, is equivalent to the more commonly used relation[41] obtained from the second-order cumulant expansion of Eq. (5.31)

$$\begin{aligned}\phi(t_1, T, t_2) = &- g(t_1) - g(t_2) + g(T) - g(t_1 + T) \\ &-g(t_2 + T) + g(t_1 + t_2 + T)\end{aligned} \tag{5.36}$$

In the short-time approximation, neglecting the decay of the frequency correlations during the two coherence times t_1 and t_2, Eq. (5.33) reduces to the relation used in the past to model 2D lineshapes[256, 223, 257, 258]

$$\phi(t_1, T, t_2) = -(\Delta^2/2)\left[t_1^2 + t_2^2 - 2\chi(T)t_1t_2\right] \tag{5.37}$$

Further, Eq. (5.33) is derived for a rephasing response function in which the phase of the transition frequency switches from $i\delta\Omega(\tau)$ on the time interval $0 \leq \tau \leq t_1$ to complex conjugate $-i\delta\Omega(\tau)$ on the time interval $t_1 + T \leq \tau \leq t_1 + T + t_2$ (Eq. (5.31)). The non-rephasing diagrams preserve the same sign $-i\delta\Omega(\tau)$ on both time intervals. The non-rephasing $\tilde{\Psi}(t_1, T, t_2)$ will, therefore, be given by Eq. (5.32) with the corresponding function $\tilde{\phi}(t_1, T, t_2)$ as follows

$$\tilde{\phi}(t_1, T, t_2) = -g(t_1) - g(t_2) - \chi(T)p(t_1)p(t_2) \tag{5.38}$$

The physical meaning of Eq. (5.33) is quite clear. Each function $g(t)$ describes the homogeneous and inhomogeneous broadening of lines produced by pump and probe pulses, while the last term shows the decay of coherence between them on the population relaxation time T, with the exponential time correlation function of the nuclear mode $\chi(T) = \exp(-T/\tau_c)$. Given physical transparency of the equation, we will preserve its general structure when extending the calculations from the L-model to the Q-model.

Adopting the full quadratic form of $\Omega(q)$ of Eq. (5.4) still allows an exact analytical solution for the line broadening function (see appendix C). The main consequence of this extension is an appearance of an effective complex relaxation time τ_c/ϵ, where

$$\epsilon^2 = 1 - 2i\tau_c\Delta\kappa/(\kappa\beta\hbar) \tag{5.39}$$

We show in appendix C that the functions $g(t)$ and $p(t)$ in Eq. (5.33) are replaced with

$$\begin{aligned} g(t) = (\Delta\tau_c)^2 \Bigg[& \frac{t}{\tau_c} - \frac{2}{\epsilon}\tanh\frac{\tilde{t}}{2} \\ & + \left(\frac{\epsilon^2+1}{2\epsilon}\right)^2 \frac{(\tanh(\tilde{t}/2))^2}{1+\epsilon\coth\tilde{t}}\Bigg] + \frac{p(\tilde{t})^2}{2} \end{aligned} \tag{5.40}$$

$\tilde{t} = \epsilon t/\tau_c$ and

$$p(\tilde{t}) = (\Delta\tau_c)\,\frac{\epsilon^2+1}{2\epsilon}\,\frac{\cosh\epsilon\tilde{t} + \epsilon\sinh\tilde{t} - 1}{\sinh\tilde{t} + \epsilon\cosh\tilde{t}} \tag{5.41}$$

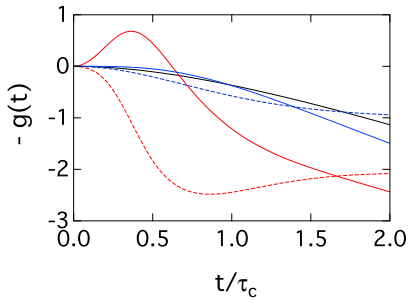

FIGURE 25: Function $-g(t)/(\Delta\tau_c)^2$ vs. t/τ_c for the Kubo lineshape (black, Eq. (5.34)) and for the Q-model (Eqs. (5.40) and (5.41)). The parameters ϵ (Eq. (5.39)) is given as $\epsilon^2 = 1 - i\epsilon''$ with $\epsilon'' = 2$ (blue) and $\epsilon'' = 10$ (red). The dashed lines refer to the imaginary part of $g(t)$.

These functions reduce to the previous expressions when $\Delta\kappa = 0$ and $\epsilon = 1$.

The short-time approximation for $g(t)$ and $p(t)$ results in

$$\begin{aligned}\phi(t_1, T, t_2) = &-(\Delta^2/8)\big[(ct_1)^2 + (c^* t_2)^2 \\ &- 2|c|^2\chi(T)t_1 t_2\big]\end{aligned} \tag{5.42}$$

where $c = 1+\epsilon^2$. This equation becomes Eq. (5.37) of L-models at $\Delta\kappa = 0$ and $\epsilon = 1$. The magnitude of ϵ can, however, be fairly large at the typical conditions of optical experiment. Given that $\beta\hbar \simeq 2.5 \times 10^{-14}$ s and $\Delta\kappa/\kappa \simeq 1$, one expects $\epsilon^2 \simeq -80i$ at $\tau_c \simeq 1$ ps. For these large magnitudes of ϵ, the short-time approximation in Eqs. (5.40) and (5.41) $t \ll \tau_c/|\epsilon|$ is limited to time-scales of tens of femtoseconds. However, for the polarizability of the OH stretch vibration[240], our estimate presented below gives $\Delta\kappa/\kappa = \alpha_g^{-1} \simeq -0.04$ and thus $\epsilon^2 \simeq 1 + 3i$.

That the short-time approximation becomes inaccurate for $|\epsilon| \gg 1$ is illustrated in Figure 25 where we compare the standard Kubo's line broadening function $-g(t)$ from Eq. (5.34) to $-g(t)$ from Eq. (5.40). The Q-model's $-g(t)$ develops a positive spike with increasing $|\epsilon|$, before turning into the negative territory, where it decays faster than Kubo's $-g(t)$. This shows that the quadratic approximation of Eq. (5.42) is insufficient since it

does not give a convergent Fourier integral at imaginary and large in magnitude ϵ; higher order expansion terms in t are required. This comparison also implies that the approximate methods of extracting the medium correlation function $\chi(t)$ from either the eccentricity function or the slope of the center line obtained from correlation spectra, which are justified by the short-time approximation[257, 223, 258], are not applicable anymore as we discuss next.

5.5.2 2D Lineshape

We use here the broadening function derived above to produce 2D correlation spectra of a two-state system[48]. The calculations are done for the commonly presented purely absorptive 2D spectrum given by the sum of the rephasing and non-rephasing spectra, after the inversion of the sign of the ω_1 variable in the rephasing part, $R_{\text{abs}}(\omega_1, \omega_3) \propto \mathrm{Re}\left[R(-\omega_1, \omega_3, T) + \tilde{R}(\omega_1, \omega_3, T)\right]$. Each spectrum component here is obtained by Fourier transform of $\Psi(t_1, T, t_2)$ (Eqs. (5.32) and (5.33) for $R(-\omega_1, \omega_3, T)$) and $\tilde{\Psi}(t_1, T, t_2)$ (Eq. (5.38) for $\tilde{R}(\omega_1, \omega_3, T)$) in time variables t_1 and t_2.

Different metrics have been proposed to access the frequency time correlation function $S_2(t)$ directly from the evolution of 2D spectra in order to avoid fitting the lineshape to a predefined broadening function. These metrics themselves are largely justified on the basis of the short-time approximation[257, 223, 258] (Eq. (5.37)) and can be considered only as guidelines, disregarding the motional narrowing, to distinguish between different relaxation patterns. In particular, the eccentricity analysis[257, 223] is based on the ratio of the line widths measured along the diagonal $\omega_1 = \omega_3$ direction ($\sigma_{\parallel}$) and along the antidiagonal direction ($\sigma_{\perp}$). The short-time approximation then predicts access to the frequency correlation function of the bath $\chi(T)$ from the combination of the diagonal and antidiagonal

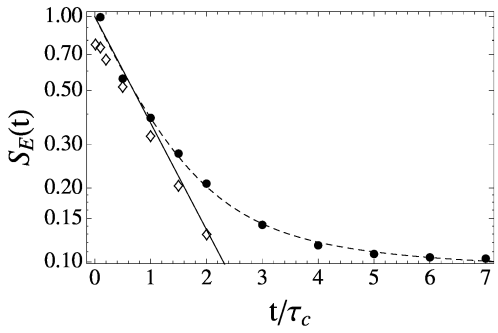

FIGURE 26: Time-dependent eccentricity function (Eq. (5.43)) calculated from the L-model (diamonds) and from the Q-model (circles). The solid line shows $S_2(t) = \chi(t)$ and the dashed line is a two-exponents plus a constant offset fit through the circles. The model parameters are the same as in Figure 25: $\Delta\tau_c = 5$, $\epsilon^2 = 1 + 0.3i$ for the Q-model and $\epsilon = 1$ for the L-model.

widths as a function of the waiting time, $S_E(T) = S_2(T) = \chi(T)$, where

$$S_E(T) = \frac{\sigma_\parallel(T)^2 - \sigma_\perp(T)^2}{\sigma_\parallel(T)^2 + \sigma_\perp(T)^2} \tag{5.43}$$

Repeating the arguments of ref [257] it is easy to show that a double Fourier transformation of the Q-model short-time expansion in Eq. (5.42) (under the conditions of convergence) should also yield $\chi(T) = S_E(T)$. The short-time approximation becomes, however, limited to very short times once an imaginary part is included in ϵ, as is seen from the tail of $S_E(T)$ in Figure 26 deviating from $\chi(T)$ at longer waiting times. The eccentricity function does not correctly reproduce the frequency correlation function $S_2(t) = \chi(t)$ in the Q-model (filled circles in Figure 26), while this metric is quite reliable in L-models (open diamonds in Figure 26).

An alternative approach to $S_2(t)$ is to measure the evolution of the slope of the center line[258, 259]. In this approach, cuts of 2D contours are made at constant ω_1 and maxima of the profiles along the ω_3 frequency are collected as a function of ω_1. The time dependence of the slope of the center line gives access to $S_2(t)$[258]. Recent experimental and theoretical studies, however, have shown that the center line develops a bend for

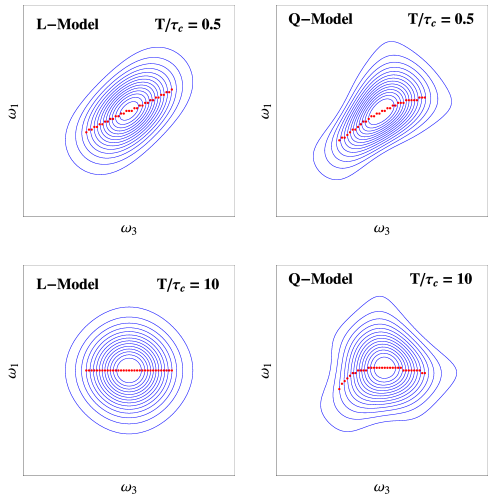

FIGURE 27: 2D spectra at different time delays T calculated from L-model ($\epsilon = 1$) and Q-model ($\epsilon^2 = 1 + 0.3i$ in Eq. (5.39)); $\Delta\tau_c = 5$. The red dots indicate the center line.

some systems[234, 235]. A similar phenomenology follows from the dynamic Q-model developed here.

To demonstrate the new qualitative features introduced by the Q-model compared to the L-model, we use the parameters typical for vibrational spectroscopy and compare purely absorptive 2D spectra of a two-state system produced with the standard Kubo's broadening function (Eqs. (5.33)–(5.35)) to the same spectra obtained with the new broadening function derived here (Eqs. (5.33), (5.40), and (5.41)). These results are presented in four panels of Figure 27, where the left two panels show the linear Kubo's result and the right two panels show the result of the Q-model. The main difference between the linear and quadratic models of line broadening is the asymmetry of the purely absorptive spectrum introduced by the complex ϵ in Eq. (5.39). The observable consequence is the bending of the center line.

5.6 Numerical Simulations

5.6.1 Polar-polarizable Chromophores

In order to test the model by numerical simulations, a particular realization of the quadratic solute-solvent coupling due to solute's polarizability[227, 120] was used. The nuclear coordinate in this setup becomes the instantaneous electric field $\mathbf{E}$ of the solvent interacting with the solute dipole $\mathbf{m}_{0i}$ and polarizing the solute as determined by its electronic polarizability α_{0i} (assumed to be isotropic). Since both the dipole moment and the polarizability change with the electronic transition, the instantaneous transition frequency in Eq. (5.4) becomes

$$\hbar\Omega(\mathbf{E}) = \hbar\Omega_0 - \Delta\mathbf{m}_0 \cdot \mathbf{E} - (\Delta\alpha_0/2)E^2 \tag{5.44}$$

where $\Delta\mathbf{m}_0 = \mathbf{m}_{0e} - \mathbf{m}_{0g}$ and $\Delta\alpha_0 = \alpha_{0e} - \alpha_{0g}$.

The problem of electronic transitions in polarizable chromophores can be completely mapped on the Q-model if one additionally assumes that the distribution of the electric field is Gaussian. This implies that the term in the Hamiltonian describing fluctuations of the electric field inside a solute carrying no charges and polarizability is quadratic, $(4a_p)^{-1}E^2$, where a_p denotes the response coefficient (susceptibility) such that the chemical potential of solvating the dipole m_{0i} is $\mu_i = -a_p f_i (m_{0i})^2$. Here,

$$f_i = [1 - 2a_p\alpha_{0i}]^{-1} \tag{5.45}$$

is a factor accounting for the enhancement of the solute dipole due to an effective, mean-field addition of the induced and permanent dipoles[65]. Therefore, if $\alpha_{0i} = 0$, a_p is the linear susceptibility of the polar liquid solvent to the solute permanent dipole. It is given by the Onsager equation[65] when the solute is a sphere of radius R in a continuum dielectric

with the static dielectric constant ϵ_s

$$a_p = \frac{1}{R^3}\frac{\epsilon_s - 1}{2\epsilon_s + 1} \tag{5.46}$$

The simulations reported below are performed in a non-polarizable force field of water. Therefore, the discussion is limited to a non-polarizable solvent. An extension to a more general case of polarizable solvents can be found elsewhere[227, 193].

With these assumptions, the Hamiltonians of the ground and excited states of the solute become

$$H_i = I_i - \mathbf{m}_{0i} \cdot \mathbf{E} - (\alpha_{0i}/2)E^2 + (4a_p)^{-1}E^2 \tag{5.47}$$

The mapping of the Q-model on Eq. (5.47) is straightforward and achieved by equating κ_i in Eq. (5.3) to $(2a_p)^{-1} - \alpha_{0i}$ and $\Delta\kappa$ to $-\Delta\alpha_0$. The reorganization energies in two electronic states become

$$\lambda_i = a_p f_i \left(\Delta\mathbf{m}_0 + 2a_p f_i \Delta\alpha_0 \mathbf{m}_{0i}\right)^2 \tag{5.48}$$

In addition, the average transition frequencies are

$$\hbar\bar{\Omega}_i = \hbar\Omega_0 - 2a_p f_i \left(\Delta\mathbf{m}_0 \cdot \mathbf{m}_{0i} + a_p f_i \Delta\alpha_0 m_{0i}^2\right) \tag{5.49}$$

The same equation can be written in a more compact form as

$$\hbar\bar{\Omega}_i = \hbar\omega_0 + \alpha_i\lambda_i \tag{5.50}$$

where $\omega_0 = \Omega_0 + (\Delta m_0)^2/(2\hbar\Delta\alpha_0)$ and

$$\alpha_i = -(2a_p f_i \Delta\alpha_0)^{-1} \tag{5.51}$$

Before proceeding to MD simulations, we provide estimates of the typical values of α_i that might be seen in optical and IR spectroscopies. For optical absorption, $\Delta\alpha_0 > 0$ and can be of the same order of magnitude as the polarizability of the ground state $\Delta\alpha_0 \sim$

α_{0g}[260, 227]. Given that polarizabilities of many organic molecules can be estimated as $\alpha_{0g} \simeq R^3/3$[261], one gets for the parameter controlling non-Gaussian behavior $\alpha_g \simeq -2$ in Eq. (5.51) ($\alpha = 1.8$ is used in Figure 22). For OH stretch, the quadratic Stark effect results in[240] $\Delta\alpha_0 \simeq 0.12$ Å^3. Assuming $\Delta\alpha_0 \simeq \alpha_{0g}$ and $R \simeq 1.4$ Å, one gets $\alpha_g \simeq -23$. Further, a nonlinear dependence of the vibrational frequency on the electric field, consistent with altering polarizability, was observed for X-H group vibrations[241]. The numerical estimate of $\Delta\alpha_0$ from these measurements is still a subject of uncertainty and cannot be used here for mapping on the Q-model.

The numerical simulations of electronic transitions in polarizable chromophores presented below separately address the statistics and dynamics of the transition frequency. We first start with analyzing the free energy surfaces of the two electronic states as functions of the transition frequency Ω. Those are given in the Q-model by Eq. (5.24), in which the two stationary states are obtained by assigning $\alpha(t)$ to its initial, $\alpha_g = \alpha(t = 0)$, and final, $\alpha_e = \alpha(t = \infty)$, values given by Eq. (5.51). We then proceed to the next step of analyzing the dynamics of the transition frequency, focusing in particular on nonlinear vs. non-Gaussian dynamics caused by the quadratic solute-solvent coupling of a polarizable chromophore.

5.6.2 Free Energy Surfaces

The system that we have chosen to analyze is made of a spherical solute with the radius $R = 3$ Å dissolved in TIP4P water (Figure 28). The solute interacts with the oxygens of water by the Lennard-Jones (LJ) potential and, additionally, carries two opposite charges q separated by the distance $R = 2d$. Polarizability of the solute is modeled by a Drude particle placed at its center (Figure 28)[262]. Isotropic polarizability of the solute $\alpha_0 = q_{\rm D}^2/k_{\rm D}$

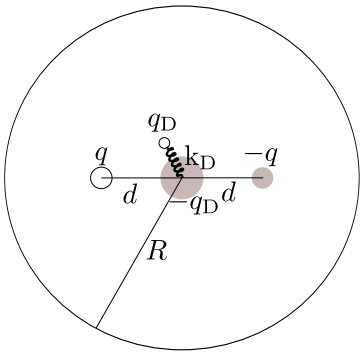

FIGURE 28: Polar-polarizable solute used in molecular dynamics simulations. A Lennard-Jones (LJ) solute of the radius R contains two opposite charges separated by $2d = R$. The negative charge $-q_{\mathrm{D}}$ at the center of the LJ solute is compensated by a Drude particle carrying the charge $+q_{\mathrm{D}}$. The charge and the spring constant k_{D} connecting the Drude particle to the LJ particle define the solute polarizability $\alpha_0 = q_{\mathrm{D}}^2/k_{\mathrm{D}}$. Altering q_{D} is used to change the polarizability of the solute. The parameters of the solute and solvent force fields are given in chapter 7.

is achieved in simulations by allowing isotropic motions of the Drude particle constrained only by the potential energy penalty of stretching the spring with the force constant k_{D}. The magnitude of the Drude particle charge q_{D} was changed to produce different values of α_0. NAMD[263] was used to integrate the MD trajectories. More details on the simulation protocol, force field parameters, and the analysis of the simulation trajectories are given in chapter 7. Here, we proceed directly to the results.

Two sets of simulations were performed to test the model. In the first set, the dipole moment of the solute was varied at zero polarizability $\alpha_{0i} = 0$. The average solvent electric field as a function of m_0 then yields the susceptibility $a_p = 0.0167$ Å^{-3}. The Onsager equation (Eq. (5.46)) predicts $a_p = 0.0181$ with $\epsilon_s = 59$ of TIP4P water[264]. A somewhat higher value from the Onsager equation with the dielectric cavity radius equated to the van der Waals radius of the solute is consistent with previous simulations[97]. The simulations of polarizable chromophores were done in two dipolar states with $m_{0g} = 5$ D and $m_{0e} = 10$ D and the corresponding polarizabilities $\alpha_{0g} = 5$ Å^3 and $\alpha_{0e} = 15$ Å^3.

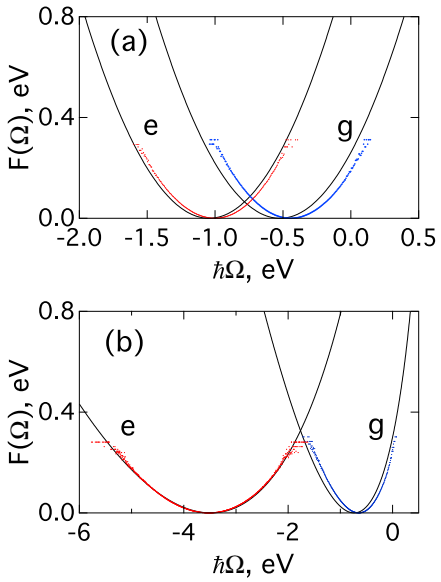

FIGURE 29: Free energy surfaces of the ground (g) and excited (e) states for non-polarizable (a) and polarizable (b) chromophores. The solid lines are the calculations with the Q-model using $a_p = 0.0167$ Å^{-3} as the sole input parameter. The dots represent distributions of the energy gap produced by MD simulations. All curves are brought to the same baseline at the positions of their minima.

For the sake of comparison, the same dipolar configurations of the solute were used to produce the free energy surfaces $F_i(\Omega) = -\beta^{-1} \ln[P_i(\Omega)]$ for polarizable and non-polarizable chromophores (Figure 29).

The parabolic free energy surfaces of the Gaussian statistics (Eq. (5.8)) are calculated with $\alpha_{0i} = 0$ in Eqs. (5.48)–(5.50). The results are compared in Figure 29a to direct sampling of the energy gap $\Omega(\mathbf{E})$ (Eq. (5.44)) along MD trajectories. Corresponding free energy surfaces for polarizable chromophores are compared to Eq. (5.24) in Figure 29b. The results for the solvent-induced shifts $\Delta\Omega_i = \bar{\Omega}_i - \Omega_0$ and reorganization energies are listed in Table 1. Simulations are in quantitative agreement with the Q-model for both purely dipolar and polarizable chromophores. A slight discrepancy between simulations and theory in the positions of the parabolas' minima at $m_{0g} = 5$ D, seen in both cases, is probably

TABLE 1: Solvent-induced spectral shifts and reorganization energies in two states of the polarizable and non-polarizable chromophore. The results of MD simulations are compared to calculations according to Eqs. (5.48)–(5.50) employing a single input parameter $a_p = 0.0167$ Å^{-3} obtained from MD simulations of non-polarizable chromophores with varying magnitude of the dipole moment (See chapter 7).

Parameters[a]		MD, eV		Theory, eV	
m_{0i}	α_{0i}	$-\hbar\Delta\Omega_i$	${\lambda_i}^b$	$-\hbar\Delta\Omega_i$	${\lambda_i}^b$
5	0	0.52	0.26	0.48	0.26
10	0	1.04	0.26	1.04	0.26
5(g)[c]	5	0.68	0.57	0.75	0.62
10(e)[c]	15	3.54	2.83	3.51	2.88

[a]Chromophore's dipole (D) and polarizability (Å^3). [b]Reorganization energies are calculated according to Eq. (5.9). [c]g and e denote ground and excited states, respectively.

caused by the non-point solute dipole in simulations and a corresponding contribution of the solute quadrupole to the solvation energy.

5.6.3 Dynamics

The free energy surfaces presented in Figure 29 suggest that dynamics of the transition frequency should slow down for states with higher solute polarizability. The curvature of $F_i(\Omega)$ is the restoring force constant of the harmonic motion, which loses its stiffness with increasing α_0. The same statement applies to the dynamics of the solvent electric field $\mathbf{E}$. The harmonic stiffness constant for the equations of field evolution is $(2a_p)^{-1} - \alpha_{0i}$ (Eq. (5.47)), and it decreases with increasing solute polarizability. As a result, the time correlation function $S_\parallel(t) \propto \langle \delta E_\parallel(t) E_\parallel(0) \rangle$ of the field projection on the solute dipole $E_\parallel(t)$ slows down with increasing solute polarizability (see Figure 47 in chapter 7)[265, 266]. This observation, goes beyond the mathematical framework of the dynamical Q-model following from the Ornstein-Uhlenbeck propagator in Eq. (5.19).

Equation (5.19) assumes that all the dependence of the dynamics of the transition fre-

quency on the electronic state of the chromophore appears as a result of the quadratic coupling to the coordinate $q(t)$, the dynamics of which are not affected by changes in the chromophore. This assumption can of course be modified by assigning the dependence of the relaxation function $\chi(t)$ on the electronic state of the chromophore $\chi(t) \rightarrow \chi_i(t)$, $i = \mathrm{g}, \mathrm{e}$. This alteration breaks the independence of the Stokes-shift and equilibrium correlation functions on the electronic state of the chromophore, but preserves the equality between $S_{2,i}(t)$ and $\chi_i(t)$. We find from our simulations that $S_{2,i}(t)$ matches $S_{\|,i}(t)$ really well. Points showing $S_{\|,i}(t)$ in Figure 30 essentially coincide on the plot scale with the solid lines representing $S_{2,i}(t)$. The origin of the dependence of $S_{2,i}(t)$ on the electronic state $i = \mathrm{g}, \mathrm{e}$ can, therefore, be assigned to the corresponding dependence of the dynamics of the nuclear coordinate.

The Q-model predicts distinctions between $S_{\sigma,i}(t)$, $S_{\Omega,i}(t)$, and $S_{2,i}(t)$ calculated in the same electronic state (Eq. (5.29)). All these predictions go beyond the standard expectations of L-models[249, 250, 252], implying that the dynamics are nonlinear. We find all these predictions to hold when tested against MD simulations: all correlation functions depend on the electronic state of the chromophore (cf. lines of different color in Figure 30) and the three correlation functions are different for the same electronic state (cf. different lines of the same color in Figure 30). However, $S_{\Omega,i}(t)$ is still a reasonable estimate of $\chi_i(t)$ and $S_{\sigma,i}(t)$ are close to both $S_{\Omega,i}(t)$ and $\chi_i(t)$. The main difference in the dynamics of two states comes from the dependence of $\chi_i(t)$ on the electronic state of the chromophore. The next question to address is whether higher-order time correlation functions are non-zero, i.e., whether the dynamics are non-Gaussian.

We start by comparing the skewness time correlation function $S_{3,i}(t)$ (Eq. (5.16)), which is identically zero for Gaussian dynamics, between MD simulations and the Q-model (Eq. (5.22)). The Q-model predicts $S_{3,i}(0) \propto -\Delta\alpha_0$ ($\alpha_i^{-1} \propto \Delta\kappa$, $\Delta\kappa = -\Delta\alpha_0$

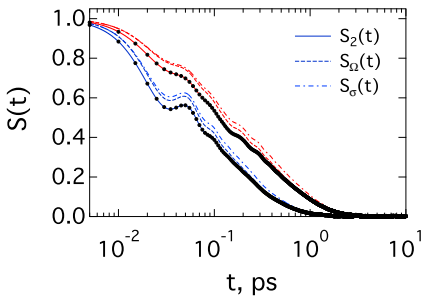

FIGURE 30: Normalized correlation functions calculated for the ground (blue, $m_{0g} = 5$ D and $\alpha_{0g} = 5$ Å^3) and excited (red, $m_{0e} = 10$ D and $\alpha_{0e} = 15$ Å^3) states of the polarizable chromophore. The solid lines refer to $S_{2,i}(t)$, with the superimposed dots showing the self-correlation function $S_{\|,i}(t)$ of the solvent field projected on the solute dipole. The dashed and dash-dotted lines show $S_{\Omega,i}(t)$ (Eq. (5.28)) and $S_{\sigma,i}(t)$ (Eqs. (5.12) and (5.25)), respectively.

in Eq. (5.22)). Since $\Delta\alpha = \alpha_{0e} - \alpha_{0g} > 0$, it implies that $S_{3,i}(0) < 0$. This is indeed observed in MD simulations for both $S_{3,g}(0)$ and $S_{3,e}(0)$ ($\Omega(t)$ is defined by Eq. (5.44) for both states). Moreover, the agreement between the skewness functions calculated from MD and from the Q-model is nearly quantitative for the ground state (cf. dashed and solid blue lines in Figure 31). Further, Eq. (5.16) predicts that the skewness function should depend on the chromophore's state and, in particular, $S_{3,e}(0)$ should be smaller in the magnitude than $S_{3,g}(0)$ because of the larger reorganization energy of the exited state, $\lambda_e > \lambda_g$ (Table 1). This is indeed confirmed by MD, but the alteration of $S_{3,e}(0)$ compared to $S_{3,g}(0)$ is greater in MD simulations than predicted by the Q-model. The agreement between the theory and simulations is only qualitative for the excited state skewness function.

The correlation functions $S_{4,i}(t)$ calculated from MD are practically indistinguishable from their corresponding Gaussian limits (Eq. (5.21), see Figure 48 in chapter 7). This is the result of the fact that the non-Gaussian corrections to Eq. (5.21) scale as $(\beta\lambda_i)^{-1}$ in $S_{4,i}(t)$ and the knowledge of the second-order correlation function $S_{2,i}(t)$ is sufficient to describe $S_{4,i}(t)$.

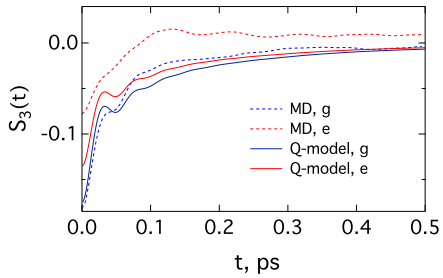

FIGURE 31: Skewness correlation function $S_{3,i}(t)$ (Eq. (5.16)) calculated from MD simulations (dashed lines) and from the Q-model (Eq. (5.22), solid lines). The calculations are done for the ground (blue, $m_{0g} = 5$ D and $\alpha_{0g} = 5$ Å^3) and excited (red, $m_{0e} = 10$ D and $\alpha_{0e} = 15$ Å^3) states of the polarizable chromophore. In both calculations, we have $\Delta m_0 = 5$ D and $\Delta\alpha_0 = 10$ Å^3 in Eq. (5.44), consistent with the definition of the transition frequency in Figure 29. The time correlation function $\chi(t) = S_{\|}(t)$ from MD simulations of a non-polarizable solute was used in Eq. (5.22) (see Figure 47 in chapter 7).

The conclusion that can be drawn from calculations of time correlation functions is that the procedure adopted in the analytical model of projecting the Gaussian dynamics of nuclear medium coordinates on the transition frequency quadratic in these coordinates is generally supported by simulations. We also conclude that transient effects in time-resolved linear spectra going beyond the standard linear models, such as the dependence of the spectral width on time shown in Figure 24, arise from moving the equilibrium distribution belonging to one free energy surface to a free energy surface with a different curvature (Figure 23). The evolution of the excited-surface packet requires two correlation functions, $S_{2,e}(t)$ and $S_{3,e}(t)$. The effect of non-Gaussian dynamics is, therefore, mostly limited to a non-zero skewness function $S_{3,i}(t)$ and does not affect the higher-order time correlation functions, which can be calculated based on the Gaussian dynamics.

5.7 Discussion

Two types of non-traditional dynamical effects of condensed materials on the time evolution of molecular spectra have recently come under scrutiny: (1) nonlinear dynamics and (2) non-Gaussian dynamics. The former puts under one umbrella all possible deviations from the results of L-models combined with the linear response approximation. The latter requires high-order time correlation functions not reducible to the second-order one.

Three consequences of nonlinear dynamics are typically recognized: (i) Stokes-shift correlation functions distinct from equilibrium correlation functions of both the transition frequency and the intrinsic nuclear coordinates of the thermal bath[250], (ii) differences between equilibrium time correlation functions in the ground and excited states of the chromophore[251, 249], and (iii) time evolution of the spectral width[244, 193, 228]. All these features are qualitatively reproduced by the Q-model.

The model achieves a more complete description of static and time-resolved lineshapes by summing an infinite series of spectral cumulants, instead of relying on the commonly applied two-cumulant approximation (zero cumulants beyond second order). The model yields non-Gaussian linear lineshapes (Eq. (5.24)) and predicts time evolution of the spectral linewidth (point (iii)).

The quadratic chromophore-medium coupling also requires a new analytical form for the line broadening function of 2D correlation spectra (Eqs. (5.33), (5.40), and (5.41)). Time evolution of 2D spectra shows bending of the center line and the deviation of the eccentricity function from the correlation function describing the bath dynamics. Given these complications, standard metrics of extracting the two-point correlation function from 2D spectra (center line, eccentricity function, etc.) do not apply here and direct fitting of

2D profiles to the line broadening function is required. Alternatives to direct fitting are clearly desirable[257, 223, 258, 259], but have not been established so far for the Q-model.

There is an important qualitative difference between two signatures of nonlinear dynamics: $S_{\Omega,i}(t) \neq S_{2,i}(t)$, $S_{\sigma,i} \neq S_{\Omega,i}$ (point (i)) and $S_{2,g}(t) \neq S_{2,e}(t)$ (point (ii)). The former inequalities require going beyond the linear response (see appendix C), which is achieved here by summing an infinite series of transition frequency cumulants. By comparison, the difference between $S_{2,g}(t)$ and $S_{2,e}(t)$ can be accommodated within the linear response approximation once different force constants κ_i for the nuclear coordinate are allowed in the ground and excited states (e.g., through solute's polarizability). The linear response approximation for these correlation functions requires the smallness of only the transition frequency $\Omega(t)$ relative to H_g for absorption and relative to H_e for emission. While linear expansion in $\Omega(t)$ is performed, different force constants κ_i will project onto state-dependent time correlation functions $\chi_i(t)$ of the nuclear mode. Even within the linear response approximation, different $S_{2,i}(t)$ will be produced for the ground and excited states.

The issue of non-Gaussian dynamics (point (2) above) is often entangled with nonlinear effects, but is in fact a separate issue. It is studied here by combining the dynamical Q-model with MD simulations. The third-order (skewness) time correlation function is nonzero for polarizable chromophores, thus corresponding to non-Gaussian dynamics of the transition frequency. The effect of non-Gaussian dynamics, within the present model, does not extend beyond the third-order correlation function.

Chapter 6

ROLE OF POLARIZABILITY OF THE ACTIVE SITE OF CYTOCHROME *C* IN THE ELECTRON TRANSFER ACTIVATION BARRIER

6.1 Summary

Enzymes in biology's energy chains operate with low energy input distributed through multiple electron transfer steps between protein active sites. The general challenge of biological design is how to lower the activation barrier without sacrificing a large negative reaction free energy. It is shown that this goal is achieved through a large polarizability of the active site. It is polarizable by allowing a large number of excited states, which are populated quantum mechanically by electrostatic fluctuations of the protein and hydration water shells. This perspective is achieved by extensive mixed quantum mechanical/ molecular dynamics simulations of the half reaction of reduction of cytochrome *c*. The barrier for electron transfer is consistently lowered by increasing the number of excited states included in the Hamiltonian of the active site diagonalized along the classical trajectory. Therefore, molecular polarizability, in addition to much studied electrostatics of permanent charges, is a key parameter to consider in order to understand how enzymes work.

6.2 Introduction

Cytochrome *c* is an essential redox protein in bacterial photosynthesis and respiratory energy chains of mitochondria. Its redox function is to shuttle electrons between membrane-bound energy complexes, such as between the bc_1 complex and cytochrome *c*

oxidase in respiration [267]. The redox activity occurs in heme *c* covalently bound to the polypeptide [268] (Fig. 32A). The mechanism of transferring the electron, which alters the redox state of the heme, is generally understood within the Marcus theory of electron transfer [6]. It stipulates that the reaction is activated by nuclear fluctuations of the thermal bath, which in the case of protein electron transfer is a highly heterogeneous protein-water interface. The prevailing modes, frequencies, and coupling strengths of those medium modes to the heme's electronic states are the parameters establishing the overall activation barrier of the reaction [114, 89, 13].

Hydration does not significantly affect vibrational cooling of the heme [269] and THz absorption of well-hydrated samples is nearly insensitive to the oxidation state [270]. These observations suggest little direct contact of water with the heme [269]. Therefore, cytochrome *c* is a good model system to which basic assumptions of the Marcus theory apply [271, 117, 47]. Potential complications of water penetrating the active site [272] and of conformational transitions upon changing the redox state [268] are largely insignificant. Our present simulations support this general assessment when applied to the active site represented by fixed atomic charges. However, the main result of this study is the finding that polarizability of the active site extends the problem of protein electron transfer beyond the standard model [119] by dramatic reduction of the activation barrier.

The established paradigm of the Marcus theory is based on the two-state description involving electronic energy levels of either the electron donor or the acceptor [6]. Nuclear fluctuations of the medium bring these two energy levels into resonance, allowing tunneling to occur [273]. The free energy (reversible work) required to create the resonance condition is determined by two parameters, the reaction free energy ΔG_0 and the medium reorganization energy λ. The formulation further simplifies when ΔG_0 is zero for either self-exchange electron transfer or for a half redox reaction occurring at the electrode. The

activation free energy (activation barrier) is then fully determined by the reorganization energy [6]

$$F^{\text{act}} = \lambda/4. \tag{6.1}$$

Early calculations and numerical simulations of protein electron transfer produced values of the reorganization energy in the range of 0.7–0.8 eV. More recent molecular dynamics (MD) simulations employing improved force field and significantly longer trajectories resulted in an upward revision of these values toward those more traditional for redox chemistry, $\sim 1.0 - 1.5$ eV [274, 47, 275, 89] (or even higher [276]). The upward revision of the reorganization energy implies a higher activation barrier in Eq. (6.1) and a much slower rate. On the other hand, electrode kinetics measurements typically report much lower values, $\lambda \sim 0.4 - 0.5$ eV [277, 278], when estimated from the Marcus relation in Eq. (6.1). It implies that either the results of numerical simulations for λ are grossly incorrect or the relation between the activation barrier and the reorganization energy needs a revision. Here we present arguments that the latter is the case. The revision of the barrier height arises from introducing polarizability of the protein's active site (Fig. 32B).

Equation (6.1) can be derived by considering two crossing parabolas $F_i(X) = (X \pm X_0)^2/(4\lambda)$ ($i = \mathrm{Red}, \mathrm{Ox}$) plotted against the energy gap reaction coordinate X as defined by Warshel [279] (Fig. 32B). The crossing point $F_1(X) = F_2(X)$ is the transition state of zero energy gap $X = 0$, where tunneling occurs [280, 281, 282]. The Marcus formulation follows from requiring $X_0 = \lambda$ as stipulated by the fluctuation-dissipation theorem [92].

Recent simulations have shown that proteins are often unable to sample their entire phase space on the reaction time-scale. This ergodicity breaking [13] eliminates the restriction on the reaction parameters imposed by the fluctuation-dissipation theorem. In particular, X_0 and λ become two separate parameters [283, 13] and finding the activation barrier requires three parameters (X_0, λ, and ΔG_0), instead of two parameters of the Marcus the-

ory. Sampling of the entire phase space is never realistically possible, but the problem is drastically elevated for proteins because of their rugged energy landscape, similar to those found for fragile glasses [284, 285]. The dynamics and statistics of proteins are characterized by many local minima, in which the protein-water system can be trapped never reaching its true thermodynamic minimum [286]. Electron-transfer reactions between non-equilibrium trapped states do not follow the strict restriction $X_0 = \lambda$ [13].

The direct mechanistic consequence of this new perspective is more flexibility in fine-tuning the activation barrier of electron transfer [13, 91]. Since X_0 refers to the average of the vertical transition energy, it defines the position of the maximum of an optical spectroscopic line [246] and can be associated with the Stokes shift of optical spectroscopy. One can therefore define the Stokes shift reorganization energy as $\lambda^{\mathrm{St}} = X_0$ [119]. The three-parameter description leads to the following activation barrier when $\Delta G_0 = 0$ [13]

$$F^{\mathrm{act}} = \lambda^{\mathrm{r}}/4 = (\lambda^{\mathrm{St}})^2/(4\lambda), \tag{6.2}$$

where the "reaction" λ^r can be identified with the Marcus reorganization energy in Eq. (6.1).

The reorganization energy in the denominator in Eq. (6.2) is defined as the variance of the reaction coordinate

$$\lambda = \langle(\delta X)^2\rangle/(2k_{\mathrm{B}}T), \tag{6.3}$$

where k_{B} is the Boltzmann constant and T is the temperature. Note that long trajectories, > 100 ns or longer [15], are required to converge λ (see Fig. 52 in chapter 7). Because of this difficulty, most simulations, with few exceptions [89], report λ^{St} instead of λ.

It is clear that the activation barrier can be lowered compared to Eq. (6.1) of the Marcus model when $\lambda^{\mathrm{St}} < \lambda$. The parameter

$$\kappa_G = \lambda/\lambda^{\mathrm{St}} \tag{6.4}$$

quantifies the difference between two reorganization energies in the three-parameter model [283]. Note that electrochemical kinetic measurements report $\lambda^{\mathrm{r}} = (\lambda^{\mathrm{St}})^2/\lambda$. The low values of such effective reorganization energies [277, 287, 288] are therefore consistent with $\kappa_G > 1$ as schematically shown in Fig. 32B. It is also clear that the rate maximum plotted against the driving force $-\Delta G_0$ (the Marcus inverted parabola [6]) gives the value of $\lambda^{\mathrm{St}} = X_0$ only.

Important for biological applications is that $\kappa_G > 1$ lowers the activation barrier without requiring more negative reaction free energy, which is a scarce commodity in biological energy chains [267]. It seems therefore possible that the evolutionary pressure has favored the glassy character of the protein fluctuations, and their high fragility [284], to promote electron transport consuming less free energy input for its operation.

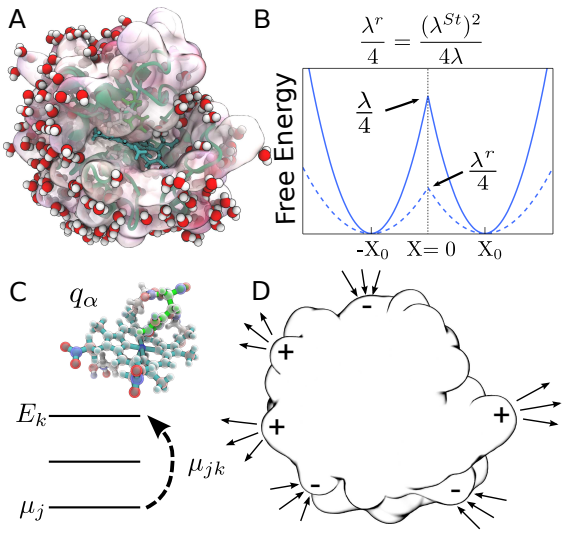

FIGURE 32: (A) Hydrated cytochrome *c* with the heme active site shown in green. (B) The free energy surfaces of a half reaction in the Marcus model (Eq. (6.1)) of fixed atomic charges (solid lines) and in the polarizable model with $\lambda^{\mathrm{St}} < \lambda$ (Eq. (6.2)). (C) The active site representation by atomic charges q_α in classical simulations and by a Hamiltonian matrix coupled to the classical bath in QM/MD simulations. (D) The mechanism of compensation of protein and water electrostatics through polarizing the interfacial water dipoles by the charged residues of the protein.

6.3 Theoretical and Computational Methods

The Marcus formulation of the electron-transfer theory can be viewed as the first-order quantum-mechanical perturbation of the electronic energy levels by the thermal bath. The perturbation Hamiltonian comes from integrating the electronic density $\rho_e(\mathbf{r})$ with the electrostatic potential of the bath $\phi(\mathbf{r})$: $H' = \int \rho_e(\mathbf{r})\phi(\mathbf{r})d\mathbf{r}$. When the electronic density is given by a set of atomic charges q_α, one arrives at the force-field formulation often implemented in classical simulations. The solute-solvent Hamiltonian is obtained by summing up partial atomic charges with the bath potentials at their locations: $H' = \sum_\alpha q_\alpha \phi_\alpha$ (Fig. 32C). However, fluctuations of the medium not only alter the donor-acceptor energy gap (between HOMO and LUMO), but also the entire manyfold of the electronic energy states. Each instantaneous nuclear configuration of the medium will produce a different extent of electronic delocalization between those available electronic states, or, alternatively, a different deformation of the electronic density.

The ability of the electronic distribution to deform in an external field is associated with its electronic polarizability. In the dipolar approximation, it is given in terms of transition dipoles μ_{km} linking different electronic sates of the molecule through the electric field of the bath E_b (Fig. 32C). The standard quantum-mechanical perturbation theory leads to the quadratic Stark effect [289], shifting the energy level k by the amount $(-\alpha_k/2)E_b^2$ scaled with the polarizability of that state

$$\alpha_k = 2\sum_{m\neq k} |\mu_{km}|^2/\Delta E_{mk} \tag{6.5}$$

determined by a set of transition dipoles and energy gaps $\Delta E_{mk} = E_m - E_k$ of all possible virtual excitations.

Perturbation theory is not required to introduce polarizability into the description of electron transfer. A more accurate formalism is achieved by using the empirical valence-

bond approximation introduced by Warshel and Weiss [290, 291, 292]. It produces the instantaneous energies of the donor and acceptor by diagonalizing the Hamiltonian matrix incorporating the coupling to the medium into the diagonal (electrostatics) and off-diagonal (transition dipoles) matrix elements. This approach has been widely used for a number of biologically relevant systems in the past [293, 88] and has recently been implemented in the form of the perturbed matrix algorithm [47] in application to protein electron transfer. We follow this general formalism in the simulations presented in this paper. Our main goal is to explore the possibility of lowering the barrier for electron transfer by including mixing between the quantum states (polarizability). From the more fundamental perspective, our study asks the question of whether including polarizability of the enzyme's active site, in contrast to the picture of fixed atomic charges, might reduce the barrier of an enzymetic reaction. In other words, the question is whether polarizability is one of the tools of biology's catalytic capability [294].

6.3.1 QM/MD Simulations

The goal of our simulation strategy is to go beyond the assumption of fixed atomic charges in the modeling of the redox active site. We introduce the ability of the electronic density of the heme in cytochrome *c* to redistribute in response to a thermal fluctuation of the bath. This goal is shared by essentially all QM/MM algorithms which all start by defining the quantum center, i.e., a part of the system which can be treated on the quantum-mechanical (QM) level [86, 87, 88, 89, 90, 91]. The choice of the level of QM calculations is dictated by the physics of the problem and, to a large degree, by the time-scale required to capture the essential collective modes of the thermal bath contributing to the activation barrier. Protein electron transfer is a difficult problem for QM algorithms because long

time scales are very essential here. Classical simulations of electron transfer have shown that a broad range of bath time-scales affects the reorganization energy [283, 89]. The time-scales of ~ 1 ns represent global elastic deformations of the protein shape, which have to be included for a realistic description of λ. These motions produce large fluctuations of electrostatic potential inside the protein by shifting charged surface residues and surface water polarized by them [13] (Fig. 32D). As more elastic modes enter the observation window (the length of the simulation trajectory), the reorganization energy grows nearly continuously through the range of time-scales up to tens of microseconds currently reached by simulations [15]. Given these constraints imposed by the physics of the problem, a QM algorithm needs to capture the entire range of thermal motions sampled by classical simulations.

The method of perturbed matrix [47] imposes essentially no QM overhead on the classical MD. It assumes that the forces acting on the atoms of the classical thermal bath can be well characterized by classical force fields. One therefore performs long classical MD simulations of the entire system producing the dynamics of the classical bath. This classical dynamics is then used to recalculate the parameters of the quantum center affected by the electrostatic interactions with the bath. Since long-range electrostatics is the main factor influencing the positions of the donor and acceptor energy levels involved in electron transfer [114], this algorithm is particularly well suited for this problem.

The QM component is implemented here by expanding the electrostatic potential of the bath $\phi(\mathbf{r})$ around the potential ϕ_{Fe} at the heme iron and truncating the expansion at the dipolar term. The matrix elements of the quantum center Hamiltonian then become

$$H_{jk} = (E_j + Q\phi_{\text{Fe}})\,\delta_{jk} - \boldsymbol{\mu}_{jk} \cdot \mathbf{E}_b, \tag{6.6}$$

where Q is the total charge of the quantum center. The quantum states $j = 0, \ldots, M$

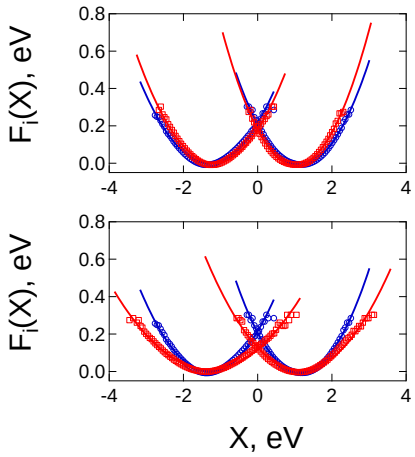

FIGURE 33: Free energy surfaces $F_i(X)$, i = Red,Ox of cytochrome *c* in the Ox (left curves) and Red (right curves) states. The blue points/lines refer to classical MD and the red points/lines refer to the QM/MD simulations. The solid lines are fits of the statistics calculated from simulation data to parabolas. Panel (A) refers to a non-polarizable quantum center ($\xi = 0$). Panel (B) refers to a polarizable quantum center with $\xi = 1$ and $\Delta\alpha = -31$ Å^3. The lower panel demonstrates the depression of the barrier height upon allowing a non-zero $\Delta\alpha$ (see Fig. 54 in chapter 7 for $\Delta\alpha = -123$ Å^3).

include the ground state of the quantum center, $j = 0$, and a number of its excited states produced here by ZINDO/S calculations for the oxidized (Ox, $Q = -1$) and reduced (Red, $Q = -2$) states. The polarizability is a slowly converging function of the number of excited states M; the results presented here were obtained for $M = 100$. Reducing M makes the quantum center less polarizable and eventually brings the system back to the Marcus domain. This was the result of a recent calculation employing $M = 12$ [47].

The Hamiltonian matrix in Eq. (6.6) is diagonalized at each instantaneous value of the potential ϕ_{Fe} and the electric field $\mathbf{E}_b$ along the simulation trajectory to produce the minimum eigenvalues $E_{\text{g}}^{\text{Ox/Red}}$ corresponding to the ground state in either oxidized or reduced states of the active site. The electron-transfer reaction coordinate, monitoring the transition to the activation state $X = 0$, is given as [279]

$$X = E_{\text{g}}^{\text{Ox}} - E_{\text{g}}^{\text{Red}}. \tag{6.7}$$

The limit of classical simulations is obtained by representing the quantum center by a set of atomic charges coupled to the bath through the corresponding electrostatic potentials ϕ_α (Fig. 32C). The reaction coordinate of electron transfer becomes in this case

$$X = \sum_\alpha \Delta q_\alpha \phi_\alpha, \tag{6.8}$$

where $\Delta q_\alpha = q_\alpha^{\text{Ox}} - q_\alpha^{\text{Red}}$. More details on the definition of the quantum center, quantum calculations, and the protocols of classical simulations are provided in Materials and Methods below and in chapter 7. Here we discuss the results of our analysis.

6.4 Results

6.4.1 Free Energy Surfaces of Electron Transfer

The free energy surfaces of electron transfer $F_i(X) = -k_{\text{B}}T \ln[P_i(X)]$ (i = Ox,Red) follow from probabilities $P_i(X)$ calculated from classical trajectories with the quantum (Eq. (6.7)) or classical (Eq. (6.8)) definitions of the reaction coordinate X. Since our focus is on a half reaction, we do not consider a more complex problem of calculating the redox potential [87, 89] and focus solely on the reorganization energies. We first note that the quantum and classical algorithms are consistent with each other when the polarizability of the active site is turned off (Fig. 33A). In order to study the effect of the active site polarizability, we introduced scaling of the transition dipoles with the scaling factor ξ: $\boldsymbol{\mu}_{mk} \rightarrow \xi \boldsymbol{\mu}_{mk}$. The non-polarizable active site corresponds to $\xi = 0$ when coupling between the quantum states is turned off. Even in that limit, the algorithms of calculating X are still somewhat different in the quantum and classical cases since we use an expansion of the potential in the quantum Hamiltonian in Eq. (6.6), in contrast to a full set of atomic charges in the classical MD. However, the free energy surfaces obtained in the two approaches are consistent

(Fig. 33A), suggesting little effect on the charge distribution within the active site on the electron-transfer barrier. One can further examine the effect of charge distribution in the active site by assuming the complete localization of the charge on the heme iron, $\Delta q_{\mathrm{Fe}} = 1$. This extreme case and the calculation with distributed charge are compared in Table 2 and give consistent results.

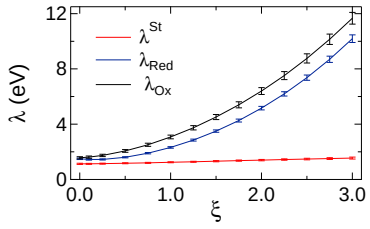

FIGURE 34: Reorganization energies λ and λ^{St} against the scaling factor altering the transition dipoles as $\boldsymbol{\mu}_{km} \rightarrow \xi \boldsymbol{\mu}_{km}$. The points are the results of calculations with error bars shown and the lines are regressions through the point to guide the eye.

This result might seem to be trivial since standard electrostatics suggests that the interaction of a point charge (localization) with the surrounding medium is equivalent to that of a charge uniformly spread over the conducting surface (delocalization). However, it is often suggested that delocalizing the electronic density of the active site is an optimization mechanism to reduce the reorganization energy [87]. While this mechanism is expected to lower the reorganization energy of localized skeletal vibrations [274, 268], we see little evidence for it altering the medium (protein and water) reorganization energy. It is also useful to keep in mind that most reactions relevant to biology's energy chains occur at relatively small magnitudes of the driving force $-\Delta G_0$ and, therefore, proceed in the normal region of electron transfer when quantum vibrations have essentially no effect on the activation barrier [245]. We instead argue here that the reorganization energy λ is maximized, and not minimized, for polarizable active sites. Since λ^{St} remains nearly unaffected, the activation

barrier in Eq. (6.2) can be reduced (Fig. 32B) due to a large value of the parameter κ_G (Eq. (6.4)).

6.4.2 Effect of Polarizability on the Reorganization Energy

The main goal of our analysis is to establish whether λ can significantly exceed $\lambda^{\rm St}$ when polarizability of the protein's active site is turned on. We first note that $\lambda \simeq \lambda^{\rm St}$, in accord with the standard Marcus theory [6], in the classical MD simulations (Table 2). This result is in agreement with previous simulations of this protein [271, 47], although we still find $\kappa_G > 1$. A reasonable agreement with the Marcus theory found here is not always shared by other redox proteins. We have found $\lambda > \lambda^{\rm St}$ for a number of redox proteins ($\kappa_G \simeq 1.7 - 3.2$ for electron transfer reactions in bacterial reaction centers [283, 13]). The reasons why cytochrome *c* falls on the lower end of κ_G values are important to understand. We discuss below the mechanism of compensation between the protein and water fluctuations lowering κ_G. Here we first look at how altering the physical model from a set of fixed atomic charges to a fluctuating charge distribution affects the activation barrier.

Table 2 and Fig. 34 summarize our findings. The reorganization energy λ is calculated according to Eq. (6.3), while $2\lambda^{\rm St} = \langle X \rangle_{\rm Red} - \langle X \rangle_{\rm Ox}$ is calculated from the average energy gaps in two redox states. The polarizability of the quantum center is continuously increased in Fig. 34 by scaling the ZINDO/S transition dipoles, $\boldsymbol{\mu}_{jk} \rightarrow \xi \boldsymbol{\mu}_{jk}$. The corresponding polarizabilities, calculated from Eq. (6.5), are listed in Table 2. As mentioned above, the polarizability significantly drops when fewer states are included and the statistics of the electron-transfer energy gap returns back to $\kappa_G \simeq 1$ of the Marcus theory (Table 7 in chapter 7).

TABLE 2: Reorganization energies (eV).[a]

Method	λ^{St}	λ_{Ox}	λ_{Red}	κ_G[b]
	Classical			
Classical MD	1.26	1.67	1.64	1.3
$\Delta q_{\mathrm{Fe}} = 1$[c]	1.13	1.57	1.50	1.4
α_{Red}, $\Delta\alpha$/Å^3 (ξ)[d]	Quantum Mechanical			
0.0, 0.0(0)	1.13	1.57	1.50	1.4
54, $-31(1)$	1.24	3.07	2.32	2.2
216, $-123(2)$	1.40	6.40	5.16	4.1
1, -3[e]	0.89	0.92	1.32	1.3

[a]The error bars are $\pm(0.04 - 0.06)$ eV for the classical calculations and $\pm(0.04 - 0.2)$ eV for the quantum calculations. More details can be found in Table 8 in chapter 7. [b]κ_G defined by Eq. (6.4). [c]Calculated from the variance of electrostatic potential at the heme iron thus assuming that charge is fully transferred to the heme iron in the half reaction. [d]The difference of the quantum center polarizability in the Ox and Red states calculated from Eq. (6.5); the number in the bracket is the factor scaling the transition dipole moments, $\boldsymbol{\mu}_{km} \to \xi\boldsymbol{\mu}_{km}$ (also see Fig. 34). [e]The results of simulations from Ref. 47, $\Delta\alpha$ is estimated from the present calculations based on $M = 10$.

Increasing the polarizability clearly separates $\lambda^{\mathrm{Ox/Red}}$ from λ^{St} (Fig. 34). According to Eq. (6.2), this should lower the activation energy, as is also seen from direct calculations shown in Fig. 33B. The main result of our calculations is that electron transfer involving polarizable active sites should proceed with lower activation barriers, without requiring more negative reaction free energy. Why this is the case can be seen from the following general arguments. The reversible work of creating a fluctuation of the bath field is a quadratic function of the field, $(\gamma/2)E_b^2$, in linear response. The negative free energy invested in polarizing the solute reduces this energy as $(\gamma - \alpha_i)E_b^2/2$. One expects, therefore, a smaller activation barrier to reach $X = 0$, as we observe. There is also a possibility of breaking the harmonic stability at $\gamma \simeq \alpha_i$, when water response passes through a spike [21]. One can anticipate that an electron-transfer enzyme can reach its lowest activation barrier in this regime.

6.4.3 Electrostatics of Protein and Water

The overall reorganization energy is a gauge of the strength of thermal fluctuations affecting the active site, with water and protein being its two main components. It is therefore of great mechanistic interest to understand what are the relative contributions of protein and water to fluctuations experienced by the active site. In contrast to some early suggestions that soluble proteins can effectively screen water from the active site and thus produce an effectively nonpolar environment, a number of recent simulations have clearly shown that water can never be neglected [89]. In fact, reorganization energies turn out to be comparable in magnitude to those traditionally reported for soluble synthetic donor-acceptor complexes [47, 275, 89, 15]. This upward revision of reorganization energies for protein electron transfer raises important mechanistic questions of how high efficiency of biological energy chains is achieved and how the motions of protein and water combine in the overall activation barrier.

One first needs to realize that there is a significant screening between the water and protein contributions to the electron-transfer energy gap. The water dipoles are oriented by the ionized surface residues of the protein to produce the electrostatic potential opposite in sign to the potential of the protein (Fig. 32D). As a result, the protein (p) and water (w) contributions to $X_0 = \langle X_w \rangle + \langle X_p \rangle$ are typically opposite in sign and similar in magnitude (Fig. 35A). The value of X_0 is the result of their incomplete compensation. The same physics applies to the variance of X, that is to the reorganization energy in Eq. (6.3).

The reorganization energy obtained from Eq. (6.3) becomes the sum of three components: protein, λ_p, water, λ_w, and a cross component, $\lambda_{pw} = \langle \delta X_p \delta X_w \rangle / (k_{\mathrm{B}} T)$, produced by correlated protein and water fluctuations. Consistent with the opposite signs of $\langle X_p \rangle$ and $\langle X_w \rangle$, the cross component is negative and compensates much larger individual pro-

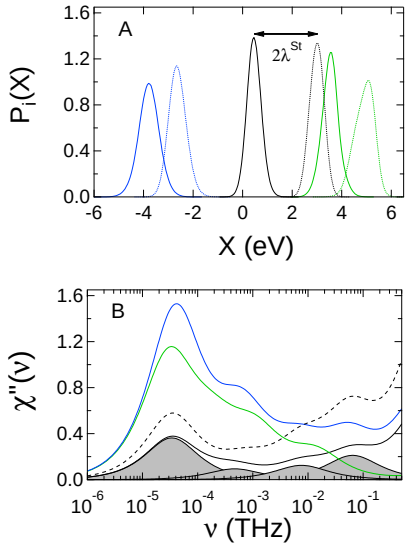

FIGURE 35: (A) Distribution of the electron-transfer coordinate (black) and its protein (green) and water (blue) parts (classical MD). The solid lines refer to the Ox state and the dashed lines refer to the Red state. The distance between the maxima of Red and Ox distributions is the Stokes shift, $2\lambda^{\mathrm{St}}$. (B) Loss function $\chi''(\nu)$, $2\pi\nu = \omega$ from protein (green), water (blue), and total (black) fluctuations of X. The solid black line shows the classical MD and the dashed line represents the QM/MD simulations at $\xi = 1$ (Table 2). The loss functions are normalized to give the corresponding reorganization component from $\int_0^\infty \chi''(\nu)d\nu/(\pi\nu)$. The shaded areas represent separate Debye relaxation processes used to fit the time correlation function $C_X(t)$ from classical MD simulations.

tein and water contributions [295]. For instance, for $\lambda_{\mathrm{Ox}} = 1.67$ eV listed in Table 2, one has $\lambda_p = 2.28$ eV, $\lambda_w = 3.39$ eV and $\lambda_{pw} = -4.0$ eV (see Table 8 in chapter 7).

6.4.4 Dynamics

The compensation between the protein and water fluctuations, displayed in the overall value of λ, shows itself even more dramatically in the Stokes shift dynamics of the energy gap variable $X(t)$. To study the dynamics, one has to turn to time correlation functions. The simplest one is the binary auto-correlation function $C_X(t) = \langle \delta X(t)\delta X(0)\rangle$, where $\delta X(t) = X(t) - X_0$. The $t = 0$ value of this correlation function is proportional to the

reorganization energy and one can anticipate that the physics of protein-water electrostatic compensation should extend into the time domain. It does, but we also find new dynamics pertinent to each component, which loses its prominence in the overall Stokes-shift dynamics due to the compensation effect.

Figure 35B shows the loss spectrum of the Stokes-shift dynamics. The loss function $\chi''(\omega)$ characterizes the rate of energy exchange, at a given frequency, between the active site and the thermal bath. It can be thought of as the rate of energy dissipation, at a given frequency, of some energy (e.g., photon) absorbed by the active site. The overall energy dissipated into surrounding is then given by integrating $\chi''(\omega)/\omega$ over all frequencies. In our calculations, $2k_{\rm B}T\chi''(\omega) = \omega C_X(\omega)$ is obtained from the frequency Fourier transform of the time correlation function [92].

The peaks of $\chi''(\omega)$ show the characteristic relaxation times of the modes coupled to the electron-transfer coordinate and their intensities represent the coupling strengths. The main striking observation from the plot is the presence of slow dynamics in both the protein and water components characterized by nearly equal relaxation times. These common dynamics, in the nanosecond time domain (see chapter 7), represent elastic modes altering the shape of the protein and simultaneously shifting the surface water molecules oriented by charged protein residues (Fig. 32D) [13]. The slow dynamics, however, nearly disappear in the overall $\chi''(\omega)$ due to a strong compensation (screening) between protein and water electrostatic contributions. It is this compensation that brings λ in a near accord with $\lambda^{\rm St}$ in the case of cytochrome *c*. The lack of this compensation makes the two reorganization energies deviate from each other, often significantly, for other proteins [13].

6.4.5 Mechanistic Aspects

Our QM/MD calculations produce the effective reorganization energy in Eq. (6.2) $\lambda^{\mathrm{r}} \simeq 0.57$ eV, $\lambda = (\lambda_{\mathrm{Ox}} + \lambda_{\mathrm{Red}})/2$ not far from ~ 0.6 eV viewed to be the average number from solution-based measurements [278]. One still has to be aware that the present simulations do not include polarizability of water and molecular groups of the protein [91]. The reorganization energies can potentially decrease if induced dipoles are included. The Pekar factor of dielectric models predicts a drop of λ by the factor $(\epsilon/\epsilon_\infty - 1)/(\epsilon - 1)$ when switching from a nonpolarizable to a polarizable dielectric; ϵ and ϵ_∞ are, correspondingly, the static and high-frequency dielectric constants of the thermal bath. However, simulations of model systems [296] show that this drop is an overestimate and the reorganization energy decreases only by $\sim 20\%$ upon the inclusion of induced dipoles. All these results apply, however, to the Marcus picture with $\lambda^{\mathrm{St}} = \lambda$. It is not currently clear how induced dipoles affect each distinct reorganization energy λ^{St} and λ. In addition, a drop in the magnitude of the reorganization energy upon including induced dipoles is mostly off-set by the reorganization energy arising from translational motions of induced dipoles (induction reorganization energy, see chapter 7).

As mentioned above, $\kappa_G > 1$ requires either incomplete sampling (ergodicity breaking), when some configurations are not accessible, or the breakdown of the Gaussian picture of the medium fluctuations and generally non-parabolic free energy surfaces. The latter scenario is indeed realized for donor-acceptor systems with polarizabilities different between the two electron-transfer states [119]. However, this scenario requires $\lambda_{\mathrm{Ox}} \neq \lambda_{\mathrm{Red}}$. This seems to be generally true for polarizable active sites (Table 2), but the extent of deviation is hard to estimate with limited sampling available from protein simulations. We also note that the dynamics of the energy gap $X(t)$ follow the Gaussian approximation. It is tested by

the ability to produce the fourth-order time correlation function of the energy gap in terms of the Stokes shift dynamics (Fig. S6 in chapter 7) [46]. Overall, we cannot clearly assign $\kappa_G > 1$ found in our simulations to non-Gaussian character of the energy gap fluctuations.

6.5 Conclusions

Energy chains of biology rely on a very short list of redox centers to transfer electrons [267]. They mostly include hemes of cytochromes, iron-sulfur clusters, and cupredoxins. One wonders if they are used to allow distinctly different electron-transfer mechanisms or have been selected based on similar mechanistic properties. A partial answer comes from biology. Cytochrome *c6*, a heme protein, is used interchangeably with plastocyanin, a cupredoxin, in cyanobacteria to catalytically connect photosystems I and II [268] (only plastocyanin is used in higher plants). Numerical simulations have shown that $\lambda \gg \lambda^{\mathrm{St}}$, attributed in this study to a high polarizability of the active site, is achieved in plastocyanin through insufficient compensation between water and protein electrostatics, which does not require a polarizable active site [283]. Does it mean that evolutionary pressure chooses redox proteins with $\lambda \gg \lambda^{\mathrm{St}}$, regardless of the mechanism producing the desired result? We do not have a definitive answer at this time. Studies of the effect of polarizability on electron transfer in all three classes of redox centers are required to address this question.

What our study convincingly shows is that increasing the polarizability of the protein's active site can significantly reduce the activation barrier of a catalytic reaction, electron transfer in this case. Interaction of atomic charges of the active site with the electrostatic potential of the surrounding medium is clearly an essential part of the enzyme's catalytic action [297]. It might be true as well that not only the distribution of molecular charge, but

also its ability to deform in the external field (polarizability) is an important tool employed by nature to catalyze biological reactions.

Chapter 7

SIMULATION AND ANALYSIS PROTOCOLS

7.1 Hard Sphere and Kihara (Non-polarizable) Solutes in Water

Monte Carlo (MC) and molecular dynamics (MD) simulations were carried out in the configuration of a single solute in the cubic box consisting of TIP3P water molecules[80]. All MC simulations were performed at 298 K in a box length of 40 Å consisting of TIP3P water molecules for two types of solutes : a hard sphere (HS) solute and a modification of the HS potential in the Kihara form that includes a Lennard-Jones layer outside of the HS core[174]. The Kihara potential thus has the form

$$U_{0s}(r) = 4\epsilon_{0\mathrm{S}} \left[\left(\frac{\sigma_{0\mathrm{s}}}{r - R_{\mathrm{HS}}} \right)^{12} - \left(\frac{\sigma_{0\mathrm{s}}}{r - R_{\mathrm{HS}}} \right)^{6} \right], \tag{7.1}$$

where "0" and "s" stand for the solute and solvent, respectively, and r is the distance between the solute center and the oxygen of water. Further, R_{HS} is the radius of the HS core and ϵ_{0s} is the solute-solvent LJ energy. The ϵ_{0s} values of 3.7 and 8.0 kJ/mol and a $\sigma_{0\mathrm{S}} = 3$ Å were used in the simulations. The solute size was varied by changing the radius of the HS core $R_{\mathrm{HS}} = 1$, 2, 3, 4, 5, 6, and 7.5 Å. For the HS solute, the size of the HS core corresponds to the distance of the closest approach of water's oxygen R_{0s}. This distance was also varied in the simulations in the range $R_{0s} = 2$–15 Å.

We have also performed NVT MC simulations of single-charged ($|q| = 1$) HS cations and anions in TIP3P water (see section 7.1.4). The ion sizes were varied in the range of 2–10 Å. All simulations were performed with the same simulation protocol as for the neutral solutes: Ewald sums were used to correct for the cutoff of the electrostatic interactions. The Ewald convergence parameter of $6.4/L$ was used for the box of size L. The value of

$k_{\text{max}} = 7$ was used for the reciprocal-space calculations, and all real-space electrostatic interactions in the simulation box were calculated. For the LJ potential, a cutoff distance of 14 Å was used, and tail corrections were added to account for the long-range contributions. Each simulation consisted of 5×10^4 equilibration MC cycles and $(4-6) \times 10^5$ production cycles (each cycle consists of N trial moves, where N is the number of molecules in the system). Translational and rotational trial moves were assigned the probabilities of 0.6 and 0.4, respectively.

Molecular dynamics (MD) simulations were carried out at 298 K in the configuration of a single Kihara solute in the cubic box consisting of $6180 - 6650$ TIP3P charmm water molecules with an original water density of 1.0 g/cm^3[80]. Simulations were performed in a box length of 60 Å. The ϵ_{0s} values of 3.7 kJ/mol and a $\sigma_{0\text{S}} = 3$ Å were used in the simulations. The solute size was varied by changing the radius of the HS core $R_{\text{HS}} = 2$, 5, 7.5, 10, and 15 Å. We also performed MD simulations of single-charged ($q = 1$) Kihara cations and anions with $R_{\text{HS}} = 7.5$ Å in TIP3P water. All simulations were performed with the same simulation protocol as for the neutral solutes.

The NAMD 2.10[175] software program was used for all MD simulations. An energy minimization was performed, followed by 5 ns NVT equilibration. Production runs were completed for 200 ns in the NVT ensemble and the time step of 2 fs. The integration used a Langevin thermostat with a Langevin coupling coefficient of 5 ps^{-1}. The hydrogen-oxygen and hydrogen-hydrogen distances in waters were constrained with the non-iterative SETTLE algorithm to make the water molecules completely rigid. We also used a cutoff distance of 12 Å for LJ and electrostatic calculations, with a smoothing function applied at 10 Å, and a pair list distance of 14 Å. Long-range electrostatics interactions were calculated with the smooth particle mesh Ewald (PME) method and a grid spacing of 1 Å. The

electrostatic potential at the center of the solute was obtained with the Ewald summation method.

7.1.1 Finite Size Effects on the Interface Susceptibility Function

The exact interface susceptibility function is given by

$$\chi_0(r) = -4\pi\beta r^2 \langle \delta P_r(r) \delta\phi \rangle \tag{7.2}$$

Here, ϕ is the electrostatic potential produced by the solvent at the center of the solute and $P_r = \hat{\mathbf{r}} \cdot \mathbf{P}$, $\hat{\mathbf{r}} = \mathbf{r}/r$, where $\mathbf{P}$ is the polarization density.

In this section, finite size effects on the interface susceptibility function are investigated. These effects may lead to significant errors in the estimation of the interface dielectric constant. We present the results which show that these finite-size effects are expected to be negligible when the ratio of the simulation box length to the diameter of the solute is relatively large, i.e., about three. Kihara solutes with $R_{\text{HS}} = 2$ and 5 Å were solvated in simulation boxes with lengths of 38.5 Å and 50 Å , respectively, where an original water density was 1.0 g/cm^3. The same simulation protocol as presented in section 7.1 above was used for these two simulations. Figure 36 compares the exact interface susceptibility for two different Kihara solutes with two different box lengths each. As can be seen, the finite size effects for these system sizes are almost negligible.

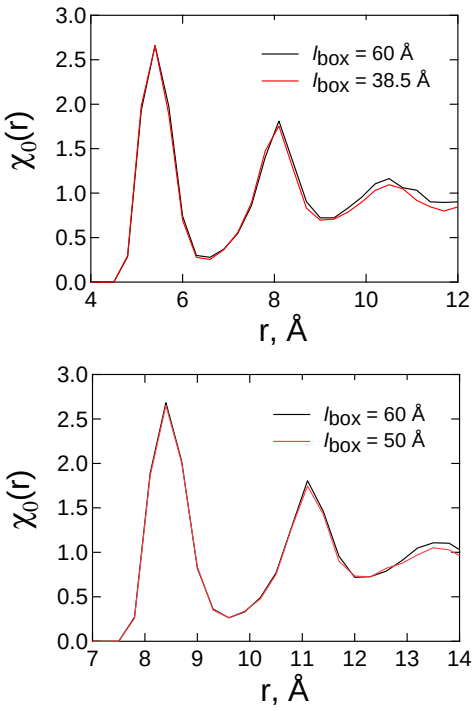

FIGURE 36: The exact interface susceptibility function as defined by Eq. (7.2) for two different sizes of Kihara solutes solvated in simulation boxes of different lengths. (Top) Comparison of the interface susceptibility for Kihara solute with $R_{\mathrm{HS}} = 2$ Å simulated in simulation boxes of 38.5 Å and 60 Å . (Bottom) Comparison of the interface susceptibility for Kihara solute with $R_{\mathrm{HS}} = 5$ Å simulated in simulation boxes of 50 Å and 60 Å .

7.1.2 Electrostatic Potential Inside Cavity

Figure 37 shows the electrostatic potential of TIP3P water inside the spherical solute carrying no charge. The results for the HS cores of varying radius and KH cores with two values of the LJ energy ϵ_{LJ} (Eq. (7.1)) are shown. The positive sign of the potential is consistent with previous simulations of uncharged HS[138] and LJ[124] solutes.

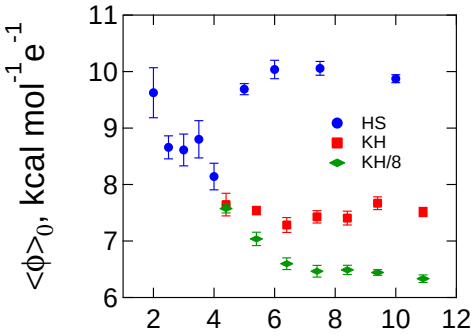

FIGURE 37: The electrostatic potential $\langle\phi\rangle_0$ inside hard-sphere (HS) and Kihara (KH) solutes of varying size; $\epsilon_{\mathrm{LJ}} = 3.7$ (KH) and 8.0 (KH/8) kJ/mol are used for the KH potential.

7.1.3 Neutral, Cation, and Anion Kihara Solutes

As shown in section 2.3.2, we did not observe significant differences between the interface dielectric constants of neutral, anion, and cation Kihara solutes with $R_{\mathrm{HS}} = 5$ Å. First, we show in Figure 38 that the difference in the exact interface susceptibilities for these solutes is also small. Next, we use pair distribution functions (PDFs) to provide more detailed information about the structure of water around these solutes.

The PDFs are defined as

$$g^{l}_{0\mathrm{S}}(r) = (V/N)\left\langle \sum_{j} P_l(\cos\theta_{mj})\delta(r_j - r)\right\rangle \tag{7.3}$$

where θ_{mj} is the angle formed by the dipole moment vector of the water molecule and the vector between the center of the solute and the water center of mass (COM), $r_{0\vec{\mathrm{COM}}}$, where $r_{0\vec{\mathrm{COM}}}$ points in the direction of COM. V and N are the system volume and the number of particles, respectively. Note that the zeroth-order distribution function is the standard radial distribution function (RDF), i.e., $g^0_{0S}(r) = g_{0S}(r)$.

The RDFs of the neutral, cation, and anion Kihara solutes are shown in Figure 38. As can be seen, the RDFs are almost the same and are characterized by a first peak centered

around 11.1 Å with a height of 4.35. This is followed by a minimum around 12.5 Å and a second peak around 13.8 Å.

In addition, one can use the first and second order solute-COM distribution functions as defined in Eq. (7.3) to characterize the orientational structures of water around the Kihara solutes. Figure 38 shows the difference in the first order distribution functions for the neutral, cation, and anion Kihara solutes. The positive values of the first order distribution function around 11.1 Å indicate that on average water dipoles preferentially orient toward the bulk. Our data shows that this situation is more pronounced for cations. We also found that the second order distribution functions are negative around 11.1 Å showing that a considerable number water dipoles are tangential to the radial projection (data not shown). Finally, we observed that the variances of the electrostatic potentials at the centers of cation, anion, and neutral Kihara solutes are the same within the statistical uncertainties (see table 3).

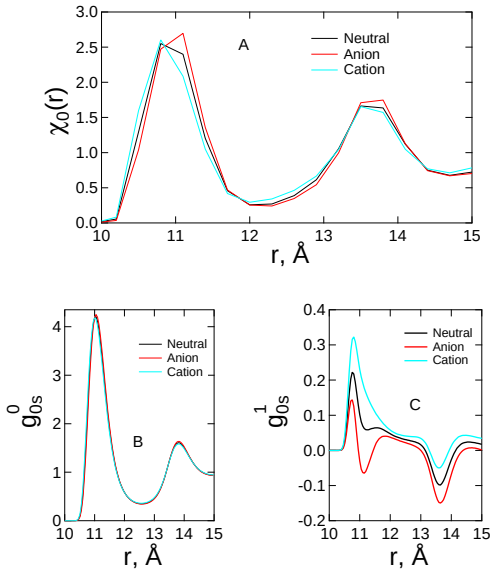

FIGURE 38: (A) The exact interface susceptibility functions for neutral, cation, and anion Kihara solutes with $R_{\mathrm{HS}} = 5$ Å (B) RDFs (C) The first order solute-COM distribution functions

TABLE 3: The variances of electrostatic potentials at the centers of cation, anion, and neutral Kihara solutes with $R_{\mathrm{HS}} = 5$ Å . β is inverse temperature and e is the elementary charge. The uncertainties are standard deviations.

Solute	$\mathrm{e}\beta\langle\delta\phi^2\rangle$ [eV/e]
Neutral	0.800 ± 0.003
Anion	0.801 ± 0.002
Cation	0.800 ± 0.003

7.1.4 HS Cations and Anions

Figure 39 shows the density profile of water around the HS cations and anions with changing the distance of the closest approach of water's oxygen $R_{0s} = r_{\mathrm{max}}$. The introduction of the ionic charge into the HS core results in an attraction to water multipoles, which, however, becomes weaker with increasing solute size. The weakening of solute-solvent attractions lowers water's density at the ion's surface, although this dewetting is less pronounced compared to the HS solute without charge (shown in Figure 4 in chapter 2).

Figure 40 shows $r_{\mathrm{max}}\chi$ vs r_{max} for anions and cations of varying size. Here one notes that the solvation free energy is more negative for anions compared to cations of the same size. The explanation of this well-established phenomenology is sought in terms of denser hydration shells of anions compared to cations. The result of this difference in the free energy is a smaller effective cavity radius for anions compared to cations.

7.2 Hard Sphere and Lennard-Jones Polarizable Solutes in Water

Hard sphere (HS) and Lennard Jones (LJ) potentials are used to model the solute-solvent interactions. The dipole moment at the center of the solute is created by placing

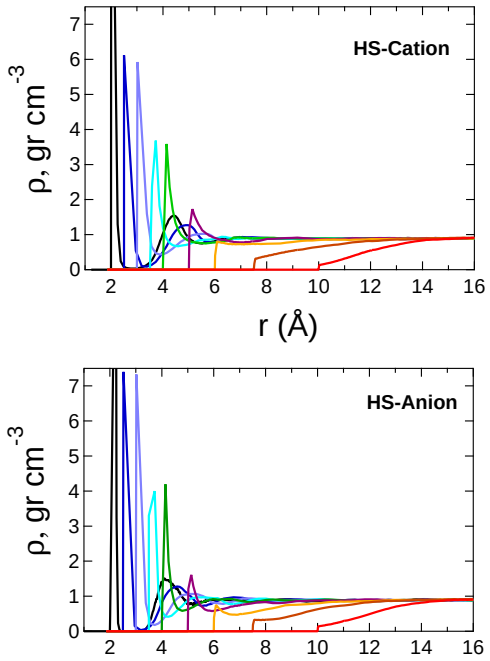

FIGURE 39: Water density profiles around the hard-sphere cations (HS-Cation) and hard-sphere anions (HS-anion) as a function of growing size of the solute hard-sphere core (R_{0s}). The density profiles are calculated from MC simulations with a single solute in the simulation cell containing TIP3P water at 298 K.

two opposite charges $+q$ and $-q$ at the distance d from the solute center. The distance between the charges is $2d$ and the dipole moment of the solute is varied by changing the magnitude of q, such that $q = m/(9.6d)$, where m is in units of D and d is in Å. The details of the simulation protocol are slightly different in Monte Carlo (MC) and molecular dynamics (MD) simulations and we discuss them separately.

7.2.1 Monte Carlo Simulations

The total potential energy is the sum of solvent-solvent, U_{ss}, and solute-solvent, U_{0s}, components in MC simulations. The solvent-solvent part is the sum of LJ and Coulomb (C) interactions defined for the TIP3P force-field water[80] $U_{ss} = U_{ss}^{\mathrm{LJ}} + U_{ss}^{\mathrm{C}}$. The

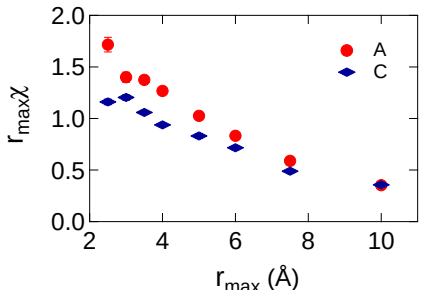

FIGURE 40: Reduced linear susceptibility $r_{\max}\chi$ for cation (C) and anion (A) HS solutes in TIP3P water at 298 K. The solvation susceptibility χ is calculated from the variance of the electrostatic potential at the position of the ion at the center of the HS solute as $\chi = \beta\langle(\delta\phi)^2\rangle_0$. For HS solutes, the position of the first maximum $r_{\max}$ coincides with the distance of the closest approach of water's oxygen to the solute's center R_{0s}.

solute-solvent part of the Hamiltonian includes the Coulomb interactions of the permanent charges, $U_{0s}^{\rm C}$, and the free energy of polarizing the solute by the electric field of the solvent E given as $-(1/2)\alpha E^2$ (isotropic polarizability α). The repulsive part of the solute-solvent potential, $U_{0s}^{\rm HS/LJ}$, is modeled by either the HS core or by the solute-solvent LJ potential. The overall solute-solvent potential thus becomes

$$U_{0s} = U_{0s}^{\rm HS/LJ} + U_{0s}^{\rm C} - (\alpha/2)E^2. \tag{7.4}$$

The radius of the HS solute was $R_{\rm HS} = 4.15$ Å (the distance between the centers of the HS solute and oxygen of water). The LJ solute had a LJ 12–6 site with the LJ diameter $\sigma_{\rm LJ} = 6$ Å and the LJ energy $\epsilon_{\rm LJ} = 280$ K. The separation between the positive and negative charges forming the solute dipole was $d = 0.05$ Å.

MC simulations were done in the canonical ensemble with 1000 TIP3P water molecules and one polar-polarizable HS or LJ solute at $T = 298$ K and the water density of 0.995 g/cm^3. Each simulation consisted of $(0.8 - 1) \times 10^5$ equilibration cycles and $(2 - 5) \times 10^5$ production cycles (each cycle involves N trial moves, where N is the number of molecules in the system). Success probabilities of 0.6 and 0.4 were adopted for translations and

rotations, respectively. The probabilities for selecting a water molecule and the solute were set equal to 0.85 and 0.15, respectively. A cutoff distance of 12 Å was used for the LJ interactions, and tail corrections were applied to incorporate long-range contributions. Periodic boundary conditions and Ewald sums were used to calculate both the solvent-solvent and solute-solvent Coulomb interactions and for the electric field E at the center of the spherical solute. The Ewald convergence parameter was 0.21 Å^{-1} and the reciprocal space maximum wavevector was set at $k_{\max} = 7$.

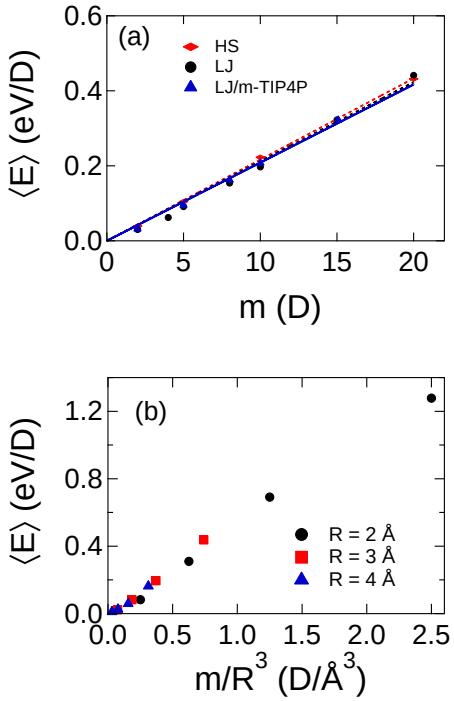

FIGURE 41: Panel (a): Onsager reaction field for the HS and LJ solutes with varying dipole moments and zero polarizability. The dashed lines show the linear fits yielding κ values of 28.7 Å^3 (HS) and 29.6 Å^3 (LJ) in TIP3P water; the value of κ in m-TIP4P water is 29.9 Å^3. The statistical errors are smaller than symbol sizes. The black and red points and lines refer to simulations in TIP3P water, the blue points and the blue dashed line refer to the modified TIP4P (m-TIP4P) water. Panel (b): MC results for the Onsager reaction field for LJ solutes in m-TIP4P water with varying solute size and dipole moment. The reaction field is plotted against m/R^3, where $R = \sigma_{\rm LJ}/2$.

Different sizes of the HS and LJ solutes were adjusted to provide nearly equal susceptibilities of TIP3P water to the solute dipole. The average solvent field $\langle E \rangle$ caused by the solute dipole m (Onsager reaction field[65]) was calculated for different magnitudes of the non-polarizable solute ($\alpha = 0$). In the linear response, $\langle E \rangle = \kappa^{-1} m$ and κ was calculated as the linear slope of $\langle E \rangle$ vs m (Figure 41a). The dipole moment of the solute was fixed at $m = 5$ D in the simulations with $\alpha > 0$.

In addition to simulations with fixed solute sizes, the LJ diameter σ_{LJ} of the LJ solute was varied to test the expected scaling of the solvation susceptibility with the solute radius R: $\chi \propto R^{-3}$. This set of MC simulations employed $\sigma_{\mathrm{LJ}} = 4$, 6, and 8 Å with 1840–1900 m-TIP4P waters in the simulation box. Both σ_{LJ} and the magnitude of the dipole moment were varied in these simulations carried out for 2×10^4 MC cycles. Figure 41b shows the collapse of all simulation data for the average solvent field plotted against m/R^3, where $R = \sigma_{\mathrm{LJ}}/2$. The expected scaling is confirmed.

7.2.1.1 Performance of MC Codes

The MC codes are developed in the Matyushov group. Both are parallelized with distributed memory, using the Message Passing Interface (MPI) standard for communication. For all simulations of polar-polarizable solutes in water, the Ewald summation method involves the triple sum over $|\mathbf{k}|$, molecule i, and molecule j. The electric field and electrostatic potential are calculated accordingly. The hot spots are the corresponding DO loops in the Ewald sum method and cyclic distributions are used for parallelization, where the iterations are assigned to processes in a round-robin fashion. The code performance for simulations of the polar-polarizable solute on the Stampede supercomputer at Texas is reported in Figure 42.

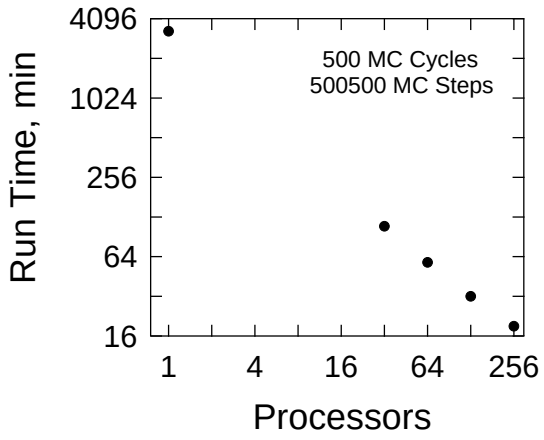

FIGURE 42: Performance scaling of the MC code for simulations of polar-polarizable solutes in water.

7.2.2 Molecular Dynamics Simulations

The kinetic energy of the solute in MD simulations is determined by the masses of the solute sites: $m_{\rm LJ} = 39.6$ amu, $m_+ = 1$ amu, $m_- = 1$ amu, and $m_{\rm D} = 0.4$ amu, where "D" denotes the Drude oscillator site used to model the solute polarizability. The potential energy is the sum of the LJ, $U_{\rm LJ}$, electrostatic, $U_{\rm el}$, and bonded, U_b, interactions and, in addition, the elastic energy of the harmonic Drude particle

$$U = \tfrac{1}{2} k_{\rm D} r_{\rm D}^2 + U_b + U_{\rm LJ} + U_{\rm el}. \tag{7.5}$$

The non-bonded interactions include the solute-solvent LJ and electrostatic interactions, $U_{\rm LJ} + U_{\rm el}$. The bonded interactions are harmonic in bond stretches and the bending angle $\theta = +{\rm LJ}-$, where "$+$" and "$-$" denote, respectively, the positive and negative sites. The resulting potential energy of the bonded interactions has the form

$$U_b = \tfrac{1}{2} \sum_{\rm bonds} k_b (r - r_{\rm eq})^2 + \tfrac{1}{2} k_\theta (\theta - \theta_{\rm eq})^2. \tag{7.6}$$

The force constants in Eqs. (7.5) and (7.6) are: $k_{\rm D} = 1000$ kcal mol^{-1} Å^{-2}, $k_{\rm LJ+} = k_{\rm LJ-} = k_{+-} = 3000$ kcal mol^{-1} Å^{-2}, $k_\theta = 500$ kcal mol^{-1} rad^{-2}. The equilibrium bond lengths and the angle are: $r_{\rm eq}({\rm LJ}+) = r_{\rm eq}({\rm LJ}-) = 1.5$ Å, $r_{\rm eq}(+-) = 3$ Å, $\theta_{\rm eq} = 180^o$.

The polarizability of the solute is modeled by a Drude particle with charge $q_{\rm D}$ attached to the center of the solute by a harmonic spring. Isotropic polarizability of the solute $\alpha = q_{\rm D}^2/k_{\rm D}$ is achieved by allowing isotropic motions of the Drude particle constrained only by the potential energy penalty of stretching the spring. The magnitude of $q_{\rm D}$ was changed to produce different values of α, i.e., $q_{\rm D} = (k_{\rm D}\alpha/332.1)^{1/2}$, where $k_{\rm D}$ and α are in units of kcal mol^{-1} Å^{-2} and Å^3, respectively.

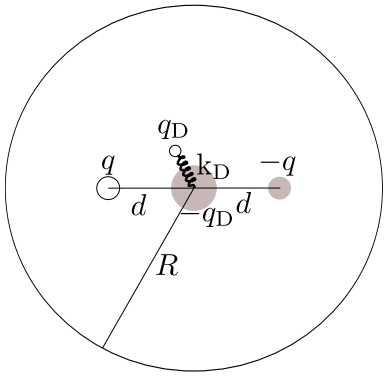

FIGURE 43: Polar-polarizable solute used in molecular dynamics simulations.

The LJ site had $\sigma_{\rm LJ} = 6$ Å and the solute-water interaction energy of $\epsilon_{\rm LJ} = 280$ K. Two other interaction sites, placed symmetrically relative to the center at the distance of $d = 1.5$ Å, carried opposite charges of $+q$ and $-q$ and a mass of 1 atomic mass unit (amu). A large force constant was used to keep the positions of these two interaction sites fixed.

The solvent model used in MD simulations is closely related to TIP4P[80] and SWM4-DP water models. The geometry of water is fixed and four interaction sites define the force field: one oxygen, two hydrogens, and an additional massless particle M located at a fixed distance $l_{\rm OM}$ along the bisector of the HOH angle (Table 4). A classical Drude oscillator is

attached by a harmonic spring with the force constant of k_{D} to the oxygen site. Its mass is set to 0.4 amu and the mass of the oxygen is set to 15.5994 amu, such that the total mass of the oxygen-Drude pair is equal to the oxygen mass of 15.9994 amu. However, in our simulations, the Drude particle was neutral and, therefore, did not introduce any solvent polarizability. This dummy particle was used to comply with the requirement, imposed by the NAMD 2.9 software program, to incorporate a Drude oscillator into the solvent model when performing molecular dynamics (MD) simulations of a Drude-polarizable solute.

TABLE 4: Parameters for the modified TIP4P (m-TIP4P) water model, compared with the TIP4P and SWM4-DP models.

Parameter	TIP4P	SWM4-DP	m-TIP4P
l_{OH}, Å	0.957	0.957	0.957
$\theta^{\circ}_{\mathrm{HOH}}$	104.52	104.52	104.52
l_{OM}, Å	0.150	0.238	0.238
$q_{\mathrm{O}}/\lvert e\rvert$	0	-1.772	0
$q_{\mathrm{M}}/\lvert e\rvert$	-1.040	-1.108	-1.040
$q_{\mathrm{H}}/\lvert e\rvert$	0.520	0.554	0.520
$q_{\mathrm{D}}/\lvert e\rvert$		1.77	0
k_{D}, kcal mol^{-1} Å^{-2}		1000	1000
ϵ_{O}, kcal mol^{-1}	0.1525	0.2057	0.2057
σ_{O}, Å	3.154	3.180	3.180

The molecular dynamics program NAMD 2.9 was used for MD simulations. The solute was solvated with 1000 water molecules and an energy minimization was performed for $100,000$ steps. The system was then heated to 300 K by 50 K increments, each evolving for $100,000$ steps. Next, a 5 ns NPT simulation at 1 atm and 300 K was performed by using the Langevin barostat and thermostat. This was followed by 5 ns NVT equilibration. Production runs were done for 50 ns in the NVT ensemble at 300 K and the time step of 1 fs.

The integration used a dual Langevin thermostat to freeze the Drude oscillators at 1 K, while maintaining the other degrees of freedom at 300 K. Cooling the polarization degrees of freedom with a separate thermostat is based on the fact that the equilibrium and diffusion properties of cold dipoles are independent of the value of the dipole inertia parameter as long as it is sufficiently small[298]. The temperature for Drude oscillators should be small enough to leave almost no kinetic energy to the Drude-atom vibrations, yet large enough to allow the Drude particles to readjust to the room-temperature motion of the atoms.

The hydrogen-oxygen and hydrogen-hydrogen distances in waters were constrained with the non-iterative SETTLE algorithm to make the water molecules completely rigid. We also used a box length of 31.95 Å, a cutoff distance of 12 Å for LJ and electrostatic calculations with a smoothing function applied at 10 Å, and a pair list distance of 14 Å. Long-range electrostatics interactions were calculated with the smooth particle mesh Ewald (PME) method and a grid spacing of 1 Å.

7.2.3 Analysis of Interfacial Structures

The solute-solvent distribution functions are defined as

$$g_{0\mathrm{s}}^{\ell}(r) = \rho^{-1} \left\langle \sum_j P_\ell(\hat{\mathbf{m}}_j \cdot \hat{\mathbf{r}}_j)\delta(\mathbf{r}_j - \mathbf{r}) \right\rangle, \tag{7.7}$$

where ρ is the number density of bulk water. Here, $\hat{\mathbf{m}}_j$ is the unit vector of water's dipole moment and $P_\ell(x)$ is the Legendre polynomial of order ℓ. In this notation, $g_{0s}^{0}(r) = g_{0s}(r)$ becomes the standard radial distribution function (RDF).

The solid lines in Figure 44a show the solute-oxygen RDFs of the HS solute with the HS radius of $R_{\mathrm{HS}} = 4.15$ Å and the dipole moment of 5 D. The dashed lines report the solute-hydrogen RDFs. The first solute-hydrogen peak shifts, with increasing α, to

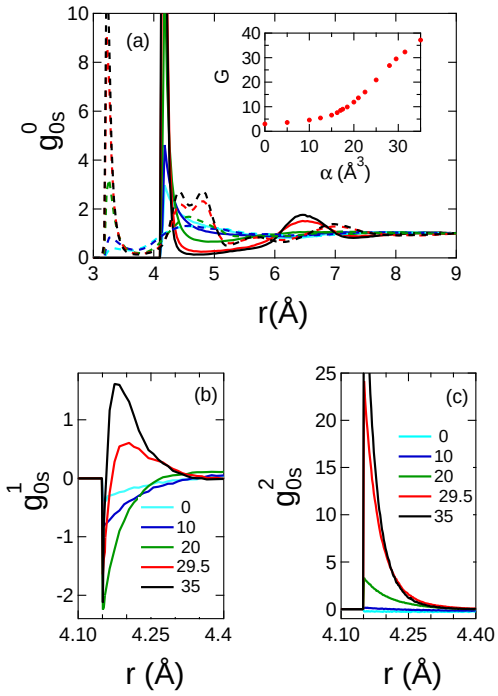

FIGURE 44: Results of Monte Carlo simulations of the HS solute with the HS radius of $R_{\rm HS} = 4.15$ Å and the dipole moment of 5 D dissolved in TIP3P water at 298 K and the density of 0.995 gr/cm^3. (a) Solute-oxygen (solid lines) and solute-hydrogen (dashed lines) RDFs with different colors marking the values of the solute polarizability: 0 (cyan), 10 (blue), 20 (green), 29.5 (red), 35 (black). The inset depicts the height of the RDF's first peak. The solute-oxygen first order (b) and second order (c) orientational functions (Eq. (7.7)) are for the same solutes as in (a).

distances shorter than the first solute-oxygen peak. This suggests that the water molecules of the first hydration shell flip their hydrogen atoms from an outward orientation at lower α to an inward orientation at higher α.

The RDF peaks can be quite sharp. Therefore, making use of a reasonably coarse grid tends to significantly reduce the peak height. On the other hand, a very small grid does not produce a sufficient statistical accuracy. Therefore, the height of the first solute-water maximum G was calculated by finding a compromise grid. Values of G at high polarizabilities show a collapse of the first hydration layer (Figure 44a).

The first- and second-order orientational distribution functions of water around the HS

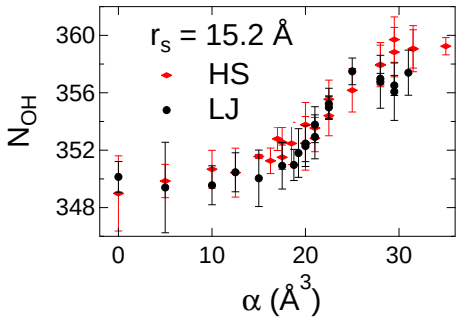

FIGURE 45: The number of unsatisfied hydrogen bonds of TIP3P water within the shell of radius 15.2 Å from the center of the solute.

solute are shown in Figures 44b-c. They also confirm preferential dipolar ordering of water molecules in the first hydration layer.

To identify unsatisfied hydrogen bonds, the Wernet *et al.*[192] definition of hydrogen bonds is used. It requires the O$\cdots$O distance, R (Å), to be bounded by a quadratic function of the H $-$ O$\cdots$O angle, θ (degrees), $R(\theta) \leq -0.00044\theta^2 + 3.3$. Making use of this definition, the number of water molecules that donate their hydrogens in hydrogen bonds is obtained. Finally, the number of unsatisfied hydrogen bonds is calculated from the numbers of zero- and single-donors. Figure 45 shows the number of unsatisfied hydrogen bonds in a spherical region of the radius $R = 15.2$ Å from the center of the solute. The calculations are done for different values of α for both the HS and LJ solutes.

7.2.4 Landau Functional and Solvation Free Energy

The average solvent field at the solute center (Onsager reaction field) obtained from MC simulations was fitted to the Landau functional in the form

$$\mathcal{F}[E] = -mE + (\kappa/2)E^2 - (\alpha/2)E^2 + G[E] \tag{7.8}$$

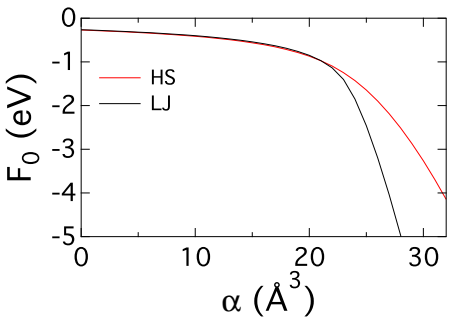

FIGURE 46: Solvation free energy of dipolar HS and LJ solutes vs the solute polarizability. The free energies are calculated by minimizing the Landau functional in the electric field (see main text for more detail).

where $G[E] = -(b/4)E^4 + (c/6)E^6$ was used in the fit. The average field is obtained from the condition $\mathcal{F}'[E] = 0$. The fit of $\langle E \rangle$ vs α shown in Figure 13 in chapter 3 required $b_{\rm LJ} = 11.6$ D^4/eV^3, $c_{\rm LJ} = 11.0$ D^6/eV^5 and $b_{\rm HS} = -1.9$ D^4/eV^3, $c_{\rm HS} = 30.2$ D^6/eV^5.

The equilibrium free energy, F_0, of HS and LJ solutes is obtained by minimizing the Landau functional in terms of the solvent electric field (Eq. (7.8)). Figure 46 shows the free energy as a function of polarizability indicating that $F_0(\alpha)$ remains uniform, despite a clear maximum of the field variance as a function of polarizability.

7.3 Q-model & Non-Gaussian Dynamics: Analysis of Time Correlation Functions

Here we present additional results and analysis of chapter 5 regarding the time correlation function of the electric field of the solvent at the center of the solute

$$S_{\|}(t) = \langle (\delta E_{\|})^2 \rangle^{-1} \langle \delta E_{\|}(t) \cdot \delta E_{\|}(0) \rangle \tag{7.9}$$

and the corresponding correlation function of the transition frequency

$$S_2(t) = \langle \delta\Omega(t)\delta\Omega(0) \rangle / \langle (\delta\Omega)^2 \rangle \tag{7.10}$$

Both time correlation functions were fitted to a function combining the initial Gaussian decay, a damped harmonic oscillator, and two exponential decay functions[299]

$$\phi(t) = A_g e^{-\omega_g^2 t^2/2} + A_h e^{-t/\tau_h} \cos \omega_h t + \sum_{i=1}^{2} B_i e^{-\alpha_i t} \tag{7.11}$$

The expansion of $\phi(t)$ in powers of t contains only even terms. Therefore, all odd time derivatives of $\phi(t)$ at $t = 0$ must vanish[60]. We therefore impose the following restrictions on the fitting parameters in eq (7.11): $\phi(0) = 1$ and $\dot{\phi}_s(0) = 0$. With these constraints, the normalized time correlation function takes the form

$$\phi(t) = e^{-\omega_g^2 t^2/2} + \sum_{i=1}^{N_e} B_i g_i(t) \tag{7.12}$$

where

$$g_i(t) = e^{-\alpha_i t} + (\alpha_i \tau_h - 1)\, e^{-\omega_g^2 t^2/2} - \alpha_i \tau_h e^{-t/\tau_h} \cos \omega_h t \tag{7.13}$$

The results of fitting $S_{\|}(t)$ and $S_2(t)$ to eq (7.12) are listed in Table 5.

TABLE 5: Fitting coefficients of the fits of $S_{\|}(t)$ and $S_2(t)$ to Eq. (7.12). Relaxation times $\tau_i = \alpha_i^{-1}$ are in fs, the frequencies are in fs^{-1}.

m_0, D	α_0, Å^3	b_1	b_2	τ_1	τ_2	ω_G	ω_h	τ_h
Field correlation function, $S_{\|}(t)$								
5	0	0.88	0.068	1983	131	0.139	0.21	23.5
5	5	0.90	0.063	2795	158	0.131	0.20	23.6
10	0	0.97	0.016	11859	144	0.089	4.66	5.1
10	15	0.98	0.011	27164	243	0.089	23.26	4.6
Frequency correlation function, $S_2(t)$								
5	0	0.51	0.13	130	438	0.125	0.20	27.8
5	5	0.54	0.17	131	447	0.125	0.20	25.3
10	0	0.53	0.12	140	580	0.120	0.19	27.2
10	15	0.44	0.48	83	591	0.157	0.21	14.9

Figure 47 shows $S_{\|}(t)$ calculated at different values of the solute polarizability α_{0i} and two values of the solute dipole m_{0i}. We observe the slowing down of the electric

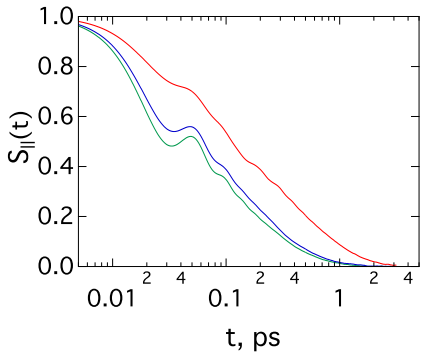

FIGURE 47: Time autocorrelation function $S_{\|}(t)$ (Eq. (7.9)) of the projection $E_{\|}(t)$ of the solvent electric field on the direction of the solute dipole moment. The lines mark the following configurations of the solute: $m_0 = 5$ D, $\alpha_0 = 0$ (green), $m_0 = 5$ D, $\alpha_0 = 5$ Å^3 (blue), and $m_0 = 10$ D, $\alpha_0 = 15$ Å^3 (red).

field relaxation as the solute polarizability increases. As discussed in the main text, and elsewhere[265], the main reason for this change is the softening of the force constant of harmonic fluctuations of the solvent field. This effect is not, however, a part of the dynamical Q-model, which instead assumes the dynamics of the nuclear variable $q(t)$ unaffected by the solute.

In order to study the non-Gaussian character of the transition frequency dynamics, higher order correlation functions $S_3(t)$, $S_4(t)$, and $S_\sigma(t)$ (see main text) were calculated from MD simulations. The function $S_3(t)$ enters the width time evolution function $S_\sigma(t)$, which recovers its Gaussian form at $S_3(t) = 0$ (eq 15 in the main text). Correspondingly, the Gaussian approximation for the correlation $S_4(t)$ function is given by eq 21 in the main text.

Time correlation functions $S_4(t)$ and $S_\sigma(t)$ calculated from MD simulations are shown in the upper and lower panels of Figure 48. The solid lines in the upper panel of Figure 48 are the fourth order correlation functions obtained directly from simulations. The dashed lines in the same figure, which are nearly indistinguishable from the solid lines on the scale

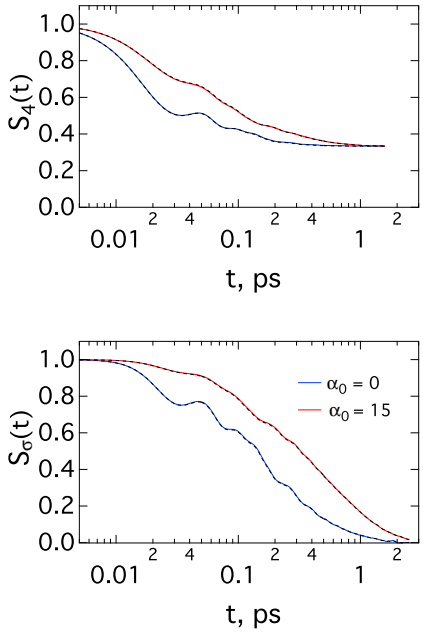

FIGURE 48: $S_4(t)$ and $S_\sigma(t)$ calculated for polarizable and non-polarizable solutes from MD simulations (solid lines) and from their Gaussian approximations (points) by using the second-order correlation function $S_2(t)$ from MD simulations; $m_0 = 10$ D.

of the plot, are the corresponding Gaussian approximations. A similar situation is seen for $S_\sigma(t)$ in the lower panel of Figure 48: the solid lines obtained with account for the skewness function $S_3(t)$ in eq 15 in the main text are indistinguishable from the dotted lines obtained by putting $S_3(t) = 0$ in the same equation. As explained in detail in the main text, these results is a consequence of scaling of non-Gaussian contributions to $S_\sigma(t)$ and to $S_4(t)$ with the small parameters $(\beta\lambda_i)^{-1/2}$ and $(\beta\lambda_i)^{-1}$, respectively. The main result of these calculation is a relatively small effect of non-Gaussian dynamics on these two time correlation functions because of this diminishing scaling of the corresponding non-Gaussian contributions.

7.4 Cytochrome *c* in Water

7.4.1 Classical Molecular Dynamics (MD) Simulations

The NMR solution structure of reduced horse heart cytochrome *c* (PDB 1GIW) was adopted as the starting configuration for classical MD simulations. The CHARMM 27 [300] force field was used for the peptide chain, while the parameters for the heme group in the reduced (Red) and oxidized (Ox) states were adopted by combining atomic charges from Leu *et al.* [301] with the bonded and van der Waals parameters from Kaszuba *et al.*[302]. Patches were applied to connect the heme group to the protein matrix through ligation of two cysteine residues (res. No 14 and 17) and a single methionine residue (No 80).

Most electron-transfer cytochromes form 6-coordinated His-Fe-Met complex[303]. The Fe-His bond is, however, weaker than the Fe-Met bond and can break in some forms of cytochrome c[304]. The stretching frequency of the Fe-His bond in 6-coordinated cytochromes is $\sim 220 - 240$ cm^{-1}[304]. The breaking of the Fe–Nϵ bond was previously modeled by QM/MM simulations[304] and the resulting potential is shown by points in Figure 49. A Morse potential was used to represent the results of the simulations

$$U(r) = D_e \left[1 - e^{-\gamma(r-r_e)}\right]^2 \tag{7.14}$$

with the well depth $D_e = 9.0$ kcal/mol, the well width $\gamma = 1.52$ Å^{-1}, and the equilibrium bond distance $r_e = 2.33$ Å (Figure 49). The potential in Eq. (7.14) was applied to the simulations in the form of the force by utilizing NAMD tclForces functionality. The bond does not break during the simulation time, but the Morse potential allows additional flexibility of the system along the bond stretch coordinate.

From the original PDB structure, crystallographic water molecules were taken from the

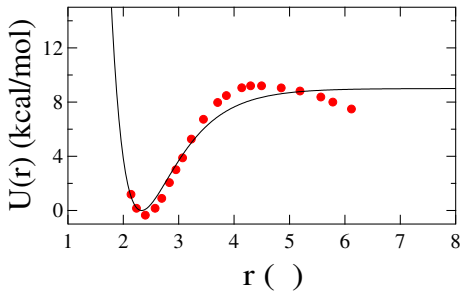

FIGURE 49: Morse potential modeling the Fe–Nϵ bond. The red points are from Ref. 304 while the black line represents the Morse potential in Eq. (7.14) with $D_e = 9.0$ kcal/mol, $\gamma = 1.52$ Å^{-1}, and the equilibrium bond distance $r_e = 2.33$ Å.

1YCC PDB file and, after aligning the two protein structures, were added to the 1GIW cytochrome *c* structure. To assure that the protein was properly saturated with water, we performed a "soaking" procedure. It consisted of making a small sphere of water surrounding the protein with a total system size of 5497 atoms. From this structure, 150 ns simulations were performed. Finally, from the last frame of these longer simulations, a box (100.1Å$\times$100.1Å$\times$ 100.1Å) consisting of a total of 101440 atoms was created and additional water molecules added to the total of 33231 molecules. This addition of water was followed by 20 ns NPT simulations allowing the newly created box to relax around the sphere. This NPT equilibration was followed by 10 ns NVT equilibration for each redox state. All force field parameters were applied using VMD's "psfgen" tool and TIP3P water molecules were added using VMD's "solvate" plugin[175].

All simulations were performed using NAMD software program[175]. For all initial systems created a steepest decent minimization was performed for 2000 steps. The NPT equilibration simulation was done using the Langevin dynamics in NAMD with the following parameter set: a damping coefficient of 1 ps^{-1}, piston period of 100 fs, the piston decay time of 50 fs, the piston target pressure of 1.01325 bar, and constant temperature control

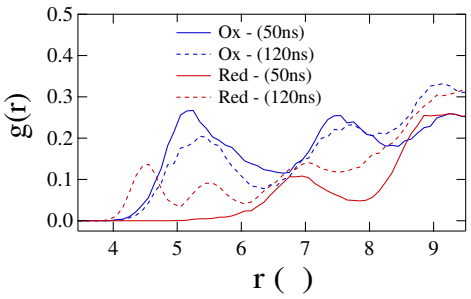

FIGURE 50: The radial distribution function for the distance between the heme iron and the water's oxygen averaged over 1 ns of the simulation trajectory taken at 50 ns and 120 ns.

set to 300 K. The NVT simulations were performed using the same parameters as the NPT simulations, but removing the constant pressure controls. Long-range electrostatic interactions were treated with the particle mesh Ewald technique using a cutoff distance of 12.0 Å. A 2.0 fs time step was used for all simulations. 250 ns MD simulations were carried out for trajectories production. Additional 10 ns simulations were performed with the saving frequency of 8 fs to study the short time dynamics.

Figure 50 shows the iron-oxygen pair distribution function in the Ox and Red states of the protein. One can detect the presence of a water molecule next to the heme in the Red state. This water molecule leaves the heme pocket on the time scale of the simulation when the protein is in the Ox state. This difference in wetting of the heme pocket, however, does not translate into any noticeable differences in the electron transfer reorganization energies in two redox states.

TABLE 6: Excitation energies for various sizes of the QC in the Red state. QC_s and QC_m are the small and medium QCs. QC denotes the quantum center adopted for QM/MD calculations. All values are obtained by the ZINDO/S method (eV).

System	ΔE_{0-1}	ΔE_{0-2}	ΔE_{0-3}	ΔE_{0-4}	ΔE_{0-5}
QC_s	-0.23	-0.11	0.79	1.19	1.79
QC_m	0.83	0.92	1.07	1.77	1.79
QC	0.84	0.89	1.01	1.76	1.78

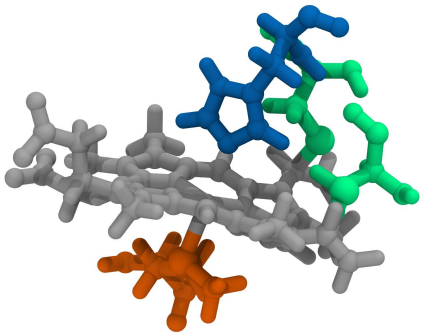

FIGURE 51: Quantum center (QC): the heme group (gray) and the amino acids bonded to the heme, cysteine (green), methionine (orange), and histidine (blue).

7.4.2 Polarizable Active Site

A portion of cytochrome *c* was chosen as the quantum center (QC) and was treated quantum mechanically, with the rest of the system treated at the classical atomistic level. Three different sizes of QC were initially chosen. The smallest QC (QC_s) only consisted of the heme. The medium size QC (QC_m) consisted of the heme, HIS, and MET ligated amino acids, and the largest QC (adopted for the analysis, Figure 51) contained the heme, HIS, MET, and two CYS ligated amino acids. In all cases, hydrogen atoms were added to satisfy valency. Table 6 shows the unperturbed excitation energies for all QCs, which shows that the results for the largest QC are not significantly different from QC_m. The geometry of QC was optimized by freezing all the atoms except the added hydrogens.

TABLE 7: Scalar polarizabilities (Å^3) calculated with ZINDO/S for different numbers of excited states M, $\Delta\alpha = \alpha_{\text{Ox}} - \alpha_{\text{Red}}$.

M	α_{Ox}	α_{Red}	$\Delta\alpha$
100	23.3	54.1	-30.8
80	21.2	53.8	-32.6
60	18.3	52.0	-33.7
40	14.2	47.3	-33.1
20	6.5	40.6	-34.1
10	1.3	4.2	-2.9
5	3.3	3.6	-0.3

The Hamiltonian matrix of the QC in the electrostatic field of the surrounding classical subsystem can be written as follows[47]

$$H_{jk} = (E_j + Q\phi_{\text{Fe}})\,\delta_{jk} - \boldsymbol{\mu}_{jk} \cdot \mathbf{E}_b. \tag{7.15}$$

Here, Q is the total charge of the quantum center, $\boldsymbol{\mu}_{jk}$ is the transition dipole between states with energies E_j and E_k, and ϕ_{Fe} and $\mathbf{E}_b$ denoting correspondingly the electrostatic potential and the electric field of the classical subsystem at the heme iron. The multipolar terms of the order higher than the dipole are omitted here.

GAUSSSIAN'09[305] was used for all quantum calculations of the QC in vacuum (Red and Ox states) using the ZINDO/S method[306]. The charges of the Red (singlet) and Ox (doublet) QC were -2 and -1, respectively. The Hamiltonian matrix was formed by using $M = 100$ excited states. These states formed the set of parameters in Eq. (7.15) and were also used to calculate the polarizability tensor of the QC according to the perturbation formula

$$\alpha_0^{\alpha\beta} = 2\sum_{j>0} \frac{\mu_{0j}^{\alpha}\mu_{j0}^{\beta}}{E_j - E_0}, \tag{7.16}$$

where E_0 is ground state energy and α, β denote the Cartesian components. Scalar polarizabilities reported in Table 7 are traces of the corresponding tensors, $\alpha = \frac{1}{3}\text{Tr}\,(\boldsymbol{\alpha}_0)$.

7.4.3 Electron Transfer Energy Gap

The energy gap in classical MD simulations is defined as

$$X = \sum_j \Delta q_j \phi_j^{\mathrm{EW}} + X'' \tag{7.17}$$

where $\Delta q_j = q_j^{\mathrm{Ox}} - q_j^{\mathrm{Red}}$, q_j^{Ox} and q_j^{Red} are the corresponding partial atomic charges in the Ox and Red states, respectively. ϕ_j^{EW} is the Ewald lattice sum electrostatic potential of the protein and water discussed below. X'' is the correction to the electrostatic energy from the interaction with the background charge of the periodic Wigner lattice [168]. The energy gap for the quantum mechanical approach is defined as the difference between the lowest eigenvalues $E_g^{\mathrm{Ox/Red}}$ of the oxidized and reduced states obtained by diagonalizing the corresponding Hamiltonian matrices in Eq. (7.15)

$$X = E_g^{\mathrm{Ox}} - E_g^{\mathrm{Red}}. \tag{7.18}$$

7.4.4 Ewald Sum Corrections

The treatment of long-range electrostatic interactions by NAMD software package [175] involves particle mesh Ewald sums. The simulation of a redox half reaction requires, in contrast to electron transfer between the donor and acceptor, changing the charge of the system. This change in the physics of the problem requires introducing corrections to the calculations of the electrostatic energies[167, 168, 307]. Most of the corrections for the Ewald sums electrostatics discussed in the literature[307] are concerned with the equilibrium solvation free energy. The problem at hand here is different. We want to establish the corrections to the instantaneous energy gap $X(t)$ due to the use of the electrostatics pro-

duced by the lattice of replicated simulations cells instead of the infinite polarized thermal bath.

The main point of concern in using the Ewald lattice sums for the calculation of the energy gap of a half reaction is the fact that the simulation cell is either explicitly neutralized or it is neutralized implicitly by a uniform background charge spread throughout the cell. In our present simulations, we do not use electrolyte to neutralize the simulation cell to avoid complications from the movement of the electrolyte ions. Similar setups, with no neutralizing electrolyte were used in early work by Hummer, Pratt, and Garcia [122]. Those are often even harder to sample adequately than the fluctuations of the multipolar polarization of the protein-water interface. The issue is clearly demonstrated by Figure 52, which shows that trajectories longer than 200 ns are required to sample water-protein fluctuations contributing to λ. Sampling ion motions would require even longer trajectories [308]. The absence of neutralizing electrolyte implies that the overall simulation cell carries the charge of $Q_{\text{Ox}} = 9$ and $Q_{\text{Red}} = 8$ in Ox and Red states, respectively. The QC charges are correspondingly -1 and -2.

The reaction coordinate X is the difference of energies of Ox and Red state, and one can think of it as the energy difference arising from bringing a single positive charge to the Red state of the QC and distributing it over all Δq_j sites where charge density is changed in the half reaction. This extra positive charge will interact with the periodic Ewald potential ψ created by the protein-water solvent and by the lattice of replicated simulation cells. The instantaneous configuration of the bath with the set of atomic charges q_k will therefore produce the energy gap component $X' = \sum_{j \neq k} \Delta q_j \psi_{jk} q_k$, where the lattice potential is usually given as[167]

$$\psi_{jk} = \frac{\operatorname{erfc}(\kappa r_{jk})}{r_{jk}} + \frac{4\pi}{L^3} \sum_{\mathbf{k} \neq \mathbf{0}} \frac{1}{k^2} e^{i\mathbf{k}\cdot\mathbf{r}_{jk} - k^2/(4\kappa^2)} - \frac{\pi}{\kappa^2 L^3}. \tag{7.19}$$

Here, $r_{jk} = |\mathbf{r}_j - \mathbf{r}_k|$, L is the side length of the cubic simulation cell, and $\mathbf{k}$ are the

wavevectors of the reciprocal lattice. Correspondingly, one gets $\phi_j^{\text{EW}} = \sum_k \psi_{jk} q_k$ in Eq. (7.17). The lattice potential in Eq. (7.19), with the last term dropped, is calculated by NAMD [175]; $\kappa = 0.2579$ Å^{-1} was adopted in the simulations and in the analysis of the simulaltion trajectories.

The calculation of the interaction of the fictitious positive charge transferred to the QC with the uniform background charge requires more care. The transferred charge will interact with the total charge Q_{Red} of the cell in the Red state, but will also create its own replicated images and the corresponding background charge. Those images and the corresponding background charge are not physical charges and one has to assume that they are created instantaneously as the extra charge is transferred to the cell (even though the transfer of electron is essentially instantaneous in respect to the nuclear coordinates). The corresponding contribution to the energy difference X will therefore be the free energy of charging, in contrast to the energy of interacting with the existing charge Q_{Red}. The result is

$$X'' = -\sum_j \frac{\Delta q_j^2}{2L} c' \zeta_{\text{EW}} - \sum_j \frac{Q_{\text{Red}} \Delta q_j}{L} c' \zeta_{\text{EW}}, \tag{7.20}$$

where $\zeta_{\text{EW}} = 2.837297$ comes from the self-energy of a point charge in the cubic Wigner lattice [168] and $c' = 1 - \epsilon_s^{-1}$ is the correction for the "under-solvation" effects [167]. The latter correction accounts for the difference of the solvent potential in a replicated lattice compared to an infinite system. It is commonly estimated from the difference in corresponding continuum solvation energies as calculated by Hummer *et al.* [168] and Hünenberger and McCammon [307]. Therefore, the correction c' involves the dielectric constant of the solvent ϵ_s entering the boundary value problem. When the charges Δq_j are spread over the active site immersed in a polarizable solvent with instantaneously responding electronic polarization, c' in Eq. (7.20) is replaced by the Pekar factor $c_0 = \epsilon_\infty^{-1} - \epsilon_s^{-1}$, where ϵ_∞ is the electronic dielectric constant [309] (not a part of our force field).

Since $\sum_j \Delta q_j = 1$, one can simplify the above equation to

$$X'' = -\frac{c'\zeta_{\text{EW}}}{2L}\sum_j \Delta q_j^2 - \frac{c'Q_{\text{Red}}}{L}\zeta_{\text{EW}}. \tag{7.21}$$

The overall instantaneous energy gap is given by the sum of the lattice part and the interaction with the background charge, $X = X' + X''$. Since the definition of the reaction coordinate is the same in the Red and Ox sampling simulations, it is easy to see that X'' causes only a constant shift of the energy gap, which does not affect either λ^{St} or λ. We additionally note that Figure 35 in chapter 6 shows the distribution of the Ewald sum component X' of the reaction coordinate only, thus omitting the X'' correction. This is done to show the relative energies of interaction of the active site with the protein and water components separately, for which the corresponding corrections due to background charge are not easy to establish. As mentioned, any changes to this procedure will only shift the corresponding distributions, without affecting the reported reorganization energies.

We also note that the effect of the system size [309] is small in our simulations. This is shown is Table 8 where we list the results of simulations of a much smaller system, with only 6626 TIP3P water molecules present in the simulation cell. Despite a smaller system size and a somewhat shorter trajectories, the results are generally consistent with those obtained for a larger system.

7.4.5 Statistics

Two reorganization energies of electron transfer are considered here: λ^{St} and λ. The former is defined in terms of the average energy gap $\langle X\rangle$ in Red and Ox states: $\lambda^{\text{St}} = \left(\langle X\rangle_{\text{Red}} - \langle X\rangle_{\text{Ox}}\right)/2$. The latter is given through the variance, $\lambda_i = \beta\langle(\delta X)^2\rangle_i/2$ averaged over the configurations in equilibrium with the corresponding redox state of the protein, $i =$ Red,Ox. Table 8 reports both reorganization energies and Figure 52 shows the evolution

TABLE 8: Reorganization energies (eV). The uncertainties are estimated from block averages along the simulation trajectory.

Classical			
State	λ	λ_{p}	λ_{w}
Ox[a]	1.67 ± 0.08	2.28 ± 0.25	3.39 ± 0.27
Red[a]	1.64 ± 0.06	2.98 ± 0.24	2.46 ± 0.20
Method	λ^{St}	λ_{Ox}	λ_{Red}
Eq. 7.17	1.26 ± 0.04	1.67 ± 0.08	1.64 ± 0.06
Localized[b]	1.13 ± 0.04	1.57 ± 0.08	1.50 ± 0.06
Small[c]	1.04	1.24	1.49

Quantum Mechanical			
$\Delta\alpha^d$/Å^3	λ^{St}	λ_{Ox}	λ_{Red}
0.0	1.13 ± 0.04	1.57 ± 0.08	1.50 ± 0.05
-7.7	1.17 ± 0.03	2.06 ± 0.10	1.60 ± 0.06
-30.8	1.24 ± 0.03	3.07 ± 0.13	2.32 ± 0.06
-69.2	1.32 ± 0.04	4.52 ± 0.19	3.50 ± 0.09
-122.9	1.40 ± 0.05	6.40 ± 0.25	5.16 ± 0.13

[a]Based on Eq. (7.17) and $\lambda = \beta \langle \delta X^2 \rangle / 2$, [b]Energy gap is obtained as $X = e\phi_{\mathrm{Fe}}$, where ϕ_{Fe} is the bath electrostatic potential at the heme iron, [c]Small simulation system with 21625 atoms, 6626 TIP3P waters, and with the trajectory length of 70 ns. [d]Based on the scaling of the transition dipole moments.

of the average energy gap and its variance obtained from classical MD simulations. The splitting of the reorganization energy λ from classical simulations into the protein and water components is also reported in Table 8. Note that λ_p (protein) and λ_w (water) do not add up to λ because the cross term λ_{pw} due to correlated protein-water fluctuations is negative and typically large in magnitude.

Figure 53 shows the free energy surfaces of the half reaction in oxidized and reduced states of cytochrome *c* when the polarizability change between Ox and Red states is equal to -122.9 Å^3. The corresponding free energy surfaces for $\Delta\alpha = -30.8$ Å^3 are shown in the main text.

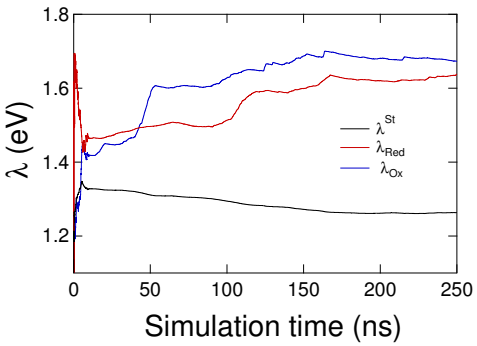

FIGURE 52: The evolution of $(\langle X\rangle_{\mathrm{Red}} - \langle X\rangle_{\mathrm{Ox}})/2$ (λ^{St}) and $\beta\langle(\delta X)^2\rangle_i/2$ (λ_i, $i = \mathrm{Red}, \mathrm{Ox}$) along classical MD trajectories obtained from simulations of cytochrome *c* in Ox and Red states.

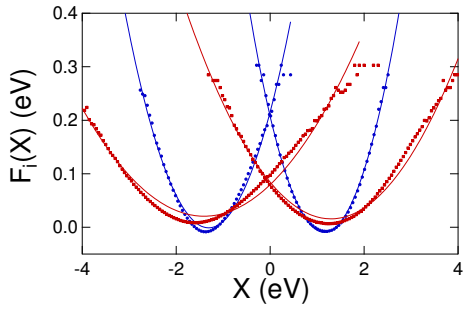

FIGURE 53: Free energy surfaces of the half reaction in Ox (left) and Red (right) states of cytochrome *c*. The transition dipoles in the quantum calculations are scaled to produce the the polarizability change in the redox reaction: $\Delta\alpha = -122.9$ Å^3. The blue circles show the results of classical MD simulations, the red squares indicate the quantum mechanical simulations, and the solid lines are fits to parabolas.

7.4.6 Dynamics

The main dynamic function studied here is the time auto-correlation function of the energy gap (Stokes-shift dynamics) $C_X(t) = \langle\delta X(t)\delta X(0)\rangle$. This correlation function calculated from MD trajectories in Red and Ox states of cytochrome *c* was fitted to five decaying exponents

$$S_2(t) = C_X(t)/C_X(0) = \sum_{n=1}^{5} A_n e^{-t/\tau_n} \tag{7.22}$$

TABLE 9: The fit parameters for the time correlation functions of the energy gap to the sum of 5 exponential functions (Eq. (7.22), relaxation times τ_n are in ps).

Component	A_1	A_2	A_3	A_4	A_5	τ_1	τ_2	τ_3	τ_4	τ_5
Red										
Total	0.55	0.14	0.14	0.05	0.12	0.10	6.8	57	746	28380
Protein	0.14	0.05	0.13	0.25	0.44	0.06	2.3	13	106	1793
Water	0.24	0.13	0.16	0.28	0.19	0.01	4.7	78	853	5725
Ox										
Total	0.53	0.13	0.07	0.06	0.22	0.08	2.5	21	339	4685
Protein	0.15	0.10	0.16	0.14	0.45	0.01	11.4	144	813	5333
Water	0.22	0.10	0.08	0.17	0.43	0.13	2.9	23	246	4038

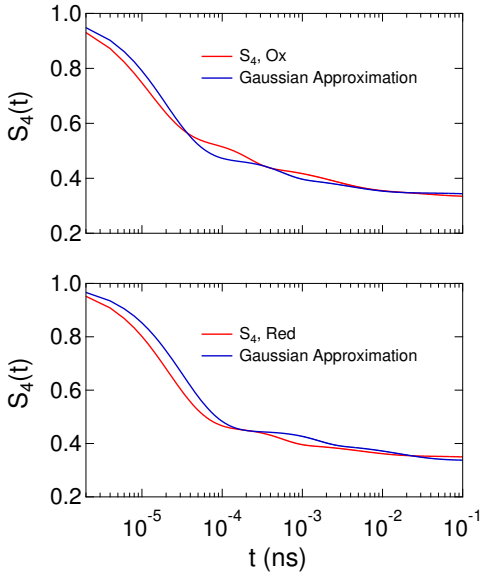

FIGURE 54: $S_4(t)$ calculated from MD simulations and from Eq. (7.24) (Gaussian approximation) by using the second-order correlation function $S_2(t)$ for oxidized and reduced states.

with the fitting parameters listed in Table 9. The fitted functions were then Laplace-Fourier transformed to obtain the loss function $\chi''(\omega)$ discussed in the main text. The procedure was repeated for the protein and water components of the energy gap to obtain the corresponding loss functions and the dynamics of the protein and water components of the thermal bath affecting electron transfer.

We have additionally studied the higher-order time correlation function in order to test whether the dynamics of the energy gap are Gaussian [46, 310]. The normalized fourth-order time correlation functions $S_4(t)$ is defined as follows

$$S_4(t) = \langle (\delta X)^4 \rangle^{-1} \langle \delta X(t)^2 \delta X(0)^2 \rangle. \tag{7.23}$$

If the dynamics are Gaussian, the fourth-order time correlation function does not carry any new dynamic information and can be determined in terms of the normalized Stokes-shift correlation function $S_2(t)$ in Eq. (7.22)

$$S_4(t) = \frac{1}{3} + \frac{2}{3} S_2(t)^2. \tag{7.24}$$

This relation was tested by MD simulations. Figure 54 compares $S_4(t)$ directly calculated from MD trajectories for $X(t)$ to Eq. (7.24). We find a good agreement between the two results in both redox states, testifying to the accuracy of the Gaussian approximation.

REFERENCES

[1] Born, M. Volumen und hydratationswärme der ionen. *Z. Phys.* **1920**, *1*, 45.

[2] Marcus, R.A. On the theory of oxidation-reduction reactions involving electron transfer. I. *J. Chem. Phys.* **1956**, *24*, 966.

[3] Marcus, R.A. Chemical and electrochemical electron-transfer theory. *Annu. Rev. Phys. Chem.* **1964**, *15*, 155.

[4] Marcus, R.A. On the theory of shifts and broadening of electronic spectra of polar solutes in polar media. *J. Chem. Phys.* **1965**, *43*, 1261.

[5] Marcus, R.A. On the theory of electron-transfer reactions. VI. Unified treatment for homogeneous and electrode reactions. *J. Chem. Phys.* **1965**, *43*, 679.

[6] Marcus, R.A.; Sutin, N. Electron transfer in chemistry and biology. *Biochim. Biophys. Acta* **1985**, *811*, 265.

[7] Newton, M.; Sutin, N. Electron Transfer Reactions in Condensed Phases. *Ann. Rev. Phys. Chem.* **1984**, *35*, 437.

[8] Marcus, R.A.; Sutin, N. Electron transfers in chemisrty and biology. *Biochim. Biophys. Acta* **1985**, *811*, 265.

[9] Chandler, D. Gaussian field model of fluids with an application to polymeric fluids. *Phys. Rev. E* **1993**, *48*, 2898.

[10] Noah-Vanhoucke, J.; Geissler, P.L. On the fluctuations that drive small ions toward, and away from, interfaces between polar liquids and their vapors. *Proc. Natl. Acad. Sci. U.S.A.* **2009**, *106*, 15125.

[11] Friesen, A.D.; Matyushov, D.V. Surface polarity and nanoscale solvation. *J. Phys. Chem. Lett.* **2012**, *3*, 3685.

[12] Dinpajooh, M.; Matyushov, D.V. Free energy of ion hydration: Interface susceptibility and scaling with the ion size. *J. Chem. Phys.* **2015**, *143*, 044511.

[13] Matyushov, D.V. Protein electron transfer: is biology (thermo)dynamic? *J. Phys.: Condens. Matter* **2015**, *27*, 473001.

[14] Ly, H.K.; Marti, M.A.; Martin, D.F.; Alvarez-Paggi, D.; Meister, W.; Kranich, A.; Weidinger, I.M.; Hildebrandt, P.; Murgida, D.H. Thermal fluctuations determine the electron-transfer rates of cytochrome c in electrostatic and covalent complexes. *ChemPhysChem* **2010**, *11*, 1225.

[15] Martin, D.R.; Matyushov, D.V. Communication: Microsecond dynamics of the protein and water affect electron transfer in a bacterial bc_1 complex. *J. Chem. Phys.* **2015**, *142*, 161101.

[16] LeBard, D.N.; Martin, D.R.; Lin, S.; Woodbury, N.W.; Matyushov, D.V. Protein dynamics to optimize and control bacterial photosynthesis. *Chem. Sci.* **2013**, *4*, 4127.

[17] Gray, H.B.; Winkler, J.R. Long-range electron transfer. *Proc. Natl. Acad. Sci. U.S.A.* **2005**, *102*, 3534.

[18] Garrido, C.; Galluzzi, L.; Brunet, M.; Puig, P.E.; Didelot, C.; Kroemer, G. Mechanisms of cytochrome c release from mitochondria. *Cell Death Differ.* **2006**, *13*, 1423.

[19] Ow, Y.L.P.; Green, D.R.; Hao, Z.; Mak, T.W. Cytochrome c: functions beyond respiration. *Nat. Rev. Mol. Cell Biol.* **2008**, *9*, 532.

[20] Matyushov, D.V. Electrostatics of liquid interfaces. *J. Chem. Phys.* **2014**, *140*, 224506.

[21] Dinpajooh, M.; Matyushov, D.V. Interfacial structural transition in hydration shells of a polarizable solute. *Phys. Rev. Lett.* **2015**, *114*, 207801.

[22] Jung, Y.; Marcus, R.A. Protruding interfacial OH groups and 'on-water' heterogeneous catalysis. *J. Phys.: Condens. Matter* **2010**, *22*, 284117.

[23] Narayan, S.; Muldoon, J.; Finn, M.G.; Fokin, V.V.; Kolb, H.C.; Sharpless, K.B. "On Water": Unique reactivity of organic compounds in aqueous suspension. *Angew. Chem. Int. Ed.* **2005**, *44*, 3275.

[24] Griffith, E.C.; Vaida, V. In situ observation of peptide bond formation at the water-air interface. *Proc. Natl. Acad. Sci. U.S.A.* **2012**, *109*, 15697.

[25] Wall, S. The history of electrokinetic phenomena. *Curr. Opin. Coll. Interf. Sci.* **2010**, *15*, 119.

[26] Hunter, R.J. *Zeta potential in colloid science*. Academic Press, London, **1981**.

[27] Marinova, K.G.; Alargova, R.G.; Denkov, N.D.; Velev, O.D. Charging of oil-water interfaces due to spontaneous adsorption of hydroxyl ions. *Langmuir* **1996**, *12*, 2045.

[28] Takahashi, M. ζ-potential of microbubbles in aqueous solutions: Electrical properties of the gas–water interface. *J. Phys. Chem. B* **2005**, *109*, 21858.

[29] Beattie, J.K.; Djerdjev, A.M.; Warr, G.G. The surface of neat water is basic. *Farad. Disc.* **2009**, *141*, 31.

[30] Zimmermann, R.; Freudenberg, U.; Schweiß, R.; Küttner, D.; Werner, C. Hydroxide and hydronium ion adsorption —a survey. *Curr. Opin. Colloid Interface Sci.* **2010**, *15*, 196.

[31] Joseph, S.; Aluru, N.R. Pumping of confined water in carbon nanotubes by rotating-translational coupling. *Phys. Rev. Lett.* **2008**, *101*, 064502.

[32] Knecht, V.; Levine, Z.A.; Vernier, P.T. Electrophoresis of neutral oil in water. *J. Colloid Interface Sci.* **2010**, *352*, 223.

[33] Ben-Amotz, D. Unveiling Electron Promiscuity. *J. Phys. Chem. Lett.* **2011**, *2*, 1216.

[34] Vácha, R.; Rick, S.W.; Jungwirth, P.; de Beer, A.G.F.; de Aguiar, H.B.; Samson, J.S.; Roke, S. The orientation and charge of water at the hydrophobic oil droplet–water interface. *J. Am. Chem. Soc.* **2011**, *133*, 10204.

[35] Vácha, R.; Marsalek, O.; Willard, A.P.; Bonthuis, D.J.; Netz, R.R.; Jungwirth, P. Charge Transfer between Water Molecules As the Possible Origin of the Observed Charging at the Surface of Pure Water. *J. Phys. Chem. Lett.* **2012**, *3*, 107.

[36] Schoeler, A.M.; Josephides, D.N.; Sajjadi, S.; Lorenz, C.D.; Mesquida, P. Charge of water droplets in non-polar oils. *J. Appl. Phys.* **2013**, *114*, 144903.

[37] Matyushov, D.V. Electrophoretic mobility without charge driven by polarisation of the nanoparticle–water interface. *Mol. Phys.* **2014**, *112*, 2029.

[38] Bonthuis, D.J.; Horinek, D.; Bocquet, L.; Netz, R.R. Electrohydraulic Power Conversion in Planar Nanochannels. *Phys. Rev. Lett.* **2009**, *103*, 144503.

[39] Bonthuis, D.J.; Horinek, D.; Bocquet, L.; Netz, R.R. Electrokinetics at aqueous interfaces without mobile charges. *Langmuir* **2010**, *26*, 12614.

[40] Suk, M.E.; Aluru, N.R. Suk and Aluru Reply. *Phys. Rev. Lett.* **2010**, *105*, 209402.

[41] Mukamel, S. *Principles of Nonlinear Optical Spectroscopy*. Oxford University Press, New York, **1995**.

[42] Kubo, R. Stochastic processes in chemical physics. K. Shuler, ed., *Adv. Chem. Phys.*, volume 15, chapter A stochastic theory of line shape, 101–127. Wiley Interscience, New York, **1969**.

[43] Barbara, P.F.; Jarzeba, W. Ultrafast photochemical intramolecular charge and excited state solvation. *Adv. Photochem.* **1990**, *15*, 1.

[44] Bagchi, B.; Chandra, A. Collective orientational relaxation in dense dipolar liquids. *Adv. Chem. Phys.* **1991**, *80*, 1.

[45] Reynolds, L.; Gardecki, J.A.; Frankland, S.J.V.; Maroncelli, M. Dipole solvation in nondipolar solvents: Experimental studies of reorganization energies and solvation dynamics. *J. Phys. Chem.* **1996**, *100*, 10337.

[46] Dinpajooh, M.; Matyushov, D.V. Non-Gaussian lineshapes and dynamics of time-resolved linear and nonlinear (correlation) spectra. *J. Phys. Chem. B* **2014**, *118*, 7925.

[47] Bortolotti, C.A.; Amadei, A.; Aschi, M.; Borsari, M.; Corni, S.; Sola, M.; Daidone, I. The Reversible Opening of Water Channels in Cytochrome c Modulates the Heme Iron Reduction Potential. *J. Am. Chem. Soc.* **2012**, *134*, 13670.

[48] Hamm, P.; Zanni, M. *Concepts and Methods of 2D Infrared Spectroscopy*. Cambridge University Press, Cambridge, UK, **2011**.

[49] Richert, R. Supercooled Liquids and Glasses By Dielectric Relaxation Spectroscopy. *Adv. Chem. Phys.* **2015**, *156*, 101.

[50] Richert, R. Triplet state solvation dynamics: Basics and applications. *J. Chem. Phys.* **2000**, *113*, 8404.

[51] Yang, M.; Richert, R. Observation of heterogeneity in the nanosecond dynamics of a liquid. *J. Chem. Phys.* **2001**, *115*, 2676.

[52] Richert, R.; Stickel, F.; Fee, R.S.; Maroncelli, M. Solvation dynamics and the dielectric response in a glass-forming solvent: from picoseconds to seconds. *Chem. Phys. Lett.* **1994**, *229*, 302.

[53] Abbyad, P.; Childs, W.; Shi, X.; Boxer, S.G. Dynamic Stokes shift in green fluorescent protein variants. *Proc. Natl. Acad. Sci. USA* **2007**, *104*, 20189.

[54] Zhang, X.X.; Schröder, C.; Ernsting, N.P. Communication: Solvation and dielectric response in ionic liquids–conductivity extension of the continuum model. *J. Chem. Phys.* **2013**, *138*, 111102.

[55] Bredenbeck, J.; Helbing, J.; Hamm, P. Solvation beyond the linear response regime. *Phys. Rev. Lett.* **2005**, *95*, 083201.

[56] Hamm, P. Three-dimensional-IR spectroscopy: Beyond the two-point frequency fluctuation correlation function. *J. Chem. Phys.* **2006**, *124*, 124506.

[57] Matyushov, D.V. On the microscopic theory of polar solvation dynamics. *J. Chem. Phys.* **2005**, *122*, 044502.

[58] Fröhlich, H. *Theory of Dielectrics*. Clarendon Press, Oxford, **1958**.

[59] Havriliak, S.; Negami, S. A complex plane representation of dielectric and mechanical relaxation processes in some polymers. *Polymer* **1967**, *8*, 161.

[60] Hansen, J.P.; McDonald, I.R. *Theory of Simple Liquids*. Academic Press, Amsterdam, **2003**.

[61] Matyushov, D.V.; Ladanyi, B.M. A perturbation theory and simulations of the dipole solvation thermodynamics: Dipolar hard spheres. *J. Chem. Phys.* **1999**, *110*, 994.

[62] Papazyan, A.; Warshel, A. Continuum and Dipole-Lattice Models of Solvation. *J. Phys. Chem. B* **1997**, *101*, 11254.

[63] Papazyan, A.; Warshel, A. Effect of solvent discreteness on solvation. *J. Phys. Chem. B* **1998**, *102*, 5348.

[64] Vath, P.; Zimmt, M.B.; Matyushov, D.V.; Voth, G.A. A failure of continuum theory: Temperature dependence of the solvent reorganization energy of electron transfer in highly polar solvents. *J. Phys. Chem. B* **1999**, *103*, 9130.

[65] Onsager, L. Electric moments of molecules in liquids. *J. Am. Chem. Soc.* **1936**, *58*, 1486.

[66] Cramer, C.J. *Essentials of Computational Chemistry: Theories and Models*. Wiley, 2nd edition, **2004**.

[67] Tomasi, J.; Tomasi, J.; Mennucci, B.; Mennucci, B.; Cammi, R.; Cammi, R. Quantum Mechanical Continuum Solvation Models. *Chem. Rev.* **2005**, *105*, 2999.

[68] Huston, S.E.; Rossky, P.J.; Zichi, D.a. Hydration effects on SN2 reactions: an integral equation study of free energy surfaces and corrections to transition-state theory. *J. Am. Chem. Soc.* **1989**, *111*, 5680.

[69] Pettitt, B.M.; Rossky, P.J. Integral equation predictions of liquid state structure for waterlike intermolecular potentials. *J. Chem. Phys.* **1982**, *77*, 1451.

[70] Rossky, P.J.; Chiles, R.a. A complete integral equation formulation in the interaction site formalism. *Molec. Phys.* **1984**, *51*, 661.

[71] Chilies, R.; Rossky, P. Evaluation of Reaction Free Energy Surfaces in Aqueous Solution: An Integral Equation Approach. *J. Am. Chem. Soc.* **1984**, *106*, 6868.

[72] Elkoubi, D.; Turq, P. Application of the HNC Approximation. *Chem. Phys. Lett.* **1977**, *52*, 493.

[73] Bacquet, R.; Rossky, P.J. Corrections to the HNC equation for associating electrolytes. *J. Chem. Phys.* **1983**, *79*, 1419.

[74] Percus, J.K.; Yevick, G.J. Analysis of Classical Statistical Mechanics by Means of Collective Coordinates. *Phys. Rev.* **1958**, *110*, 1.

[75] Valleau, J.P.; Cohen, L.K.; Card, D.N. Primitive model electrolytes. II. The symmetrical electrolyte. *J. Chem. Phys.* **1980**, *72*, 5942.

[76] Wertheim, M.S. Exact Solution of the Mean Spherical Model for Fluids of Hard Spheres with Permanent Electric Dipole Moments. *J. Chem. Phys.* **1971**, *55*, 4291.

[77] Pitard, E.; Rosinberg, M.L.; Stell, G.; Tarjus, G. Critical Behavior of a Fluid in a Disordered Porous Matrix: An Ornstein-Zernike Approach. *Phys. Rev. Lett.* **1995**, *74*, 4361.

[78] Hirata, F. Application of an extended RISM equation to dipolar and quadrupolar fluids. *J. Chem. Phys.* **1982**, *77*, 509.

[79] Hayaki, S.; Yokogawa, D.; Sato, H.; Sakaki, S. Solvation effects in oxidative addition reaction of Methyliodide to Pt(II) complex: A theoretical study with RISM-SCF method. *Chem. Phys. Lett.* **2008**, *458*, 329.

[80] Jorgensen, W.L.; Chandrasekhar, J.; Madura, J.D.; Impey, R.W.; Klein, M.L. Comparison of simple potential functions for simulating liquid water. *J. Chem. Phys.* **1983**, *79*, 926.

[81] Jorgensen, W.L.; Maxwell, D.S.; Tirado-Rives, J. Development and testing of the opls all-atom force field on conformational energetics and properties of organic liquids. *J. Am. Chem. Soc.* **1996**, *118*, 11225.

[82] Brooks, B.R.; Bruccoleri, R.E.; Olafson, B.D.; States, D.J.; Swaminathan, S.; Karplus, M. Charmm. *J. Comput. Chem.* **1983**, *4*, 187.

[83] Car, R.; Parrinello, M. Unified approach for molecular dynamics and density-functional theory. *Phys. Rev. Lett.* **1985**, *55*, 2471.

[84] Turi, L.; Rossky, P.J. Theoretical studies of spectroscopy and dynamics of hydrated electrons. *Chem. Rev.* **2012**, *112*, 5641.

[85] Warshel, A.; Levitt, M. Theoretical studies of enzymic reactions: Dielectric, electrostatic and steric stabilization of the carbonium ion in the reaction of lysozyme. *J. Mol. Biol.* **1976**, *103*, 227.

[86] Truhlar, D.G.; Gao, J.; Alhambra, C.; Garcia-Viloca, M.; Corchado, J.; Sánchez, M.L.; Villà, J. The incorporation of quantum effects in enzyme kinetics modeling. *Acc. Chem. Res.* **2002**, *35*, 341.

[87] Cascella, M.; Magistrato, A.; Tavernelli, I.; Carloni, P.; Rothlisberger, U. Role of protein frame and solvent for the redox properties of azurin from *Pseudomonas aeruginosa*. *Proc. Natl. Acad. Sci.* **2006**, *103*, 19641.

[88] Senn, H.M.; Thiel, W. QM/MM Methods for Biomolecular Systems. *Angew. Chem. Int. Ed.* **2009**, *48*, 1198.

[89] Blumberger, J. Recent Advances in the Theory and Molecular Simulation of Biological Electron Transfer Reactions. *Chem. Rev.* **2015**, *115*, 11191.

[90] de la Lande, A.; Gillet, N.; Chen, S.; Salahub, D.R. Progress and challenges in simulating and understanding electron transfer in proteins. *Arch. Biochem. Biophys.* **2015**, *582*, 28.

[91] Cailliez, F.; Müller, P.; Firmino, T.; Pernot, P.; de la Lande, A. Energetics of photoinduced charge migration within the tryptophan tetrad of an animal (6-4) photolyase. *J. Am. Chem. Soc.* **2016**, ASAP.

[92] Kubo, R. The fluctuation-dissipation theorem. *Rep. Prog. Phys.* **1966**, *29*, 255.

[93] Henery, R.J. The generalized langevin equation and the fluctuation-dissipation theorems. *J. Phys. A: Gen. Phys.* **1971**, *4*.

[94] Friesen, A.D. *Electrostatic Properties of Water at Interfaces with Nanoscale Solutes*. Ph.D. thesis, Arizona State University, **2012**.

[95] Song, X.; Chandler, D.; Marcus, R.a. Gaussian Field Model of Dielectric Solvation Dynamics. *J. Phys. Chem.* **1996**, *100*, 11954.

[96] Li, H.; Kardar, M. Fluctuation-induced forces between rough surfaces. *Phys. Rev. Lett.* **1991**, *67*, 3275.

[97] Matyushov, D.V. Dipole solvation in dielectrics. *J. Chem. Phys.* **2004**, *120*, 1375.

[98] LeBard, D.N.; Matyushov, D.V. Redox entropy of plastocyanin: Developing a microscopic view of mesoscopic solvation. *J. Chem. Phys.* **2008**, *128*, 155106.

[99] Eyges, L. *The Classical Electromagnetic Field*. Dover Publications, Ney York, **1972**.

[100] Thompson Lord Kelvin, W. *Reprint of Papers on Electrostatics and Magnetism*. MacMillan and Co., London, 2nd edition, **1884, sec 479**.

[101] Liptay, W. The solvent dependence of the wavenumber of optical absorption and emission. O. Sinanoğlu, ed., *Modern quantum chemistry*. Academic Press, New York, **1965**.

[102] Fried, S.D.; Boxer, S.G. Measuring Electric Fields and Noncovalent Interactions Using the Vibrational Stark Effect. *Acc. Chem. Res.* **2015**, *48*, 998.

[103] Martin, D.R.; Friesen, A.D.; Matyushov, D.V. Electric field inside a "Rossky cavity" in uniformly polarized water. *J. Chem. Phys.* **2011**, *135*, 084514.

[104] Steffen, M.A.; Lao, K.; Boxer, S.G. Dielectric asymmetry in the photosynthetic reaction center. *Science* **1994**, *264*, 810.

[105] Landau, L.D.; Lifshitz, E.M. *Electrodynamics of Continuous Media*. Pergamon, Oxford, **1984**.

[106] Jeanmairet, G.; Levesque, M.; Vuilleumier, R.; Borgis, D. Molecular Density Functional Theory of Water. *J. Phys. Chem. Lett.* **2013**, *4*, 619.

[107] Ballenegger, V.; Hansen, J.P. Dielectric permittivity profiles of confined polar liquids. *J. Chem. Phys.* **2005**, *122*, 114711.

[108] Horváth, L.; Beu, T.; Manghi, M.; Palmeri, J. The vapor-liquid interface potential of (multi)polar fluids and its influence on ion solvation. *J. Chem. Phys.* **2013**, *138*, 154702.

[109] Jackson, J.D. *Classical Electrodynamics*. Wiley, New York, **1999**.

[110] Ballenegger, V.; Hansen, J.P. Local dielectric permittivity near the interface. *Europhys. Lett.* **2003**, *63*, 381.

[111] Stern, H.A.; Feller, S.E. Calculation of the dielectric permittivity profile for a nonuniform system: Application to a lipid bilayer simulation. *J. Chem. Phys.* **2003**, *118*, 3401.

[112] Ballenegger, V.; Blaak, R.; Hansen, J.P. Dipolar fluctuations in the bulk and at interfaces. M. Ferrario; G. Ciccotti; K. Binder, eds., *Computer simulations in condensed matter systems : from materials to chemical biology*, volume 2 of *Lecture Notes in Physics*, 45–63. Springer, Berlin, **2006**.

[113] Bonthuis, D.J.; Netz, R.R. Beyond the continuum: How molecular solvent structure affects electrostatics and hydrodynamics at solid-electrolyte interfaces. *J. Phys. Chem. B* **2013**, *117*, 11397.

[114] Simonson, T. Electrostatics and dynamics of proteins. *Rep. Prog. Phys.* **2003**, *66*, 737.

[115] Friesen, A.D.; Matyushov, D.V. Non-gaussian statistics of electrostatic fluctuations of hydration shells. *J. Chem. Phys.* **2011**, *135*, 104501.

[116] Martin, D.R.; Matyushov, D.V. Dipolar nanodomains in protein hydration shells. *J. Phys. Chem. Lett.* **2015**, *6*, 407.

[117] Simonson, T. Gaussian fluctuations and linear response in an electron transfer protein. *Proc. Natl. Acad. Sci.* **2002**, *99*, 6544.

[118] Simonson, T.; Archontis, G.; Karplus, M. Free energy simulations come of age: Protein-ligand recognition. *Acc. Chem. Res.* **2002**, *35*, 430.

[119] Matyushov, D.V.; Voth, G.A. Modeling the free energy surfaces of electron transfer in condensed phases. *J. Chem. Phys.* **2000**, *113*, 5413.

[120] Small, D.W.; Matyushov, D.V.; Voth, G.A. The theory of electron transfer: What may be missing? *J. Am. Chem. Soc.* **2003**, *125*, 7470.

[121] Åqvist, J.; Hansson, T. On the validity of electrostatic linear response in polar solvents. *J. Phys. Chem.* **1996**, *100*, 9512.

[122] Hummer, G.; Pratt, L.R.; Garcia, A.E. Free energy of ionic hydration. *J. Phys. Chem.* **1996**, *100*, 1206.

[123] Hummer, G.; Pratt, L.R.; Garcia, A.E. Molecular theories and simulation of ions and polar molecules in water. *J. Phys. Chem. A* **1998**, *102*, 7885.

[124] Rajamani, S.; Ghosh, T.; Garde, S. Size dependent ion hydration, its asymmetry, and convergence to macroscopic behavior. *J. Chem. Phys.* **2004**, *120*, 4457.

[125] Noyes, R.M. Thermodynamics of Ion Hydration as a Measure of Effective Dielectric Properties of Water. *J. Am. Chem. Soc.* **1962**, *84*, 513.

[126] Marcus, Y. *Ion Solvation*. Wiley, **1985**.

[127] Hünenberger, P.; Reif, M. *Single-Ion Solvation. Experimental and Theoretical Approaches to Elusive Thermodynamic Quantities*. RSC Publishing, Cambridge, UK, **2011**.

[128] Madden, P.A.; Impey, R.W. On the infrared and Raman spectra of water in the region 5–250 cm^{-1}. *Chem. Phys. Lett.* **1986**, *123*, 502.

[129] Kivelson, D.; Friedman, H. Longitudinal dielectric relaxation. *J. Phys. Chem.* **1989**, *93*, 7026.

[130] Latimer, W.M.; Pitzer, K.S.; Slansky, C.M. The Free Energy of Hydration of Gaseous Ions, and the Absolute Potential of the Normal Calomel Electrode. *J. Chem. Phys.* **1939**, *7*, 108.

[131] Ashbaugh, H.S.; Asthagiri, D. Single ion hydration free energies: A consistent comparison between experiment and classical molecular simulation. *J. Chem. Phys.* **2008**, *129*, 204501.

[132] Chan, D.Y.C.; Mitchell, D.J.; Ninham, B.W. A model of solvent structure around ions. *J. Chem. Phys.* **1979**, *70*, 2946.

[133] Babu, C.S.; Lim, C. Theory of ionic hydration: Insights from molecular dynamics simulations and experiment. *J. Phys. Chem. B* **1999**, *103*, 7958.

[134] Jayaram, B.; Fine, R.; Sharp, K.; Honig, B. Free energy calculations of ion hydration. *J. Phys. Chem.* **1989**, *93*, 4320.

[135] Roux, B.; Yu, H.A.; Karplus, M. Molecular basis for the Born model of ion solvation. *J. Phys. Chem.* **1990**, *94*, 4683.

[136] Linder, B.; Hoernschemeyer, D. Cavity concept in dielectric theory. *J. Chem. Phys.* **1967**, *46*, 784.

[137] Lynden-Bell, R.M.; Rasaiah, J.C. From hydrophobic to hydrophilic behaviour: A simulation study of solvation entropy and free energy of simple solutes. *J. Chem. Phys.* **1997**, *107*, 1981.

[138] Ashbaugh, H.S. Convergence of molecular and macroscopic continuum descriptions of ion hydration. *J. Phys. Chem. B* **2000**, *104*, 7235.

[139] Rogers, D.M.; Beck, T.L. Modeling molecular and ionic absolute solvation free energies with quasichemical theory bounds. *J. Chem. Phys.* **2008**, *129*, 134505.

[140] Paluch, M. Electrical properties of free surface of water and aqueous solutions. *Adv. Colloid Interface Sci.* **2000**, *84*, 27.

[141] Pratt, L.R. Contact potentials of solution interfaces: phase equilibrium and interfacial electric fields. *J. Phys. Chem.* **1992**, *96*, 25.

[142] Sokhan, V.P.; Tildesley, D.J. The free surface of water: molecular orientation, surface potential and nonlinear susceptibility. *Mol. Phys.* **1997**, *92*, 625.

[143] Remsing, R.C.; Baer, M.D.; Schenter, G.K.; Mundy, C.J.; Weeks, J.D. The Role of Broken Symmetry in Solvation of a Spherical Cavity in Classical and Quantum Water Models. *J. Phys. Chem. Lett.* **2014**, *5*, 2767.

[144] Shi, Y.; Beck, T.L. Length scales and interfacial potentials in ion hydration. *J. Chem. Phys.* **2013**, *139*, 044504.

[145] Gray, C.G.; Gubbins, K.E. *Theory of Molecular Liquids*. Clarendon Press, Oxford, **1984**.

[146] Milischuk, A.A.; Matyushov, D.V. Equlibrium solvation in quadrupolar solvents. *J. Chem. Phys.* **2005**, *123*, 044501.

[147] Beck, T.L. Hydration free energies by energetic partitioning of the potential distribution theorem. *J. Stat. Phys.* **2011**, *145*, 335.

[148] Bardhan, J.P.; Jungwirth, P.; Makowski, L. Affine-response model of molecular solvation of ions: Accurate predictions of asymmetric charging free energies. *J. Chem. Phys.* **2012**, *137*, 124101.

[149] Gong, H.; Freed, K.F. Langevin-debye model for nonlinear electrostatic screening of solvated ions. *Phys. Rev. Lett.* **2009**, *102*, 057603.

[150] Song, X.; Chandler, D.; Marcus, R.A. Gaussian field model of dielectric solvation dynamics. *J. Phys. Chem.* **1996**, *100*, 11954.

[151] Dolgov, O.V.; Kirzhnits, D.A.; Maksimov, E.G. On an admissible sign of the static dielectric function of matter. *Rev. Mod. Phys.* **1981**, *53*, 81.

[152] Abe, T. A modification of the Born equation. *J. Phys. Chem.* **1986**, *90*, 713.

[153] Mallik, B.; Masunov, A.; Lazaridis, T. Distance and exposure dependent effective dielectric function. *J. Comput. Chem.* **2002**, *23*, 1090.

[154] Friesen, A.D.; Matyushov, D.V. Local polarity excess at the interface of water with a nonpolar solute. *Chem. Phys. Lett.* **2011**, *511*, 256.

[155] Ghoufi, A.; Szymczyk, A.; Renou, R.; Ding, M. Calculation of local dielectric permittivity of confined liquids from spatial dipolar correlations. *EPL* **2012**, *99*, 37008.

[156] Bonthuis, D.J.; Gekle, S.; Netz, R.R. Dielectric profile of interfacial water and its effect on double-layer capacitance. *Phys. Rev. Lett.* **2011**, *107*, 166102.

[157] Takae, K.; Onuki, A. Molecular Dynamics Simulation of Water between Metal Walls under an Electric Field: Dielectric Response and Dynamics after Field Reversal. *J. Phys. Chem. B* **2015**, *119*, 9377.

[158] Matyushov, D.V. Solvent reorganization energy of electron transfer in polar solvents. *J. Chem. Phys.* **2004**, *120*, 7532.

[159] Madden, P.; Kivelson, D. A consistent molecular treatment of dielectric phenomena. *Adv. Chem. Phys.* **1984**, *56*, 467.

[160] Raineri, F.O.; Resat, H.; Friedman, H.L. Static longitudinal dielectric function of model molecular fluids. *J. Chem. Phys.* **1992**, *96*, 3068.

[161] Fonseca, T.; Ladanyi, B.M. Wave vector dependent static dielectric properties of associated liquids: Methanol. *J. Chem. Phys.* **1990**, *11*, 8148.

[162] Stell, G.; Patey, G.N.; Høye, J.S. Dielectric constants of fluid models: Statistical mechanical theory and its quantitayive implementation. *Adv. Chem. Phys.* **1981**, *48*, 183.

[163] Gradshteyn, I.S.; Ryzhik. *Table of Integrals, Series, and Products*. Academic Press, San Diego, **1994**.

[164] Bader, J.S.; Cortis, C.M.; Berne, B.J. Solvation and reorganization energies in polarizable molecular and continuum solvents. *J. Chem. Phys.* **1997**, *106*, 2372.

[165] Felderhof, B.U. Fluctuations of polarization and magnetization in dielectric and magnetic media. *J. Chem. Phys.* **1977**, *67*, 493.

[166] Høye, J.S.; Stell, G. Statistical mechanics of polar fluids in electric fields. *J. Chem. Phys.* **1980**, *72*, 1597.

[167] Figueirido, F.; Del Buono, G.S.; Levy, R.M. On finite-size effects in computer simulations using the Ewald potential. *J. Chem. Phys.* **1995**, *103*, 6133.

[168] Hummer, G.; Pratt, L.R.; García, A.E. Ion Sizes and Finite-Size Corrections for Ionic-Solvation Free Energies. *J. Chem. Phys.* **1997**, *107*, 9275.

[169] Reif, M.M.; Hünenberger, P.H. Computation of methodology-independent single-ion solvation properties from molecular simulations. IV. Optimized Lennard-Jones interaction parameter sets for the alkali and halide ions in water. *J. Chem. Phys.* **2011**, *134*, 144104.

[170] Berne, B.J.; Weeks, J.D.; Zhou, R. Dewetting and hydrophobic interaction in physical and biological systems. *Annu. Rev. Phys. Chem.* **2009**, *60*, 85.

[171] Huang, D.M.; Chandler, D. Cavity formation and the drying transition in the lennard-jones fluid. *Phys. Rev. E* **2000**, *61*, 1501.

[172] Chandler, D. Interfaces and the driving force of hydrophobic assembly. *Nature* **2005**, *437*, 640.

[173] Rajamani, S.; Truskett, T.M.; Garde, S. Hydrophobic hydration from small to large lengthscales: Understanding and manipulating the crossover. *Proc. Natl. Acad. Sci.* **2005**, *102*, 9475.

[174] Kihara, T.; Miyoshi, K. Geometry of three convex bodies applicable to three-molecule clusters in polyatomic gases. *J. Stat. Phys.* **1975**, *13*, 337.

[175] Phillips, J.C.; Braun, R.; Wang, W.; Gumbart, J.; Tajkhorshid, E.; Villa, E.; Chipot, C.; Skeel, R.D.; Kalé, L.; Schulten, K. Scalable molecular dynamics with NAMD. *J. Comput. Chem.* **2005**, *26*, 1781.

[176] Milischuk, A.A.; Matyushov, D.V.; Newton, M.D. Activation entropy of electron transfer reactions. *Chem. Phys.* **2006**, *324*, 172.

[177] Renou, R.; Szymczyk, A.; Maurin, G.; Ghoufi, A. Dielectric anisotropy of water confined into the MIL-53(Cr) metal–organic framework. *Mol. Sim.* **2014**, *41*, 483.

[178] Renou, R.; Szymczyk, A.; Maurin, G.; Malfreyt, P.; Ghoufi, A. Superpermittivity of nanoconfined water. *J. Chem. Phys.* **2015**, *142*, 184706.

[179] Böttcher, C.J.F. *Theory of Electric Polarization*, volume 1. Elsevier, Amsterdam, **1973**.

[180] Kihara, T. Intermolecular forces and equation of state of gases. *Adv. Chem. Phys.* **1958**, *1*, 267.

[181] Guillot, B. A reapraisal of what we have learnt during three decaded of computer simulations of water. *J. Mol. Liq.* **2002**, *101*, 219.

[182] Rick, S.W.; Berne, B.J. The aqueous solvation of water: A comparison of continuum models with Molecular Dynamics. *J. Am. Chem. Soc.* **1994**, *116*, 3949.

[183] Stanley, H.E. *Introduction to phase transitions and critical phenomena*. Oxford University Press, New York, **1987**.

[184] Lee, C.Y.; McCammon, J.A.; Rossky, P.J. The structure of liquid water at an extended hydrophobic surface. *J. Chem. Phys.* **1984**, *80*, 4448.

[185] Daub, C.D.; Bratko, D.; Ali, T.; Luzar, A. Microscopic dynamics of the orientation of a hydrated nanoparticle in an electric field. *Phys. Rev. Lett.* **2009**, *103*, 207801.

[186] Garde, S.; et al. Origin of entropy convergence in hydrophobic hydration and protein folding. *Phys. Rev. Lett.* **1996**, *77*, 4966.

[187] Giovambattista, N.; Debenedetti, P.G.; Rossky, P.J. Effect of surface polarity on water contact angle and interfacial hydration structure. *J. Phys. Chem. B* **2007**, *111*, 9581.

[188] Brovchenko, I.; Oleinikova, A. *Interfacial and confined water*. Elsevier, Amsterdam, **2008**.

[189] Sarupria, S.; Garde, S. Quantifying water density fluctuations and compressibility of hydration shells of hydrophobic solutes and proteins. *Phys. Rev. Lett.* **2009**, *103*, 037803.

[190] Du, Q.; Superfine, R.; Freysz, E.; Shen, Y.R. Vibrational spectroscopy of water at the vapor/water interface. *Phys. Rev. Lett.* **1993**, *70*, 2313.

[191] Davis, J.G.; et al. On the cooperative formation of non-hydrogen-bonded water at molecular hydrophobic interfaces. *Nat. Chem.* **2013**, *5*, 796.

[192] Wernet, P.; et al. The structure of the first coordination shell in liquid water. *Science* **2004**, *304*, 995.

[193] Matyushov, D.V. Time-resolved spectroscopy of polarizable chromophores. *J. Chem. Phys.* **2001**, *115*, 8933.

[194] Wang, F.; et al. Exciton polarizability in semiconductor nanocrystals. *Nat. Mater.* **2006**, *5*, 861.

[195] Frank, H.S.; Evans, M.W. Free volume and entropy in condensed systems iii. entropy in binary liquid mixtures; partial molal entropy in dilute solutions; structure and thermodynamics in aqueous electrolytes. *J. Chem. Phys.* **1945**, *13*, 507.

[196] Buch, V.; Milet, A.; Vácha, R.; Jungwirth, P.; Devlin, J.P. Water surface is acidic. *Proc Natl Acad Sci U S A* **2007**, *104*, 7342.

[197] Baer, M.D.; Stern, A.C.; Levin, Y.; Tobias, D.J.; Mundy, C.J. Electrochemical surface potential due to classical point charge models drives anion adsorption to the air–water interface. *J. Phys. Chem. Lett.* **2012**, *3*, 1565.

[198] Petersen, P.B.; Saykally, R.J. Is the liquid water surface basic or acidic? macroscopic vs. molecular-scale investigations. *Chem. Phys. Lett.* **2008**, *458*, 255.

[199] Yamaguchi, S.; Tahara, T. Development of Electronic Sum Frequency Generation Spectroscopies and Their Application to Liquid Interfaces. *J. Phys. Chem. C* **2015**, *119*, 14815.

[200] Samson, J.S.; Scheu, R.; Smolentsev, N.; Rick, S.W.; Roke, S. Sum frequency spectroscopy of the hydrophobic nanodroplet/water interface: Absence of hydroxyl ion and dangling OH bond signatures. *Chem. Phys. Lett.* **2014**, *615*, 124.

[201] Shapovalov, V.L.; Möhwald, H.; Konovalov, O.V.; Knecht, V. Negligible water surface charge determined using Kelvin probe and total reflection X-ray fluorescence techniques. *Phys. Chem. Chem. Phys.* **2013**, *15*, 13991.

[202] Tian, C.S.; Shen, Y.R. Recent progress on sum-frequency spectroscopy. *Surf. Sci. Rep.* **2014**, *69*, 105.

[203] Bonn, M.; Nagata, Y.; Backus, E.H.G. Molecular Structure and Dynamics of Water at the Water-Air Interface Studied with Surface-Specific Vibrational Spectroscopy. *Angew. Chem. Int. Ed.* **2015**, *54*, 5560.

[204] Mazur, P.; Overbeek, J. On electro-osmosis and streaming-potentials in diaphragms: II. General quantitative relationship between electro-kinetic effects. *Rec. Trav. Chim.* **1951**, *70*, 83.

[205] Strazdaite, S.; Versluis, J.; Bakker, H.J. Water orientation at hydrophobic interfaces. *J. Chem. Phys.* **2015**, *143*, 084708.

[206] Wen, Y.C.; Zha, S.; Liu, X.; Yang, S.; Guo, P.; Shi, G.; Fang, H.; Shen, Y.R.; Tian, C. Unveiling Microscopic Structures of Charged Water Interfaces by Surface-Specific Vibrational Spectroscopy. *Phys. Rev. Lett.* **2016**, *116*, 016101.

[207] Nihonyanagi, S.; Yamaguchi, S.; Tahara, T. Direct evidence for orientational flip-flop of water molecules at charged interfaces: A heterodyne-detected vibrational sum frequency generation study. *J. Chem. Phys.* **2009**, *130*, 204704.

[208] Wang, F.; Shan, J.; Islam, M.A.; Herman, I.P.; Bonn, M.; Heinz, T.F. Exciton polarizability in semiconductor nanocrystals. *Nat. Mater.* **2006**, *5*, 861.

[209] Ohshima, H. *Theory of Colloid And Interfacial Electric Phenomena*. Academic Press, London, **2006**.

[210] Beck, T.L. The influence of water interfacial potentials on ion hydration in bulk water and near interfaces. *Chem. Phys. Lett.* **2013**, *561-562*, 1.

[211] Luzar, A.; Bratko, D.; Blum, L. Monte Carlo simulation of hydrophobic interaction. *J. Chem. Phys.* **1987**, *86*, 2955.

[212] Scatena, L.F.; Richmond, G.L. Orientation, hydrogen bonding, and penetration of water at the organic/water interface. *J. Phys. Chem. B* **2001**, *105*, 11240.

[213] Strazdaite, S.; Versluis, J.; Backus, E.H.G.; Bakker, H.J. Enhanced ordering of water at hydrophobic surfaces. *J. Chem. Phys.* **2014**, *140*, 054711.

[214] Bonthuis, D.J.; Rinne, K.F.; Falk, K.; Kaplan, C.N.; Horinek, D.; Berker, A.N.; Bocquet, L.; Netz, R.R. Theory and simulations of water flow through carbon nanotubes: prospects and pitfalls. *J. Phys.: Condens. Matter* **2011**, *23*, 184110.

[215] Einstein, A. *Investigations on the theory of the Brownian movement*. BN Publishing, **2011**.

[216] Bratko, D.; Daub, C.D.; Leung, K.; Luzar, A. Effect of field direction on electrowetting in a nanopore. *J. Am. Chem. Soc.* **2007**, *129*, 2504.

[217] Falkenhagen, H. *Electrolytes*. Clarendon Press, Oxford, **1934**.

[218] Knecht, V.; Klasczyk, B.; Dimova, R. Macro- versus Microscopic View on the Electrokinetics of a Water–Membrane Interface. *Langmuir* **2013**, *29*, 7939.

[219] Pieniazek, P.A.; Tainter, C.J.; Skinner, J.L. Interpretation of the water surface vibrational sum-frequency spectrum. *J. Chem. Phys.* **2011**, *135*, 044701.

[220] Roy, S.; Gruenbaum, S.M.; Skinner, J.L. Theoretical vibrational sum-frequency generation spectroscopy of water near lipid and surfactant monolayer interfaces. *J. Chem. Phys.* **2014**, *141*, 18C502.

[221] Drzymala, J.; Sadowski, Z.; Holysz, L.; Chibowski, E. Ice/water interface: Zeta potential, point of zero charge, and hydrophobicity. *J. Colloid Interface Sci.* **1999**, *220*, 229.

[222] Fleming, G.R.; Cho, M. Chromophore-solvent dynamics. *Annu. Rev. Phys. Chem.* **1996**, *47*, 109.

[223] Roberts, S.T.; Loparo, J.J.; Tokmakoff, A. Characterization of spectral diffusion from two-dimensional line shapes. *J. Chem. Phys.* **2006**, *125*, 084502.

[224] Mataga, N.; Kubota, T. *Molecular interactions and electronic spectra*. Marcel Dekker, New York, **1970**.

[225] Gardiner, C.W. *Handbook of Stochastic Methods*. Springer, Berlin, **1997**.

[226] Tanimura, Y. Stochastic Liouville, Langevin, Fokker-Planck, and Master Equation Approaches to Quantum Dissipative Systems. *J. Phys. Soc. Jpn.* **2006**, *75*, 082001.

[227] Matyushov, D.V.; Voth, G.A. A theory of electron transfer and steady-state optical spectra of chromophores with varying electronic polarizability. *J. Phys. Chem. A* **1999**, *103*, 10981.

[228] Sajadi, M.; Obernhuber, T.; Kovalenko, S.A.; Mosquera, M.; Dick, B.; Ernsting, N.P. Dynamic Polar Solvation Is Reported by Fluorescing 4-Aminophthalimide Faithfully Despite H-Bonding. *J. Phys. Chem. A* **2009**, *113*, 44.

[229] Fischer, G. *Vibronic coupling*. Academic Press, London, **1984**.

[230] Lawrence, C.P.; Skinner, J.L. Vibrational spectroscopy of HOD in liquid D_2O. II. Infrared line shapes and vibrational Stokes shift. *J. Chem. Phys.* **2002**, *117*, 8847.

[231] Fecko, C.J.; Eaves, J.D.; Loparo, J.J.; Tokmakoff, A.; Geissler, P.L. Ultrafast hydrogen-bond dynamics in the infrared spectroscopy of water. *Science* **2003**, *301*, 1698.

[232] Kwac, K.; Lee, H.; Cho, M. Non-Gaussian statistics of amide I mode frequency fluctuation of N-methylacetamide in methanol solution: Linear and nonlinear vibrational spectra. *J. Chem. Phys* **2004**, *120*, 1477.

[233] Bredenbeck, J.; Helbing, J.; Hamm, P. Solvation beyond the Linear Response Regime. *Phys. Rev. Lett.* **2005**, *95*, 083201.

[234] Roy, S.; Pshenichnikov, M.S.; Jansen, T.L.C. Analysis of 2D CS Spectra for Systems with Non-Gaussian Dynamics. *J. Phys. Chem. B* **2011**, *115*, 5431.

[235] Dutta, S.; Li, Y.L.; Rock, W.; Houtman, J.C.D.; Kohen, A.; Cheatum, C.M. 3-Picolyl Azide Adenine Dinucleotide as a Probe of Femtosecond to Picosecond Enzyme Dynamics. *J. Phys. Chem. B* **2012**, *116*, 542.

[236] Muljarov, E.; Zimmermann, R. Dephasing in Quantum Dots: Quadratic Coupling to Acoustic Phonons. *Phys. Rev. Lett.* **2004**, *93*, 237401.

[237] Garrett-Roe, S.; Hamm, P. What can we learn from three-dimensional infrared spectroscopy? *Acc. Chem. Res.* **2009**, *42*, 1412.

[238] Jansen, T.L.C.; Cringus, D.; Pshenichnikov, M.S. Dissimilar dynamics of coupled water vibrations. *J. Phys. Chem. A* **2009**, *113*, 6260.

[239] Auer, B.M.; Skinner, J.L. IR and Raman spectra of liquid water: Theory and interpretation. *J. Chem. Phys.* **2008**, *128*, 224511.

[240] Yang, M.; Skinner, J.L. Signatures of coherent vibrational energy transfer in ir and raman line shapes for liquid water. *Phys. Chem. Chem. Phys.* **2010**, *12*, 982.

[241] Saggu, M.; Levinson, N.M.; Boxer, S.G. Experimental quantification of electrostatics in $X - H \ldots \pi$ hydrogen bonds. *J. Am. Chem. Soc.* **2012**, *134*, 18986.

[242] Chaikin, P.M.; Lubensky, T.C. *Principles of condensed matter physics*. Cambridge University Press, Cambridge, **1995**.

[243] Wang, M.C.; Uhlenbeck, G.E. On the theory of the brownian motion II. *Rev. Mod. Phys.* **1945**, *17*, 323.

[244] Stephens, M.D.; Saven, J.G.; Skinner, J.L. Molecular theory of electronic spectroscopy in nonpolar fluids: Ultrafast solvation dynamics and absorption and emission line shapes. *J. Chem. Phys.* **1997**, *106*, 2129.

[245] Bixon, M.; Jortner, J. Electron transfer – from isolated molecules to biomolecules. *Adv. Chem. Phys.* **1999**, *106*, 35.

[246] Marcus, R.A. Relation between charge transfer absorption and fluorescence spectra and the inverted region. *J. Phys. Chem.* **1989**, *93*, 3078.

[247] Richert, R. Triplet state solvation dynamics: Basics and applications. *J. Chem. Phys.* **2000**, *113*, 8404.

[248] Mahan, G.D. *Many-Particle Physics*. Plenum Press, New York, **1990**.

[249] Carter, E.A.; Hynes, J.T. Solvation dynamics for an ion pair in a polar solvent: Time-dependent fluorescence and photochemical charge transfer. *J. Chem. Phys.* **1991**, *94*, 5961.

[250] Ladanyi, B.M.; Skaf, M.S. Computer simulation of hydrogen-bonding liquids. *Annu. Rev. Phys. Chem.* **1993**, *44*, 335.

[251] Maroncelli, M.; Fleming, G.R. Computer simulation of the dynamics of aqueous solvation. *J. Chem. Phys.* **1988**, *89*, 5044.

[252] Laird, B.B.; Thompson, W.H. Time-dependent fluorescence in nanoconfined solvents: Linear-response approximations and Gaussian statistics. *J. Chem. Phys.* **2011**, *135*, 084511.

[253] Ramasesha, K.; De Marco, L.; Horning, A.D.; Mandal, A.; Tokmakoff, A. A phenomenological approach to modeling chemical dynamics in nonlinear and two-dimensional spectroscopy. *J. Chem. Phys.* **2012**, *136*, 134507.

[254] Kinoshita, S. Theory of transient hole-burning spectrum for molecules in solution. *J. Chem. Phys.* **1989**, *91*, 5175.

[255] Kleinert, H. *Path Integrals in Quantum Mechanics, Statistics, Polymer Physics, and Financial Markets*. World Scientific, New Jersey, 3rd edition, **2004**.

[256] Piryatinski, A.; Skinner, J.L. Determining Vibrational Solvation-Correlation Functions from Three-Pulse Infrared Photon Echoes. *J. Phys. Chem. B* **2002**, *106*, 8055.

[257] Lazonder, K.; Pshenichnikov, M.S.; Wiersma, D.A. Easy interpretation of optical two-dimensional correlation spectra. *Opt. Lett.* **2006**, *31*, 3354.

[258] Kwak, K.; Park, S.; Finkelstein, I.J.; Fayer, M.D. Frequency-frequency correlation functions and apodization in two-dimensional infrared vibrational echo spectroscopy: A new approach. *J. Chem. Phys.* **2007**, *127*, 124503.

[259] Kraemer, D.; Cowan, M.L.; Paarmann, A.; Huse, N.; Nibbering, E.T.J.; Elsaesser, T.; Miller, R.J.D. Temperature dependence of the two-dimensional infrared spectrum of liquid H_2O. *Proc. Natl. Acad. Sci. USA* **2008**, *105*, 437.

[260] Renge, I. On the determination of molecular polarizability changes upon electronic excitation from the solvent shifts of absorption band maxima. *Chem. Phys.* **1992**, *167*, 173.

[261] Suppan, P. Excited-state dipole moments from absorption/fluorescence solvatochromic ratios. *Chem. Phys. Lett.* **1983**, *94*, 272.

[262] Lamoureux, G.; Roux, B. Modeling induced polarization with classical Drude oscillators: Theory and molecular dynamics simulation algorithm. *J. Chem. Phys.* **2003**, *119*, 3025.

[263] and, J.C.P. Scalable molecular dynamics with NAMD. *J. Comp. Chem.* **2005**, *26*, 1781.

[264] Aragones, J.L.; MacDowell, L.G.; Vega, C. Dielectric Constant of Ices and Water: A Lesson about Water Interactions. *J. Phys. Chem. A* **2011**, *115*, 5745.

[265] Bursulaya, B.D.; Zichi, D.A.; Kim, H.J. Role of solute electronic polarizability in solvation dynamics. *J. Phys. Chem.* **1995**, *99*, 10069.

[266] Kumar, P.V.; Maroncelli, M. Polar solvation dynamics of polyatomic solutes: Simulation studies in acetonitrile and methanol. *J. Chem. Phys.* **1995**, *103*, 3038.

[267] Nicholls, D.G.; Ferguson, S.J. *Bioenergetics 3*. Academic Press, London, **2002**.

[268] Liu, J.; Chakraborty, S.; Hosseinzadeh, P.; Yu, Y.; Tian, S.; Petrik, I.; Bhagi, A.; Lu, Y. Metalloproteins Containing Cytochrome, Iron–Sulfur, or Copper Redox Centers. *Chem. Rev.* **2014**, *114*, 4366.

[269] Zhang, Y.; Straub, J.E. Diversity of solvent dependent energy transfer pathways in heme proteins. *J. Phys. Chem. B* **2009**, *113*, 825.

[270] He, Y.; Chen, J.Y.; Knab, J.R.; Zheng, W.; Markelz, A.G. Evidence of protein collective motions on the picosecond timescale. *Biophys. J.* **2011**, *100*, 1058.

[271] Muegge, I.; Qi, P.X.; Wand, A.J.; Chu, Z.T.; Warshel, A. The reorganizatiom energy of cytochrome *c* revisited. *J. Phys. Chem. B* **1997**, *101*, 825.

[272] Chakrabarty, S.; Warshel, A. Capturing the energetics of water insertion in biological systems: The water flooding approach. *Proteins* **2013**, *81*, 93.

[273] Gray, H.B.; Winkler, J.R. Long-range electron transfer. *Proc. Natl. Acad. Sci.* **2005**, *102*, 3534.

[274] Blumberger, J.; Klein, M.L. Reorganization free energies of long-range electron transfer in porphyrin-binding four-helix bundle protein. *J. Am. Chem. Soc.* **2006**, *128*, 13854.

[275] McCullagh, M.; Voth, G.A. Unraveling the Role of the Protein Environment for [FeFe]-Hydrogenase: A New Application of Coarse-Graining. *J. Phys. Chem. B* **2013**, *117*, 4062.

[276] Woiczikowski, P.B.; Steinbrecher, T.; Kubar, T.; Elstner, M. Nonadiabatic QM/MM Simulations of Fast Charge Transfer in Escherichia coli DNA Photolyase. *J. Phys. Chem. B* **2011**, *115*, 9846.

[277] Yue, H.; Khoshtariya, D.; Waldeck, D.H.; Grochol, J.; Hildebrandt, P.; Murgida, D.H. On the electron transfer mechanism between cytochrome *c* and metal electrodes. Evidence for dynamic control at short distances. *J. Phys. Chem. B* **2006**, *110*, 19906.

[278] Alvarez-Paggi, D.; Zitare, U.; Murgida, D.H. The role of protein dynamics and thermal fluctuations in regulating cytochrome c/cytochrome c oxidase electron transfer. *Biochim. Biophys. Acta - Bioenergetics* **2014**, *1837*, 1196.

[279] Warshel, A. Dynamics of reactions in polar solvents. Semiclassical trajectory studies of electron-transfer and proton-transfer reactions. *J. Phys. Chem.* **1982**, *86*, 2218.

[280] Beratan, D.N.; Betts, J.N.; Onuchic, J.N. Tunneling pathway and redox-state-dependent electronic couplings at nearly fixed distance in electron transfer proteins. *J. Phys. Chem.* **1992**, *96*, 2852.

[281] Hayashi, T.; Stuchebrukhov, A.A.; Gray, H.B. Electron tunneling in respiratory complex I. *Proc. Natl. Acad. Sci. USA* **2010**, *107*, 19157.

[282] Zhang, Y.; Liu, C.; Balaeff, A.; Skourtis, S.S.; Beratan, D.N. Biological charge transfer via flickering resonance. *Proc. Natl. Acad. Sci. USA* **2014**, *111*, 10049.

[283] LeBard, D.N.; Matyushov, D.V. Protein-water electrostatics and principles of bioenergetics. *Phys. Chem. Chem. Phys.* **2010**, *12*, 15335.

[284] Angell, C.A. Formation of glasses from liquids and biopolymers. *Science* **1995**, *267*, 1924.

[285] Debenedetti, P.G.; Stillinger, F.H. Supercooled liquids and glass transitions. *Nature* **2001**, *410*, 259.

[286] Frauenfelder, H.; Chen, G.; Berendzen, J.; Fenimore, P.W.; Jansson, H.; McMahon, B.H.; Stroe, I.R.; Swenson, J.; Young, R.D. A unified model of protein dynamics. *Proc. Natl. Acad. Sci. USA* **2009**, *106*, 5129.

[287] Monari, S.; Battistuzzi, G.; Borsari, M.; Millo, D.; Gooijer, C.; van der Zwan, G.; Ranieri, A.; Sola, M. Thermodynamic and kinetic aspect of electron transfer reaction of bovide cytochrome c immobilized on 4-mercaptopyridine and 11-mercapto-1-undecanoid acid films. *J. Appl. Electrochem.* **2008**, *38*, 885.

[288] Monari, S.; Battistuzzi, G.; Bortolotti, C.A.; Yanagisawa, S.; Sato, K.; Li, C.; Salard, I.; Kostrz, D.; Borsari, M.; Ranieri, A.; Dennison, C.; Sola, M. Understanding the mechanism of short-range electron transfer using an immobilized cupredoxin. *J. Am. Chem. Soc.* **2012**, *134*, 11848.

[289] Lockhart, D.J.; Boxer, S.G. Stark effect spectroscopy of Rhodobacter sphaeroides and Rhodopseudomonas viridis reaction centers. *Proc. Natl. Acad. Sci. USA* **1988**, *85*, 107.

[290] Warshel, A.; Weiss, R.M. An empirical valence bond approach for comparing reactions in solutions and in enzymes. *J. Am. Chem. Soc.* **1980**, *102*, 6218.

[291] Warshel, A. *Computer modeling of chemical reactions in enzymes and solutions.* Wiley Interscience, New York, **1991**.

[292] Kamerlin, S.C.L.; Warshel, A. The empirical valence bond model: theory and applications. *Wiley Interdisciplinary Reviews: Comput. Mol. Sci.* **2011**, *1*, 30.

[293] Gao, J.; Truhlar, D.G. Quantum Mechanical Methods for Enzyme Kinetics. *Annu. Rev. Phys. Chem.* **2002**, *53*, 467.

[294] Garcia-Viloca, M.; Gao, J.; Karplus, M.; Truhlar, D.G. How enzymes work: Analysis by modern rate theory and computer simulations. *Science* **2004**, *303*, 186.

[295] Nilsson, L.; Halle, B. Molecular origin of time-dependent fluorescence shift in proteins. *Proc. Natl. Acad. Sci.* **2005**, *102*, 13867.

[296] Gupta, S.; Matyushov, D.V. Solvent and solute polarizability effects on the reorganization energy of electron transfer. *J. Phys. Chem. A* **2004**, *108*, 2087.

[297] Warshel, A.; Sharma, P.K.; Kato, M.; Xiang, Y.; Liu, H.; Olsson, M.H.M. Electrostatic basis for enzyme catalysis. *Chem. Rev.* **2006**, *106*, 3210.

[298] Sprik, M. Computer simulation of the dynamics of induced polarization fluctuations in water. *J. Phys. Chem.* **1991**, *95*, 2283.

[299] Martin, D.R.; Fioretto, D.; Matyushov, D.V. Depolarized light scattering and dielectric response of a peptide dissolved in water. *J. Chem. Phys.* **2014**, *140*, 035101.

[300] Feller, S.E.; Mackerell Jr, A.D.; Mackerell, A.D.J. An Improved Empirical Potential Energy Function for Molecular Simulations of Phospholipids Supporting 2. *J. Phys. Chem. B* **2000**, *104*, 7510.

[301] Leu, B.M.; Zhang, Y.; Bu, L.; Straub, J.E.; Zhao, J.; Sturhahn, W.; Alp, E.E.; Sage, J.T. Resilience of the iron environment in heme proteins. *Biophys. J.* **2008**, *95*, 5874.

[302] Kaszuba, K.; Postila, P.A.; Cramariuc, O.; Sarewicz, M.; Osyczka, A.; Vattulainen, I.; Róg, T. Parameterization of the prosthetic redox centers of the bacterial cytochrome bc1 complex for atomistic molecular dynamics simulations. *Theor. Chem. Acc.* **2013**, *132*, 1.

[303] Kleingardner, J.G.; Bren, K.L. Biological Significance and Applications of Heme c Proteins and Peptides. *Acc. Chem. Res.* **2015**, *48*, 1845.

[304] Marti, M.A.; Capece, L.; Crespo, A.; Doctorovich, F.; Estrin, D.A. Nitric oxide interaction with cytochrome c' and its relevance to guanylate cyclase. Why does the iron histidine bond break? *J. Am. Chem. Soc.* **2005**, *127*, 7721.

[305] Frisch, M.J.; et al. Gaussian 09 Revision E.01, **2009**.

[306] Zerner, M.C.; Loew, G.H.; Kirchner, R.F.; Mueller-Westerhoff, U.T. An intermediate neglect of differential overlap technique for spectroscopy of transition-metal complexes. Ferrocene. *J. Am. Chem. Soc.* **1980**, *102*, 589.

[307] Hünenberger, P.H.; McCammon, J.A. Ewald artifacts in computer simulations of ionic solvation and ion–ion interaction: A continuum electrostatics study. *J. Chem. Phys.* **1999**, *110*, 1856.

[308] Martin, D.R.; Matyushov, D.V. Non-Gaussian statistics and nanosecond dynamics of electrostatic fluctuations affecting optical transitions in a green fluorescent protein. *J. Phys. Chem. B* **2012**, *116*, 10294.

[309] Ayala, R.; Sprik, M. A Classical Point Charge Model Study of System Size Dependence of Oxidation and Reorganization Free Energies in Aqueous Solution †. *J. Phys. Chem. B* **2008**, *112*, 257.

[310] Roy, S.; Pshenichnikov, M.S.; Jansen, T.L.C. Analysis of 2D CS spectra for systems with non-gaussian dynamics. *J. Phys. Chem. B* **2011**, *115*, 5431.

[311] Landau, L.D.; Lifshits, E.M. *Fluid Mechanics*. Elsevier, Amsterdam, 2nd edition, **2004**.

APPENDIX A

LOCAL INTERFACIAL SUSCEPTIBILITY

Here the local susceptibility of the interface $\chi_0(r)$ is derived based on the formalism of pair distribution functions of the theory of liquids[145]. The starting expression for the susceptibility is

$$\chi_0(r) = 4\pi\beta\langle\delta P_r(r)\delta M_r\rangle_0, \tag{A.1}$$

where $\beta = 1/(k_{\mathrm{B}}T)$. The instantaneous value of the fluctuating radial projection of the solvent polarization density is given by the expression

$$P_r(\mathbf{r}) = \sum_j (\mathbf{m}_j \cdot \hat{\mathbf{r}}_j)\, \delta(\mathbf{r} - \mathbf{r}_j) \tag{A.2}$$

and $\delta P_r(\mathbf{r}) = P_r(\mathbf{r}) - \langle P_r(\mathbf{r})\rangle_0$. Further, M_r is the integral of $P_r(\mathbf{r})$ over the volume occupied by the solvent and $\mathbf{m}_j$ is the dipole moment of molecule j with the position $\mathbf{r}_j$. The equation for $\chi_0(\mathbf{r})$ can be split into the two-particle (solute-solvent) and three particle (solute-solvent-solvent) terms

$$\begin{aligned}\chi_0(r) = 4\pi\beta &\sum_j \langle(\mathbf{m}_j \cdot \hat{\mathbf{r}}_j)^2 \delta(\mathbf{r} - \mathbf{r}_j)\rangle_0 \\ + 4\pi\beta &\sum_{j\neq k} \langle(\mathbf{m}_j \cdot \hat{\mathbf{r}}_j)(\mathbf{m}_k \cdot \hat{\mathbf{r}}_k)\delta(\mathbf{r} - \mathbf{r}_j)\rangle_0.\end{aligned} \tag{A.3}$$

The first summand is given in terms of the solute-solvent pair distribution function $g_{0s}(\mathbf{r}\omega_1)$ as

$$\chi_0^{(1)}(r_1) = 4\pi\beta\rho \int \frac{d\omega_1}{4\pi} (\mathbf{m}_1 \cdot \hat{\mathbf{r}}_1)^2 g_{0s}(\mathbf{r}_1\omega_1), \tag{A.4}$$

where ρ is the number density of the liquid. For dipolar liquids, the pair distribution function can be expanded in rotational invariants as follows[145, 60]

$$g_{0s}(\mathbf{r}_1\omega_1) = g_{0s}^{(0)}(r_1) + g^{\Delta}(r_1)\Delta(1, \hat{\mathbf{r}}_1) + \ldots, \tag{A.5}$$

where $\Delta(1, \hat{\mathbf{r}}_1) = (\hat{\mathbf{e}}_1 \cdot \hat{\mathbf{r}}_1)$. The angular integral involving angular projections of the pair distribution function is zero and one gets

$$\chi_0^{(1)}(r) = 3y g_{0s}^{(0)}(r), \tag{A.6}$$

where $y = (4\pi/9)\beta\rho m^2$ is the usual density of dipoles in a polar liquid[162, 60].

The second, three-particle term in Eq. (A.3) can be expressed in terms of the three-particle solute-solvent-solvent distribution function $g(\mathbf{r}_1\omega_1, \mathbf{r}_2\omega_2)$ as follows

$$\begin{aligned}\chi_0^{(2)}(r_1) =& 9y\rho \int d\mathbf{r}_2 \frac{d\omega_1 d\omega_2}{(4\pi)^2}(\hat{\mathbf{e}}_1 \cdot \hat{\mathbf{r}}_1)(\hat{\mathbf{r}}_2 \cdot \hat{\mathbf{e}}_2) \\ & [g(\mathbf{r}_1\omega_1, \mathbf{r}_2\omega_2) - g_{0s}(\mathbf{r}_1\omega_1) g_{0s}(\mathbf{r}_2\omega_2)]\end{aligned} \tag{A.7}$$

With the use of the Kirkwood superposition approximation[145], this equation becomes

$$\begin{aligned}\chi_0^{(2)}(r_1) =& 9y\rho \int d\mathbf{r}_2 \frac{d\omega_1 d\omega_2}{(4\pi)^2}(\hat{\mathbf{e}}_1 \cdot \hat{\mathbf{r}}_1)(\hat{\mathbf{r}}_2 \cdot \hat{\mathbf{e}}_2) \\ & g_{0s}(\mathbf{r}_1\omega_1) g_{0s}(\mathbf{r}_2\omega_2) h_{ss}(12),\end{aligned} \tag{A.8}$$

where $h_{ss}(12) = g_{ss}(12) - 1$ is the solvent-solvent pair correlation function depending on the positions and orientations of two solvent molecules, $1 = \{\mathbf{r}_1\omega_1\}$. As before, the solvent-solvent correlation function is expanded in rotational invariants as follows

$$h_{ss}(12) = h^{(0)}(r_{12}) + h^{\Delta}(r_{12})\Delta(12) + h^{D}(r_{12}) D_{12}(12), \tag{A.9}$$

where and $D_{12}(1,2) = 3(\hat{\mathbf{e}}_1 \cdot \hat{\mathbf{r}}_{12})(\hat{\mathbf{r}}_{12} \cdot \hat{\mathbf{e}}_2) - (\hat{\mathbf{e}}_1 \cdot \hat{\mathbf{e}}_2)$, $\mathbf{r}_{12} = \mathbf{r}_2 - \mathbf{r}_1$, and $\hat{\mathbf{e}}_i$ are unit vectors along molecular dipoles. Further, $h^{\Delta}(r_{12})$ and $h^{D}(r_{12})$ are the radial projections of the pair correlation function on the corresponding rotational invariants.

The calculation of the integral over the orientations of two molecules of the solvent is performed similarly for each projection h^{Δ} and h^{D}; the $h^{(0)}$ projection gives zero from angular integration. For the Δ-projection one obtains upon transferring to the inverted $\mathbf{k}$-space

$$\begin{aligned}\chi_{0\Delta}^{(2)}(r) = y\rho g_{0s}^{(0)}(r) & \int d\mathbf{r}_2 g_{0s}^{(0)}(r_2) \\ & \int \frac{d\mathbf{k}}{(2\pi)^3} j_1(kr) j_1(kr_2) \tilde{h}^{\Delta}(k),\end{aligned} \tag{A.10}$$

where $\tilde{h}^{\Delta}(k)$ is the zero-order Hankel transform (Ref. 162, p. 235) of $h^{\Delta}(r)$ and $j_n(x)$ is the spherical Bessel function of the order n. A similar relation for the D-projection leads

to the expression containing $\tilde{h}^D(k)$, which is the second-order Hankel transform of $h^D(r)$. For a general order ℓ one has[162]

$$\tilde{h}_\ell(k) = 4\pi i^\ell \int_0^\infty r^2 j_\ell(kr) h(r) dr. \tag{A.11}$$

In order to arrive at a closed-form expression for the local susceptibility $\chi_0(r)$, we will simplify the problem by considering the $k \to 0$ limit of both $\tilde{h}^\Delta$ and $\tilde{h}^D$ projections. This approximation is valid in the limit of large solutes, substantially exceeding in size the solvent molecules. The problem then significantly simplifies due to the orthogonality property of the spherical Bessel functions

$$\int_0^\infty j_n(kr) j_n(kr') k^2 dk = \frac{\pi}{2r^2} \delta(r - r'). \tag{A.12}$$

We get as the result for the sum of Δ and D terms contributing to $\chi_0^{(2)}$ the following simple relation

$$\chi_0^{(2)}(r) = y\rho \left[g_{0s}^{(0)}(r) \right]^2 \left(\tilde{h}^\Delta(0) + 2\tilde{h}^D(0) \right). \tag{A.13}$$

One can connect this expression to the longitudinal dielectric susceptibility since the term in the round brackets in Eq. (A.13) is directly related to the $k = 0$ value of the longitudinal structure factor[60, 162]

$$S^L(k) = 1 + (\rho/3) \left[\tilde{h}^\Delta(k) + 2\tilde{h}^D(k) \right]. \tag{A.14}$$

We finally obtain for the local susceptibility

$$\chi_0(r) = \left(1 - \epsilon^{-1}\right) \left[g_{0s}^{(0)}(r) \right]^2 - 3y g_{0s}^{(0)}(r) h_{0s}^{(0)}(r), \tag{A.15}$$

where $h_{0s}^{(0)}(r) = g_{0s}^{(0)}(r) - 1$. The second term in this relation represents electrostatic potential fluctuations due to translational motions of the solvent multipoles. In contrast to orientational dipolar fluctuations, these fluctuations are short-ranged with the result that the proportionality to β in the density of dipoles y is not eliminated. The term appearing

here is a result of the perturbation approach to these density fluctuations, which becomes unreliable for highly polar solvents with large values of y. Renormalization of the polarity dependence by higher-order correlations (such as Stell's Padé approximation[145]) is required in the limit of $y \gg 1$. Since any theory of this kind[61] would significantly complicate our discussion, this term is dropped from the final expression for $\chi_0(r)$ used in the main text. Note also that this term is identically zero in the limit of a structureless continuum surrounding the solute since in that case $g_{0s}^{(0)}(r) = \theta(r - r_{\max})$ and $g_{0s}^{(0)} h_{0s}^{(0)} = 0$.

APPENDIX B

ELECTRO-OSMOTIC CURRENT: ONSAGER RECIPROCAL RELATIONS

In order to prove the Onsager reciprocal relations for the problem of electro-osmotic current, one needs to consider the volume transport V in response to the applied gradient of the external electrostatic potential $\nabla\phi_{\text{ext}}$ and the streaming current I in response to the applied pressure gradient ∇p: $V = L_{12}\nabla\phi_{\text{ext}}$, $I = L_{21}\nabla p$. The Onsager reciprocal relations then require $L_{12} = L_{21}$.

We start with the equation of motion for the stationary flow of an incompressible fluid ($\nabla \cdot \mathbf{v} = 0$) along the z-axis of a capillary [311]

$$-\eta\nabla^2 v_z + \rho(\mathbf{v}\cdot\nabla)v_z = -\nabla_z p + f_z. \tag{B.1}$$

Here, $v_z(x, y)$ changes only along the cross section of the capillary (x, y axes) and, therefore, $\nabla^2 = \partial^2/\partial x^2 + \partial^2/\partial y^2$. Further, η is the viscosity and ρ is the fluid density. Since no convective motion of the liquid occurs, $(\mathbf{v}\cdot\nabla)v_z$ vanishes.

In contrast to the standard textbook description considering free charges only, the force density f_z in Eq. (B.1) is caused by a constant external field, $E_z = -\nabla_z\phi_{\text{ext}}$, applied to the entire, free and bound, charge: $f_z = \rho(\mathbf{r})E_z$, $\rho = \rho_i - \nabla\cdot\mathbf{P}$. Since the curl of $\mathbf{P}$ disappears in the divergence $\nabla\cdot\mathbf{P}$, one can put $\mathbf{P} = -\nabla\phi_b$ with the results

$$\rho = -\frac{1}{4\pi}\nabla^2\phi, \quad \phi = \phi_i - 4\pi\phi_b, \tag{B.2}$$

where ϕ_i is the electrostatic potential of free charges.

We now proceed to calculate v_z under the action of the force f_z assuming no pressure applied to the capillary. The result from Eqs. (B.1) and (B.2) is

$$v_z = -\frac{\phi_0 - \phi}{4\pi\eta}E_z, \tag{B.3}$$

where ϕ_0 is the potential at the shear surface at which $v_z = 0$. In standard notations $\phi_0 = \epsilon_s\zeta$, where ζ is the ζ-potential and ϵ_s accounts for the screening by bound charges. Here, the potential of bound charges is a part of ϕ and ϵ_s does not appear explicitly. A

similar line of arguments can be applied to the potential of free charges ϕ_i connected to ϕ through a closure relation. When the constitutive relations of continuous dielectrics are used, one has $\phi = \epsilon_s \phi_i$, where ϕ_i can be determined from solving the Poisson-Boltzmann equation for the electrolyte next to the capillary wall. These details are irrelevant to our purpose since the derivation requires only the Coulomb law and the corresponding Laplace equation.

From Eq. (B.3), one gets the volume transport

$$V = \int v_z dS = L_{12} \nabla_z \phi_{\text{ext}} \tag{B.4}$$

with

$$L_{12} = \frac{\phi_0}{4\pi\eta} \int (1 - \phi/\phi_0) dS. \tag{B.5}$$

We now turn to the streaming current when the capillary is subjected to the pressure gradient $-\nabla_z p$. The current is given by the equation

$$I = \int v_z \rho dS = \frac{1}{4\pi} \int (\phi_0 - \phi) \nabla^2 v_z dS. \tag{B.6}$$

We now put $f_z = 0$ in Eq. (B.1), which results in

$$I = L_{21} \nabla_z p. \tag{B.7}$$

It is easy to see that

$$L_{21} = L_{12}, \tag{B.8}$$

where L_{12} is given by Eq. (B.5).

B.0.7 ζ potential

Here we present the calculation of the ζ-potential based on the MD data for the Kihara solute in SPC/E water[154]. In the absence of electrolyte effects, the ζ-potential is given

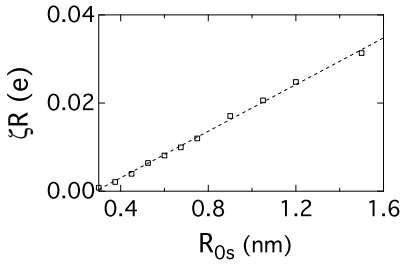

FIGURE B1: ζR calculated from Eq. (B.9) for the Kihara solutes with $\epsilon_{0s} = 0.65$ kJ/mol in SPC/E water ($\epsilon_s = 71$). The dashed line is the linear fit: $-0.0076 + 0.0264(R_{0s}/\mathrm{nm})$.

by the relation

$$\zeta = \frac{4\pi R_{0s}^2 \sigma_0}{\epsilon_s R}. \tag{B.9}$$

We have noticed that $\sigma_0 R_{0s}^2$ is well reproduced by a linear dependence at large R_{0s}: $\zeta \simeq 0.026(R_{0s}/R)(\mathrm{e/nm})$ (Fig. B1). Neglecting the difference between R_{0s} and R at large sizes of the solutes, one gets $\zeta = 38$ mV in the limit of large solutes.

B.1 Power of the external source

It is instructive to derive the power required from an external source to move the dissolved colloidal particles. The rate of doing work on altering polarization of the liquid is

$$P = \int \dot{\mathbf{P}} \cdot \mathbf{E} d\mathbf{r}. \tag{B.10}$$

If the reference frame is placed at the particle drifting with the velocity u, then the solvent moves with the velocity $-u$ opposite to the direction of the drift and $\dot{\mathbf{P}} = \dot{\mathbf{r}} \partial P_r/\partial r = -\mathbf{u}\partial P/\partial r$. One gets for the power

$$P = -N_0 u E \int (\partial P_r/\partial r) d\mathbf{r} = 4\pi N_0 u \left[a^2 P_a - R^2 P_R\right] E, \tag{B.11}$$

where N_0 is the number of colloidal particles. From Eq. (5) in the main text, when the flux of free charge is added to the polarization current, one gets for the colloidal particles

$$P = N_0 u E \langle Q_R \rangle. \tag{B.12}$$

APPENDIX C

LINEAR RESPONSE FOR SPECTRAL CORRELATION FUNCTIONS

Here the derivations of the Stokes-shift, $S_\omega(t)$ and spectral width, $S_\sigma(t)$ in terms of time correlation functions are presented using the Kubo-Zwanzig linear response [60].

One can consider propagation of the dynamics by either employing statistical averages over the ground-state or excited-state equilibrium ensemble [249]. In the former case, the time-dependent Hamiltonian is $H(t) = H_g(t) + \omega(t)\theta(t)$, where $\omega(t) = H_e(t) - H_g(t)$ is considered as the linear response perturbation and $\theta(t)$ is the Heaviside function. In the latter case, one has $H(t) = H_e(t) - \omega(t)\theta(-t)$. We assume that the ground-state equilibrium distribution of the chromophores is promoted to the excited state at $t = 0$ and starts to evolve on the excite surface for $t > 0$. The derivation repeats the same steps in either definition of the perturbation. We provide here the derivation steps when the statistical average is taken over the ground-state equilibrium distribution.

C.1 Stokes-shift correlation function

The linear response to the perturbation $H'(t) = \omega(t)\theta(t)$ is given by [60]

$$\langle\omega\rangle_t - \langle\omega\rangle_0 = -\beta\hbar \int_{-\infty}^{t} \langle\omega(t-s)\dot{\omega}(0)\rangle\theta(s)ds \tag{C.1}$$

where $\beta = 1/(k_{\mathrm{B}}T)$ and $\langle\omega\rangle_0 = \langle\omega\rangle_{t=0}$. After integration, one obtains

$$\langle\omega\rangle_t - \langle\omega\rangle_0 = \beta\hbar\sigma^2\left[S_2(t) - 1\right] \tag{C.2}$$

where $\sigma^2 = \langle(\delta\omega)^2\rangle$, and $S_2(t) = \frac{\langle\delta w(t)\delta w(0)\rangle}{\langle(\delta\omega)^2\rangle}$ is the time equilibrium correlation function. From Eq. (C.2), one immediately gets $S_\Omega(t) = S_2(t)$.

C.2 Width dynamics

The spectral linewidth, $\sigma(t)$, at time t is given by the relation

$$\sigma^2(t) = \langle\omega^2\rangle_t - (\langle\omega\rangle_t)^2 \tag{C.3}$$

One can obtain the linear response prediction for the evolution of spectral linewidth to the perturbation $H'(t) = \hbar\omega(t)\theta(t)$ by integrating the following equations from the Kubo-Zwanzig linear response approximation:

$$\langle\omega^2\rangle_t - \langle\omega^2\rangle_0 = -\beta\hbar \int_{-\infty}^{t} \langle\omega(t-s)^2\dot{\omega}(0)\rangle\theta(s)ds \tag{C.4}$$

where $\beta = 1/(k_{\mathrm{B}}T)$ and $\langle\omega\rangle_0 = \langle\omega\rangle$ and the statistical averages in the angular brackets are over the equilibrium ensemble described by the Hamiltonian H_g.

After integration of Eq. C.4, one obtains

$$\langle\omega^2\rangle_t - \langle\omega^2\rangle_0 = \beta\hbar\langle\omega(t)^2\omega(0)\rangle - \beta\hbar\langle\omega^3\rangle \tag{C.5}$$

The above equation can be re-written as

$$\langle\omega^2\rangle_t - \langle\omega^2\rangle_\infty = \beta\hbar\sigma^3 S_3(t) + 2\beta\hbar\sigma^2\langle\omega\rangle S_2(t) \tag{C.6}$$

where

$$S_3(t) = \frac{\langle\delta\omega(t)^2\delta\omega(0)\rangle}{\langle\delta\omega^2\rangle^{3/2}} \tag{C.7}$$

Making use of Eqs. C.2 and C.5 one can obtain

$$\begin{aligned}(\langle\omega\rangle_t)^2 - (\langle\omega\rangle_\infty)^2 &= 2\beta\hbar\sigma^2\langle\omega\rangle_0 S_2(t) \\ &\quad + (\beta\hbar)^2\sigma^4\left(S_2(t)^2 - 2S_2(t)\right)\end{aligned} \tag{C.8}$$

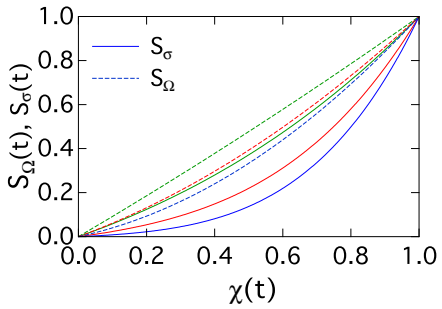

FIGURE C1: $S_\Omega(t)$ and $S_\sigma(t)$ vs. $\chi(t)$ for different values of $\Delta\kappa/\kappa_g$: 0.2 (green), 1.5 (red), and 4 (blue); $\Delta C/C_g = 2$ was kept for all curves.

Figure C1 shows the Stokes-shift and width time correlation functions vs. $\chi(t)$. The deviation from the straight line thus quantifies the distinction between the dynamics of spectroscopic observables and the medium dynamics. The figure illustrates the point made in the main text that the width dynamics is a significantly more sensitive measure of the non-linear chromophore-bath coupling than the Stokes shift dynamics. The latter appears to remain a reliable probe of the medium dynamics even at the conditions of severe nonlinearity.

C.3 $P(q_f, t_f|q_i, t_i)$

Here we present the derivation of the path integral combining the Lagrangian of the stochastic variable satisfying the stochastic Langevin equation of motion with the evolution of the off-diagonal element of the density matrix of the two state system. We first simplify the notation introducing the variable $x = \delta q = q - q_0$ of deviation of q from its equilibrium value q_0 and write the transition frequency in the form[119]

$$\Omega(x) = ax + \tfrac{1}{2}bx^2 \tag{C.9}$$

where $\hbar a = -\Delta C + \Delta\kappa q_g$ and $\hbar b = \Delta\kappa$. In this notation, the propagator we are seeking to calculate is given by the equation

$$\begin{aligned} P(x_f, t_f|x_i, t_i) = &\int_{\{x_f, x_i\}} \mathcal{D}x(\tau) \\ &\exp\left[i\int_{t_i}^{t_f} d\tau\Omega(x) - \int_{t_i}^{t_f} L(x,\dot{x})d\tau\right] \end{aligned} \tag{C.10}$$

The effective Lagrangian defining the equation of motion minimizing the action[255] is then found from the equation

$$\frac{d}{dt}\frac{\partial\tilde{L}}{\partial\dot{x}} - \frac{\partial\tilde{L}}{\partial x} = 0 \tag{C.11}$$

where

$$\tilde{L}(x,\dot{x}) = \frac{1}{4D}(\dot{x} + \gamma x)^2 - i\Omega(x) \tag{C.12}$$

The equation of motion reads

$$\ddot{x} - \epsilon^2 x = \gamma^2 f, \quad f = -2iaD/\gamma^2 \tag{C.13}$$

where

$$\epsilon^2 = \gamma^2 - 2ibD. \tag{C.14}$$

The solution of eq (C.12) with $x_i = x(t_i)$ and $x_f = x(t_f)$ is

$$\begin{aligned} x(\tau) =& x_i\frac{\sinh\epsilon(t_f-\tau)}{\sinh\epsilon\Delta t} + x_f\frac{\sinh\epsilon(\tau-t_i)}{\sinh\epsilon\Delta t} \\ &+ q(\tau-t_i) - q(\Delta t)\frac{\sinh\epsilon(\tau-t_i)}{\sinh\epsilon\Delta t} \end{aligned} \tag{C.15}$$

where $\Delta t = t_f - t_i$ and

$$q(\tau) = f\left(\cosh\epsilon\tau - 1\right) \tag{C.16}$$

According to the standard rules of performing Gaussian path integrals (with the Lagrangian bilinear in the path variable)[255], the result of integration can be obtained by

calculating the action on the trajectory satisfying the equation of motion. The corresponding action (neglecting a constant term affecting normalization) is

$$\begin{aligned} S(x_f, t_f|x_i, t_i) = &- \frac{1}{4D} x\dot{x}\Big|_{t_i}^{t_f} - \frac{1}{4\sigma_q^2}(x_f^2 - x_i^2) \\ &+ i\int_{t_i}^{t_f} d\tau(\Omega(x) - \frac{x}{2}\Omega'(x)) \end{aligned} \tag{C.17}$$

where $D = \gamma\sigma_q^2$ and $\sigma_q^2 = \langle(\delta q)^2\rangle$ were used.

As is easy to see, the term quadratic in x disappears from the integral in eq (C.17) and only the linear term survives. The substitution of eq (C.15) into eq (C.17) leads to the following expression

$$\begin{aligned} S(x_f, t_f|x_i, t_i) = &-\frac{x_f^2 - x_i^2}{4\sigma_q^2} - \frac{\epsilon}{4D}(x_i^2 + x_f^2)\coth\epsilon\Delta t \\ &+\frac{\epsilon}{2D}\frac{x_i x_f}{\sinh\epsilon\Delta t} - \frac{f\tilde{\epsilon}}{2D}(x_i + x_f)\tanh\frac{\epsilon\Delta t}{2} + \psi(\Delta t) \end{aligned} \tag{C.18}$$

where $\tilde{\epsilon} = (\epsilon^2 + \gamma^2)/(2\epsilon)$ and

$$\psi(t) = \frac{f^2}{4\sigma_q^2}\left[\gamma t - \frac{2\gamma}{\epsilon}\tanh\frac{\epsilon t}{2}\right] \tag{C.19}$$

The propagator in eq (C.10) is therefore given in terms of the minimum action in eq (C.18) as

$$P(x_f, t_f|x_i, t_i) = \mathcal{N}\exp\left[S(x_f, t_f|x_i, t_i)\right] \tag{C.20}$$

where $\mathcal{N}$ is a normalization constant.